Multiphase modelling of tissue growth in dynamic culture conditions

Reuben O'Dea, MMath

Thesis submitted to The University of Nottingham
for the degree of Doctor of Philosophy

October, 2007

Abstract

In this thesis, a series of mathematical models suitable for describing biological tissue growth are developed. The motivation for this work is a bioreactor system which provides perfusion and compressive mechanical stimulation to a cell-seeded scaffold; however, the formulation is sufficiently general to be applied to a vast range of tissue engineering applications. Our models are used to investigate the influence of (i) cell-cell and cell-scaffold interactions, and (ii) the mechanical environment, on tissue growth.

In the first part of the thesis, we extend a model due to Franks (2002) (in which the cell and culture medium phases are represented by viscous fluids) by including perfusion and coupling the cells' response to their environment. Specifically, we consider the effect of the cell density and pressure on tissue growth. We analyse the model using analytic and numerical techniques; numerical simulations suggest that comparison of construct morphology in the presence and absence of perfusion provides a means to identify the dominant regulatory growth stimulus.

The solid characteristics of the construct and interactions between the cells and scaffold are necessarily neglected in the two phase model. Guided by this, we develop more complex three phase models. Using numerical simulations, the influence of cell-cell and cell-scaffold interactions is investigated and less porous scaffolds are shown to improve control over cell behaviour. We use the model to compare the cells' response to different regulatory stimuli, including flow-induced shear stress. Our results suggest that uniform initial cell seeding and stimulating cell movement are crucial in maintaining the mechanical integrity of tissue constructs.

We also study the effect of scaffold compression on the mechanical environment of the cells contained within, developing both a classical Biot formulation and a multiphase model. We demonstrate that the bioreactor geometry introduces significant spatial variation in the mechanical stimuli relevant to tissue growth and that such considerations will play a key role in comprehensive models of mechanotransduction-affected growth.

Acknowledgements

I would like, primarily, to thank my supervisors Sarah Waters and Helen Byrne who have provided an enormous amount of help, guidance and encouragement. I owe an especial debt of gratitude to Sarah whose support and patience during the writing-up stage was invaluable. I would like to acknowledge the EPSRC for providing funding for this project and also to thank Gary Mirams for lending his impressive parallel-computing expertise and Hannah Woollard for help with numerical matters.

Thanks are due to my parents for their support and guidance and a roof over my head, and to all my friends (notably to Ollie for unstinting dedication displayed in the pursuit and consumption of coffee), but most especially to Emma, for everything.

"I am so smart! I am so smart! S-M-R-T! I mean S-M-A-R-T... "

H. Simpson

Contents

Chapter 1

Introduction

The growth of biological tissue is a complex phenomenon, resulting from the interaction of numerous processes on several different spatio-temporal scales. Due to its importance in the field of tissue engineering, the study of tissue growth processes has been the subject of a huge range of experimental and theoretical studies (reviews are given by Curtis & Riehle (2001), Sipe (2002), Araujo & McElwain (2004a), Cowin (2000, 2004)). Tissue engineering is the construction, repair or replacement of damaged or missing tissue. This thesis is concerned with *in vitro* tissue engineering, which is the logical extension of transplant surgery, and involves growing replacement tissue outside the body in a bioreactor from a sample of healthy cells (in the context of tissue engineering, a bioreactor is an advanced tissue culture apparatus). This approach has the potential to alleviate the chronic shortage of tissue available from donors.

The motivation for the work contained in this thesis is a bioreactor system being employed at the Institute for Science and Technology in Medicine (ISTM), Keele University, which provides both perfusion and macroscale compression to a culture of human-derived bone cells contained within a poly(L-lactide) (PLLA) scaffold. In a wider context, the applications of this study within the field of tissue engineering are myriad, aspects of the models being relevant to biological systems in which the influence of the mechanical environment on the cells' response is of interest, such as bone, muscles and blood vessels. In the following introduction, and in the remainder of this thesis, we concentrate upon the applications of this work associated with the above bioreactor system and its pertinence to bone tissue culture; however, the broader relevance of the model predictions to tissue engineering is also discussed.

In this chapter, a general introduction to human bone physiology and tissue engineering is presented and the relevant experimental and theoretical literature is reviewed. In

addition, a general multiphase model is presented, and an illustrative derivation of the volume-averaged mass and momentum conservation equations for a two phase system is given; in each case, relevant modelling considerations are discussed. This multiphase formulation (in a number of simplified incarnations) will be employed in subsequent chapters of this thesis.

1.1 Biological background

The human skeletal system performs many important functions; in addition to providing support, protection and allowing movement, it is responsible for blood cell production and mineral storage. Human bone is organised into three distinct regions. The *periosteum*, a dense membrane of fibrous tissue containing blood vessels and nerves, covers the outer surface of all bone except the articular surfaces (the surfaces of joints), which are covered by a synovial membrane. The next layer is *cortical*, or compact, bone which consists of closely packed *osteons* and accounts for approximately 80% of skeletal bone mass (Salgado *et al.*, 2004). Osteons comprise a central Haversian canal containing blood vessels (which interconnect with vessels in the periosteum via Volkmann's canals), surrounded by concentric rings of matrix called *lamellae*; between the lamellae are small spaces known as *lacunae*, connected by tiny channels known as *canaliculi*. The innermost layer is *cancellous*, or spongy, bone which accounts for approximately 20% of bone mass and is less dense than cortical bone, consisting of plates (trabeculae) and bars of bone. This organisation is shown in figure 1.1a; a cross-section of cortical bone illustrating the central Haversian canal and lamellar/lacunar structure is shown in figure 1.1b.

The remodelling of bone tissue results from the interaction of three cell types: *osteoblasts*, *osteocytes* and *osteoclasts* (Berne & Levy, 1993; Salgado *et al.*, 2004). Bone resorption (the destruction, disappearance, or dissolution of bone by biochemical activity) is effected by osteoclasts, which adhere to the surface of cortical and cancellous bone on the yet unmineralised matrix (Kaspar *et al.*, 2000). These cells form a moving resorption front in the existing bone, along the direction of dominant daily loading, which is subsequently filled with new bone derived from osteoblasts. Osteoblasts are responsible for extracellular matrix (ECM) deposition and mineralisation (Mullender *et al.*, 2004; Salgado *et al.*, 2004) and extrude collagen into the adjacent extracellular space; the interaction between these two cell types causes new osteons to be aligned along the direction of predominant loading (Bakker *et al.*, 2004). Slowly, mineralised bone accumulates around the osteoblast, which

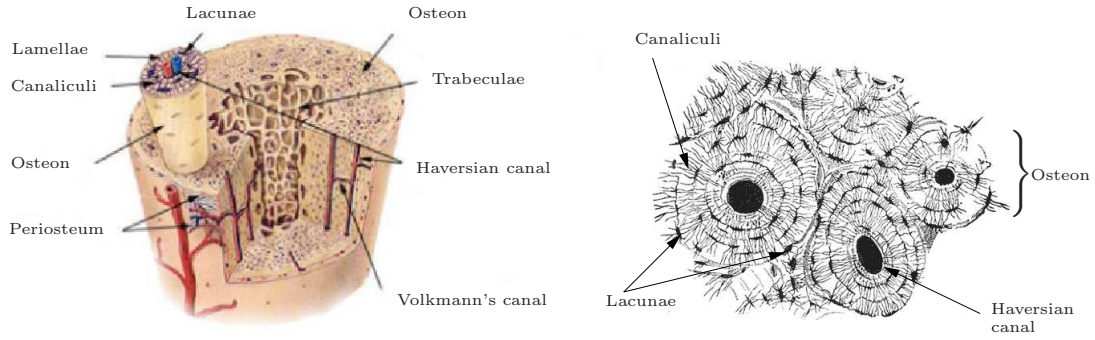

(a) (b)

Figure 1.1: (a) A schematic showing the hierarchical structure of bone, illustrating its layered and osteonic structure and, (b) a cross section of cortical bone showing the Haversian canal and lamellar/lacunar structure. Figures taken from Young *et al.* (2006) and Gray (2000) respectively.

decreases its synthetic activity causing it to become an interior osteocyte (Berne & Levy, 1993); osteocytes are terminally-differentiated human bone cells, located in the lacunae of cortical bone. The interconnecting canaliculi are filled with interstitial fluid; additionally, osteocytes have several thin cell processes which extend into these channels. The cell processes are structurally similar to intestinal microvilli, although they are an order of magnitude longer (Han *et al.*, 2004). The canalicular system, therefore, enables osteocytes to communicate with each other and to exchange substances via diffusion. The role of osteocytes in bone remodelling is controversial; however, there is a growing consensus that they are the most mechanosensitive cells in bone and direct the formation and resorption of bone tissue at the microscopic level (Noble & Reeve, 2000).

1.2 Bone tissue engineering

Each year approximately one million cases of serious skeletal defect require a bone-graft procedure (Salgado *et al.*, 2004). Autologous bone grafts (taken from the patient's own body) provide the greatest percentage of success; however, both the range and type of cases in which this technique may be applied are severely restricted due to limited graft availability and donor site morbidity. An alternative strategy is allograft (graft from another individual); however, the rate of graft incorporation is lower and the possibility of immune rejection and pathogen transmission is increased (Cerroni *et al.*, 2002; Salgado *et al.*, 2004). In cases for which bone grafts are impractical, artificial implants, which are typically metal

or ceramic, may be used. These materials present a number of disadvantages: metal implants provide adequate mechanical support but exhibit poor integration with tissue and can fail due to infection or fatigue loading; in contrast, ceramics are brittle, have low tensile strength and may not be subjected to significant levels of torsion, bending or shear (Salgado *et al.*, 2004).

It is clear, therefore, that an adequate replacement for bone is urgently needed to meet the demands of patients. Tissue engineering has the potential to provide a valid solution to the problems discussed above. In contrast to the classic biomaterials approach, tissue engineering is "based upon the understanding of tissue formation and regeneration, and aims to induce new functional tissues, rather than just to implant new spare parts" (Salgado *et al.*, 2004). In the following sections, a brief introduction to tissue engineering is given.

1.2.1 Tissue engineering - an introduction

The aim of tissue engineering is to repair or replace tissues and organs by delivering implanted cells, scaffolds, DNA and proteins at surgery (Butler *et al.*, 2000). Broadly, there are two approaches to tissue engineering: *in vivo* and *in vitro* tissue engineering.

In vitro tissue engineering is the logical extension of transplant surgery and involves growing replacement tissue in a bioreactor from a sample of healthy cells (in the context of tissue engineering, a bioreactor is an advanced tissue culture apparatus; bioreactors for tissue engineering applications will be discussed in more detail in later sections of this chapter). This approach has the potential to alleviate the chronic shortage of tissue available from donors and, where autologous cells are used, allows replacement organs or tissues to be implanted with reduced risk of rejection and disease transmission (Curtis & Riehle, 2001).

In contrast, *in vivo* tissue engineering uses the human body as a bioreactor. One approach is to implant a biodegradable porous scaffold into the relevant area which is populated by cells either spontaneously by the body or by cellular augmentation (the scaffold is artificially seeded with cells prior to *in vivo* implantation) (Zdrahala & Zdrahala, 1999). The scaffold then degrades, leaving a re-formed tissue behind. Alternative approaches include injecting cells contained within a gel into the affected area. The use of injectable gels has some advantages over pre-formed scaffolds in the context of *in vivo* tissue engineering, including the ability to fill any shape of defect and the ease of inclusion of agents such as growth factors; see Gutowska *et al.* (2001) for a review of different gels and their applications in tissue engineering. Where *in vivo* defects are small and self-contained, introduction

of tissue growth-inducing substances (such as growth and differentiation factors) to the appropriate location may be sufficient (Ma, 2004). These approaches could have considerable benefits over *in vitro* tissue engineering since the human body naturally offers the correct physical and biochemical cues to enable creation of functional, viable tissue; however, the mechanisms by which these cues are employed by the cells are not well understood. A thorough review of *in vivo* tissue engineering considerations is given by Zdrahala & Zdrahala (1999).

The engineering of scaffolds with appropriate physical and biochemical properties which induce the cells to populate the scaffold and prevent de-differentiation (regression of cells from a specialised state to an earlier developmental stage) poses significant challenges, being hampered by both the lack of information about the regulation of cellular function and problems with cell population expansion (Sipe, 2002). These challenges have inspired many experimental studies, including the bioreactor system used in the ongoing study at ISTM, Keele University which is the focus of the theoretical work contained in this thesis (more details regarding this system will be given in §1.2.3).

The concept behind tissue engineering is relatively simple; however, practically it poses a great many problems. In addition to the problems discussed above, procuring sufficient numbers of cells whilst minimising morbidity at the donor site is a non-trivial process, confounded by the fact that these cells may have insufficient ability to proliferate or undergo differentiation. Consequently, research is increasingly being focused on tissue generation using tissue precursor cells or multipotent stem cells (Risbud & Sittinger, 2002). These cells have high proliferative capacity and can be induced to differentiate to a number of different cell types; of particular interest to bone tissue engineering applications is the study of Buttery *et al.* (2001) in which osteoblasts were derived from embryonic stem cells. The literature regarding the use of stem cells in tissue engineering and, for instance, the methods by which they can be induced to differentiate along different cell lines is extensive; a good introduction to this field is given by Salgado *et al.* (2004) and references therein. We choose not to give a thorough review of this literature here since implicit in the mathematical models that we develop in this thesis are the assumptions that, on the timescale of interest, the cell population has sufficient proliferative capacity and is unable to de-differentiate.

A wide variety of cell culture techniques is employed in *in vitro* tissue engineering. Monolayer culture, which involves growing a single layer of cells on a two-dimensional surface, is the simplest and cheapest method and has, therefore, been widely used; however, it has been noted that a feature of this method is rapid cell de-differentiation and loss of

tissue-specific function (*e.g.* Hamilton *et al.* (2001) and others, who observed that monolayer culture of liver cells results in rapid loss of liver-specific function). It has been widely reported that some semblance of *in vivo* cellular organisation is required in order that viable tissue constructs be produced (Powers *et al.*, 1997). To this end a number of authors have investigated the benefits of the following culture techniques:

1. Co-culture of different cell types to mimic the *in vivo* environment (*e.g.* Yagi *et al.* (1995), Yoffe *et al.* (1999), Bhandari *et al.* (2001), Riccalton-Banks *et al.* (2003) and Higashiyama *et al.* (2004) in which the effect of co-culture of two types of liver cells was investigated, finding that the longevity of liver-specific function was significantly enhanced when co-culture was employed);

2. culture as multicellular spheroids, which maximises cell-cell contacts and has been found to positively affect functionality and biochemical properties (*e.g.* Yoffe *et al.* (1999), Hamilton *et al.* (2001), Ma *et al.* (2003) and Riccalton-Banks *et al.* (2003));

3. creation of engineered tissue constructs via culture on artificial scaffolds, whose surface chemistry and pore size may be altered to encourage cell anchorage or increased population of the scaffold by the cells and the use of which lends improved mechanical integrity to the construct (*e.g.* Yamada *et al.* (2001) and Karp *et al.* (2004)).

The latter technique is especially important in bone tissue engineering applications where the three-dimensional architecture and material properties of the tissue are important (Salgado *et al.*, 2004) and in the creation of engineered constructs of appropriate size for implantation (Ma, 2004). Due to the importance of the scaffold to the creation of viable tissue, we pause to highlight some of the key characteristics it must display for tissue engineering applications. We remark that these include aspects of the scaffold relevant to implantation *in vivo*.

The most obvious requirement is that of *biocompatibility*: the scaffold should permit cell life and should not elicit an immune response in the host (Curtis & Riehle, 2001; Salgado *et al.*, 2004). Secondly, the scaffold must be *porous*. A highly porous, interconnected structure facilitates cell penetration thoughout the scaffold and vascularisation of the construct from surrounding tissue. Additionally, this promotes good transfer of nutrients and waste products through the scaffold; this is of particular importance to bone tissue engineering (in contrast to, for instance, cartilage) where relatively high rates of mass transfer are expected following *in vivo* implantation due to, for example, vascularisation (Freed & Vunjak-Novakovic, 1998). It is well accepted that a pore size of 200-900μm

is appropriate for bone tissue engineering (Salgado *et al.* (2004) and references therein). Cerroni *et al.* (2002) report a number of threshold pore size values: a pore size of less than 10μm inhibits cellular in-growth; 15–50μm helps vascular and fibrous tissue colonisation; 150μm or greater facilitates mineralised bone formation. Holy *et al.* (2000) report bone tissue growth and mineralisation throughout three-dimensional scaffolds with macroporous interconnected structure with pore size ranging from 1.5-2.2mm. These scaffolds allow cell, tissue and blood vessel in-growth; however, the large pore size will have implications for the mechanical properties of the scaffold which are clearly of great importance in bone tissue engineering applications (Salgado *et al.*, 2004).

As indicated above, the surface properties, both chemical and topographical, of the scaffold are important. Most normal cells are anchorage-dependent, their growth being affected by interaction with the ECM or a substrate (Freed & Vunjak-Novakovic, 1998). Indeed, it is clear that the ECM is an important growth regulator; as a result of ECM attachments, cell-surface receptors transduce biochemical signals to the nucleus using the same intracellular signalling pathways as those used by growth factor receptors (Huang & Ingber, 1999). Cells may adhere to surfaces with forces that are three or four orders of magnitude greater than their own weight; furthermore, cells can control this adhesion and some have the ability to detach from a surface of their own volition (Cowin, 2000). Appropriate surface chemistry enables cells to adhere effectively to the scaffold as well as aiding cell/scaffold protein interactions and directing cell differentiation (Salgado *et al.*, 2004); for example, scaffolds may be engineered to deliver growth factors or DNA (Sipe, 2002), or to contain specific cellular recognition molecules (Freed & Vunjak-Novakovic, 1998). Additionally, the topographical properties of the scaffold surface may be altered to encourage and direct cell movement; for example, cell locomotion is guided and enhanced by straight edges or long fibres within the scaffold. This phenomenon is known as contact guidance (Anselme, 2000; Cowin, 2000). Lastly, the scaffold must be *biodegradable*; furthermore, the rate of degradation must match that of nascent tissue growth so that the scaffold is completely degraded by the time the injury site has fully regenerated (Ma, 2004; Salgado *et al.*, 2004).

In addition to the biochemical environment, cell cultures are greatly affected by the *mechanical* environment. In the following section we give a brief introduction to the mechanosensory ability of bone tissue and its implications for the viability of bone tissue cultures.

1.2.2 Mechanotransduction

The mechanism by which forces are converted into biochemical signals and integrated into cellular responses that influence, for example, gene expression, protein synthesis, cell proliferation and morphogenesis, is referred to as *mechanotransduction* (Walsh *et al.*, 2004). The stresses experienced by cells can be *residual*, arising due to incompatibility of growth strains in the tissue (Skalak *et al.*, 1996; Araujo & McElwain, 2004b, 2005a); alternatively, they can be the result of external loading. The importance of mechanical stimuli to tissue function is noted by many authors including Fung (1991), who asserts that the correct function of organs is dependent on the level of internal stress. Indeed, the way in which cells respond to mechanical forces is "critical in homoeostasis and in many diseases" (Huang *et al.*, 2004) (homoeostasis is the term given to the regulation of a system's internal environment to maintain a stable state and is crucial in the functioning of biological organisms). For example, the response of vascular endothelial cells to mechanical stimulation associated with blood flow (*e.g.* cell remodelling) constitutes a homoeostatic mechanism which aids in the prevention of atherosclerosis (an inflammatory vascular disease) (Chien, 2007).

Understanding the molecular basis for mechanotransduction requires detailed knowledge of the force distribution within individual cells at a molecular level; the discovery of the way in which these forces influence the cell response will provide new insight into many tissue engineering applications. To this end, many authors have used a wide range of techniques to investigate the effect of mechanical stimulation at the individual-cell level; the cellular response is multifaceted and diverse. Furthermore, the mechanochemical environment required for optimum growth will be peculiar to the tissue under consideration. This inherent complexity is exacerbated by the non-linear nature of the cellular response to mechanical stimulation. For example, Helmke *et al.* (2003) report that the displacements within a cell resulting from haemodynamic shear stress occur in many directions, being only weakly correlated with the direction of stress application, suggesting that the transmission of force within a cell is highly complex. We do not give a thorough review of the literature pertinent to intracellular force transduction pathways and their influence on cell response since we employ a continuum model in this work, assuming that the gross result of these effects is captured on the macroscale; however, the reader is directed to Huang *et al.* (2004) for a review of some of this literature, including discussion of transduction pathways, cell probing techniques and the molecular responses of cells and tissues to mechanical stimuli.

In summary, it is clear that mechanical stimuli are crucial in the formation of functional tissue *in vivo*; despite a great many "proof of principle" studies illustrating the beneficial

effect of mechanical conditioning on the structural and functional properties of engineered tissues, little is known about either the manner in which these forces should be applied for specific tissues or how these stimuli are employed by the cells (Martin *et al.*, 2004). It is, therefore, of great value to tissue engineers to identify these mechanisms (via theoretical and experimental studies) so that appropriate methods can be employed to produce functional tissues *in vitro* for implantation.

Under normal physiological conditions, bone tissue is inevitably exposed to a variety of mechanical stresses and strains imposed by muscular contractions, body movement and external loading and it has been widely reported that mechanical stimulation has an important effect on bone adaptation and formation (You *et al.*, 2000). Placing patients with broken limbs under traction to prevent incorrect bone repair or misshapen bones is a simple example of this phenomenon and has been practised in hospitals for many years. The ability of bone tissue to adapt functionally to its mechanical environment depends upon the ability of bone cells to sense and respond to mechanical stimuli. There are two theories in the literature regarding these mechanosensory mechanisms. The first is that cells respond directly to the mechanical strain they experience as a result of physiological loading. This has been investigated by a number of authors using substrate deformation to stretch bone cells with promising results (*e.g.* Kaspar *et al.* (2000, 2002) showed that cyclic substrate deformation of physiological magnitudes causes increased osteoblast proliferation); however, many studies have been criticised for employing strains well in excess of those encountered *in vivo* or for employing stimulatory systems that induce unintended physical effects such as fluid flow (You *et al.*, 2000).

Mineralisation of the ECM makes bone tissue extremely stiff; as a consequence, bone tissue experiences very low strains (0.03–0.4%) under physiological loading (Rubin & Lanyon, 1984; Klein-Nulend *et al.*, 1995b; Fritton *et al.*, 2000). A fundamental paradox in bone tissue remodelling is that these tissue-level strains resulting from physiological loading are far smaller than those required to initiate cellular responses directly; using *in vitro* experiments, many authors have reported that under substrate straining comparable to that encountered *in vivo* during vigorous exercise, no biological response of the bone cells is observed and substrate strains are required to be at least an order of magnitude larger (1-10%) in order for a biological response to occur; such large strains *in vivo* would result in bone fracture (Klein-Nulend *et al.*, 1995b, 1998; You *et al.*, 2000; Han *et al.*, 2004). To resolve this, a second theory has been proposed, summarised as follows. Mechanical loading of bone causes a flow of interstitial fluid through the canalicular network and the resulting fluid drag forces,

acting on osteocyte cell processes, allow these cells to amplify the small strains encountered within the calcified matrix, encouraging increased metabolic activity and longevity of these cells (Klein-Nulend *et al.*, 1995b, 1998; You *et al.*, 2000; Bakker *et al.*, 2004; Han *et al.*, 2004).

A number of theoretical studies of bone tissue mechanosensory mechanisms strongly indicate loading-induced fluid shear stress as a mechanical stimulus for bone remodelling; for example, Weinbaum *et al.* (1994), You *et al.* (2001) and Han *et al.* (2004) show that fluid drag forces acting on cell processes are able to produce cell-level circumferential strain of two orders of magnitude greater than the whole tissue strain. This, along with ultrastructural analysis of the structural components around osteocytes *in vivo* (You *et al.*, 2004) and a growing body of theoretical and experimental studies, suggests that the lacunar-canalicular fluid flow is likely to be the dominant mechanosensory mechanism.

Experimental studies that directly compare the effects of fluid flow and mechanical strain on bone cells include Owan *et al.* (1997), Smalt *et al.* (1997) and Mullender *et al.* (2004) in which it is shown that cells are more sensitive to flow stimulation. These studies employed monolayer culture; in the following section, we introduce a bioreactor system which provides both perfusion with culture medium and compressive mechanical stimulation to a *three-dimensional* tissue construct. This study is the motivation for the work contained in this thesis.

1.2.3 A bioreactor system for bone tissue engineering

A significant problem with the three-dimensional culture techniques described above (§1.2.1) is that limitations in the diffusion of nutrients and waste products through large constructs often result in the formation of a tissue construct with viable, proliferating cells at its periphery but a necrotic core. Necrosis refers to accidental cell death due to (for instance) insufficient oxygen or nutrients, injury and infection, as distinct from apoptosis which is part of programmed cell death. Early studies have shown that cellular spheroids of diameter greater than 1mm generally develop a necrotic core (Sutherland *et al.*, 1986). Engineered constructs must be relatively large to serve as grafts for tissue replacement; it is clear, therefore, that mass-transfer limitations represent one of the greatest challenges for *in vitro* tissue engineers (Martin *et al.*, 2004). To rectify this, bioreactors are widely used to improve nutrient supply and waste removal, employing perfusion and circulation/mixing strategies to improve mass transfer within the culture; additionally, bioreactors allow monitoring and control of factors such as pH, and the provision of growth factors and other cell-signalling

molecules.

For tissue engineering applications, bioreactors must fulfil a further requirement: they must provide physiologically relevant loads to the tissue (Cartmell & El Haj, 2005) so that, via the mechanotransduction process described above, functional, viable tissue constructs are produced. This is particularly important in bone tissue engineering where load-bearing is a major requirement for any replacement tissue (Cartmell & El Haj, 2005). A variety of different bioreactor systems has been developed to provide mechanical stimuli to cells. A common method of applying mechanical loading to cells is via fluid shear stress. A frequently used example of this in monolayer culture is a parallel plate flow chamber in which the fluid is forced across the cell monolayer by a pressure gradient; the flow may be steady, oscillatory or pulsatile. In three-dimensional culture, fluid shear stimulation may be achieved using spinner flasks, rotating wall vessels or perfusion systems. Macroscale mechanical stimulation may also be provided via application of tensile or compressive forces to tissue constructs or, in monolayer culture, by substrate deformation. Alternatively, cell-scale forces may be applied via magnetic particles embedded in the cell membrane: application of an oscillatory magnetic field causes a strain and torque to be applied to the cell (Hughes *et al.*, 2007). A thorough review of these bioreactor systems and others is given in Martin *et al.* (2004) and Cartmell & El Haj (2005).

El-Haj *et al.* have employed a bioreactor system which allows a culture of cells in a PLLA scaffold to be subjected to simultaneous perfusion with media and direct compression using a piston (see, for example, El-Haj *et al.* (1990)); see figure 1.2. The system comprises a cell-seeded scaffold within a culture medium-filled cylinder along which a flow is driven. This system allows mechanical stimulation via fluid shear, pressure and direct mechanical force application and is currently being applied to osteoblast cultures at ISTM, Keele University. The cell-seeded PLLA scaffold has a diameter of 9mm, length 4mm and mean porosity of 97% (Freyria *et al.*, 2005). Perfusion is effected using a peristaltic pump at a rate of 0.1ml/min and the piston subjects the PLLA scaffold to a periodic strain of amplitude 1.5% at 1Hz. In this study, following three weeks of static culture, cell-seeded constructs are placed in the bioreactor and subjected to compression for one hour per day for one week.

The structure of the PLLA scaffold employed in this study is highly heterogeneous; figure 1.3a shows the cross section-averaged porosity along the axial length of a typical PLLA scaffold of the type employed in this study, evaluated using microfocus computer tomography (μCT). Figure 1.3b shows the typical decrease in averaged porosity following

culture, indicating the level of mineralisation in such a scaffold.[1]

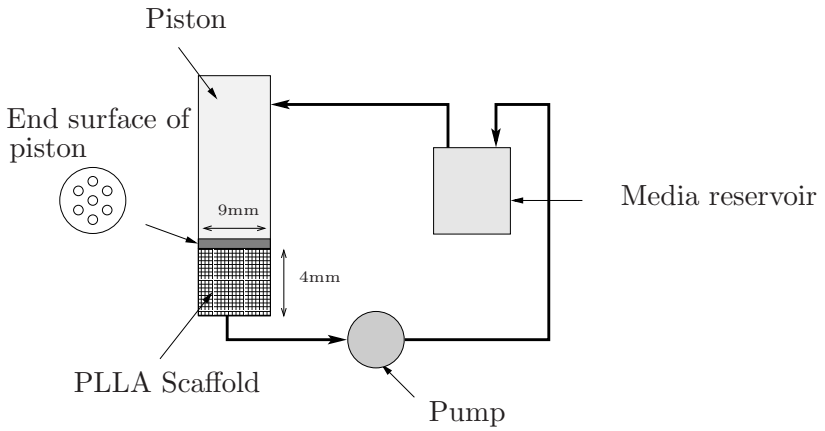

Figure 1.2: The compression/perfusion system of El-Haj *et al.*

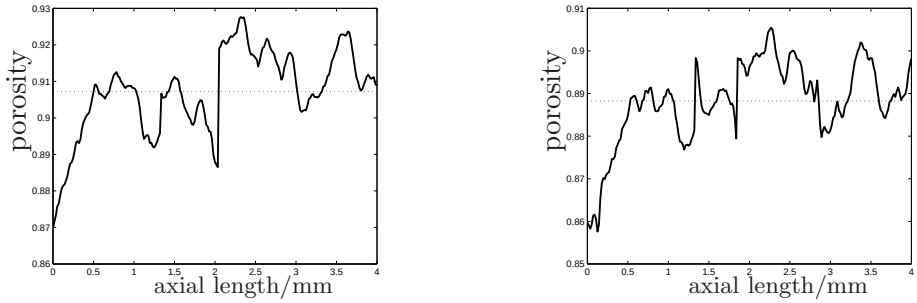

(a) (b)

Figure 1.3: The axial variation of the cross section-averaged scaffold porosity (–) and the mean scaffold porosity ($\cdots$) (a) before and, (b) after culture.

In this thesis we formulate a mathematical model relevant to the growth of a tissue construct within such a dynamic culture environment. We neglect the effect of nutrient availability on the growth and morphology of a tissue construct, assuming that perfusion provides an abundant supply of nutrient; instead, our focus is on the effect of the mechanical environment on tissue growth. Our modelling framework is used to investigate the influence of (i) cell-cell and cell-scaffold interactions and, (ii) the local mechanical environment, on the evolution and eventual morphology of a tissue construct. In particular, we consider in detail the effect of flow-induced mechanical stimulation on the phenotypic progression of the cells as well as macroscale mechanical compression. The results of our investigations are interpreted in the context of the above tissue culture system but are also of relevance

[1]We are grateful to E. Baas, ISTM, Keele University for the provision of this data.

to more general *in vitro* tissue engineering applications.

1.3 Mathematical background

In this section we review some of the mathematical models in the literature which are pertinent to the modelling of tissue growth within a dynamic culture environment.

In constructing a deterministic mathematical model for the dynamics of a cell population, one must decide whether to formulate it by considering the interactions between individual cells in the population or whether to consider the system as a continuum. Stochastic modelling of biological systems is a wide field of research, lending itself naturally to complex biological systems such as the modelling of subcellular biology and gene networks; however, we eschew a review of this literature here since we employ deterministic techniques in this thesis.

Formulating a model based upon the interactions of individual cells, demands that the position and velocity of each individual within the system must be considered, whilst in the continuum case, "averaged" quantities are considered. Individual cell-based models provide comprehensive and detailed information about the dynamics of the cell population and offer distinct advantages over continuum-based modelling; for example, the ease of inclusion of specific rules governing cell behaviour and the ability to track the movement of individual cells (Armstrong *et al.*, 2006); however, since the behaviour of each cell must be considered (realistic simulations demand large numbers of cells), these models are extremely complex and heavily reliant on numerical simulations. In contrast, continuum models may be expressed in terms of a system of partial differential equations (PDEs), allowing the mathematical techniques of PDE theory to be exploited, and in some cases this allows analytic or asymptotic solutions to be obtained, as well as numerical simulations. We therefore employ a continuum model in this thesis in order to exploit this ease of analysis. We remark, however, that this approach can make validation difficult since experimental data may be presented in terms of discrete individuals. In this case, the relevant model parameters may be directly measureable, and an important consideration in continuum-based modelling is relating these measureable individual-based parameters to those that appear in continuum models.

Perhaps the most well-known subject for individual-based mathematical models is the slime-mold *Dictyostelium discoideum*. This organism has been widely used as a model system for studying many aspects of basic developmental processes including cell-cell signalling,

signal transduction, pattern formation and cell motility and aggregation. Palsson & Othmer (2000) and Palsson (2001) presented an individual-based model in which each cell can adhere to neighbouring cells, is able to generate an active motile force and may deform (whilst conserving its volume); the individual cell's response was determined by its internal parameter state and the external environment (which may include, for example, interactions between adjacent cells, ECM or chemical signals). Additionally, a great many continuum models have been presented to model this system, based on the chemotaxis-based model of Keller & Segel (1970, 1971); see Luca *et al.* (2003) for a thorough review of chemotaxis models.

Mathematical models which consider explicitly the mechanical forces experienced by a single cell in the context of mechanotransduction include those developed by Tracqui & Ohayon (2004), in which the distribution of intracellular stresses due to magnetic twisting cytometry was investigated; and McGarry *et al.* (2004) who compared the deformation produced when a cell is exposed to fluid shear stress or substrate strain. Both of these studies used a finite element method to compute the cellular response.

The finite element method has been widely used to compute the behaviour of tissue engineered constructs; the ease with which three-dimensional simulations may be performed allows consideration of complex geometrical factors such as pore size and shape. Kelly & Prendergast (2003) investigated the effect of a core of underdeveloped tissue within a construct on its material properties using a bi-phasic poroelastic model in the context of cartilage tissue. Inhomogeneity of the construct was shown to reduce dramatically its mechanical integrity. Adachi *et al.* (2006) developed a poroelastic model to study the effect of the interplay between bone tissue growth and scaffold degradation due to hydrolysis on the mechanical function of the tissue/scaffold construct. The influence of pore shape on the construct response was investigated and the results applied to create a framework for optimal design of a porous scaffold microstructure. Jaecques *et al.* (2004) exploited μCT in tandem with finite element solution techniques to calculate the stress and strain distribution within bone; again, procedures to optimise scaffold design were discussed.

In this thesis, we analyse our model equations using a combination of analytic and numerical techniques. In the main, numerical solutions are obtained using the finite-difference method; however, the ease with which mesh-refinement may be performed using the finite-element software COMSOL Multiphsyics is exploited in Appendix B.1 to validate our simulations.

A simple continuum model for ECM deposition by cells in response to the local concen-

tration of a single diffusible nutrient (in this case, oxygen) within a polymeric scaffold was presented by Obradovic *et al.* (2000), using the deposition of glycosaminoglycans (GAG) as an indicator of matrix regeneration. The concentrations of oxygen (O_2) and GAG were modelled using diffusion equations as follows:

$$\frac{\partial C_i}{\partial t} = D_i \nabla^2 C_i + q_i, \tag{1.1}$$

wherein C_i represents the concentration and D_i, the diffusion coefficients of each chemical species ($i = O_2, G$ respectively). The oxygen consumption/GAG synthesis rates, q_i, were assumed to be of the following form:

$$q_{O_2} = -\frac{\rho Q_m C_{O_2}}{C_m + C_{O_2}}, \qquad q_G = \rho k \left(1 - \frac{C_G}{C_\infty}\right) C_{O_2}, \tag{1.2}$$

where ρ is the cell density, Q_m is the maximum oxygen consumption rate, C_m is the C_{O2} concentration when the O_2 consumption rate is half-maximal, k represents the rate of GAG synthesis and C_∞ is the maximum GAG concentration. The predicted GAG concentration was shown to be in good qualitative agreement with experiment, and the study concluded that variation in oxygen tension leads to the development of spatial heterogeneities in engineered constructs. A similar mathematical model was employed by Lewis *et al.* (2005) to show that cell-scaffold constructs which rely solely on diffusion for oxygen supply will produce constructs with heterogeneous tissue growth concentrated around the construct periphery. A great many other studies have considered the effect of limited nutrient availability and/or the presence of inhibitors on tissue growth (for example Greenspan (1972), Maggelakis (1990) and Byrne & Chaplain (1995) have considered such effects in the context of tumour growth). In this thesis, however, we consider tissue growth within a nutrient-rich environment, neglecting the effect of nutrient availability on the growth and morphology of a tissue construct.

Of greater relevance to the work contained in this thesis are models derived using a multiphase approach. The above studies (Greenspan, 1972; Maggelakis, 1990; Byrne & Chaplain, 1995; Obradovic *et al.*, 2000; Lewis *et al.*, 2005) model the tissue as a homogeneous mass; however, biological tissue is a composite material, formed of "a collection of cells and ECM" (Cowin, 2000) as well as accompanying interstitial fluid. A distinguishing feature of many biological systems is the complex interaction between these different constituent materials; furthermore, the tissue composition may change over time due, for instance, to metabolism, mitosis, apoptosis, necrosis and (de-)differentiation (Lemon *et al.*, 2006). Multiphase models allow explicit consideration of these interactions. Each material

constituent is considered as a distinct phase within a multiphase material with attendant constitutive laws describing its material properties and its interactions with neighbouring phases; the inherent complexity of this approach is reduced by an averaging process (a discussion of the averaging method together with a derivation of averaged mass and momentum conservation equations for a multiphase material is given in §1.4), which effectively removes the interfaces between the phases, the governing equations for each phase now holding everywhere within the material. Derivation of multiphase models has been given extensive treatment by many authors including Bowen (1982), Marle (1982), Whitaker (2000), Kolev (2002), Araujo & McElwain (2005a), and for two-phase flows, Drew (1971, 1983), Drew & Segel (1971).

Galban & Locke (1999) analysed a simple two phase model for cell growth and nutrient diffusion in a polymer scaffold. A single, averaged reaction-diffusion for the nutrient concentration in the two phase system was derived using a volume-averaging method and the effective diffusion coefficient and reaction rate was calculated as a function of the local cell volume fraction. The cell volume fraction was determined (as a function of time) by considering an appropriate cell mass balance equation. Many two phase *fluid* models for tissue growth have been presented (*e.g.* Landman & Please (2001), Breward *et al.* (2002), Franks (2002), Franks *et al.* (2003) and Byrne *et al.* (2003) which have investigated tumour growth); however, the applicability of these fluid-based models is restricted to cases for which the solid characteristics of the tissue are unimportant. Furthermore, these models are unable to capture the genesis of residual stresses within a growing tissue which arise due to incompatibility of growth strains (Skalak *et al.*, 1996; Araujo & McElwain, 2004b, 2005a).

Jones *et al.* (2000) considered the stresses induced by non-uniform tissue growth within a linear-elastic framework using a single phase model within the context of tumour growth. The proliferation of the tumour cells was regulated by the availability of a single diffusible nutrient and the calculation of the stress generated by this spatially-varying isotropic growth was the novel aim of this study. Araujo & McElwain (2004b, 2005b) extended this model to incorporate anisotropic growth, whilst adhering to the linear-elastic assumption of Jones *et al.* (2000). The study showed that growth anisotropy can induce significant stress-relaxation of the type observed in hydrated soft tissues (Araujo & McElwain, 2004b), affording the model many of the advantages of more complex viscoelastic models.

Explicit consideration of the stresses induced by tissue growth within a multiphase context has been investigated by Roose *et al.* (2003). The two phase tissue was modelled

as a poroelastic material consisting of a solid phase, representing the cells and ECM, and a fluid phase, representing the interstitial fluid. To describe the stresses created during tissue growth, the standard stress-strain relationship for poroelastic materials was used and combined with a volumetric tissue growth term as follows:

$$\boldsymbol{\sigma} = -p\,\mathbf{I} - K\eta\,\mathbf{I} + G\left(\nabla \boldsymbol{r} + \nabla \boldsymbol{r}^T\right) + \left(K - \frac{2G}{3}\right)\nabla \cdot \boldsymbol{r}\,\mathbf{I}, \tag{1.3}$$

wherein K and G are the bulk and shear moduli of the tissue respectively, p is the local interstitial fluid pressure, $\boldsymbol{r}$ is the displacement, η represents volumetric growth and $\mathbf{I}$ is the identity matrix. It was shown using this model and experimental evidence that tumour cell size is reduced by internal solid stress build-up.

Araujo & McElwain (2005a) have presented a thorough derivation of the governing equations which form the framework for a multiphase study of the genesis of residual stresses, including the derivation of appropriate constitutive laws consistent with the second law of thermodynamics; these equations were derived for n-phases and features of the system were illustrated using a simple two phase mixture of a linear-elastic solid and an inviscid fluid.

A weakness of the above models is that the polymer scaffold and/or ECM are not treated as distinct phases; rather, many two phase models assume that they may be modelled within a lumped "cell" phase. A multiphase model consisting of three or more phases allows separate modelling of the ECM or polymer scaffold and can include, for example, degradation of the polymer scaffold and deposition of ECM by cells. Lassuex *et al.* (2004) studied a model for tissue growth on a polymer scaffold in which the cells, nutrient and polymer scaffold were treated as distinct phases. Following Galban & Locke (1999), the model was re-cast as a single reaction-diffusion equation governing the evolution of the nutrient concentration within the scaffold. The effective reaction rate and diffusion coefficients appearing in this equation are related to the parameters associated with individual phases through a closure problem. Lemon *et al.* (2006) presented a thorough derivation of the governing equations for a multiphase mixture in which an arbitrary number of phases was considered. Some general constitutive laws were suggested and the implications of including a solid phase discussed. In addition, intraphase and interphase pressures were considered and appropriate functional forms given; these pressures are a manifestation of the forces generated by mechanically active phases. Within this model, intraphase pressures represented cell-cell interactions, whilst interphase pressures modelled cell-scaffold interactions. The model behaviour was illustrated by performing a linear stability analysis (about a constant, homogeneous cell distribution) on a three-phase system comprising a viscous cell

phase, an inviscid interstitial fluid phase and an inert, rigid, scaffold phase. The interplay between the stresses induced by cell-cell and cell-scaffold interactions results in two dynamical regimes depending on the values of the model parameters: either the cells aggregate or they diffuse to a uniform distribution. In a subsequent paper (Lemon & King, 2007), the effect of nutrient depletion was analysed within this framework, showing that increasing cell motility (by reducing the cell-scaffold drag) overcomes the effects of nutrient depletion.

1.3.1 Poroelasticity

To study the stresses induced by, for instance, volumetric tissue growth or mechanical forcing and the effect of this on the cells, one must consider how the tissue deforms. The theory of poroelasticity, which describes the mechanics of porous elastic solids with fluid-filled pores has been widely exploited in soil consolidation, rock mechanics (Biot, 1941) and industrial filtration (Barry & Holmes, 2001). More recently, many studies of biological soft tissue have employed this formulation (*e.g.* Lai & Mow (1980), Gu *et al.* (1999) and many others: some of these authors were cited in the preceding section).

The presence of a fluid within the porous material modifies its mechanical response in the following manner. An increase in pore pressure causes the porous structure to dilate; conversely, compression of the material causes the pore pressure to increase. If this pressure is allowed to dissipate via fluid transport, further deformation of the material takes place (Detournay & Cheng, 1993). A theory of three-dimensional linear poroelasticity consistent with these concepts was first presented by Biot (1941) (and developed further in many subsequent papers), as a theoretical extension of soil consolidation models (in one dimension, Terzaghi (1923); and in three-dimensions, Rendulic (1936)).

The governing equations of Biot were derived using an "effective medium" approach based on traditional solid mechanics theory. In forming a continuum model, an averaging process over a Representative Volume Element (RVE) was used to develop constitutive equations for the fluid-filled material and to determine effective material parameters; the size of the RVE is assumed to be much larger than the lengthscale of the microstructure (Cowin, 1999). Other authors have reformulated essentially the same theory using this approach in increasingly sophisticated forms (including, for example, Rice & Cleary (1976), Carroll (1979) and Thompson & Willis (1991)). In contrast, equations governing the behaviour of fluid-saturated media have also been derived using mixture theory, or multiphase methods; these studies contain the linear poroelasticity equations of Biot as a special case. Much attention has been given to deriving models of multiphase flow in porous materi-

als, especially with respect to the choice of constitutive laws: many authors appeal to the thermodynamics of the multiphase mixture in order to derive appropriate constitutive equations; see Bowen (1982), Katsube (1985), Katsube & Carroll (1987), De Boer (1998) and Ahmadi *et al.* (2003) for a thorough derivation of the governing equations of mixture theory and a discussion of thermodynamic considerations and their application to a fluid-filled porous material.

The multiphase approach presents an advantage over the traditional effective medium approach when a number of different interacting fluid phases are present and in relative motion (Cowin, 1999) since the multiphase formulation naturally lends itself to these systems; self-evidently, this has considerable benefits when modelling biological systems and has been used by many authors (including some mentioned in the literature review given in the preceding section).

The validity of the equations of linear poroelasticity has been called into question (Cleary, 1978). To address this, Burridge & Keller (1981) re-derived the equations of linear poroelasticity using a homogenisation procedure in which the scale of the material's pores was assumed to be small in comparison to the macroscopic scale; periodicity of the material is not assumed. The derivation of these equations is based upon the equations of linear elasticity in the elastic matrix, the linearised Navier-Stokes equations in the pore fluid and appropriate continuity conditions at the solid-fluid interface. It was shown that when the dimensionless viscosity of the fluid is small the equations of Biot (1962a) are obtained; furthermore, the constitutive relations assumed by Biot are confirmed. When the dimensionless viscosity is of order one, the equations obtained are those of a viscoelastic solid, as suggested by Cleary (1978). A similar derivation is given by Skotheim & Mahadevan (2004).

The governing equations and modelling considerations of the Biot model as well as an appropriate multiphase model are given in chapter 6 of this thesis.

1.4 Averaged equations for a multiphase tissue growth model

In many of the above studies, averaging techniques were used to derive the governing equations. In this thesis, we will exploit this method to derive equations which govern the behaviour of the multiphase material. In this section, an illustrative derivation of mass and momentum conservation equations is given using a volume-averaging method; alternative averaging techniques are also briefly discussed.

The aim of averaging is to derive a set of governing equations that describe adequately the macroscopic properties of a multiphase material. The averaging process allows us to obtain macroscopic, continuum-based equations for a multiphase material that do not contain the precise details of the material at the microscopic level, but whose terms are shown to arise from appropriate microscopic considerations (Drew, 1983). Insight can be gained into the types of terms required in the macroscopic constitutive relations which specify the behaviour of each phase (Drew, 1983); furthermore, the resulting macroscopic variables are related to microscopic variables. In classical models of some systems (especially in modelling multiphase transport phenomena in porous media), consistency between the well-understood microscale physics and the macroscale formulation is not achieved; the averaging method ensures correspondence between the well-described microscale physics and the formulation and closure of less-well-understood macroscale models (see Gray & Miller (2005) for a thorough discussion of this issue).

The typical microscopic mass and momentum conservation equations for each phase (in the absence of mass sources) have the form

$$\frac{\partial \rho}{\partial t} + \nabla \cdot (\rho \boldsymbol{u}) = 0, \tag{1.4}$$

$$\frac{\partial}{\partial t}(\rho \boldsymbol{u}) + \nabla \cdot (\rho \boldsymbol{u}\, \boldsymbol{u}) = \nabla \cdot \boldsymbol{\sigma} + \rho \mathbf{F}, \tag{1.5}$$

where $\rho(\boldsymbol{x}, t)$ is the density, $\boldsymbol{u}(\boldsymbol{x}, t)$ is the velocity field, $\boldsymbol{\sigma}(\boldsymbol{x}, t)$ is the stress tensor and $\mathbf{F}(\boldsymbol{x}, t)$ is a body force associated with each phase; $\boldsymbol{x}$ is the position vector and t represents time. We remark that the microscopic equations (1.4) and (1.5) for each phase hold only within the region occupied by that phase, whilst the averaged equations for each phase hold *everywhere* in the material. The averaging process therefore smooths the discontinuities present at the interface between phases.

There is a variety of ways in which the microscopic equations may be averaged: Whitaker & Howes (1985) and Whitaker (2000) consider volume-averaged equations, while Kolev (2002) considers volume- and subsequently time-averaged equations. Other commonly-used averages are weighted spatial averages and ensemble averages. Denoting the average of a microscopic scalar field, $\psi(\boldsymbol{x}, t)$, by $\langle \psi \rangle(\boldsymbol{x}, t)$, the aforementioned averages are typically defined as follows:

$$\text{Time average:} \qquad \langle \psi \rangle_1 = \frac{1}{T} \int_{t-T}^{t} \psi(\boldsymbol{x}, t') \mathrm{d}t' \tag{1.6}$$

$$\text{Ensemble average:} \qquad \langle \psi \rangle_2 = \frac{1}{N} \sum_{n=1}^{N} \psi_n(\boldsymbol{x}, t) \tag{1.7}$$

$$\text{Weighted space average:} \qquad \langle\psi\rangle_3 = \iiint_{R^3} g(\boldsymbol{x}-\boldsymbol{x}')\psi(\boldsymbol{x}',t)\mathrm{d}\boldsymbol{x}' \tag{1.8}$$

$$\text{Spatial (volume) average:} \qquad \langle\psi\rangle_4 = \frac{1}{V}\iiint_{V_\alpha} \psi(\boldsymbol{x},t)\mathrm{d}V \tag{1.9}$$

In equation (1.6), T is an averaging timescale that is much smaller than the timescale characterising the process in question; in (1.7), N is the number of realisations of the problem; in (1.8), g is a weighting function; in (1.9), V denotes an averaging volume and V_α denotes the part of that volume occupied by the α phase. Equation (1.9) is known as the "local volume average" of a multiphase mixture; in the following, we derive averaged governing equations using a volume-averaging technique. We remark that thermodynamic relations are not considered in this formulation; in particular, we assume that the interfaces between phases have no thermodynamic properties. For many multiphase flows these considerations are important, especially in the choice of constitutive laws; however, in the following illustrative derivation, we neglect these effects for simplicity and consider a two phase system as in Drew (1983). For a detailed derivation of multiphase flow equations including these considerations see Hassanizadeh & Gray (1993), Gray & Hassanizadeh (1998), Araujo & McElwain (2004b).

In deriving the volume-averaged governing equations for the two phase system defined in figure 1.4, we employ the indicator function approach of Drew (1971, 1983), Drew & Segel (1971) and Gray & Lee (1977) in preference to the "averaging theorem" approach of Whitaker & Howes (1985), Whitaker (2000) and Kolev (2002) since we consider it to be more elegant. It remains to note that the averaging procedure has been shown to yield meaningful results provided that the characteristic lengths, d (distance over which variations in exact quantities occur), l (characteristic length for the averaging procedure) and L (characteristic length for the process) obey $d \ll l \ll L$ (Whitaker, 2000).

Following Drew (1983), we consider hereafter the volume-averaging operator defined by

$$\langle\cdot\cdot\rangle = \frac{1}{V}\iiint_V \cdot\cdot\,\mathrm{d}V, \tag{1.10}$$

where V is a fixed, bounded, and smooth control volume; thus, if f and g are smooth scalar fields defined everywhere in space and c is a constant, then the following averaging identities hold:

$$\langle f+g\rangle = \langle f\rangle + \langle g\rangle, \quad \langle\langle f\rangle g\rangle = \langle f\rangle\langle g\rangle, \tag{1.11a,b}$$

$$\langle c\rangle = c, \quad \langle\frac{\partial f}{\partial t}\rangle = \frac{\partial}{\partial t}\langle f\rangle, \quad \langle\nabla f\rangle = \nabla\langle f\rangle. \tag{1.12a,b,c}$$

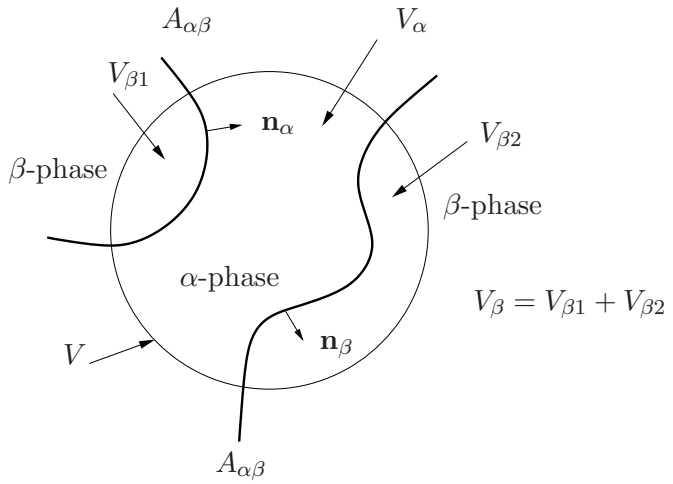

Figure 1.4: A two phase system with averaging volume, V, phases denoted α, β and interfaces $A_{\alpha\beta}$ (after Gray & Lee (1977)).

We now introduce an indicator function for phase α, $I_\alpha(\boldsymbol{x}, t)$, which 'picks out' phase α from the two phase material and is defined by

$$I_\alpha(\boldsymbol{x}, t) = \begin{cases} 1 & \text{if } \boldsymbol{x} \text{ is in phase } \alpha \text{ at time } t, \\ 0 & \text{otherwise,} \end{cases} \tag{1.13}$$

and we remark that in view of our averaging operator (1.10) and (1.9), $\langle\psi\rangle_4 \equiv \langle I_\alpha\psi\rangle$.

Assuming there are no voids within the material, we have the saturation constraint,

$$\sum_\alpha I_\alpha = 1, \tag{1.14}$$

(except on interface between the phases, $A_{\alpha\beta}$) and the average local volume fraction occupied by phase α is given by

$$\phi_\alpha(\boldsymbol{x}, t) = \langle I_\alpha \rangle. \tag{1.15}$$

The spatial and temporal derivatives of I_α will feature in the averaging through two identities that we now describe briefly. Since the indicator function is constant except at the interface between the two phases, where it has a jump of unit magnitude, ∇I_α is a delta-function concentrated at the interface, $A_{\alpha\beta}$, and multiplied by the unit normal, $\mathbf{n}_\alpha$, pointing into phase α, *i.e.*

$$\nabla I_\alpha = \delta(\boldsymbol{x} - \boldsymbol{x}_i)\mathbf{n}_\alpha \quad \text{for} \quad \boldsymbol{x}_i \in A_{\alpha\beta}; \tag{1.16}$$

see Gray & Lee (1977), Drew (1983), who also show that

$$\frac{\partial I_\alpha}{\partial t} = -\boldsymbol{u}_i \cdot \nabla I_\alpha, \tag{1.17}$$

where $\boldsymbol{u}_i$ is the velocity of the interface $A_{\alpha\beta}$. Result (1.17) is proved in Drew (1983), Fowler (1997) as follows: if ϑ is a smooth test function with compact support in space and time, then, using integration by parts,

$$\begin{aligned}\iint \vartheta \left[\frac{\partial I_\alpha}{\partial t} + \boldsymbol{u}_i \cdot \nabla I_\alpha\right] \mathrm{d}V\mathrm{d}t &= \int_V \left[I_\alpha \vartheta\Big|_0^\infty - \int I_\alpha \frac{\partial \vartheta}{\partial t}\mathrm{d}t\right] \mathrm{d}V \\ &\qquad + \int \left[\vartheta \boldsymbol{u}_i I_\alpha\Big|_{-\infty}^{\infty} - \int_V I_\alpha \nabla\cdot\vartheta\boldsymbol{u}_i \mathrm{d}V\right]\mathrm{d}t \\ &= -\iint I_\alpha \left[\frac{\partial \vartheta}{\partial t} + \nabla\cdot(\vartheta\,\boldsymbol{u}_i)\right]\mathrm{d}V\mathrm{d}t \\ &= -\int_0^\infty \int_{V_\alpha} \left[\frac{\partial \vartheta}{\partial t} + \nabla\cdot(\vartheta\,\boldsymbol{u}_i)\right]\mathrm{d}V\mathrm{d}t \\ &= -\int_0^\infty \frac{d}{dt}\int_{V_\alpha} \vartheta\ \mathrm{d}V\mathrm{d}t \\ &= -\int_{V_\alpha} \vartheta \mathrm{d}V\Big|_0^\infty = 0.\end{aligned}$$

We note also that it follows from the product rule that

$$\langle I_\alpha \nabla\psi\rangle = \nabla\langle I_\alpha\psi\rangle - \langle\psi\nabla I_\alpha\rangle, \tag{1.18}$$

$$\langle I_\alpha \frac{\partial\psi}{\partial t}\rangle = \frac{\partial}{\partial t}\langle I_\alpha\psi\rangle - \langle\psi\frac{\partial I_\alpha}{\partial t}\rangle, \tag{1.19}$$

wherein the spatial and temporal derivatives of I_α on the right-hand sides of these expressions are given by (1.16) and (1.17), respectively.

Lastly, we define two closely related averages that we shall require shortly. The "phasic average" for any field f is denoted $\overline{f}$, and the "mass-weighted average" denoted $\hat{f}$, are defined:

$$\overline{f}_\alpha = \frac{\langle I_\alpha f\rangle}{\phi_\alpha}, \tag{1.20}$$

$$\hat{f}_\alpha = \frac{\langle I_\alpha \rho f\rangle}{\phi_\alpha \overline{\rho}_\alpha}. \tag{1.21}$$

We remark that the phasic average (1.20) differs from the local volume average (1.9) by a factor ϕ_α^{-1}. From these definitions and equation (1.12a), it can be seen that in the special case in which the density in phase α is constant, we have

$$\overline{f}_\alpha = \hat{f}_\alpha = \frac{\langle I_\alpha f\rangle}{\phi_\alpha}.$$

1.4.1 Averaged equations for a two phase material

Averaged conservation of mass equations

Multiplying equation (1.4) by the indicator function, I_α, and re-arranging using the product rule of differentiation, we obtain

$$\frac{\partial}{\partial t}(\rho I_\alpha) + \nabla \cdot (\rho \boldsymbol{u} I_\alpha) = \rho \left(\frac{\partial I_\alpha}{\partial t} + \boldsymbol{u} \cdot \nabla I_\alpha \right). \tag{1.22}$$

Averaging (1.22) and appealing to equations (1.12c,d) we have

$$\frac{\partial}{\partial t}\langle \rho I_\alpha \rangle + \nabla \cdot \langle \rho \boldsymbol{u} I_\alpha \rangle = \left\langle \rho \left(\frac{\partial I_\alpha}{\partial t} + \boldsymbol{u} \cdot \nabla I_\alpha \right) \right\rangle. \tag{1.23}$$

We then use (1.17) to eliminate $\partial I_\alpha / \partial t$ from the right-hand side of (1.23), to find that the "mass source" term (*i.e.* the averaged macroscopic rate at which mass is transferred into phase α from phase β) is given by

$$\Gamma_\alpha = \left\langle \rho \left(\frac{\partial I_\alpha}{\partial t} + \boldsymbol{u} \cdot \nabla I_\alpha \right) \right\rangle = \langle \rho \, (\boldsymbol{u} - \boldsymbol{u}_i) \cdot \nabla I_\alpha \rangle. \tag{1.24}$$

In view of (1.24) and on invoking (1.20) and (1.21), we arrive at the averaged conservation of mass expression:

$$\frac{\partial}{\partial t} (\overline{\rho}_\alpha \phi_\alpha) + \nabla \cdot (\overline{\rho}_\alpha \hat{\boldsymbol{u}}_\alpha \phi_\alpha) = \Gamma_\alpha. \tag{1.25}$$

Averaged conservation of momentum equations

Multiplying the microscopic conservation of momentum expression (1.5) by the indicator function, applying the product rule of differentiation and averaging, we find that

$$\frac{\partial}{\partial t}\langle I_\alpha \rho \boldsymbol{u} \rangle + \nabla \cdot \langle I_\alpha \rho \boldsymbol{u} \, \boldsymbol{u} \rangle = \nabla \cdot \langle I_\alpha \boldsymbol{\sigma} \rangle + \langle I_\alpha \rho \mathbf{F} \rangle + \left\langle \rho \boldsymbol{u} \frac{\partial I_\alpha}{\partial t} \right\rangle + \langle \rho \boldsymbol{u} \boldsymbol{u} \cdot \nabla I_\alpha \rangle - \langle \boldsymbol{\sigma} \cdot \nabla I_\alpha \rangle, \tag{1.26}$$

wherein the final three terms arise from the three applications of the product rule that result in the first three terms, respectively. We may now rewrite each term in (1.26) as follows.

For the first and fourth terms in (1.26) we write (employing (1.20), (1.21))

$$\langle I_\alpha \rho \boldsymbol{u} \rangle = \phi_\alpha \overline{\rho}_\alpha \hat{\boldsymbol{u}}_\alpha, \qquad \langle I_\alpha \rho \mathbf{F} \rangle = \phi_\alpha \overline{\rho}_\alpha \hat{\mathbf{F}}_\alpha. \tag{1.27}$$

For the second term we separate the microscopic velocity in phase α into its (mass-weighted) mean and fluctuating parts by writing

$$\boldsymbol{u} = \hat{\boldsymbol{u}}_\alpha + \boldsymbol{u}'; \tag{1.28}$$

since $\langle I_\alpha \rho \boldsymbol{u}' \rangle = \mathbf{0}$, we have, by (1.11a,b):

$$\langle I_\alpha \rho \boldsymbol{u}\, \boldsymbol{u} \rangle = \phi_\alpha \overline{\rho}_\alpha \hat{\boldsymbol{u}}_\alpha \hat{\boldsymbol{u}}_\alpha + \langle I_\alpha \rho \boldsymbol{u}' \boldsymbol{u}' \rangle; \tag{1.29}$$

in (1.29), the second term is an averaged Reynolds stress, which we denote by $-\phi_\alpha \boldsymbol{\tau}'_\alpha = \langle I_\alpha \rho \boldsymbol{u}' \boldsymbol{u}' \rangle$. For the third term we begin by decomposing the microscopic stress tensor into a pressure, p, and deviatoric stress, $\boldsymbol{\tau}$:

$$\boldsymbol{\sigma} = -p\mathbf{I} + \boldsymbol{\tau}; \tag{1.30}$$

thus

$$\langle I_\alpha \boldsymbol{\sigma} \rangle = \phi_\alpha \bar{\boldsymbol{\sigma}}_\alpha = -\phi_\alpha \bar{p}_\alpha \mathbf{I} + \phi_\alpha \bar{\boldsymbol{\tau}}_\alpha, \tag{1.31}$$

and in the fifth-term, we substitute for $\partial I_\alpha / \partial t$ using (1.17), to find that

$$\left\langle \rho \boldsymbol{u} \frac{\partial I_\alpha}{\partial t} \right\rangle = -\langle \rho \boldsymbol{u} \boldsymbol{u}_i \cdot \nabla I_\alpha \rangle. \tag{1.32}$$

Substituting (1.27), (1.29), (1.31) and (1.32) into (1.26), we find that

$$\begin{aligned} \frac{\partial}{\partial t}(\phi_\alpha \overline{\rho}_\alpha \hat{\boldsymbol{u}}_\alpha) + \nabla \cdot (\phi_\alpha \overline{\rho}_\alpha \hat{\boldsymbol{u}}_\alpha \hat{\boldsymbol{u}}_\alpha) = & -\nabla(\phi_\alpha \bar{p}_\alpha) + \nabla \cdot \left(\phi_\alpha (\overline{\boldsymbol{\tau}}_\alpha + \boldsymbol{\tau}'_\alpha) \right) + \phi_\alpha \overline{\rho}_\alpha \hat{\mathbf{F}}_\alpha + \\ & \langle (\rho \boldsymbol{u}(\boldsymbol{u} - \boldsymbol{u}_i) + p\mathbf{I} - \boldsymbol{\tau}) \cdot \nabla I_\alpha \rangle; \end{aligned} \tag{1.33}$$

the "momentum source" term (*i.e.* the averaged macroscopic rate at which momentum is transfer ed into phase α from phase β) is thus given by

$$\mathbf{M}_\alpha = \langle (\rho \boldsymbol{u}(\boldsymbol{u} - \boldsymbol{u}_i) + p\mathbf{I} - \boldsymbol{\tau}) \cdot \nabla I_\alpha \rangle, \tag{1.34}$$

in which it is customary to decompose the various contributions as follows. The inertial contribution is related to the mass source, Γ_α, and the "interfacial velocity" of phase α, $\boldsymbol{u}_{\alpha,i}$ say, by

$$\Gamma_\alpha \boldsymbol{u}_{\alpha,i} = \langle \rho \boldsymbol{u}(\boldsymbol{u} - \boldsymbol{u}_i) \cdot \nabla I_\alpha \rangle. \tag{1.35}$$

For the the remaining components of the momentum source term, namely $\langle (p\mathbf{I} - \boldsymbol{\tau}) \cdot \nabla I_\alpha \rangle$, the contribution to diffusive transport down the gradient of phase α is associated with the interphase pressure of phase α, $p_{\alpha,i}$ say, which is defined by

$$p_{\alpha,i} |\nabla \phi_\alpha|^2 = \langle p \nabla I_\alpha \rangle \cdot \nabla \phi_\alpha, \tag{1.36}$$

so that (since $\langle \nabla I_\alpha \rangle = \nabla \phi_\alpha$)

$$\langle (p\mathbf{I} - \boldsymbol{\tau}) \cdot \nabla I_\alpha \rangle = p_{\alpha,i} \nabla \phi_\alpha + \mathbf{M}^d_\alpha; \; \mathbf{M}^d_\alpha = \langle (p - p_{\alpha,i}) \nabla I_\alpha - \boldsymbol{\tau} \cdot \nabla I_\alpha \rangle, \tag{1.37}$$

the latter term being the "interfacial force density". Finally, substituting (1.35) and (1.37) into (1.34), we find

$$\mathbf{M}_\alpha = \Gamma_\alpha \boldsymbol{u}_{\alpha,i} + p_{\alpha,i}\nabla\phi_\alpha + \mathbf{M}^d_\alpha, \tag{1.38}$$

so that (1.33) becomes

$$\frac{\partial}{\partial t}(\phi_\alpha\overline{\rho}_\alpha\hat{\boldsymbol{u}}_\alpha) + \nabla\cdot(\phi_\alpha\overline{\rho}_\alpha\hat{\boldsymbol{u}}_\alpha\hat{\boldsymbol{u}}_\alpha) = -\phi_\alpha\nabla\overline{p}_\alpha + \nabla\cdot\left(\phi_\alpha(\overline{\boldsymbol{\tau}}_\alpha + \boldsymbol{\tau}')\right) + \phi_\alpha\overline{\rho}_\alpha\hat{\mathbf{F}}_\alpha + \Gamma_\alpha\boldsymbol{u}_{\alpha,i} + (p_{\alpha,i} - \overline{p}_\alpha)\nabla\phi_\alpha + \mathbf{M}^{\mathbf{d}}_\alpha. \tag{1.39}$$

1.5 Governing equations for multiphase tissue growth

In this section, the averaged equations for a multiphase model relevant to tissue engineering applications are presented in generality and for an arbitrary number of phases. We remark that the derivation presented in this section follows that given in Lemon *et al.* (2006). This formulation (in a number of simplified incarnations) will be employed in subsequent chapters of this thesis. The equations are averaged in the manner presented in §1.4 so we omit the details here.

We consider a multiphase system comprising an arbitrary number of phases (N), each of which occupies an averaged volume fraction, ϕ_i, where $i = 1, \ldots, N$ and we associate with each phase a volume-averaged velocity, pressure, stress tensor and density ($\boldsymbol{u}_i$, p_i, $\boldsymbol{\sigma}_i$, ρ_i). Following the averaging process described earlier, we obtain the following local volume-averaged mass conservation equation:

$$\frac{\partial\phi_i}{\partial t} + \nabla\cdot(\phi_i\boldsymbol{u}_i) = S_i\,; \qquad S_i = \sum_{j\neq i}\frac{S_{ij}}{\rho_i}, \tag{1.40}$$

where S_{ij}/ρ_i is the net averaged macroscopic rate at which material is transferred into phase i from phase j and the total rate of transfer into phase i is denoted S_i. Comparison with equation (1.25) shows that writing the mass conservation equation in this form carries the tacit assumption that each phase is intrinsically incompressible with fixed density ρ_i. The function S_{ij} is given by

$$S_{ij} = \widetilde{S}_{ij}\rho_j - \widetilde{S}_{ji}\rho_i, \tag{1.41}$$

for transfer rates $\widetilde{S}_{ij}$ and we remark here that for multiphase materials in which mass transfer between phases involves negligible changes in density it may be assumed that $\rho_i = \rho$. In general, these mass transfer rates vary both spatially and temporally and will depend upon the cells' mechanochemical environment; for instance, nutrient availability, growth factors, local cell density, pressure or stress. Functional forms for the mass transfer

rates S_{ij} will be chosen to reflect different physical processes at various points in this thesis; however, we remark here that the effect of nutrient availability on the growth of the tissue will not be considered.

A conservation condition arises from the assumption that there are no voids within the multiphase material (*i.e.* the mixture is *saturated*; see equation (1.14)):

$$\sum_{i=1}^{N} \phi_i = 1. \tag{1.42}$$

A further conservation condition may be obtained by summing equations (1.40) over all phases and exploiting (1.42); this may be expressed:

$$\sum_{i=1}^{N} \nabla \cdot (\phi_i \boldsymbol{u}_i) = 0, \tag{1.43}$$

where we have assumed that the mass source terms obey $\sum S_i = 0$ so that mass is conserved.

Following Lemon *et al.* (2006) and others, a porous flow model is used to describe the dynamics of the multiphase system. The momentum balance equation is derived using the method outlined in §1.4.1 and is based upon the two-phase flow model of Drew (1983), which we extend to an arbitrary number of phases. Neglecting inertial effects (including mass transfer effects) and body forces, the momentum balance equation for each phase is

$$\nabla \cdot (\phi_i \boldsymbol{\sigma}_i) + \sum_{j \neq i} \mathbf{F}_{ij} = \mathbf{0}, \tag{1.44}$$

where $\mathbf{F}_{ij}$ is the interphase force exerted by phase j on phase i and we assume $\mathbf{F}_{ij} = -\mathbf{F}_{ji}$. The momentum balance for the multiphase mixture may be obtained by summing (1.44) over all phases; exploiting the property of the interphase force terms described above, we find:

$$\nabla \cdot \left\{ \sum_{i=1}^{N} \phi_i \boldsymbol{\sigma}_i \right\} = \mathbf{0}. \tag{1.45}$$

We pause here to discuss the implications of extending the derivation outlined in §1.4.1 to three or more phases. The main complications come from the choice of appropriate interphase interaction terms and from the modelling of the interfacial regions which separate different phases at the microscale. In multiphase systems of three or more phases, these regions may manifest themselves as surfaces, common lines (interfacial regions between three neighbouring phases) and common points (intersection of different common lines). In a three phase system, only one type of common line may exist; in a four phase system, four common lines types may exist (Gray & Hassanizadeh, 1998). As mentioned

previously (§1.4), some modelling approaches consider these interfaces as singular surfaces across which a discontinuity in phase properties occurs, with no thermodynamic properties of their own; however, citing a number of studies of two-phase processes and flow in unsaturated media, Gray & Hassanizadeh (1998) contend that the "inclusion of interfacial properties is essential if gross errors in the description of some multiphase systems are to be avoided"; and furthermore, that "all features of a multiphase system that affect the thermodynamic behaviour must be accounted for".

Thermodynamic behaviour is considered in many studies (see Gray & Hassanizadeh (1998), Araujo & McElwain (2005a), and others) to derive constraints on the constitutive laws that are consistent with the second law of thermodynamics. Individual phases in biological tissues may be considered separate and distinct and so we may appeal to the Principle of Phase Separation. Under this principle, the material-specific dependent variables associated with each phase (such as stress) depend only on the variables of that phase; interactive terms (such as the interphase momentum transfer term), may depend upon all variables (Araujo & McElwain, 2005a); furthermore, these quantities must be objective (that is, they must be independent of the frame of reference). We do not treat these considerations in great detail; however, we expect that the constitutive laws and interphase momentum transfer terms chosen here and in the proceeding chapters will be consistent with these assumptions. For more details see Drew & Segel (1971), Passman *et al.* (1984) and Araujo & McElwain (2005a).

Following Lemon *et al.* (2006), the interphase forces are assumed to be of the form:

$$\mathbf{F}_{ij} = p_{ij}\phi_j\nabla\phi_i - p_{ji}\phi_i\nabla\phi_j + K_{ij}(\boldsymbol{u}_j - \boldsymbol{u}_i), \tag{1.46}$$

where $p_{ij} = p_{ji}$ is the *interphase* pressure exerted by phase j on i. The first two terms in equation (1.46) represent the interfacial force exerted by phase j on i and the resulting reactionary force supplied by phase i. The final term represents an interphase viscous drag, where $K_{ij} = K_{ji}$ is the drag coefficient which may depend upon ϕ_i and ϕ_j. We remark that this form of interphase momentum transfer term is similar to that used in many other multiphase models in the literature (*e.g.* Barocas & Tranquillo (1997), Barry & Holmes (2001) and Ahmadi *et al.* (2003)); this form is, of course, objective.

The pressures p_{ij}, referred to above, represent the interphase forces generated by the mechanically-active cellular components in our multiphase mixture; additionally, these components may generate intraphase forces. Within our model, these forces manifest themselves as pressure differences between the phases (we note that for a mixture comprised entirely

of passive constituents, these pressures will tend to equilibrate (Lemon *et al.*, 2006)). Following Lemon *et al.* (2006), the interphase pressure is assumed to have the form

$$p_{ij} = p + \psi_{ij}, \tag{1.47}$$

for $i \neq j$, where p is a common "mixture" pressure and $\psi_{ij} = \psi_{ji}$ is an extra pressure contribution due to tractions between phases i and j. Additionally, the pressure in each phase is assumed to have the form

$$p_i = p + \Sigma_i + \sum_{j \neq i} \phi_j \psi_{ij}, \tag{1.48}$$

where Σ_i is an additional *intraphase* pressure resulting from interactions *within* phase i such as osmotic stresses or surface tension within cell membranes. More detail regarding the modelling considerations behind these choices is given in Lemon *et al.* (2006). We remark here that surface tension within the interfaces between phases is neglected from this work. Functional forms for the extra pressures described above will be specified together with appropriate constitutive laws for each phase in later chapters when the general model given here is applied to the study of *in vitro* tissue growth processes.

1.6 Thesis objectives and structure

The aim of this thesis is to present and analyse a general multiphase mathematical model which provides the means to study the effect of dynamic culture conditions on the response of a tissue construct. In the following analysis, this is illustrated by specialising the general multiphase model derived above to a two-dimensional model of a cell population growing within a porous scaffold; specifically, the effect of fluid flow and mechanical compression is considered. The results of this model are interpreted in the context of the bioreactor system of El Haj *et al.* (see §1.2.3) and of tissue engineering in general.

As we progress through the thesis, the mathematical models increase in complexity towards a more realistic representation of a cell culture growing within a deformable porous scaffold, which allows consideration of intraphase and interphase forces and the influence of fluid flow, pressure, scaffold deformation and local cell density on the growth response of the cell culture.

Following many studies of tissue growth which exploit a multiphase formulation (for example, Landman & Please (2001), Breward *et al.* (2002), Franks (2002) and King & Franks (2004) which investigate tumour growth), in chapter 2, we initially restrict attention to two

viscous fluid phases and concentrate on the interaction between an imposed flow of passive culture medium and the response of the "cell phase". In the context of the bioreactor system discussed previously, this phase is interpreted as comprising cells and ECM; the scaffold is neglected. The above studies are extended by the addition of an imposed flow of culture medium (representing perfusion) and the coupling of the cells' response to their environment. Simplification of the field equations and reduction of the number of dependent variables is achieved by exploiting the limit of large interphase viscous drag in which each phase is subject to a common velocity and pressure field, recovering the model equations of Franks (2002) and Franks & King (2003). The single velocity and pressure approximation is valid for the outer flow in the bioreactor; the inner flow problem in a boundary layer near the bioreactor walls requires consideration of the individual velocity and pressure fields of each phase. Boundary conditions on the outer problem are derived via a boundary layer analysis which deviate from those employed in Franks (2002) by the absence of slip. In the interest of comparison with this study (and others) we permit slip in our analysis of the model.

Employing both analytic and numerical techniques, we analyse the stability of a one-dimensional growing tissue (defined by two sharp interfaces) to transverse perturbations, showing that introducing a perturbation to the tissue density results in markedly different behaviour to that presented by Franks (2002) in the case of uniform density. Considering a tissue defined by diffuse boundaries and using numerical simulations in one and two dimensions, we show that the one-dimensional, sharp interface model (for which we may obtain analytic solutions) captures much of the behaviour of these more complex models. The model is then developed to consider mechanotransduction-affected tissue growth. Using numerical simulations in two dimensions, we demonstrate that comparison of construct morphology in static and dynamic culture conditions provides a means to identify the dominant regulatory growth stimulus.

In chapter 3, we develop a three phase model which allows the presence of the PLLA scaffold to be considered, introducing a rigid porous phase (whose volume fraction is assumed constant) in addition to the two viscous fluid phases. These phases are now interpreted as representing the cells and ECM ("cell phase") and culture medium, respectively. This allows explicit modelling of the interaction between the cells and the scaffold. The long-wavelength limit is exploited to allow the three-phase system to be expressed as a pair of coupled partial differential equations: a second order differential equation governs the pressure of the culture medium and a parabolic equation governs the evolution of the cell

phase volume fraction. We develop a numerical scheme for the solution of these equations and validate the resulting numerical simulations using analytic solutions constructed in the limit of asymptotically-small cell phase density. Our investigations reveal stark differences in the behaviour of the cell phase depending upon the relative importance of cell aggregation and attachment compared to repulsion.

This model is further analysed in chapter 4, where we exploit the numerical scheme developed in chapter 3 to investigate the effect of varying key parameters associated with cell aggregation and cell-scaffold interactions. We show that the manufacture of denser scaffolds improves control over the aggregative/attachment behaviour of cells. In addition, we present simulations demonstrating the effect of coupling the external fluid mechanics and local cell density to the growth response of the cell population. As in chapter 3, we conclude that the model provides a simple means to determine the dominant regulatory stimulus.

In chapters 3 and 4, we model the scaffold phase as a rigid material of constant porosity. This assumption is relaxed in chapter 5 and we re-interpret the scaffold phase as a lumped scaffold and ECM phase, introducing an equation to govern its evolution in response to scaffold degradation and ECM deposition. This modification enables modelling of the progression of cells from a proliferative to an ECM-depositing phenotype, without increasing the total number of phases in the system. Adapting the numerical scheme developed in chapter 3, we present numerical simulations which, in addition to the ability to isolate regulatory mechanisms, demonstrate that a uniform cell seeding and the encouragement of cell penetration throughout the scaffold are crucial in maintaining the mechanical integrity of engineered constructs.

In chapter 6, we further extend the model to accommodate the influence of the mechanical compression supplied by the piston on the cells' response, developing a framework to investigate the interplay between perfusion, mechanical compression and cell differentiation. To do so, we exploit both a classical poroelasticity formulation as well as a multiphase model of the type employed previously (with a poroelastic constitutive law for the scaffold phase). Employing analytical and numerical techniques, we investigate the behaviour of a scaffold subject to time-dependent compression, demonstrating that the bioreactor geometry has a dramatic effect on the mechanical environment of a cell population contained with the scaffold.

We review the thesis and re-iterate the main conclusions in chapter 7; additionally, we outline a number of possible extensions to this work.

Chapter 2

A two-fluid model for the growth of a tissue construct

2.1 Introduction

We now formulate and analyse a mathematical model applicable to the compression/perfusion system introduced in §1.2.3 and tissue engineering in general, based on the derivation presented in §1.5. As a first approximation, the presence of the scaffold and the mechanical forcing from the piston are neglected and we employ a two phase formulation of the type presented in Drew (1983), Franks (2002), Byrne *et al.* (2003), Franks *et al.* (2003), Franks & King (2003) and King & Franks (2004). We model the bioreactor system as a rigid-walled, two-dimensional channel containing a two phase fluid. The cells and extracellular matrix are modelled as one phase which grows in a prescribed manner; the second phase represents the culture medium. Our model accommodates cell proliferation and death as well as ECM deposition and degradation. Perfusion is represented by an imposed flow of culture medium.

In §2.2.1, the governing multiphase equations (§1.5) are simplified by exploiting the limit of large interphase viscous drag in which the two phases are subject to a common velocity and pressure field, recovering the model of Franks (2002) and Franks & King (2003). In §2.3, the impact of an ambient flow on the growth of a one-dimensional tissue, whose net rates of proliferation and ECM deposition are assumed constant, is investigated. Analytic solutions are presented in the limit for which the interfaces between the tissue and surrounding culture medium are sharp and the stability of these interfaces to transverse perturbations is investigated (§2.3.1). In §2.3.2, numerical simulations are presented corresponding to a one-dimensional tissue defined by diffuse interfaces which grows at a constant rate, and in §2.4.1, two-dimensional numerical simulations are presented. Lastly, in §2.4.2

the model is extended by linking the cells' proliferation and ECM deposition rate to the local mechanical environment, thereby allowing consideration of a simple mechanotransduction mechanism. We illustrate the effect of such a mechanism by coupling the cells' proliferative behaviour to (i) the local cell density and, (ii) the pressure, showing how comparison of tissue construct morphology resulting from static and dynamic culture conditions provides a simple way to identify the dominant regulatory tissue growth stimulus. A discussion of our results and their applications within a tissue engineering context is presented in §2.5.

2.2 Model formulation

In this section, we apply the general multiphase formulation given in §1.5 to develop a simple model for the bioreactor of El-Haj *et al.* (§1.2.3).

We consider the growth of a tissue construct within a nutrient-rich culture medium and investigate the effect of an imposed flow on the response of the cells. The presence of the scaffold and the mechanical forcing from the piston are neglected and we represent the system as a two-dimensional channel containing a tissue construct surrounded by culture medium. For simplicity, a two-dimensional Cartesian geometry is chosen; however, generalisation to a cylindrical geometry is straightforward. The channel contents are modelled as a two-phase mixture of interacting viscous fluids. The cells and extracellular matrix (ECM) are modelled as a single phase (henceforth termed the "cell phase"); the second phase represents the culture medium. Perfusion is represented by a flow of culture medium generated by an imposed axial pressure drop. In the following we will employ the term "tissue construct" to distinguish the region occupied by the interacting system of cell and culture medium phases from the remainder of the channel containing only culture medium. We remark here that at certain stages in this chapter, the interfaces between the construct and the surrounding culture medium will be assumed to be sharp or diffuse to allow different analyses to be performed.

A Cartesian coordinate system $\boldsymbol{x^*} = (x^*, y^*)$ is chosen with corresponding coordinate directions $(\hat{\boldsymbol{x}}, \hat{\boldsymbol{y}})$ and the channel occupies $0 \leqslant x^* \leqslant L^*$, $0 \leqslant y^* \leqslant h^*$ (see figure 2.1). In this thesis, asterisks distinguish dimensional quantities from their dimensionless equivalents. We associate with the cell and culture medium phases a volume fraction denoted n, w, respectively and a volume-averaged velocity, $\boldsymbol{u}_i^* = (u_i^*, v_i^*)$, pressure, p_i^*, stress tensor, $\boldsymbol{\sigma}_i^*$ and density, ρ_i^* (where $i = n, w$ denotes variables associated with the cell and culture medium phases, respectively) and assume that these are functions of $\boldsymbol{x}^*$ and t^*, where t^*

represents time.

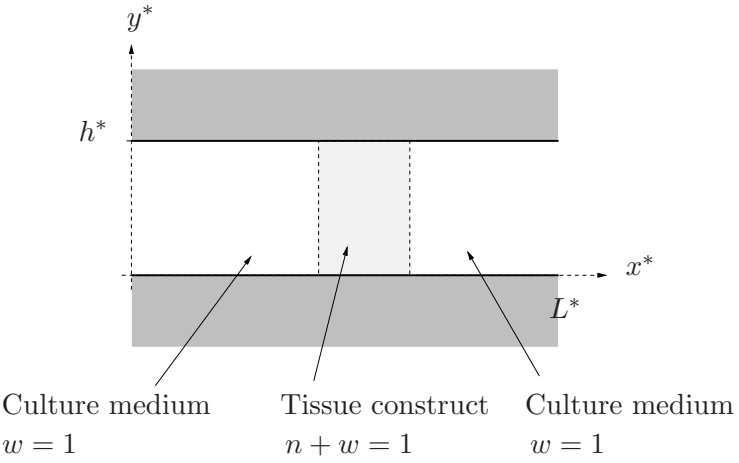

Figure 2.1: An idealised model of a perfusion bioreactor as a two-dimensional channel of length L^* and width h^* containing a tissue construct.

The multiphase model outlined in §1.5 is simplified by assuming that the two phases are incompressible with the same density, so that $\rho_i^* = \rho^*$ $(i = n, w)$. Under these assumptions, in dimensional form, equations (1.40), (1.42), (1.43), (1.44) and (1.45) are as follows:

$$\text{conservation of mass:} \qquad \frac{\partial n}{\partial t^*} + \nabla^* \cdot (n \boldsymbol{u}_n^*) = S_n^* + D_n^* \nabla^{*2} n, \tag{2.1}$$

$$\nabla^* \cdot (n \boldsymbol{u}_n^* + w \boldsymbol{u}_w^*) = S_n^* + S_w^*; \tag{2.2}$$

$$\text{conservation of momentum:} \qquad \nabla^* \cdot (w \boldsymbol{\sigma}_w^*) + \mathbf{F}_{wn}^* = \mathbf{0}, \tag{2.3}$$

$$\nabla^* \cdot (n \boldsymbol{\sigma}_n^* + w \boldsymbol{\sigma}_w^*) = \mathbf{0}; \tag{2.4}$$

$$\text{no voids:} \qquad n + w = 1, \tag{2.5}$$

where S_i^* is the rate of material transfer into phase i and $\mathbf{F}_{ij}^*$ is the interphase force exerted on phase i by phase j. We remark that a diffusive term has been added to the mass conservation equation (2.1); these terms are expected to be negligible in many cases (King & Franks, 2004) but are included for numerical convenience since they eliminate the moving boundaries which would otherwise require tracking (for simplicity, we choose $D_i^* = D^*$ as implied by equation (2.2)). In the analysis for which the interface between the tissue construct and culture medium is sharp, we set $D^* = 0$.

To close equations (2.1)–(2.5), we require constitutive laws for the interphase forces ($\mathbf{F}_{ij}^*$), the stress tensors ($\boldsymbol{\sigma}_n^*$, $\boldsymbol{\sigma}_w^*$) and the transfer rates (S_n^*, S_w^*), which describe the behaviour of the cell and culture medium phases.

We simplify the formulation given in §1.5 by assuming that interphase tractions may be neglected and that the culture medium acts as a "passive" phase, generating no intraphase

pressures; we therefore set $\psi^*_{nw} = 0 = \Sigma^*_w$ in equations (1.47) and (1.48). We further assume that the common "mixture" pressure introduced in equation (1.47) is equal to the fluid pressure so that $p^* = p^*_w$ and that the coefficients of interphase viscous drag in (1.46) obey $K^*_{nw} = K^*_{wn} = k^*$, where k^* is constant. From equation (1.46), the interphase force is therefore given by

$$\mathbf{F}^*_{wn} = p^*_w \nabla^* w + k^*(\boldsymbol{u}^*_n - \boldsymbol{u}^*_w). \tag{2.6}$$

In view of the above assumptions, we find from equation (1.48) that the cell phase pressure (p^*_n) is related to that in the culture medium by:

$$p^*_n = p^*_w + \Sigma^*_n. \tag{2.7}$$

In equation (2.7), Σ^*_n is an intraphase pressure function, representing cell-cell and cell-ECM interactions.

We model the cell and culture medium phases as viscous fluids and therefore specify the volume-averaged stress tensors for each phase in the following manner:

$$\boldsymbol{\sigma}^*_i = -p^*_i \mathbf{I} + \mu^*_i(\nabla^* \boldsymbol{u}^*_i + \nabla^* \boldsymbol{u}^{*T}_i) + \lambda^*_i(\nabla^* \cdot \boldsymbol{u}^*_i)\mathbf{I}; \quad i = n, w, \tag{2.8}$$

where μ^*_i and λ^*_i represent the dynamic shear and bulk viscosity coefficients of the i^{th} phase and $\mathbf{I}$ is the identity matrix. This model is of the form employed by, for instance, Franks (2002) and Byrne *et al.* (2003). A functional form for the intraphase pressure function Σ^*_n (*e.g.* that employed in Lemon *et al.* (2006)) is not specified here since, in this chapter, we will employ a lumped pressure field which encapsulates this function (the fluid pressure p^*_w may, in principle, be calculated from our lumped pressure field on specification of an appropriate form for Σ^*_n). Functional forms for the mass transfer rates S^*_n, S^*_w will be specified in the following section.

Appropriate boundary conditions on this problem are as follows:

$$\frac{\partial n}{\partial y^*} = 0, \quad \boldsymbol{u}^*_w = \mathbf{0} = \boldsymbol{u}^*_n, \qquad \text{on } y^* = 0, h^*, \tag{2.9a,b}$$

$$n = 0, \quad p^*_w = P^*_u, \qquad \text{on } x^* = 0, \tag{2.10a,b}$$

$$n = 0, \quad p^*_w = P^*_d, \qquad \text{on } x^* = L^*. \tag{2.11a,b}$$

Equations (2.9) guarantee no-penetration and no-slip on the channel walls $y^* = 0, h^*$. Equations (2.10) and (2.11) ensure that the tissue construct does not extend along the channel's length and, additionally, define the imposed axial pressure drop, $P^*_u - P^*_d$, which drives a flow. Initial cell phase distributions suitable for the analyses presented in this chapter will be specified subsequently.

The governing equations are non-dimensionalised by choosing the following dimensionless variables

$$\boldsymbol{x}^* = L^*\boldsymbol{x},\ t^* = \frac{L^*}{U_w^*}t,\ \boldsymbol{u}_i^* = U_w^*\boldsymbol{u}_i,\ (p_w^*, \Sigma_n^*) = \frac{U_w^*\mu_w^*}{L^*}(p_w, \Sigma_n),\ S_i^* = \frac{U_w^*}{L^*}S_i, \tag{2.12}$$

wherein U_w^* is a fluid velocity scale which will be determined subsequently. We have employed a viscous scaling for the culture medium and intraphase pressures (p_w, Σ_n) since we assume that viscous effects dominate inertia in the momentum equations. We pause to remark here that in view of the non-dimensionalisation $t^* = L^*t/U_w^*$, the timescale of interest is the time taken for a fluid particle to travel along the length of the bioreactor. The flow rate for the bioreactor system given in §1.2.3 is 0.1ml/min and the scaffold has a diameter of 9mm and height 4mm, giving a timescale of approximately 2.5 minutes. We note that this is very short in comparison to the duration of dynamic culture over which tissue growth occurs (1 week) given in §1.2.3. We therefore expect the ratio of the growth timescale to the flow timescale to be large; however, in this chapter (and the proceeding chapters of this thesis), we consider this ratio to be of $\mathcal{O}(1)$, employing fast growth rates to minimise computation time and to illustrate features of the system. Realistic growth time-scales may be obtained by manipulating the problem parameters.

The dimensionless form of the conservation of mass and momentum equations (2.1)–(2.4) is as follows:

$$\frac{\partial n}{\partial t} + \nabla\cdot(n\boldsymbol{u}_n) = S_n + D\nabla^2 n, \tag{2.13}$$

$$\nabla\cdot(n\boldsymbol{u}_n + w\boldsymbol{u}_w) = S_n + S_w, \tag{2.14}$$

$$w\nabla p_w + k(\boldsymbol{u}_w - \boldsymbol{u}_n) - \nabla\cdot\left[w(\nabla\boldsymbol{u}_w + \nabla\boldsymbol{u}_w^T) + \gamma_w w(\nabla\cdot\boldsymbol{u}_w)\mathbf{I}\right] = \mathbf{0}, \tag{2.15}$$

$$\nabla\cdot\big[-(p_w + n\Sigma_n)\mathbf{I} + \mu_n n(\nabla\boldsymbol{u}_n + \nabla\boldsymbol{u}_n^T) + \gamma_n n(\nabla\cdot\boldsymbol{u}_n)\mathbf{I} + w(\nabla\boldsymbol{u}_w + \nabla\boldsymbol{u}_w^T) + \gamma_w w(\nabla\cdot\boldsymbol{u}_w)\mathbf{I}\big] = \mathbf{0}, \tag{2.16}$$

and equation (2.5) is used to eliminate w. The boundary conditions (2.9)–(2.11) transform naturally and are not repeated here. For clarity, the dimensionless upstream and downstream pressures are defined as follows:

$$P_u = \frac{P_u^* L^*}{U_w^*\mu_w^*}, \quad P_d = \frac{P_d^* L^*}{U_w^*\mu_w^*}. \tag{2.17}$$

The dimensionless parameters D, μ_n, k, γ_w and γ_n are given by

$$D = \frac{D^*}{U_w^* L^*}, \quad \mu_n = \frac{\mu_n^*}{\mu_w^*}, \quad k = \frac{k^* L^{*2}}{\mu_w^*}, \quad \gamma_w = \frac{\lambda_w^*}{\mu_w^*}, \quad \gamma_n = \frac{\lambda_n^*}{\mu_w^*}, \tag{2.18}$$

and the channel now occupies $0 \leqslant x \leqslant 1$, $0 \leqslant y \leqslant h = h^*/L^*$. The physical interpretation of the dimensionless diffusion coefficient (or inverse Peclet number) D, relative viscosity μ_n, and drag coefficient k is obvious. The parameter γ_i describes the relative importance of the viscosity associated with the rate of change of volume of the i^{th} phase compared to that associated with fluid shear. It is usual to take $\lambda_i^* = -2\mu_i^*/3$ implying $\gamma_w = -2/3$ and $\gamma_n = -2\mu_n^*/3\mu_w^*$ (Franks, 2002; Franks & King, 2003; King & Franks, 2004; Lemon *et al.*, 2006). We expect $\mu_n^* \geqslant \mu_w^*$ and therefore assume $\gamma_n \leqslant -2/3$.

2.2.1 Large drag limit

By considering the Stokes drag due to water flowing past a sphere, Lubkin & Jackson (2002) calculated the following estimate for the drag coefficient between cells and water: $k^* = 4.5 \times 10^7 \mathrm{N} \cdot \mathrm{m}^{-4} \cdot \mathrm{s}$. Recalling that the lengthscale for the system is the bioreactor length, L^* (see figure 2.1), and assuming that this is of the same order as the scaffold length, we choose $L^* = 4 \times 10^{-3}\mathrm{m}$ (see §1.2.3). Lastly, we take the culture medium viscosity to be equal to that of water, $\mu_w = 1 \times 10^{-3}\mathrm{N} \cdot \mathrm{m}^{-2} \cdot \mathrm{s}$ (Lemon & King, 2007), and the dimensionless drag coefficient may then be calculated from equation (2.18) to give:

$$k = \frac{k^* L^{*2}}{\mu_w^*} = 7.2 \times 10^5. \tag{2.19}$$

Motivated by this, we now consider the limit in which the interphase viscous drag is large ($k \gg 1$) and derive appropriate governing equations and boundary conditions.

We consider a power series expansion of the dependent variables as follows:

$$n(\boldsymbol{x}, t) = n_0(\boldsymbol{x}, t) + \frac{1}{\sqrt{k}} n_1(\boldsymbol{x}, t) + \frac{1}{k} n_2(\boldsymbol{x}, t) + \cdots, \tag{2.20}$$

with similar expansions for $\boldsymbol{u}_n$, $\boldsymbol{u}_w$, p_w and Σ_n; at leading order, equation (2.15) gives $\boldsymbol{u}_{n0} = \boldsymbol{u}_{w0}$ so that we may approximate the local velocity field of each phase with a common velocity, denoted $\boldsymbol{u}_0$. As adopted *ab initio* in Franks (2002) and Franks & King (2003), we assume that each phase has the same material properties ($\gamma_i = -2/3$, $\mu_n = 1$) and that at leading order the mass transfer terms S_{n0}, S_{w0} are given by

$$S_{n0} = (k_m - k_d) n_0, \qquad S_{w0} = k_d n_0, \tag{2.21}$$

in which $k_m = (k_m^* L^*)/U_w^*$ represents the dimensionless rate of cell mitosis and ECM deposition, $k_d = (k_d^* L^*)/U_w^*$ represents the dimensionless rate of cell death and ECM degradation, and k_m^*, k_d^* are the corresponding dimensional rates. For brevity, we will henceforth refer to k_m and k_d as the "growth rate" and "death rate", respectively. In general, k_m and k_d

will depend upon the cells' mechanochemical environment (*e.g.* nutrient availability, growth factors, local cell density or stress) and in the following derivation we therefore allow both spatial and temporal variation in these functions: $k_m(\boldsymbol{x}, t)$, $k_d(\boldsymbol{x}, t)$. These choices imply that cell death (and ECM degradation) results in a corresponding increase in culture medium. We therefore view cells (and ECM) as constituting essentially the same matter as the culture medium (which is consistent with our assumption of uniform material properties in the two phase mixture). However, since these choices of mass transfer terms do not obey $\sum S_{i0} = 0$, this model does not conserve mass and cell phase growth therefore represents spontaneous mass generation in the system.

From (2.14)–(2.16), we obtain the following equations at leading order for p_0 and $\boldsymbol{u}_0$:

$$\nabla \cdot \boldsymbol{u}_0 = k_m n_0, \tag{2.22}$$

$$\nabla p_0 = \nabla^2 \boldsymbol{u}_0 + \frac{1}{3}\nabla\left(\nabla \cdot \boldsymbol{u}_0\right). \tag{2.23}$$

In (2.23) we have introduced the lumped pressure field: $p_0 = p_{w0} + n_0\Sigma_{n0}$ and in the following, we work in terms of this lumped pressure, obviating the need to specify Σ_{n0}. Equation (2.22) states that the rate at which the tissue grows is determined by the rate of cell proliferation and ECM deposition. Taking the divergence of equation (2.23) yields an expression for $\nabla^2(\nabla \cdot \boldsymbol{u}_0)$; substituting this into the Laplacian of (2.22) allows us to eliminate $\boldsymbol{u}_0$, yielding an equation for the pressure in terms of the cell volume fraction only. We may then express the model equations in the more natural form given in Franks (2002) and Franks & King (2003):

$$\frac{\partial n_0}{\partial t} + \nabla \cdot (n_0 \boldsymbol{u}_0) = (k_m - k_d)n_0 + D\nabla^2 n_0, \tag{2.24}$$

$$\nabla^2 p_0 = \frac{4}{3}\nabla^2\left(k_m n_0\right), \tag{2.25}$$

$$\nabla^2 \boldsymbol{u}_0 = \nabla p_0 - \frac{1}{3}\nabla\left(k_m n_0\right). \tag{2.26}$$

Appropriate boundary conditions (*e.g.* those employed in Franks (2002)) for equations (2.24)–(2.26) are not immediately obvious. Inspection of the large drag limit of the momentum equations (2.14) and (2.15) indicates that in a boundary layer of thickness $\mathcal{O}(1/\sqrt{k})$ near the channel walls the large drag model (2.24)–(2.26) breaks down. We show below that boundary conditions on the outer problem may be derived by considering the behaviour in the boundary layer.

Boundary layer analysis

We consider the behaviour in a boundary layer near the channel wall at $y = 0$ by introducing a boundary layer coordinate, Y ($y = Y/\sqrt{k}$) and boundary layer variables N, $\boldsymbol{U}_i = (U_i, V_i/\sqrt{k})$, P_w and $P = P_w + N\Sigma$; P is the lumped pressure in the boundary layer (*cf.* the outer variable, p_0). The scaling $V_i/\sqrt{k}$ is indicated by equation (2.14). As in (2.20), we consider an expansion of our boundary layer variables of the form:

$$N(x,Y,t) = N_0(x,Y,t) + \frac{1}{\sqrt{k}}N_1(x,Y,t) + \frac{1}{k}N_2(x,Y,t) + \cdots, \tag{2.27}$$

with similar expansions for $\boldsymbol{U}_i$, P_w and P. At leading order, the governing equations (2.14)–(2.16) in the boundary layer yield:

$$K_m N_0 = \frac{\partial}{\partial x}\big[N_0 U_{n0} + (1-N_0)U_{w0}\big] + \frac{\partial}{\partial Y}\big[N_0 V_{n0} + (1-N_0)V_{w0}\big], \tag{2.28}$$

$$U_{w0} - U_{n0} = (1-N_0)\frac{\partial^2 U_{w0}}{\partial Y^2} - \frac{\partial U_{w0}}{\partial Y}\frac{\partial N_0}{\partial Y}, \tag{2.29}$$

$$\begin{aligned} V_{w0} - V_{n0} = {} & (1-N_0)\left[-\frac{\partial P_{w0}}{\partial Y} + \frac{4}{3}\frac{\partial^2 V_{w0}}{\partial Y^2} + \frac{1}{3}\frac{\partial^2 U_{w0}}{\partial x \partial Y}\right] - \frac{\partial U_{w0}}{\partial Y}\frac{\partial N_0}{\partial x} \\ & - \frac{\partial N_0}{\partial Y}\left[\frac{4}{3}\frac{\partial V w0}{\partial Y} - \frac{2}{3}\frac{\partial U_w 0}{\partial x}\right], \end{aligned} \tag{2.30}$$

$$\frac{\partial^2 U_{n0}}{\partial Y^2} = \frac{(N_0-1)}{N_0}\frac{\partial^2 U_{w0}}{\partial Y^2} + \frac{1}{N_0}\frac{\partial N_0}{\partial Y}\left[\frac{\partial U_{w0}}{\partial Y} - \frac{\partial U_{n0}}{\partial Y}\right], \tag{2.31}$$

$$\begin{aligned} \frac{\partial P_0}{\partial Y} = {} & N_0\left[\frac{4}{3}\frac{\partial^2 V_{n0}}{\partial Y^2} + \frac{1}{3}\frac{\partial^2 U_{n0}}{\partial x \partial Y}\right] + (1-N_0)\left[\frac{4}{3}\frac{\partial^2 V_{w0}}{\partial Y^2} + \frac{1}{3}\frac{\partial^2 U_{w0}}{\partial x \partial Y}\right] \\ & + \left[\frac{4}{3}\left(\frac{\partial V_{n0}}{\partial Y} - \frac{\partial V_{w0}}{\partial Y}\right) - \frac{2}{3}\left(\frac{\partial U_{n0}}{\partial x} - \frac{\partial U_{w0}}{\partial x}\right)\right]\frac{\partial N_0}{\partial Y}, \\ & + \frac{\partial N_0}{\partial x}\left[\frac{\partial U_{n0}}{\partial Y} - \frac{\partial U_{w0}}{\partial Y}\right]. \end{aligned} \tag{2.32}$$

In equation (2.28), K_m is the growth rate in the boundary layer (the corresponding death rate is denoted K_d) which is assumed $\mathcal{O}(1)$. For simplicity, we consider rates of tissue growth and death whose spatial variation is confined to the axial direction: $K_m(x,t)$, $K_d(x,t)$.

We derive appropriate boundary conditions for the core flow equations (2.24)–(2.26) by considering matching conditions at the boundary layer edge ($Y \to \infty$):

$$\left\{n_0 + \frac{Y}{\sqrt{k}}\frac{\partial n_0}{\partial y} + \frac{1}{\sqrt{k}}n_1 + \cdots\right\}\Big|_{y=0} = \lim_{Y\to\infty}\left\{N_0 + \frac{1}{\sqrt{k}}N_1 + \cdots\right\}, \tag{2.33}$$

$$\left\{\boldsymbol{u}_0 + \frac{Y}{\sqrt{k}}\frac{\partial \boldsymbol{u}_0}{\partial y} + \frac{1}{\sqrt{k}}\boldsymbol{u}_1 + \cdots\right\}\Big|_{y=0} = \lim_{Y\to\infty}\left\{\boldsymbol{U}_{i0} + \frac{1}{\sqrt{k}}\boldsymbol{U}_{i1} + \cdots\right\};\ \ i = n, w, \tag{2.34}$$

$$\left\{p_0 + \frac{Y}{\sqrt{k}}\frac{\partial p_0}{\partial y} + \frac{1}{\sqrt{k}}p_1 + \cdots\right\}\Big|_{y=0} = \lim_{Y\to\infty}\left\{P_0 + \frac{1}{\sqrt{k}}P_1 + \cdots\right\}. \tag{2.35}$$

These conditions ensure that the cell volume fraction, velocity of each phase and lumped pressure within the boundary layer match with the cell volume fraction, common velocity and lumped pressure in the core. Guided by these requirements, we postulate the following forms for the leading-order velocities: $\boldsymbol{U}_{i0}(x,Y,t) = \widetilde{\boldsymbol{U}}(x,Y,t)$; $\widetilde{\boldsymbol{U}} = (\widetilde{U},\widetilde{V})$.

Equation (2.31) together with the no-slip condition (2.9b) yields $\widetilde{U} = 0$, in view of which, equations (2.31) and (2.32) imply $N_0 = N_0(x,t)$. This is consistent with the requirement that the volume fractions of the cell and culture medium phases remain bounded. The mass conservation equation (2.28) may then be integrated, and on application of the no-penetration condition (2.9b), yields $\widetilde{V} = K_m N_0 Y$, which in turn implies $P_0 = P_0(x,t)$.

We now consider the solutions at next order since to these are required in order to determine the appropriate boundary conditions on the leading order solutions N_0 and P_0 (see equations (2.33) and (2.35)). Taking into account the form of the leading order solutions given above, we find that similar equations govern N_1, $\boldsymbol{U}_{i1}$ and P_1:

$$K_m N_1 = \frac{\partial}{\partial x}\left[N_0 U_{n1} + (1-N_0)U_{w1}\right] + \frac{\partial}{\partial Y}\left[N_0 V_{n1} + (1-N_0)V_{w1}\right], \tag{2.36}$$

$$U_{w1} - U_{n1} = (1-N_0)\frac{\partial^2 U_{w1}}{\partial Y}, \tag{2.37}$$

$$V_{n1} - V_{w1} = (1-N_0)\left[\frac{\partial P_{w1}}{\partial Y} - \frac{4}{3}\frac{\partial^2 V_{w1}}{\partial Y^2} - \frac{1}{3}\frac{\partial^2 U_{w1}}{\partial x \partial Y}\right] - \frac{\partial N_0}{\partial x}\frac{\partial U_{w1}}{\partial Y} - \frac{4K_m}{3}N_0\frac{\partial N_1}{\partial Y}, \tag{2.38}$$

$$\frac{\partial^2 U_{n1}}{\partial Y^2} = \frac{N_0 - 1}{N_0}\frac{\partial^2 U_{w1}}{\partial Y^2}, \tag{2.39}$$

$$\begin{aligned}\frac{\partial P_1}{\partial Y} = {} & \frac{\partial}{\partial Y}\left[N_0\left(\frac{4}{3}\frac{\partial V_{n1}}{\partial Y} + \frac{1}{3}\frac{\partial U_{n1}}{\partial x}\right) + (1-N_0)\left(\frac{4}{3}\frac{\partial V_{w1}}{\partial Y} + \frac{1}{3}\frac{\partial U_{w1}}{\partial x}\right)\right] \\ & + \frac{\partial N_0}{\partial x}\left(\frac{\partial U_{n1}}{\partial Y} - \frac{\partial U_{w1}}{\partial Y}\right).\end{aligned} \tag{2.40}$$

Equations (2.37) and (2.39) together with no-slip indicate that the axial velocities are equal and linear in Y: $U_{i1} = a(x,t)Y$ for arbitrary $a(x,t)$. Motivated by this, we seek solutions for the transverse velocity of the form: $V_{i1} = \widetilde{V}_1(x,Y,t)$. Consideration of (2.38) and (2.40) then yields the following relation:

$$\left[(N_0 - 1)\Lambda' - \frac{4K_m N_0}{3}\right]\frac{\partial N_1}{\partial Y} - a\frac{\partial N_0}{\partial x} = 0, \tag{2.41}$$

where Λ is the $\mathcal{O}(1/\sqrt{k})$ contribution to the lumped pressure from cell-cell and cell-ECM interactions and $'$ represents differentiation with respect to N. Applying (2.9a) implies $a(x,t) = 0$. Since, in general, the expression in square brackets is non-zero, we conclude $N_1 = N_1(x,t)$. It is then straightforward to show $P_1 = P_1(x,t)$ and $V_{i1} = k_m N_1 Y$ (details omitted for brevity).

Using (2.33)–(2.35) to match these boundary layer solutions to the leading-order outer solutions at $y = 0$, we ascertain the following boundary conditions (conditions on $y = h$ are obtained using an identical method):

$$\boldsymbol{u}_0 = \mathbf{0}, \ \frac{\partial n_0}{\partial y} = 0, \ \frac{\partial p_0}{\partial y} = 0, \ \text{at } y = 0, \ h, \tag{2.42}$$

so that there is no-slip or penetration at the boundary layer edge. We remark that these boundary conditions deviate from those employed by Franks (2002), in which slip was permitted. In the remainder of this chapter, we employ the model of Franks (2002), allowing slip along $y = 0, h$; for clarity, the boundary conditions to be employed henceforth are:

$$\frac{\partial u_0}{\partial x} = k_m n_0 - \frac{\partial v_0}{\partial y}, \ v_0 = 0, \ \frac{\partial n_0}{\partial y} = 0, \ \frac{\partial p_0}{\partial y} = 0, \ \text{at } y = 0, \ h. \tag{2.43}$$

We pause here to highlight a restriction on the choice of the rates of growth and death. For simplicity, we have assumed $K_m(x,t)$ and $K_d(x,t)$. Since these must match with the outer rates ($k_m, \ k_d$) at $y = 0, h$, we require $\partial k_m/\partial y = 0 = \partial k_d/\partial y$ there; dependence of the cells' proliferative response on the velocity field (or its gradient) is therefore prohibited and we may not include (for instance) fluid shear stress-enhanced proliferation pertinent to the modelling of bone tissue engineering (see §1.2.2) in this formulation.

In summary, our model comprises equations (2.24)–(2.26) and the boundary conditions given by the dimensionless versions of (2.10) and (2.11) and equations (2.43). In the following sections, we present solutions to the model equations in various limits.

In an extension to Franks (2002) and Franks & King (2003), in §§2.3 and 2.4.1 we investigate the effect of an ambient flow on a uniformly proliferating tissue, for which the growth and death rates are constant. In §2.3, solutions are obtained in the one-dimensional limit: in §2.3.1 analytic solutions are presented in the case for which the tissue is delineated by two planar sharp interfaces ($D = 0$) and their stability to transverse perturbations is determined; in §2.3.2, numerical solutions for a tissue defined by diffuse interfaces ($D \neq 0$) are presented and compared with the analytic solutions from §2.3.1. In §2.4.1, corresponding two-dimensional numerical solutions are presented. In §2.4.2, the model is further extended by postulating functional forms for the growth rate, $k_m(\boldsymbol{x}, t)$, which allow the influence of a range of mechanical stimuli on the growth response of the cells to be accommodated. For simplicity, the death rate, k_d, is kept constant in each case. The effect of these stimuli is illustrated by considering the cells' response to the local cell density and pressure using two-dimensional simulations. We remark here that due to the absence of experimental data on which to base our model parameter values and the fast timescale chosen, in all subsequent

numerical simulations, the parameter values are selected to illustrate the behaviour of the model under a particular growth regime.

2.3 One-dimensional growth

In this section, the formulation presented in §2.2.1 is simplified by assuming that the tissue undergoes one-dimensional growth parallel to the x-axis and that the associated pressure and velocity fields are functions of x and t only. For mathematical convenience, we initially consider growth within a channel of infinite length. Dropping the subscript notation for brevity, equations (2.24)–(2.26) reduce to give

$$\frac{\partial n}{\partial t} + \frac{\partial}{\partial x}(nu) = (k_m - k_d)n + D\frac{\partial^2 n}{\partial x^2}, \tag{2.44}$$

$$\frac{\partial^2 p}{\partial x^2} = \frac{4k_m}{3}\frac{\partial^2 n}{\partial x^2}, \tag{2.45}$$

$$\frac{\partial^2 u}{\partial x^2} = \frac{\partial p}{\partial x} - \frac{k_m}{3}\frac{\partial n}{\partial x}, \tag{2.46}$$

and we emphasise that we consider uniform growth here, for which k_m and k_d are assumed constant.

The axial boundary conditions presented in §2.2.1 require some modification since the channel is now infinite in extent. Integration of equation (2.45) yields:

$$p = \frac{4k_m}{3}n + \alpha(t)x + \beta(t), \tag{2.47}$$

where $\alpha(t)$, $\beta(t)$ are arbitrary functions of time; application of the boundary conditions $p = P_u$, $n = 0$ at $x = 0$, $p = P_d$, $n = 0$ as $x \to \infty$ indicates that we require $\alpha = 0$, $\beta = P_u = P_d$. A pressure drop-induced flow may therefore not be imposed. Instead, we impose an upstream flow, $\overline{U}^*$, corresponding to the condition $u(x = 0, t) = \overline{U}$, where $\overline{U} = \overline{U}^*/U_w^*$ is the dimensionless upstream flowspeed. In the following, we choose $\overline{U} = 1$ which implies that the velocity scale in the non-dimensionalisation (2.12) is $U_w^* = \overline{U}^*$. The value of the upstream and downstream pressure is arbitrary and we choose $P_u = 0 = P_d$ without loss of generality. In view of this, appropriate boundary conditions on this problem are

$$p = 0, \quad n = 0, \quad u = 1, \qquad \text{at} \quad x = 0, \tag{2.48}$$

$$p = 0, \quad n = 0, \quad \frac{\partial u}{\partial x} = 0, \qquad \text{as} \quad x \to \infty. \tag{2.49}$$

From (2.47) (with $\alpha = \beta = 0$), we deduce that the pressure is directly proportional to the cell phase distribution, allowing us to obtain a reduced model in terms of the cell volume fraction (n) and axial velocity (u) only (details omitted).

2.3.1 Sharp interface limit: $D = 0$

We now consider the regime in which the interfaces between the tissue construct and surrounding culture medium are sharp, corresponding to the choice $D = 0$ in equation (2.44). The domain is then separated into three distinct regions by two planar interfaces. We denote the interfacial positions by $x = L(t), R(t)$, across which we impose continuity of velocity and normal stress:

$$[u]^+_- = 0, \qquad \left[-p + \frac{4}{3}\frac{\partial u}{\partial x}\right]^+_- = 0 \quad \text{at} \quad x = L(t),\ R(t). \tag{2.50}$$

In (2.50), we have adopted the notation $[..]^+_-$ to denote the jump across an interface, the superscript + indicating the limiting value $x = L$ (or R) from within $L(t) \leqslant x \leqslant R(t)$. The evolution of the interfacial positions $x = L(t), R(t)$ is determined by imposing the following kinematic conditions which demand that particles on the interfaces remain there:

$$\frac{\mathrm{d}L}{\mathrm{d}t} = u(L,t), \quad \frac{\mathrm{d}R}{\mathrm{d}t} = u(R,t). \tag{2.51}$$

For simplicity we consider a growing construct of spatially-uniform density, represented as follows:

$$n(x,t) = \begin{cases} \overline{n}(t) & L(t) \leqslant x \leqslant R(t), \\ 0 & \text{otherwise.} \end{cases} \tag{2.52}$$

It is then trivial to integrate the one-dimensional equations in each region to determine:

$$u = 1, \qquad p = 0, \qquad 0 \leqslant x < L(t), \tag{2.53}$$

$$u = k_m \overline{n}\,(x - L(t)) + 1, \qquad p = \frac{4}{3} k_m \overline{n}, \qquad L(t) \leqslant x \leqslant R(t), \tag{2.54}$$

$$u = k_m \overline{n}\,(R(t) - L(t)) + 1, \quad p = 0, \qquad x > R(t). \tag{2.55}$$

We remark that the linear velocity profile ensures that there are no viscous losses in this model (see equation (2.46)), consistent with the absence of an imposed pressure drop.

The evolution of the cell distribution is determined from equation (2.44), which yields the following well-known logistic growth behaviour:

$$\overline{n}(t) = \frac{\overline{n}(0) K e^{rt}}{K + \overline{n}(0)(e^{rt} - 1)}, \tag{2.56}$$

in which $\overline{n}(0)$ is the initial cell density, $r = k_m - k_d$ is the net growth rate and $K = 1 - k_d/k_m$ is the carrying capacity which defines the stable steady-state density: if $\overline{n}(0) > K$, the cell density decreases monotonically to K; if $K/2 < \overline{n}(0) < K$, the density increases monotonically to K; if $\overline{n}(0) < K/2$, the increase is sigmoidal (Murray, 2002).

The interfacial positions of the growing tissue construct are then given by equations (2.51), from which we find:

$$L(t) = t + L(0), \quad R(t) = \frac{R(0) - L(0)}{K}\left[K + \overline{n}(0)\left(e^{rt} - 1\right)\right] + t + L(0), \tag{2.57}$$

where $L(0)$ and $R(0)$ are the initial interfacial positions. These solutions show that the construct is advected with the imposed flow ($u(x = 0, t) = 1$); furthermore, its width, given by $R(t) - L(t)$, increases exponentially due to cell proliferation and ECM deposition. We note here that our model predicts axially asymmetric tissue growth: equations (2.57) show that the upstream interface is advected at the speed of the imposed flow, whilst advection of the downstream interface is augmented by tissue growth. This growth asymmetry is evident for both static and dynamic culture conditions. This is because we require continuity of velocity on $x = L(t)$ which, in the absence of an imposed flow, requires that the upstream interface remains stationary. The solutions (2.53)–(2.55) indicate that the pressure is discontinuous across the interface between the tissue construct and surrounding culture medium, with tissue growth responsible for the increased pressure. This behaviour is, of course, an artefact of the sharp interface limit.

Linear stability analysis

The stability properties of such one-dimensional tissues have been analysed by a number of authors, especially in the context of solid tumour growth; see, for example, Franks (2002), Franks *et al.* (2003) and Franks & King (2003), in which the effect of nutrient limitations and material properties on the stability of tumours of constant density is considered and the results used to characterise to the malignancy and fingering instability of such tumours. Here, we consider the effect of an imposed flow on the stability of a growing tissue to disturbances in the transverse direction.

We perturb the interfaces $L(t)$, $R(t)$ as follows. Denoting the planar interfaces defined in (2.57) by $L_0(t)$, $R_0(t)$, we introduce a transverse perturbation such that

$$L(y, t) = L_0(t) + \epsilon L_1(y, t) + \cdots, \tag{2.58}$$

$$R(y, t) = R_0(t) + \epsilon R_1(y, t) + \cdots, \tag{2.59}$$

where $0 < \epsilon \ll 1$ and L_1, R_1 are perturbations. Correspondingly, we seek solutions to the governing equations of the following form:

$$n(x,y,t) = n_0(x,t) + \epsilon n_1(x,y,t) + \cdots, \tag{2.60}$$

$$u(x,y,t) = u_0(x,t) + \epsilon u_1(x,y,t) + \cdots, \tag{2.61}$$

$$v(x,y,t) = \epsilon v_1(x,y,t) + \cdots, \tag{2.62}$$

$$p(x,y,t) = p_0(x,t) + \epsilon p_1(x,y,t) + \cdots, \tag{2.63}$$

where n_0, u_0, p_0 are the one-dimensional solutions (2.53)–(2.56) corresponding to the planar interfaces. We remark that the subscript notation which previously indicated the terms in the large drag expansion (2.27) has been replaced by subscripts denoting the solutions associated with the planar interfaces and perturbations. This calculation follows the methodology presented in Franks (2002) and Franks & King (2003) and so much of the detail is omitted.

Returning to the two-dimensional system given by equations (2.22), (2.24) and (2.26), we find that the perturbations to the cell volume fraction, pressure and velocity satisfy

$$\nabla \cdot \boldsymbol{u}_1 = k_m n_1, \quad \nabla^2 \boldsymbol{u}_1 = \nabla p_1 - \frac{k_m}{3} \nabla n_1, \tag{2.64}$$

$$\frac{\partial n_1}{\partial t} + 2k_m n_0 n_1 + u_0 \frac{\partial n_1}{\partial x} = (k_m - k_d) n_1. \tag{2.65}$$

We note that following Franks (2002) we have employed equation (2.22) in preference to (2.25). Appropriate boundary conditions, consistent with the leading-order axial conditions (2.48) and (2.49) and the transverse conditions (2.43), are

$$u_1 = 0, \quad v_1 = 0, \quad p_1 = 0, \quad n_1 = 0, \quad \text{at} \quad x = 0, \tag{2.66}$$

$$\frac{\partial u_1}{\partial x} = 0, \quad v_1 = 0, \quad p_1 = 0, \quad n_1 = 0, \quad \text{as} \quad x \to \infty, \tag{2.67}$$

$$\frac{\partial u_1}{\partial x} = k_m n_1 - \frac{\partial v_1}{\partial y}, \quad v_1 = 0, \quad \frac{\partial p_1}{\partial y} = 0, \quad \frac{\partial n_1}{\partial y} = 0, \quad \text{at} \quad y = 0, h. \tag{2.68}$$

Jump conditions on the moving boundary, $x = L(y,t)$, are derived by Taylor-expanding the following two-dimensional stress and velocity continuity conditions about the planar interface $x = L_0(t)$:

$$[\hat{\boldsymbol{n}} \cdot \boldsymbol{\sigma} \cdot \hat{\boldsymbol{n}}]_-^+ = 0, \qquad \left[\hat{\boldsymbol{t}} \cdot \boldsymbol{\sigma} \cdot \hat{\boldsymbol{n}}\right]_-^+ = 0, \qquad [\boldsymbol{u}]_-^+ = \boldsymbol{0}. \tag{2.69}$$

In equations (2.69), $\boldsymbol{\sigma}$ is the stress tensor (2.8) defined in terms of the outer pressure and velocity fields $(p, \boldsymbol{u})$, $[..]_-^+$ denotes the jump across the construct/fluid interface and $\hat{\boldsymbol{n}}$ and

$\hat{\boldsymbol{t}}$ are the unit normal and tangent to the interfaces, defined for $x = L(y,t)$ as follows:

$$\hat{\boldsymbol{n}} = \frac{\left(1, -\frac{\partial L}{\partial y}\right)}{\sqrt{1 + \left(\frac{\partial L}{\partial y}\right)^2}}, \qquad \hat{\boldsymbol{t}} = \frac{\left(\frac{\partial L}{\partial y}, 1\right)}{\sqrt{1 + \left(\frac{\partial L}{\partial y}\right)^2}}, \tag{2.70}$$

and similarly for the surface, $x = R(y,t)$. At $\mathcal{O}(\epsilon)$, we obtain the following conditions at $x = L_0(t)$:

$$\left[-p_1 + \frac{4}{3}\frac{\partial u_1}{\partial x} - \frac{2}{3}\frac{\partial v_1}{\partial y}\right]_-^+ = 0, \qquad \left[2k_m\overline{n}\frac{\partial L_1}{\partial y} + \frac{\partial u_1}{\partial y} + \frac{\partial v_1}{\partial x}\right]_-^+ = 0, \tag{2.71}$$

$$u_1^+ + k_m\overline{n}L_1 = u_1^-, \qquad [v_1]_-^+ = 0. \tag{2.72}$$

Similar conditions apply at $x = R_0$. The perturbations to the interfaces are governed by the following kinematic conditions:

$$\frac{\partial L_1}{\partial t} = u_1^- = u_1^+ + k_m\overline{n}L_1, \qquad \frac{\partial R_1}{\partial t} = u_1^- = u_1^+ + k_m\overline{n}R_1, \tag{2.73}$$

which are applied at $x = L_0(t)$ and $x = R_0(t)$, respectively.

The stability of the one-dimensional tissue defined by equations (2.52) and (2.56) may now be determined from solution of the system (2.64)–(2.73). We proceed by assuming that the perturbations to the interfacial positions are separable, of the form

$$L_1(y,t) = l_1(t)\cos(\lambda y), \qquad R_1(y,t) = r_1(t)\cos(\lambda y), \tag{2.74}$$

for arbitrary wavenumber, λ, and seek solutions for n_1 of a like form:

$$n_1(x,y,t) = \begin{cases} \widetilde{n}(t)\cos(\lambda y) & L(y,t) \leqslant x \leqslant R(y,t), \\ 0 & \text{otherwise.} \end{cases} \tag{2.75}$$

The temporal variation of n_1 is determined from equation (2.65), yielding:

$$\widetilde{n}(t) = \frac{Ge^{rt}}{\left[K + \overline{n}(0)(e^{rt} - 1)\right]^2}, \tag{2.76}$$

in which G is arbitrary (we set $G = 1$ in the following without loss of generality). In view of the boundary condition (2.68), equation (2.75) indicates $\lambda = m\pi/h$, for integer m.

We now introduce a subscript i to denote the region in which the solution is valid; the regions $i = 1, 2, 3$ correspond to $0 \leqslant x < L(y,t)$, $L(y,t) \leqslant x \leqslant R(y,t)$, $x > R(y,t)$, respectively. Following Franks (2002), we write $u_{1i} = f_i(x,t)\cos(\lambda y)$ and from equations (2.64) we obtain

$$v_{12} = \left(k_m\widetilde{n} - \frac{\partial f_2}{\partial x}\right)\frac{\sin(\lambda y)}{\lambda}, \quad p_{12} = \left(\frac{1}{\lambda^2}\frac{\partial^3 f_2}{\partial x^3} - \frac{\partial f_2}{\partial x} + \frac{4k_m\widetilde{n}}{3}\right)\cos(\lambda y), \tag{2.77}$$

$$v_{1i} = -\frac{\partial f_i}{\partial x}\frac{\sin(\lambda y)}{\lambda}, \qquad p_{1i} = \left(\frac{1}{\lambda^2}\frac{\partial^3 f_i}{\partial x^3} - \frac{\partial f_i}{\partial x}\right)\cos(\lambda y); \quad i = 1, 3, \tag{2.78}$$

which are consistent with the remaining transverse boundary conditions (2.68). Considering the axial component of the second of (2.64), we find that the functions f_i are given by:

$$f_i(x,t) = [\mathcal{A}_i(t) + \mathcal{B}_i(t)x]\, e^{\lambda x} + [\mathcal{C}_i(t) + \mathcal{D}_i(t)x]\, e^{-\lambda x}. \tag{2.79}$$

After some algebra, the twelve functions, $\mathcal{A}_i(t)$–$\mathcal{D}_i(t)$ may be specified in terms of the planar interfaces $L_0(t)$, $R_0(t)$, the interface perturbation amplitudes $l_1(t)$, $r_1(t)$ and the cell distributions $\overline{n}(t)$, $\widetilde{n}(t)$:

$$\mathcal{A}_1 = \frac{k_m\overline{n}}{2}\left(l_1 e^{-\lambda L_0} - r_1 e^{-\lambda R_0}\right) + \frac{k_m\widetilde{n}}{2\lambda}\left(e^{-\lambda R_0} - e^{-\lambda L_0}\right) = -\mathcal{C}_1, \tag{2.80}$$

$$\mathcal{A}_2 = \frac{k_m e^{-\lambda R_0}}{2\lambda}(\lambda\overline{n}r_1 - \widetilde{n}), \tag{2.81}$$

$$\mathcal{C}_2 = \frac{k_m\overline{n}}{2}\left[r_1 e^{-\lambda R_0} - 2l_1\cosh(\lambda L_0)\right] - \frac{k_m\widetilde{n}}{2\lambda}\left[2\sinh(\lambda L_0) + e^{-\lambda R_0}\right], \tag{2.82}$$

$$\mathcal{C}_3 = k_m\overline{n}\,[r_1\cosh(\lambda R_0) - l_1\cosh(\lambda L_0)] + \frac{k_m\widetilde{n}}{\lambda}\,[\sinh(\lambda R_0) - \sinh(\lambda L_0)]\,, \tag{2.83}$$

$$\mathcal{B}_1 = 0, \quad \mathcal{D}_1 = 0, \quad \mathcal{B}_2 = 0, \quad \mathcal{D}_2 = 0, \quad \mathcal{A}_3 = 0, \quad \mathcal{B}_3 = 0, \quad \mathcal{D}_3 = 0. \tag{2.84}$$

As found for the one-dimensional base state of uniform density (equation (2.52)), it can be shown that the perturbation to the pressure is directly proportional to the cell volume fraction:

$$p_1(x,y,t) = \begin{cases} \frac{4k_m}{3}\widetilde{n}(t)\cos(\lambda y) & L(y,t) \leqslant x \leqslant R(y,t), \\ 0 & \text{otherwise}, \end{cases} \tag{2.85}$$

and the corresponding axial and transverse velocity perturbations ensure that the viscous losses in the momentum equations (2.64) and (2.65) sum to zero, consistent with the absence of a pressure drop.

Equations (2.73) then give

$$\frac{\mathrm{d}l_1}{\mathrm{d}t} = \mathcal{A}_1\left[e^{\lambda L_0} - e^{-\lambda L_0}\right], \qquad \frac{\mathrm{d}r_1}{\mathrm{d}t} = \mathcal{C}_3 e^{-\lambda R_0}, \tag{2.86}$$

where L_0, R_0 are defined by (2.57).

Equations (2.86) are solved numerically using the initial value problem solver, `ode45` in MATLAB (which employs an explicit Runge-Kutta formula to compute the solution to non-stiff problems) to determine the evolution of the perturbations. Numerical accuracy checks are performed by refining error tolerance parameters (results omitted). Figure 2.2 shows how the perturbations evolve over time for different values of the growth rate, k_m.

We note from figure 2.2 that there are marked differences in the behaviour of the perturbations to each interface: the amplitude of the upstream perturbation (l_1) decreases

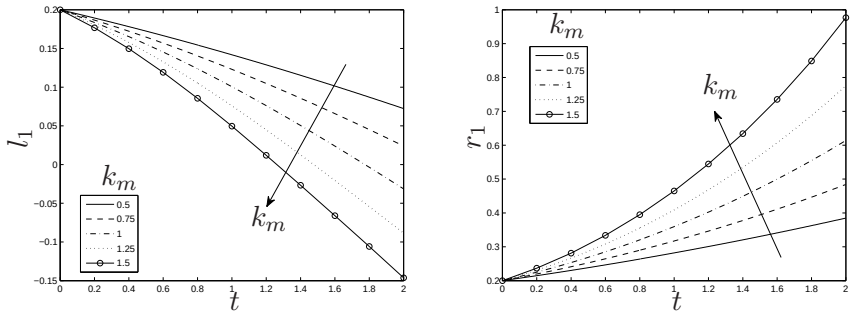

(a) (b)

Figure 2.2: The growth of the perturbation amplitudes l_1 and r_1 for different values of the growth rate, k_m; the arrows indicate the direction of increasing k_m. Parameter values: $k_d = 0.1$, $m = 2$, $h = 1$, $\overline{n}(0) = 0.2$, $L_0(0) = 4$, $R_0(0) = 6$. Initial conditions: $l_1(0) = 0.2 = r_1(0)$.

monotonically with time, passing through zero; conversely, the amplitude of the downstream perturbation (r_1) increases monotonically. The effect of this phenomenon on the behaviour of the interfaces $x = L(y,t), R(y,t)$ for the $m = 2$ mode is illustrated in figure 2.3, showing how the reversal of sign of l_1 corresponds to a dramatic difference in the behaviour of the up- and downstream interfaces. This behaviour is a result of the transverse perturbation to the cell volume fraction, $n_1 = \widetilde{n}\cos(\lambda y)$. The transverse variation results in a tissue with reduced density near $y = (2q+1)h/m$ and increased density near $y = 2qh/m$, for integer q, causing invagination in the sparse regions and protrusion in the dense regions, as depicted in figure 2.3. In the absence of transverse perturbations to the cell volume fraction ($n_1 = 0$), the tissue density is spatially uniform and the perturbations to each interface do not exhibit this behaviour, both l_1 and r_1 increasing monotonically at exactly the same rate (as reported by Franks (2002)); we note that in this case, the growth rate of the up- and downstream perturbation amplitudes is lower than that observed for the downstream interface in the regime for which $n_1 \neq 0$ (details omitted).

Inspection of equations (2.80), (2.83) and (2.86) indicates that the influence of the transverse perturbation to the cell volume fraction (n_1) on the stability of the interfaces diminishes with increasing wavenumber, $\lambda(m)$: as λ increases, the growth of the perturbation amplitudes (l_1, r_1) tends to that observed in the absence of perturbations to the cell volume fraction ($n_1 = 0$). Furthermore, equation (2.76) shows that for large time ($t \gg r^{-1}$), the perturbation n_1 decays to zero (in order that we remain within the linear regime we require

$\epsilon\, e^{rt} \ll 1$); indeed, for large time, the differential equations (2.86) reduce to

$$\frac{\mathrm{d}l_1}{\mathrm{d}t} \sim \frac{k_m - k_d}{2} l_1, \qquad \frac{\mathrm{d}r_1}{\mathrm{d}t} \sim \frac{k_m - k_d}{2} r_1, \tag{2.87}$$

and the one-dimensional solution for which $n(x,t) = \overline{n}(t)$, $L_0(t) \leqslant x \leqslant R_0(t)$ is therefore unstable to small transverse perturbations if the net growth rate is positive (we remark that both the amplitude of the perturbations and the construct width increase exponentially with time). It is interesting to note that the stability properties of the interfaces $x = L_0, R_0$ are largely unaffected by the presence of the ambient flow, which only enters the analysis through the advection of the interfaces; see equation (2.57). Qualitatively similar results are thus obtained in the zero flow regime (results omitted).

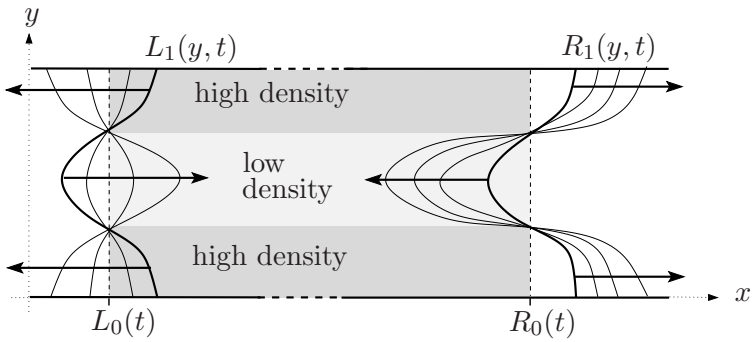

Figure 2.3: A diagram showing the effect of the transverse perturbation to the cell volume fraction (n_1) on the evolution of the perturbations $L_1(y,t)$ and $R_1(y,t)$ for the $m = 2$ mode; the arrows show the direction of increasing time.

In the preceding analysis, we have considered the growth and stability of a tissue defined by two planar interfaces within a perfusion bioreactor. For convenience, the bioreactor was modelled as a channel of infinite length; the influence of considering a finite-length bioreactor on the stability properties of this tissue is determined by performing a linear stability analysis in an identical fashion to that given above, with the conditions at infinity now imposed on the truncated boundary, $x = X$ (for brevity, the details are omitted here). Equations (2.73) are then integrated numerically to yield the behaviour of the perturbations. We find that the up- and downstream planar interfaces are again unstable to transverse perturbations; the growth rates of the perturbations, l_1 and r_1 match those predicted by the linear stability analysis on an infinite domain provided that the interfaces do not approach $x = X$ (as reported in Franks (2002) and Franks & King (2003)). Figure 2.4 shows a comparison between the growth of the perturbations l_1 and r_1 in the infinite and finite domains; the divergent behaviour occurs when $R_0(t)$ approaches $x = X$.

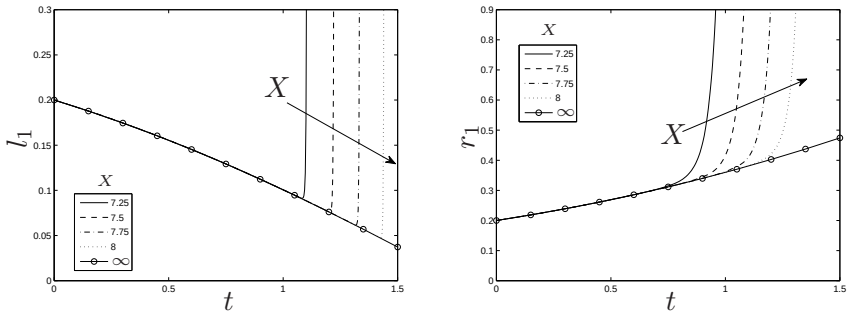

(a) (b)

Figure 2.4: Comparison of the growth of the amplitude of the perturbations (l_1, r_1) for the infinite and finite domains as the domain length, X, varies. $k_m = 1$, other parameter values as in figure 2.2.

2.3.2 Numerical simulation: $D \neq 0$

We now present numerical solutions of the one-dimensional equations (2.44)–(2.46) on the truncated domain $0 \leqslant x \leqslant 1$ subject to (2.48) and (2.49); the conditions specified for $x \to \infty$ are imposed at $x = 1$. We emphasise that in contrast to the previous section, this system represents a tissue construct defined by two diffuse interfaces. A suitably smooth initial condition for n is chosen to be

$$n(x,0) = 0.1\left[\tanh(50(x-0.15)) - \tanh(50(x-0.2))\right]. \tag{2.88}$$

Solutions to equations (2.44)–(2.46) are calculated with the NAG routine D03PCF which uses a backward differentiation formula method to solve the system of ordinary differential equations resulting from the application of the method of lines to a system of partial differential equations. The evolution of n and u is shown in figure 2.5; the arrows indicate the direction of increasing time. Results for the pressure, p, are omitted since it is directly proportional to n (see equation (2.47)).

In figure 2.6, we compare the positions of the construct boundaries predicted by the sharp interface analysis (equations (2.57)) and the numerically-calculated results for a diffuse construct. The positions of the boundaries of the diffuse construct are taken to be the up- and downstream half-maximal values of n; in equations (2.57), $\overline{n}(0)$ is approximated by the maximum value of $n(x,0)$. In figure 2.7, we compare the evolution of the numerically-computed maximum cell volume fraction and the logistic growth predicted by (2.56).

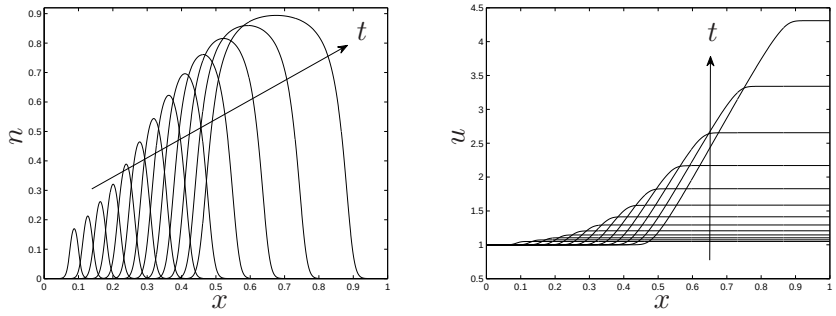

(a) (b)

Figure 2.5: A plot of (a) the cell volume fraction, n, and (b) the velocity, u, at $t = 0-0.48$ in steps of $t = 0.04$. Parameter values: $D = 0.0005$, $k_m = 10$, $k_d = 0.1$.

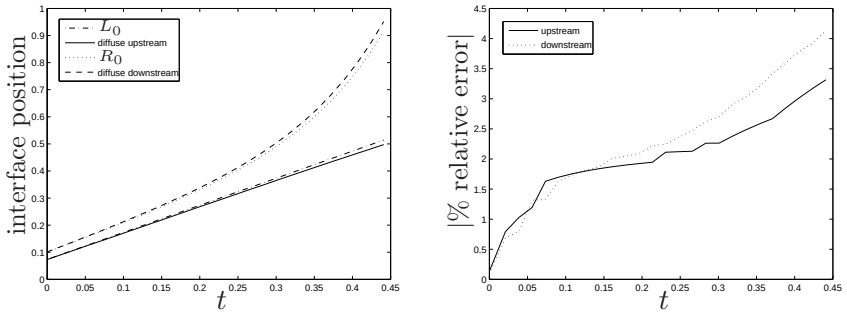

(a) (b)

Figure 2.6: (a) A comparison between the numerically-computed positions of the up- and downstream diffuse interfaces and those predicted by the sharp interface analysis ($L_0(t)$, $R_0(t)$, equations (2.57)); (b) the % relative error between the position of the diffuse up- and downstream interfaces and the corresponding sharp interfaces.

Inspection of figures 2.5 and 2.6 shows that the analytical solutions (2.53)–(2.57), corresponding to a growing tissue construct of uniform density defined by two sharp interfaces, capture much of the qualitative behaviour of the full one-dimensional model. Figure 2.5 shows how the cell population is advected downstream by the flow: the diffuse upstream interface is advected at a constant rate, while the downstream interface is advected at a rate which increases with increasing cell density, and the construct domain elongates accordingly. Figure 2.6 shows that the numerically-calculated positions of these diffuse interfaces are in good agreement with the sharp interfaces defined by equations (2.57). We highlight that, as indicated by figure 2.5a, as t increases towards $t = 0.48$, the construct approaches the

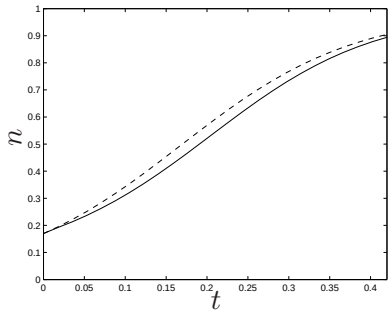

Figure 2.7: A comparison between the numerically-computed peak cell density (–) and the logistic growth predicted by the sharp interface solution (2.56) (- -).

downstream domain boundary and meaningful comparison cannot be made. In addition, figure 2.5a indicates that the time evolution of the peak cell density approximates the sigmoidal growth profile predicted by the sharp interface solution (2.56): following the initial fast growth phase, the peak cell density increases more slowly, tending towards the carrying capacity, $K = 1 - k_d/k_m$; figure 2.7 shows a comparison between the numerically-calculated peak cell density and that predicted by the solution (2.56) indicating good agreement. We remark that the imposed flow advects the construct to the end of the domain before the steady-state value $n = K = 0.99$ can be attained.

The numerically-computed velocity profile is constant prior to, and after, the tissue, increasing approximately linearly within. It may be shown that the velocity increases with gradient $k_m n(x,t)$ (*cf.* equation (2.54)) as demanded by the continuity equation (2.22); the downstream velocity increases approximately exponentially with time, as predicted by equations (2.55)–(2.57) (details omitted).

In this section, we have analysed the effect of an ambient flow on a one-dimensional tissue construct whose rates of growth and death remain constant. Analytic solutions, constructed in the limit for which the interfaces between the growing construct and the surrounding culture medium are sharp, were shown to be in good qualitative agreement with numerical simulations for a construct defined by two diffuse interfaces. In each case, the effect of the flow is to advect the cells downstream. We find that the stability of the sharp interfaces to transverse perturbations is largely unaffected by the imposed flow; however, it is shown that the early-time behaviour of these interfaces is dramatically altered by introducing a corresponding perturbation to the cell volume fraction.

In the context of the bioreactor system described in §1.2.3, this model predicts that the cells and ECM will be advected through the bioreactor at the speed of the imposed

perfusion. Very low flow rates are therefore required to prevent tissue from being flushed out of the bioreactor before tissue growth can be achieved. This prediction is due to the simplifying limit of large interphase drag employed in this chapter, in which each phase is subject to a common velocity field.

2.4 Two-dimensional growth

2.4.1 Uniform growth

We now present numerical solutions to the two-dimensional equations (2.24)–(2.26) in the domain $0 \leqslant x \leqslant 1$, $0 \leqslant y \leqslant h$ subject to the dimensionless versions of (2.10), (2.11) and (2.43). Equation (2.24) is solved using a semi-implicit time-stepping method; the linear systems associated with the discretised versions of equations (2.24)–(2.26) and corresponding boundary conditions are solved using the Gaussian elimination routine in MATLAB at each time step. The value of $n_{i,j}^{k+1}$ at each mesh point (i,j) and new time step, $k+1$, is computed from $n_{i,j}^{k}$, $u_{i,j}^{k}$, $v_{i,j}^{k}$ using the following semi-implicit approximation for equation (2.24):

$$\begin{aligned}\frac{n_{i,j}^{k+1}-n_{i,j}^{k}}{\Delta t} = \frac{1}{2}\Bigg\{ & \left(k_m - k_d - \frac{u_{i+1,j}^{k}-u_{i-1,j}^{k}}{2\Delta x} - \frac{v_{i,j+1}^{k}-v_{i,j-1}^{k}}{2\Delta y}\right) n_{i,j}^{k+1} - u_{i,j}^{k}\frac{n_{i,j}^{k+1}-n_{i-1,j}^{k+1}}{\Delta x} \\ & - v_{i,j}^{k}\frac{n_{i,j}^{k+1}-n_{i,j-1}^{k+1}}{\Delta y} + D\left(\frac{n_{i+1,j}^{k+1}-2n_{i,j}^{k+1}+n_{i-1,j}^{k+1}}{(\Delta x)^2} + \frac{n_{i,j+1}^{k+1}-2n_{i,j}^{k+1}+n_{i,j-1}^{k+1}}{(\Delta y)^2}\right) \\ & + \left(k_m - k_d - \frac{u_{i+1,j}^{k}-u_{i-1,j}^{k}}{2\Delta x} - \frac{v_{i,j+1}^{k}-v_{i,j-1}^{k}}{2\Delta y}\right) n_{i,j}^{k} - u_{i,j}^{k}\frac{n_{i,j}^{k}-n_{i-1,j}^{k}}{\Delta x} \\ & - v_{i,j}^{k}\frac{n_{i,j}^{k}-n_{i,j-1}^{k}}{\Delta y} + D\left(\frac{n_{i+1,j}^{k}-2n_{i,j}^{k}+n_{i-1,j}^{k}}{(\Delta x)^2} + \frac{n_{i,j+1}^{k}-2n_{i,j}^{k}+n_{i,j-1}^{k}}{(\Delta y)^2}\right)\Bigg\}, \end{aligned} \tag{2.89}$$

wherein Δt, Δx, Δy represent the size of the time step and the mesh spacing in the x- and y- directions, respectively, and $n_{i,j}^{k} \approx n(i\Delta x, j\Delta y, k\Delta t)$. We choose $h = 1$ and a uniform spatial grid is chosen with $\Delta x = 5 \times 10^{-3}$, $\Delta y = 1 \times 10^{-2}$ and the time step is $\Delta t = 1 \times 10^{-3}$. Convergence of the numerical scheme is ascertained via spatial and temporal mesh refinement (the results of this are omitted here). We note that an upwind scheme is used for the convective terms in equation (2.24): backward or forward differences are used depending on the sign of the velocities u and v (in (2.89), the velocities are assumed to be positive and so backward differences have been used).

Suitably smooth initial conditions for a y-independent cell population centred at $x =$

0.45 read:

$$n(\boldsymbol{x}, 0) = 0.1\left[\tanh(50(x - 0.4)) - \tanh(50(x - 0.5))\right], \tag{2.90}$$

and a surface plot of these initial conditions is shown in figure 2.8.

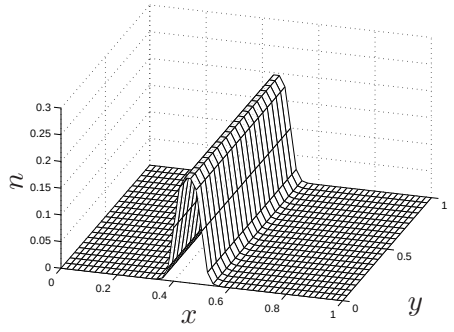

Figure 2.8: A surface plot showing the initial cell distribution $n(\boldsymbol{x}, t = 0)$ given by equation (2.90).

Plots of the cell volume fraction, pressure and axial and transverse velocity components for the regime of dynamic culture conditions are shown in figures 2.9–2.12. Where appropriate, surface and contour plots are included to add clarity. Figure 2.13 shows a contour and surface plot of the predicted tissue construct for static culture conditions (in which we choose $P_u = P_d = 0$). In the following (for dynamic culture conditions) we choose $P_u = 1$, $P_d = 0$, $h = 1$, $k_m = 4$, $k_d = 0.2$ and $D = 0.001$ and we emphasise that these parameter values are not physiologically motivated, being chosen to illustrate the behaviour of the model. We note that the choices $P_u = 1$, $P_d = 0$ set the velocity scale, U_w^*, used in the non-dimensionalisation (2.12) to be $U_w^* = P_u^* L^*/\mu_w^*$; $P_d = 0$ corresponds to $P_d^* = 0$ (see equations (2.17)). In the absence of cells, the maximum axial velocity is given by $u_{max}^* = P_u^* h^{*2}/(8\mu_w^* L^*)$; for the parameter choice given we therefore expect to see the maximum upstream dimensionless velocity to be $u = 1/8$. Inspection of figure (2.11) confirms this.

Figure 2.9 shows how the initially small, y-independent construct given by (2.90) grows and spreads through the channel. The cells are also advected along the channel to a limited extent by the axial velocity, u, which is parabolic in y. This pressure-induced parabolic flow causes increased advection in the channel centre where flow speed is maximal, introducing significant transverse variation. We remark that the solution for the axial velocity, u, is unique up to the addition of an arbitrary one-dimensional solution, $\hat{u}$; we have chosen $\hat{u} = 0$ so that no-slip is assured prior to the tissue; within and downstream from it, a significant

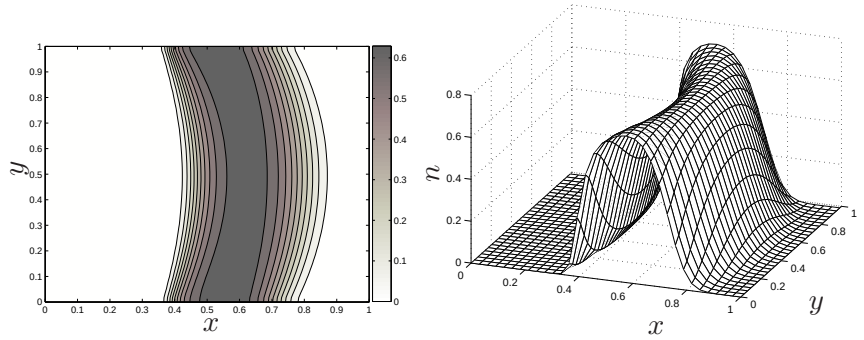

(a) (b)

Figure 2.9: (a) A contour plot and (b) a surface plot of the cell volume fraction showing the effect of a pressure-induced flow on tissue construct morphology at $t = 0.6$. Parameter values: $h = 1$, $k_m = 4$, $k_d = 0.2$, $D = 0.001$, $P_u = 1$, $P_d = 0$.

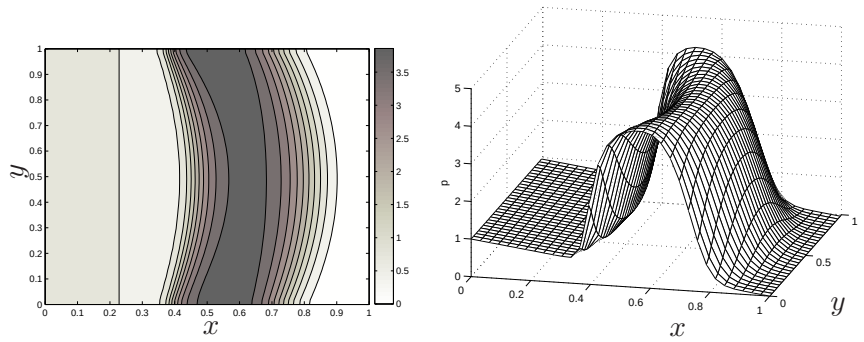

(a) (b)

Figure 2.10: (a) A contour plot and (b) a surface plot showing the pressure distribution corresponding to the tissue construct in figure 2.9. Parameter values as given in figure 2.9.

slip velocity is created.

The advection/growth behaviour of the tissue construct warrants further discussion. Comparison of the profile shown in figure 2.9 and the initial condition illustrated in figure 2.8 shows that advection of the upstream periphery of the diffuse construct is confined to a region near the channel centreline ($y = 1/2$) where the parabolic flow is maximal. Near the channel walls, where the flow speed is low, limited upstream movement is observed due to the presence of diffusion (for a higher diffusion coefficient than that employed in §2.3.2, this behaviour is, of course, also observed in the case of a one-dimensional diffuse tissue). Advection of the downstream periphery introduces corresponding transverse variation; however,

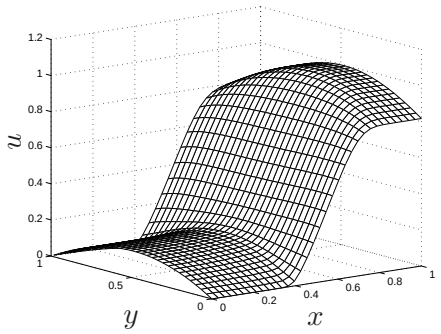

Figure 2.11: A surface plot of the axial velocity profile corresponding to the tissue construct in figure 2.9. Parameter values as given in figure 2.9.

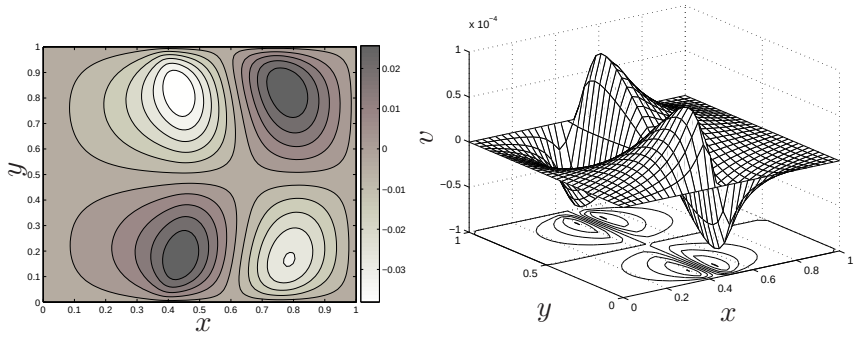

(a) (b)

Figure 2.12: (a) A contour plot and (b) a surface plot showing the transverse velocity corresponding to the tissue construct in figure 2.9. Parameter values as given in figure 2.9.

there is significantly greater axial advection due to the greater flow speed there. Figure 2.13 shows that in the absence of an imposed flow ($P_u = 0 = P_d$), the cell population remains (almost) independent of the transverse coordinate (small transverse variation is evident from close inspection of the contours in figure 2.13a). However, the population does not grow in an axially-symmetric manner about the midpoint of the initial distribution: the upstream periphery remains almost stationary (small upstream progression is made due to diffusion) while the downstream periphery spreads downstream; furthermore, the cell density gradient is greater on the upstream periphery. Mesh refinement and increasing the diffusion coefficient, D, removes the transverse variation and reduces the axial growth asymmetry; however, the construct still does not grow symmetrically about the midpoint of the initial distribution. For both dynamic and static culture conditions, this type of

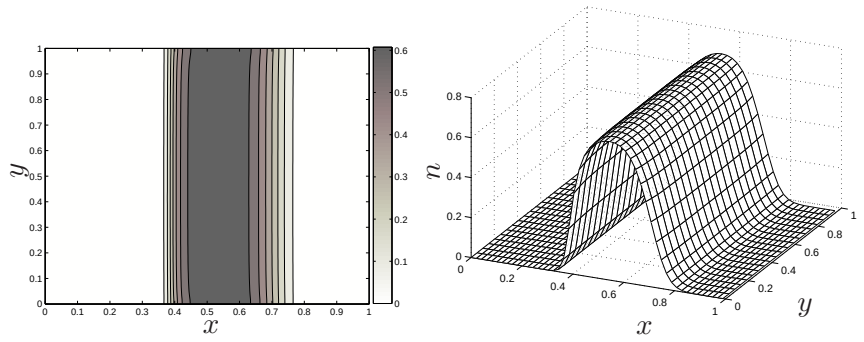

(a) (b)

Figure 2.13: (a) A contour plot and (b) a surface plot showing the predicted tissue construct morphology for static culture conditions at $t = 0.6$. $P_u - P_d = 0$, other parameter values as in figure 2.9.

axially asymmetric growth behaviour was predicted by the one-dimensional, sharp interface analysis which indicated that the upstream interface moves at the speed of the imposed flow, the advection of the downstream interface being increased by cell proliferation and ECM deposition; see equation (2.57).

Figure 2.10 shows how the pressure distribution is affected by the cells. Up- and downstream from the tissue the pressure field decreases linearly with x; an increase to this culture medium pressure is observed in the area in which cells are present. As in the one-dimensional case (§2.3), the deviation from the linear pressure profile mirrors the cell distribution shown in figure 2.9. Similarly, the parabolic velocity distribution created by this pressure gradient is greatly affected by the cells' presence. Upstream, the cells do not influence the flow and u remains x-invariant; however, where $n \neq 0$ the axial flow speed increases with x in an approximately linear fashion, the gradient increasing over time with increasing n. Again, this type of behaviour was indicated by the one-dimensional analysis; see equations (2.53)–(2.55) and figure 2.5b, §2.3. We note that the maximum axial velocity at $x = 0$ is $u = 1/8$ as expected. It may be shown (results omitted) that, as in the one-dimensional case (§2.3), the gradient of the axial velocity ($\partial u/\partial x$) increases with the cell density; however, in the two-dimensional case, this is now modified by the gradient of the transverse velocity ($\partial v/\partial y$), as required by equation (2.22).

The transverse component of velocity (v) is initially small due to the one-dimensional initial cell population. However, as n increases, transverse variation is introduced within the tissue construct through the convective terms in the governing equation (2.24) and v

increases, achieving maxima on the periphery of the construct (see figures 2.9 and 2.12). We note that the magnitude of the axial velocity, u, is much greater than the transverse velocity, v. This is because we impose an axial pressure gradient to drive the flow and, due to the no-penetration boundary conditions, the resistance to transverse motion in the channel is greater.

2.4.2 Mechanotransduction

We now further extend our model to investigate how coupling the growth rate of the cell phase to the local mechanical environment affects the morphology of the tissue construct. This is achieved by modifying the mass transfer term, S_n. For illustrative purposes, we consider choices corresponding to the response of the cells to the following stimuli: contact inhibition caused by cell-cell interactions, the effect of stress caused by increases in local cell density and the influence of the external fluid dynamics. The first two stimuli are not considered explicitly in this formulation; however, we consider that the gross effect of such mechanisms is captured in the functional forms specified below. We remark that since the "cell" phase comprises cells and ECM, modifying the growth and death rates (k_m, k_d) in response to local environmental factors enables crude modelling of a phenotypic switch due to mechanical stimuli from, for instance, a proliferative phase to an ECM-producing phase.

The relevance of the following work hinges upon the appropriate choice of the mass transfer term. As remarked previously (§2.2.1), for simplicity, the formulation employed here precludes dependence of the cells' proliferative response on the velocity field. Consideration of shear stress-enhanced proliferation pertinent to the modelling of the bioreactor system of El-Haj *et al.* (as discussed in §1.2.2) is therefore not included here. We restrict attention to the following cell density and pressure-dependent responses.

1. Cell density-dependent response: $S_n(n) = [k_m(n) - k_d]\, n = \kappa(n)n;$
2. pressure-dependent response: $S_n(n,p) = [k_m(p) - k_d]\, n = \kappa(p)n;$

where k_m, k_d are the rates of growth and death, respectively. More detail regarding the effects that these functional forms capture is given below and we remark that for ease, the death rate k_d is kept constant in each case; the coupling of cell behaviour and the mechanical environment is captured entirely through the growth rate, k_m.

Cell density-dependent response: $k_m(n)$

We begin with the case for which $S_n = S_n(n)$, motivated by the well-known phenomenon of contact-inhibition (see Chaplain *et al.* (2006) and references therein), in which the proliferation rate of cells decreases when they come into contact with other cells. In addition, the level of residual stress induced by the growth of living tissues has a profound effect on cell growth (Fung, 1991): a moderate level of stress appears to enhance cell growth (Chaplain *et al.*, 2006); however, Roose *et al.* (2003) observed that high stress levels created within growing tumours may inhibit cell division. We emphasise that contact inhibition and residual stresses are not considered explicitly within this model; however, the gross effect of these phenomena may be incorporated by an appropriate choice of $k_m(n)$.

As a simple model of the phenomena described above, we identify three distinct phases in the behaviour of the cell population: (i) a proliferative phase, (ii) an ECM-producing phase, and (iii) an apoptotic phase. At low density, the cells proliferate at a rate, $k_m(n) = k_{1n}$; at intermediate density, due to the additional production of ECM, the growth rate of the cell phase is modified to a new value, $k_m(n) = k_{2n}$ (and we assume $k_{2n} > k_{1n}$); finally, when the local density is too high, the cells enter an apoptotic phase ($k_m(n) = 0$). For clarity, we remark that in each of these growth phases, cell phase death is occurring at a rate, k_d (we note that the "death rate", k_d, includes ECM degradation as well as cell death). The threshold cell densities that separate the different types of behaviour are denoted n_1' and n_2'. The variation of the net growth rate, $\kappa(n) = k_m(n) - k_d$, corresponding to this behaviour is illustrated in figure 2.14.

Pressure-dependent response: $k_m(p)$

An alternative way to model the tendency of cells to adapt their behaviour in response to their local density is to consider the "lumped pressure" (defined as $p = p_{w0} + n_0\Sigma_{n0}$; see §2.2.1) as an indicator of cell density; *i.e* $k_m(p)$. This choice has the added advantage of including the response of cells to the local culture medium pressure. It has been widely reported that bone cells are more sensitive to flow stimulation than hydrostatic loading and a great many studies have shown this to be the case; however, certain studies have found that bone cells also respond to hydrostatic loads. Klein-Nulend *et al.* (1995a) and references therein have reported that intermittent hydrostatic compression "inhibits bone resorption and stimulates bone formation"; Haskin *et al.* (1993) found that bone cells respond with increased adhesion; and Owan *et al.* (1997) showed that increased osteopontin (a protein

implicated in the bone remodelling process) expression is induced by fluid pressure. We therefore modify the mass transfer term for the cell phase, S_n, that appears in our mathematical model to illustrate the effect that this mechanism might have on the evolution of the tissue construct and to demonstrate the versatility of the formulation.

To represent a simple pressure-dependent response, we assume that at intermediate pressures, the cells exhibit enhanced proliferation and ECM deposition ($k_m(p) = k_{2p}$); at low pressures, the cells enter a quiescent state in which proliferation and ECM deposition is greatly reduced ($k_m(p) = k_{1p} < k_{2p}$); at high pressures, the cells enter apoptosis ($k_m(p) = 0$). The corresponding thresholds are denoted p_1', p_2' and the net growth rate, $\kappa(p) = k_m(p) - k_d$, is shown in figure 2.14.

Numerical simulations

We now present numerical solutions of the two-dimensional equations (2.24)–(2.26) subject to the boundary conditions (2.10), (2.11) and (2.43) in which we employ the above choices for S_n. We assume that the rates of growth and death of the cell phase (k_{1n}, k_{1p}, k_{2n}, k_{2p}, k_d) are constant and represent the proliferative responses described above with a smoothed step function, as defined below:

$$\kappa(\varphi) = \frac{k_{2\varphi} - k_{1\varphi}}{2}\left\{\tanh\left(g\left[\varphi - \varphi_1'\right]\right) - 1\right\} - \frac{k_{2\varphi}}{2}\left\{\tanh\left(g\left[\varphi - \varphi_2'\right]\right) - 1\right\} - k_d, \tag{2.91}$$

where $\varphi = n, p$ represents the stimulus in question, with corresponding threshold values φ_1', φ_2', and the parameter, g, dictates the level of smoothing; we note that smoothing is necessary to obtain numerical solution since spatial derivatives of k_m appear in the governing equations. Figure 2.14 shows a sketch of the function $k(\varphi)$, highlighting the progression from one proliferative phase to the next.

The effect of these choices of mass transfer on the morphology of the resulting tissue is shown in figures 2.15 and 2.16.

Figure 2.15 illustrates that when the cell proliferation is density-dependent, due to the smoothed progression from cell proliferation to ECM production ($\kappa(n) = k_{2n} - k_d$) and apoptosis ($\kappa(n) = -k_d$), the growth of the cell phase is arrested at $n = n_2'$. We note that despite the presence of apoptosis in this formulation, regression back to the proliferative phase ensures that, once reached, the cell density does not fall below $n = n_2'$.

Figure 2.16 shows the response of the cell phase when proliferation is pressure-dependent. Rather than being arrested at a threshold density, the cell density profile is

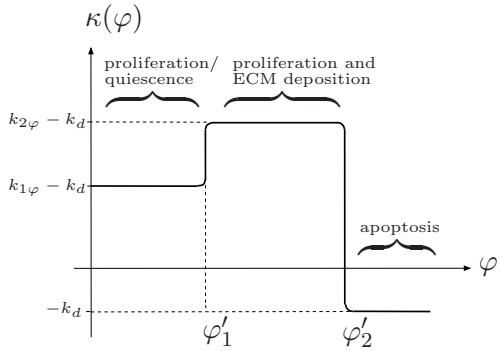

Figure 2.14: Schematic representation of the growth behaviour defined by equation (2.91), modelling the progression of a cell population through a number of growth phases in response to a stimulus, $\varphi = n, p$.

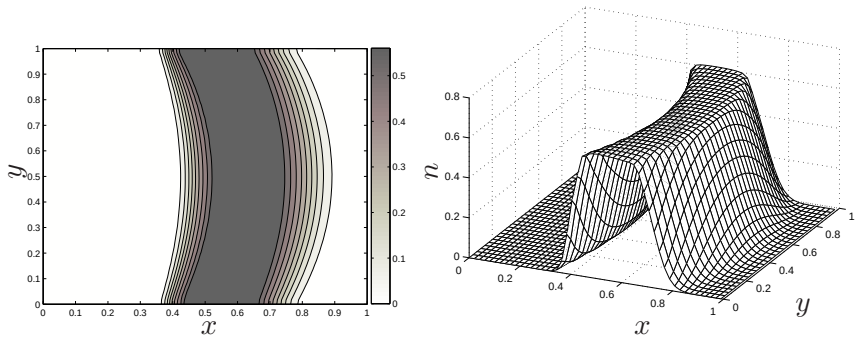

(a) (b)

Figure 2.15: (a) A contour plot and (b) a surface plot showing the effect of the cell density-dependent proliferative response given by (2.91) on tissue construct morphology at $t = 0.65$. Parameter values: $h = 1$, $k_{1n} = 4$, $k_{2n} = 5$, $k_d = 0.2$, $n_1' = 0.5$, $n_2' = 0.6$, $g = 60$, $D = 0.001$, $P_u = 1$, $P_d = 0$.

distorted, with cells becoming apoptotic where the pressure is high (near the upstream diffuse interface and in regions of high cell density; see figure 2.10) and proliferation is reduced near $x = 1$ (where the pressure is low); between these regions, growth is enhanced. The result of this spatial variation in proliferative rate is that the tissue construct grows preferentially downstream in the regions of intermediate pressure.

Comparison of the cell phase distribution in each of the above growth regimes with that obtained in the case of constant growth and death rates (figures 2.9, 2.15 and 2.16) shows that the composition of the tissue construct is dramatically affected by coupling the growth response of the cells to their environment. When cell proliferation and ECM deposition is density-dependent, a uniform tissue construct is obtained; in the pressure-dependent case,

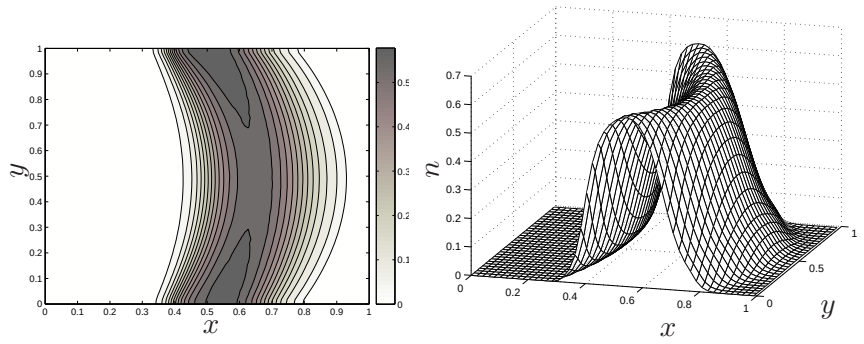

(a) (b)

Figure 2.16: (a) A contour plot and (b) a surface plot showing the effect of the pressure-dependent proliferative response given by (2.91) on tissue construct morphology at $t = 0.8$. $k_{1p} = 5$, $k_{2p} = 7$, $p_1' = 0.5$, $p_2' = 0.8$, $g = 15$; other parameter values as in figure 2.15.

the predicted tissue construct composition is far less uniform. It is interesting to note that in the absence of an imposed flow, the pressure field is directly proportional to the cell phase distribution (see equation (2.47)) and the cell density- and pressure-dependent responses are identical.

2.4.3 Two-dimensional growth: summary

In this section, we have presented two-dimensional, time-dependent numerical solutions to the large drag limit of a two phase model of tissue growth which show the effect of an ambient pressure-driven flow on the growth of a tissue construct when the rates of tissue growth and death are assumed constant. In addition, we have studied the effect on the tissue construct morphology of assuming that the tissue growth rate depends upon environmental stimuli; specifically, the cell density and pressure.

Our simulations showed that in the constant growth rate regime, the cells are advected downstream by the ambient flow with the advection of the diffuse downstream periphery being augmented by tissue growth. In the absence of an imposed flow, the tissue construct still grows preferentially in the downstream direction. Comparison with previous analysis suggested that this type of advection/growth behaviour is captured qualitatively by the far simpler one-dimensional limit in which the tissue construct is defined by two sharp interfaces, between which the cell density is spatially invariant. This advection behaviour implies that a very low rate of perfusion is required to prevent the tissue from being flushed

out of the bioreactor before tissue growth can occur. As remarked in §2.3, this behaviour is a consequence of the limit of large interphase drag employed in this chapter.

By considering two illustrative models of mechanotransduction-affected growth, we have further demonstrated that the composition of the tissue construct is profoundly affected by coupling cell proliferation/ECM deposition to the mechanical environment. The proliferation/ECM deposition functions were chosen to reflect a simple mechanotransduction mechanism. Our model admits more complex functional forms and dependence on combinations of the field variables; however, the simpler form employed here allows clearer illustration of the importance of mechanotransduction-affected growth within a tissue growth modelling framework. In the absence of perfusion, the density- and pressure-regulated proliferative responses of the cells are indistinguishable; in principle, this model therefore provides a means to form hypotheses regarding the dominant mechanotransduction mechanism in the growth of a cell population simply by observing the tissue construct morphology resulting from static and dynamic culture.

2.5 Summary

In this chapter, we have shown explicitly that the two-fluid model for tissue growth of Franks (2002) and Franks & King (2003), may be recovered from a more general multiphase formulation by taking the limit of large interphase viscous drag. We applied this framework to tissue growth processes in a perfusion bioreactor, represented by a two-dimensional channel containing a two-phase mixture of interacting viscous fluids. The cells and ECM were modelled as a single phase, the second phase representing the culture medium. Motivated by parameter estimation, we employed the simplifying limit of large interphase drag, in which we may describe each phase as being subject to a common velocity and lumped pressure field. At distances of $\mathcal{O}(1/\sqrt{k})$ from the channel walls (where k is the coefficient of viscous drag), this approximation is no longer valid, and we employed a boundary layer analysis to derive boundary conditions on the outer flow. These conditions deviated from those employed in Franks (2002) in which slip was permitted. For ease of comparison with Franks (2002) (and other studies), we obtained solutions to the model equations in the presence of slip.

We have considered the effect of a dynamic flow environment on tissue growth processes. Analytic predictions were obtained in the limit of a one-dimensional growing tissue defined by two sharp interfaces, between which the cell density remains spatially invariant. The

cell phase displayed logistic growth, the interfaces were advected by the ambient flow and the tissue width increased exponentially due to growth of the cell population. The stability of this tissue to periodic transverse perturbations was investigated, and the interfaces were found to be unstable, the long-time stability being regulated only by the net growth rate. In the presence of a corresponding perturbation to the cell volume fraction, we observed markedly different behaviour to that reported in Franks (2002) for a spatially-invariant tissue construct: the perturbation to the upstream interface reversed sign due to the variation in construct density. This effect diminished with increasing perturbation wavenumber and decayed to zero for large time.

Using numerical simulations in one and two-dimensions, the behaviour of a tissue construct defined by two diffuse interfaces subject to an ambient flow was calculated for constant growth and death rates. In each case, the type of advection behaviour predicted by the sharp interface analysis was observed, indicating that this simple limit captures much of the qualitative behaviour of the full system. In the two-dimensional case, transverse variation in the tissue construct was induced by the parabolic flow of culture medium; small transverse flows were induced at the construct periphery.

Our analysis indicates that cells and ECM are advected through the bioreactor at the speed of the imposed flow. This implies that a very low rate of perfusion is required in order to prevent the tissue from being flushed from the scaffold before tissue growth can occur. This is a consequence of the simplifying limit of large interphase drag employed in this chapter which demands that the cell and culture medium phases are subject to a common velocity field.

The model formulation was further extended to account for coupling between the cells' proliferative response and their local environment. This was achieved by replacing the constant growth and death rates (k_m, k_d) with appropriate functional forms. Specifically, motivated by a range of studies, we considered the response of a cell population to the local density and the local pressure. Simulations were presented showing that the growth of the cell population is profoundly altered by these effects, dramatically changing the composition of the construct. These simulations clearly demonstrate the importance of considering the effect of mechanotransduction mechanisms within tissue growth models. Furthermore, our model suggests that in static culture, regulation of proliferative behaviour by cell density and culture medium pressure results in indistinguishable tissue constructs. In principle, this conclusion suggests that inspection of the morphology of tissue constructs produced in static and dynamic culture provides a simple means for the identification of the dominant

regulatory mechanism in a given cell population. We note that we have neglected the effect of nutrient availability on the growth of the construct. This is expected to become important in static culture conditions; an interesting extension to this work is to determine the influence of such a consideration on the predicted construct morphology in static and dynamic culture conditions.

We concede that we have employed highly simplified functional forms to model the different growth effects and that they were considered in isolation; physiologically, these effects will work together in a complex way to produce the cells' overall response. However, we remark that the mathematical formulation and numerical scheme developed is highly versatile, permitting the study of more complex functional forms and an investigation of the interplay between many competing growth stimuli should appropriate experimental data become available.

Inspection of equation (2.22) shows that since the source terms of the conservation laws (2.21) are not equal and opposite, mass is spontaneously generated at a rate k_m. This is illustrated by figures 2.5b and 2.11 in which it is clear that the flux leaving the channel at $x = 1$ exceeds that entering at $x = 0$. The required flux condition is

$$\frac{\partial Q}{\partial x} + v|_h - v|_0 \;=\; \int_0^h k_m n \,\mathrm{d}y, \quad \text{where} \quad Q = \int_0^h u \,\mathrm{d}y. \tag{2.92}$$

In numerical simulations, this condition was found to be satisfied to within 0.07% at all time steps. This error can be reduced further by decreasing the mesh size; however, this is computationally expensive.

An additional limitation of our model is that since we represent the contents of the bioreactor by a multiphase *fluid*, we are unable to model any of the solid characteristics of the system. The implications of this are threefold: firstly, we are unable to consider the effect of the mechanical forcing from the piston; secondly, the residual stresses generated from volumetric tissue growth must be neglected (see §1.3); and thirdly, the interaction between cells and the scaffold is not considered.

In the chapters that follow, we relax the assumption of large interphase viscous drag and develop mathematical models which allow retention of the individual phase variables and consideration of the interaction between the cells and a solid scaffold, as well as the effect of mechanical compression.

Chapter 3

A simplified three phase model for the growth of a tissue construct

3.1 Introduction

The model presented in chapter 2 is now extended to include a third phase which accounts for the solid characteristics of the PLLA scaffold used in the bioreactor system introduced in §1.2.3. As a simple first approximation, we consider the scaffold phase to be rigid and neglect the mechanical forcing provided by the piston; however, the model of chapter 2 is extended by: (i) retention of the individual phase variables in the formulation, and (ii) explicit consideration of interphase tractions and intraphase forces, resulting in a more complex coupling between the dynamic culture environment and the tissue response.

We consider the uniform growth of a tissue construct within a two-dimensional channel, for which the rates of growth and death are constant. The governing equations are simplified by considering the limit for which the aspect ratio of the channel is small and the interfaces between the construct and the surrounding culture medium are sharp (§3.2.1), allowing the equations to be solved in three distinct regions. The system then reduces to a second-order differential equation for the culture medium pressure coupled to a parabolic equation for the cell volume fraction (§3.3). These equations are solved numerically using a semi-implicit method (§3.3.1); the numerical simulations are validated by studying the model equations in the limit for which the volume fraction of the cell phase is asymptotically small (§3.3.2), a limit for which analytic solutions can be constructed. In contrast to the results presented in chapter 2, we show that in the absence of perfusion, this more complex model predicts symmetric growth; in addition, by modelling cell-cell and cell-scaffold interactions, we find that the advective behaviour reported in chapter 2 is curtailed by cell aggregation and

attachment of cells to the scaffold. Furthermore, we reveal markedly different cell behaviour depending upon the relative importance of cell aggregation and attachment forces compared to those associated with cell-cell and cell-scaffold repulsion. The chapter concludes with a brief discussion of the relevance of the model solutions to tissue engineering and the bioreactor system introduced in §1.2.3.

3.2 Model formulation

We consider the growth of a tissue construct within a nutrient-rich culture medium and investigate the effect of cell-cell and cell-scaffold interactions as well as perfusion on the response of the cells. As in chapter 2, the mechanical forcing from the piston is neglected and we represent this system as a two-dimensional rigid-walled channel containing a tissue construct surrounded by fluid culture medium. The channel contents are modelled as a three-phase mixture comprising two viscous fluids and one rigid phase; the "cell phase" (constituting both cells and extracellular matrix) and the culture medium are modelled as viscous fluids, whilst the PLLA scaffold is modelled as a rigid, porous material. Perfusion is represented by a flow generated by an imposed axial pressure drop. The terminology "tissue construct" will again be employed to distinguish the region occupied by the cell, scaffold and culture medium phases from the remainder of the channel which contains only culture medium. At certain stages in this chapter, the interfaces between the growing cell phase (within the porous scaffold) and the surrounding culture medium will be assumed to be sharp or diffuse to allow different analyses to be performed.

A Cartesian coordinate system $\boldsymbol{x^*} = (x^*, y^*)$ is chosen with corresponding coordinate directions $(\hat{\boldsymbol{x}}, \hat{\boldsymbol{y}})$ and the channel occupies $0 \leqslant x^* \leqslant L^*$, $0 \leqslant y^* \leqslant h^*$. Perfusion is driven by an imposed axial pressure drop, $P_u^* - P_d^*$. We adopt the same notation as previously and associate with each phase a volume-averaged fraction, ϕ_i, pressure, p_i^*, stress tensor, $\boldsymbol{\sigma}_i^*$, velocity, $\boldsymbol{u}_i^* = (u_i^*, v_i^*)$ and density, ρ_i^*, and denote dimensional quantities with asterisks.

We employ the multiphase model presented in §1.5, with attention restricted to three incompressible phases. The mass and momentum balance equations for the i^{th} phase are

$$\frac{\partial \phi_i}{\partial t^*} + \nabla^* \cdot (\phi_i \boldsymbol{u}_i^*) = S_i^* + D_i^* \nabla^{*2} \phi_i, \tag{3.1}$$

$$\nabla^* \cdot (\phi_i \boldsymbol{\sigma}_i^*) + \sum_{j \neq i} \mathbf{F}_{ij}^* = \mathbf{0}, \tag{3.2}$$

where S_i^* is the rate of material production associated with the i^{th} phase and $\mathbf{F}_{ij}^*$ is the interphase force exerted on phase i by phase j. We remark that we have again included

diffusive effects for numerical ease; D_i^* are the diffusion coefficients for each phase. In the proceeding analysis, we assume that the diffusion coefficients for the cell and culture medium phases are small and equal so that $D_w^* = D_n^* = D^*$ (see §2.2, page 34). For notational convenience and for consistency with the model presented in chapter 2, the volume-averaged fractions, ϕ_i, are denoted n, w, s and associated variables are labelled with a corresponding subscript, $i = n, w, s$.

We now specify how our multiphase system interacts. As a first approximation, we simplify the three phase formulation by assuming that the scaffold phase neither deforms nor degrades. We therefore consider the limit $\boldsymbol{u}_s^* \longrightarrow \mathbf{0}$. Setting $D_s^* = 0$, $S_s^* = 0$, $s =$ constant, we find that equation (3.1) is redundant for this phase and the no-voids condition, equation (1.42), becomes

$$n + w = \theta, \tag{3.3}$$

where $\theta = 1 - s$ is the porosity of the scaffold phase, and in the following we work in terms of θ in preference to s. We further assume that the culture medium is a "passive" phase, and set $\Sigma_w^* = 0 = \Sigma_s^*$, so that the culture medium and scaffold phases generate no intraphase pressures. In addition, we assume that the tractions exerted by the cells on the culture medium and the extra pressure exerted by the culture medium on the scaffold are negligible, leading to $\psi_{nw}^* = 0 = \psi_{ws}^*$ (see equations (1.47) and (1.48), §1.5 for more details regarding these choices). Under these assumptions, equations (1.47) and (1.48) reduce to

$$p^* \;=\; p_w^* \;=\; p_s^*, \quad p_n^* \;=\; p_w^* + \Sigma_n^* + (1-\theta)\psi_{ns}^*, \tag{3.4}$$

$$p_{wn}^* \;=\; p_w^* \;=\; p_{ws}^*, \quad p_{ns}^* \;=\; p_w^* + \psi_{ns}^*, \tag{3.5}$$

where the functions Σ_n^* and ψ_{ns}^* represent the intraphase pressure generated by the cell phase and the interphase traction between the cell and scaffold phases. We further extend the model presented in chapter 2 by assuming that the drag coefficients, K_{ij}^* (equation (1.46), §1.5) are given by

$$K_{ij}^* = k^* \phi_i \phi_j, \tag{3.6}$$

where k^* is assumed constant. This simple form includes the necessary dependence of the interphase drag on the degree of contact between the relevant phases (Lemon *et al.*, 2006). From equation (1.46) we find that the interphase forces $\mathbf{F}_{ij}^*$ are given by:

$$\mathbf{F}_{nw}^* = \theta p_w^* \nabla^* n + k^* n w \left(\boldsymbol{u}_w^* - \boldsymbol{u}_n^*\right) = -\mathbf{F}_{wn}^*, \tag{3.7}$$

$$\mathbf{F}_{sw}^* = p_w^* (1-\theta) \nabla^* n + k^* (\theta - n)(1-\theta) \boldsymbol{u}_w^* = -\mathbf{F}_{ws}^*, \tag{3.8}$$

$$\mathbf{F}_{ns}^* = \left(p_w^* + \psi_{ns}^*\right)(1-\theta)\nabla^* n - k^* n (1-\theta) \boldsymbol{u}_n^* = -\mathbf{F}_{sn}^*. \tag{3.9}$$

To close the model, it remains to specify constitutive laws for the stress tensors $(\boldsymbol{\sigma}_n^*, \boldsymbol{\sigma}_w^*, \boldsymbol{\sigma}_s^*)$, the mass transfer rates (S_n^*, S_w^*) and the intraphase and interphase pressure functions $(\Sigma_n^*, \psi_{ns}^*)$.

We model the cell and culture medium phases as viscous fluids and therefore use equations (2.8) to define the volume-averaged stress tensors for each phase, and we assume that $\rho_i^* = \rho^*$ $(i = n, w)$. For consistency, we choose the same form for the stress tensor associated with the scaffold phase and take the limit in which the scaffold viscosity is infinite: $\mu_s^* \longrightarrow \infty$. Functional forms for the mass transfer rates and intraphase and interphase pressure functions will be specified in §3.2.1.

Appropriate boundary conditions on this model are given by (2.9)–(2.11) and initial cell distributions suitable for the analyses presented in this chapter will be specified subsequently.

We remark here that within this simplified three-phase formulation, the scaffold phase enters into the governing equations only via the constant porosity, θ.

3.2.1 Non-dimensionalisation

As in chapter 2, the governing equations are non-dimensionalised by choosing the following dimensionless variables:

$$\boldsymbol{x}^* = L^*\boldsymbol{x}, \quad t^* = \frac{L^*}{U_w^*}t, \quad \boldsymbol{u}_i^* = U_w^*\boldsymbol{u}_i, \quad (p_w^*, \Sigma_n^*, \psi_{ns}^*) = \frac{U_w^*\mu_w^*}{L^*}(p_w, \Sigma_n, \psi_{ns}), \quad S_i^* = \frac{U_w^*}{L^*}S_i, \tag{3.10}$$

wherein U_w^* is a velocity scale which will be determined subsequently. We have again employed a viscous scaling for the pressure since we assume that viscous effects dominate inertia in the momentum equations and we note that, as remarked in chapter 2, we consider tissue growth on a fast flowspeed-based timescale. Using (3.3) and (3.10), the dimensionless equations read:

$$\frac{\partial n}{\partial t} + \nabla\cdot(n\boldsymbol{u}_n) = S_n + D\nabla^2 n, \tag{3.11a}$$

$$\nabla\cdot(n\boldsymbol{u}_n + (\theta - n)\boldsymbol{u}_w) = S_n + S_w, \tag{3.11b}$$

$$\begin{aligned}(\theta - n)\nabla p_w + kn(\theta - n)(\boldsymbol{u}_w - \boldsymbol{u}_n) + k(1-\theta)(\theta - n)\boldsymbol{u}_w - \\ \nabla\cdot\left[(\theta - n)(\nabla\boldsymbol{u}_w + \nabla\boldsymbol{u}_w^T) + \gamma_w(\theta - n)\nabla\cdot\boldsymbol{u}_w\mathbf{I}\right] = \mathbf{0},\end{aligned} \tag{3.11c}$$

$$\begin{aligned}\nabla\cdot\big[-(\theta p_w + n\Sigma_n + n(1-\theta)\psi_{ns})\,\mathbf{I} + \mu_n n(\nabla\boldsymbol{u}_n + \nabla\boldsymbol{u}_n^T) + \\ \gamma_n n\nabla\cdot\boldsymbol{u}_n\mathbf{I} + (\theta - n)(\nabla\boldsymbol{u}_w + \nabla\boldsymbol{u}_w^T) + \gamma_w(\theta - n)\nabla\cdot\boldsymbol{u}_w\mathbf{I}\big] + \\ \nabla n(1-\theta)\psi_{ns} - kn(1-\theta)\boldsymbol{u}_n - k(\theta - n)(1-\theta)\boldsymbol{u}_w = \mathbf{0}.\end{aligned} \tag{3.11d}$$

The dimensionless parameters D, μ_n, k, γ_w and γ_n are defined by equations (2.18), with identical physical interpretation. Equations (3.11a) and (3.11b) are statements of conservation of mass for the cell phase and the multiphase mixture respectively, (3.11c) expresses conservation of momentum for the culture medium phase and (3.11d) is a statement of conservation of momentum for the two-phase mixture of cells and culture medium obtained by summing equations (3.2) over $i = n, w$. We employ this equation in preference to the momentum balance equation for the three phase mixture (see (1.45), §1.5) since in the limit $\boldsymbol{u}_s \longrightarrow \mathbf{0}$, $\mu_s = \mu_s^*/\mu_w^* \longrightarrow \infty$, the combination $\mu_s(\nabla \boldsymbol{u}_s + \nabla \boldsymbol{u}_s^T)$ gives a non-negligible contribution to the stress; this is a consequence of the fact that although the scaffold does not deform, it may still carry stress. The value of this contribution (in terms of the other variables n, p_i, $\boldsymbol{u}_i$; $i = n, w$) may, in principle, be determined by considering the momentum balance of the three phase mixture.

The channel now occupies $0 \leqslant x \leqslant 1$, $0 \leqslant y \leqslant h = h^*/L^*$ and the corresponding dimensionless boundary conditions transform naturally and are not given; the dimensionless up- and downstream pressures are given by equations (2.17).

In a departure from chapter 2, we assume that the mass transfer terms are given by $S_n = (k_m - k_d)n = -S_w$, where $k_m = (k_m^* L^*)/U_w^*$ represents the rate of cell mitosis and ECM deposition and $k_d = (k_d^* L^*)/U_w^*$ represents the dimensionless rate of cell death and ECM degradation (with corresponding dimensional rates k_m^* and k_d^*). In the interests of brevity, we refer to k_m and k_d as the "growth rate" and "death rate" and in this chapter we consider uniform growth for which these are constant. As in the previous chapter, these choices correspond to assuming that the cell and culture medium phases are comprised of essentially the same matter; the difference in material properties between the cell phase and the culture medium is therefore attributed to the presence of the cells' cytoskeleton, and it is implicitly assumed that this breaks down upon cell death.

To simplify the model, we consider the limit in which the interface between the tissue construct and the surrounding culture medium is "sharp"; however, since the tissue construct is now defined by the region in which $s > 0$, we need not specify $D = 0$ as in the two-fluid model (*cf.* chapter 2). For simplicity, we confine the tissue construct to the region $a \leqslant x \leqslant b$ (see figure 3.1) and stipulate that the cell phase must remain confined within the scaffold (the values of a and b are arbitrary, provided that $a < b < 1$). We achieve this by imposing a no-flux boundary condition on the cell phase, n at the scaffold edge. Formulating the problem in this way allows us to simplify the governing equations (3.11) in the up- and downstream regions, whilst retaining the full complexity of the three phase

system within the construct region. The problem may then be solved separately in each region, and the solutions coupled together via appropriate conditions; boundary conditions for equations (3.11) will be considered in §3.2.3.

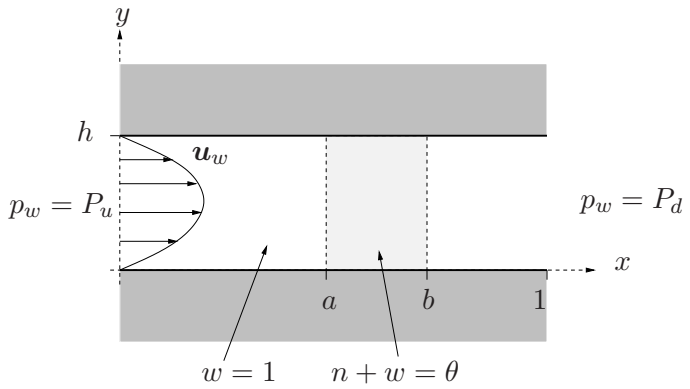

Figure 3.1: Definition sketch for an idealised three phase model of a perfusion bioreactor.

It remains to define the functions ψ_{ns} and Σ_n, which specify the extra pressure generated due to traction between the cell and scaffold phases and the intracellular pressure created due to interactions *within* the cell phase, respectively. Following the approach given in other multiphase modelling studies (Breward *et al.*, 2002; Byrne *et al.*, 2003; Lemon *et al.*, 2006), appropriate expressions are taken to be

$$\Sigma_n = -n\nu + \frac{\delta_a n^{m+1}}{(\theta - n)^m}, \quad \psi_{ns} = -\chi + \frac{\delta_b n^m}{(\theta - n)^m}, \tag{3.12}$$

for constants ν, δ_a, χ, δ_b, $m > 0$. The first term in each of these expressions reflects the cells' tendency to aggregate at low densities and their affinity for the scaffold, respectively. The second term represents the repulsive forces between cells and between the cells and scaffold which arise when they come into close contact (Lemon *et al.*, 2006). To clarify, dominance of the first term in the intraphase pressure function corresponds to $\Sigma_n < 0$, resulting in a reduction in cell pressure and subsequent aggregation. The opposite behaviour is reflected by dominance of the second term in Σ_n. A similar mechanism is modelled by the intraphase traction function. The behaviour of these functions for different parameter values is shown in figures 3.2–3.4. Figure 3.2a shows how increasing the "aggregation parameter", ν, causes the first term in Σ_n to dominate for small n; Σ_n becomes initially more negative. As discussed above, this reflects the tendency of sparse cell populations to aggregate. As n increases, repulsive forces begin to dominate and the function becomes singular when the cells have filled all available pore space: $n = \theta$. Similar behaviour is observed in figure 3.3a: as the "scaffold affinity parameter", χ, increases, the cells exhibit a strong affinity

for the scaffold when n is small; repulsive forces dominate when the cell density increases. The effect of increasing the intraphase (δ_a) and interphase (δ_b) "repulsion parameters" is shown in figures 3.2b and 3.3b: as these parameters are increased, the repulsive terms in Σ_n and ψ_{ns} dominate the behaviour at progressively smaller values of n. The influence of the parameter, m is illustrated by figure 3.4: an increase in m corresponds to repulsive effects dominating over cell aggregation or scaffold affinity at progressively smaller values of n.

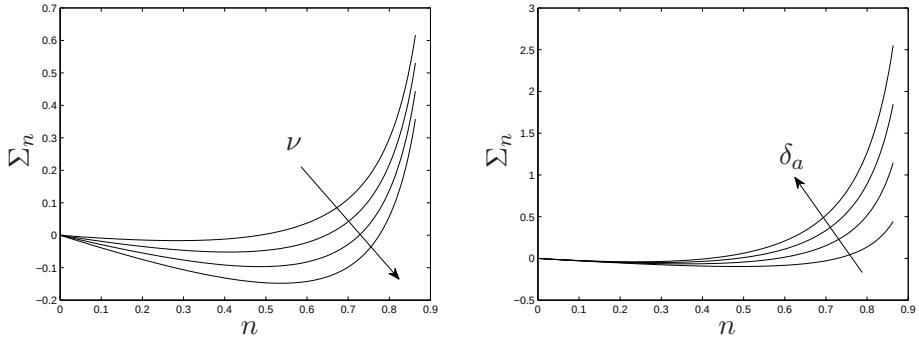

(a) (b)

Figure 3.2: The behaviour of the intraphase pressure function, Σ_n for (a) $\nu = 0.1, 0.2, 0.3, 0.4$, $\delta_a = 0.1$, (b) $\delta_a = 0.1, 0.2, 0.3, 0.4$, $\nu = 0.3$; $\theta = 0.97$, $m = 1$. The arrows indicate the direction of increasing parameter values.

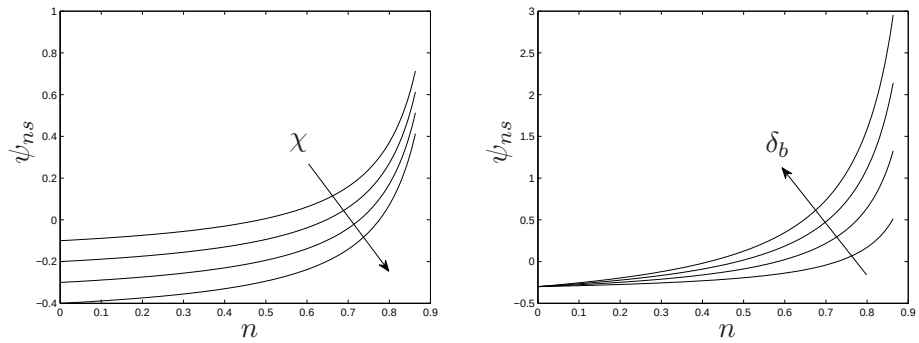

(a) (b)

Figure 3.3: The behaviour of the interphase traction function, ψ_{ns} for (a) $\chi = 0.1, 0.2, 0.3, 0.4$, $\delta_b = 0.1$, (b) $\delta_b = 0.1, 0.2, 0.3, 0.4$, $\chi = 0.3$; $\theta = 0.97$, $m = 1$. The arrows indicate the direction of increasing parameter values.

Values for the parameters, m, ν, χ, δ_a, δ_b are not readily available in the literature since they will depend upon the characteristics of the cell culture in question (including, for

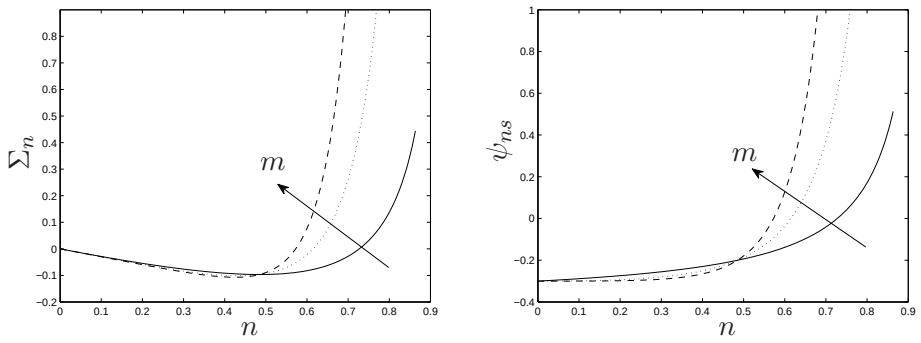

(a) (b)

Figure 3.4: The influence of the parameter, m on the intraphase pressure and interphase traction functions, Σ_n, ψ_{ns} for $\nu = \chi = 0.3$, $\delta_a = \delta_b = 0.1$, $\theta = 0.97$, $m = 1, 2, 3$. The arrows indicate the direction of increasing m.

instance, the level of (de-)differentiation) and the topography and surface chemistry of the scaffold in a complex way. In the following, we assume $m = 1$ for simplicity and we choose $\delta_a = \delta_b$, so that the extra pressures arising from interphase and intraphase repulsions are equal. Additionally, we choose $\nu = \chi$ so that cell-scaffold and cell-cell affinity are the same; furthermore, we expect that for $n < \theta$, the extra pressures associated with aggregation and cell-scaffold affinity dominate those associated with repulsion and we therefore specify $(\nu, \chi) > (\delta_a, \delta_b)$. In the following we arbitrarily choose $\delta_a = \delta_b = 0.1$, $\nu = \chi = 0.3$; however, we emphasise that these parameter values are not physiologically motivated, being chosen simply to illustrate the type of behaviour that can arise (a thorough investigation of the effect of these parameters, as well as the relative viscosity μ_n, on the behaviour of the cell population is presented in chapter 4).

We note that our model reduces to the simpler two-fluid model employed in chapter 2 (with the exception of the mass transfer terms) if we set $\theta = 1$, we neglect interphase tractions ($\psi_{ij} = 0$) and assume that the drag coefficients are constant ($K^*_{ij} = k^*$).

3.2.2 Long wavelength limit

We may further simplify the governing equations by considering the limit for which the aspect ratio of the channel is small, corresponding to $h \ll 1$. We therefore choose the following rescalings:

$$y = h\hat{y}, \quad v_i = h\hat{v}_i, \quad p_w = \hat{p}_w/h^2, \quad \Sigma_n = \hat{\Sigma}_n/h^2, \quad \psi_{ns} = \hat{\psi}_{ns}/h^2, \tag{3.13}$$

and the channel now occupies $0 \leqslant x \leqslant 1$, $0 \leqslant \hat{y} \leqslant 1$. The rescaling of the intraphase pressure and interphase traction functions implies: $(\nu, \delta_a, \chi, \delta_b) = (\hat{\nu}, \hat{\delta}_a, \hat{\chi}, \hat{\delta}_b)/h^2$; the remaining parameters k_m, k_d, k, μ_n, γ_w and γ_n are $\mathcal{O}(1)$. This scaling ensures that the cell-cell and cell-scaffold interactions are retained at leading order.

We deduce from the $\hat{y}$-component of the momentum equations (3.11c), (3.11d) that, at leading order, the pressure (p_w and p_n) and the volume fraction (n and w) of each phase are functions of x and t only. Neglecting terms of $\mathcal{O}(h^2)$ and dropping the carets for brevity, we obtain the following equations for n, $\boldsymbol{u}_w$, $\boldsymbol{u}_n$ and p_w at leading order:
conservation of mass:

$$\frac{\partial n}{\partial t} + \nabla \cdot (n\boldsymbol{u}_n) = (k_m - k_d)n + D\frac{\partial^2 n}{\partial x^2} + D\frac{\partial^2 \widetilde{n}}{\partial y^2}, \tag{3.14a}$$

$$\nabla \cdot (n\boldsymbol{u}_n + (\theta - n)\boldsymbol{u}_w) = 0; \tag{3.14b}$$

conservation of culture medium momentum:

$$\frac{\partial p_w}{\partial x} \;=\; \frac{\partial^2 u_w}{\partial y^2}; \tag{3.14c}$$

conservation of momentum for the culture medium/cell mixture:

$$\theta\frac{\partial p_w}{\partial x} + \frac{\partial}{\partial x}\left[n\Sigma_n + n(1-\theta)\psi_{ns}\right] = \mu_n n\frac{\partial^2 u_n}{\partial y^2} + (\theta - n)\frac{\partial^2 u_w}{\partial y^2} + \frac{\partial n}{\partial x}(1-\theta)\psi_{ns}. \tag{3.14d}$$

In equation (3.14a), $\widetilde{n}(\boldsymbol{x}, t)$ is the $\mathcal{O}(h^2)$ term in the expansion for n.

We remark that the values $x = a, b$ which define the construct width must now obey a, $b - a$, $1 - b \gg h$. Additionally, in contrast to chapter 2, since we assume $k = \mathcal{O}(1)$, the influence of interphase viscous drag is neglected in this formulation.

3.2.3 Boundary conditions

Boundary conditions at $x = 0, 1$ and $y = 0, 1$ are given by the dimensionless versions of (2.9)–(2.11). To clarify, as indicated in figure 3.1, we impose a dimensionless pressure drop, $P_u - P_d$ along the channel to drive a flow; additionally, since the cell and culture medium phases are modelled as viscous fluids, we impose no-slip and no-penetration (and no cell flux) at the channel walls: $\boldsymbol{u}_w = \boldsymbol{u}_n = \partial n/\partial y = \partial \widetilde{n}/\partial y = 0$ at $y = 0, h$. Appropriate jump conditions across the boundaries $x = a, b$ may be constructed by imposing continuity of flux and normal stress as follows. Averaging the conservation of mass equation (3.14b) across the channel, we find that the flux, Q, in each region is independent of the axial coordinate,

x, and is given by:

$$Q(t) = \langle u_w \rangle, \qquad 0 \leqslant x < a, \tag{3.15}$$

$$Q(t) = \langle n u_n + (\theta - n) u_w \rangle, \quad a \leqslant x \leqslant b, \tag{3.16}$$

$$Q(t) = \langle u_w \rangle, \qquad b < x \leqslant 1, \tag{3.17}$$

where $\langle \cdot\cdot \rangle$ is the averaging operator defined as follows:

$$\langle \cdot\cdot \rangle = \int_0^1 \cdot\cdot \, \mathrm{d}y. \tag{3.18}$$

The normal stress exerted on the interfaces at $x = a, b$ is given by $\sigma_{xx} = \hat{\boldsymbol{n}} \cdot \boldsymbol{\sigma}_T \cdot \hat{\boldsymbol{n}}$, where $\hat{\boldsymbol{n}}$ is the outward unit normal to the interfaces at $x = a, b$ and $\boldsymbol{\sigma}_T = n\boldsymbol{\sigma}_n + (\theta - n)\boldsymbol{\sigma}_w$. The leading-order normal stress exerted on $x = a, b$ by the fluid exterior to the construct region is found to be $\sigma_{xx} = -p_w$; the interior stresses are found to be $\sigma_{xx} = np_n + (\theta - n)p_w$. By requiring continuity of flux and normal stress across the two boundaries, we obtain the following jump conditions:

$$[p_w]^- = [np_n + (\theta - n)p_w]^+, \tag{3.19a}$$

$$[\, \langle u_w \rangle \,]^- = [\, n\langle u_n \rangle + (\theta - n)\langle u_w \rangle \,]^+, \tag{3.19b}$$

with p_n given by (3.4) and, as in chapter 2, the superscript + indicates the limiting value $x = a$ (or b) from within $a \leqslant x \leqslant b$ and the superscript $-$ denotes the limiting value from the exterior. An additional condition governing the behaviour of the cell volume fraction at $x = a, b$ may be derived by requiring that the cell phase be confined within the scaffold region $a \leqslant x \leqslant b$ as follows. Writing the conservation of mass equation for the cell phase (3.11a) in conservative form and averaging across the channel, we obtain:

$$\frac{\partial n}{\partial t} + \frac{\partial}{\partial x} \langle \, \mathrm{J} \, \rangle \; = \; (k_m - k_d)n, \tag{3.20}$$

wherein $\langle \, \mathrm{J}(\boldsymbol{x}, t) \, \rangle = n\langle u_n \rangle - D\partial n/\partial x$ is the averaged flux of cells and we have employed the no cell flux condition at $y = 0, 1$ to eliminate $\widetilde{n}$. To ensure no efflux of cells from the region $a \leqslant x \leqslant b$, we impose $\langle \, \mathrm{J} \, \rangle = 0$ at $x = a, b$, implying

$$n\langle u_n \rangle \; = \; D\frac{\partial n}{\partial x} \quad \text{on} \quad x = a, b. \tag{3.21}$$

3.3 Solution

In this section, we reduce equations (3.14) to a pair of coupled partial differential equations for the cell volume fraction (n) and the pressure in the culture medium phase (p_w) and, using

§3.2.3, derive appropriate boundary conditions. Numerical solutions are presented (§3.3.1) and, in an appropriate asymptotic regime, analytical solutions are constructed (§3.3.2).

Integration of equations (3.14c) and (3.14d) yields expressions for the axial velocities in each region. For clarity, the regions $0 \leqslant x < a$, $a \leqslant x \leqslant b$, $b < x \leqslant 1$ are denoted 1,2 and 3, respectively, and the variables are labelled appropriately. We obtain:

$$u_{w1} = \frac{1}{2}\frac{\partial p_{w1}}{\partial x} y(y-1), \quad \boldsymbol{u}_{n1} = \mathbf{0}, \tag{3.22}$$

$$u_{w2} = \frac{1}{2}\frac{\partial p_{w2}}{\partial x} y(y-1), \quad u_{n2} = \frac{1}{2\mu_n}\frac{\partial \overline{p}}{\partial x} y(y-1), \tag{3.23}$$

$$u_{w3} = \frac{1}{2}\frac{\partial p_{w3}}{\partial x} y(y-1), \quad \boldsymbol{u}_{n3} = \mathbf{0}, \tag{3.24}$$

wherein the culture medium pressures $p_{wi}(x,t)$ are unknown and $\overline{p}(x,t)$ is given by

$$\frac{\partial \overline{p}}{\partial x} = \frac{\partial p_{w2}}{\partial x} + \frac{1}{n}\frac{\partial}{\partial x}\left(n\Sigma_n\right) + (1-\theta)\frac{\partial \psi_{ns}}{\partial x}. \tag{3.25}$$

Equations (3.23) and (3.25) indicate that the velocity of the cell phase is driven by a combination of the culture medium pressure gradient and contributions from cell-cell and cell-scaffold interactions rather than $\partial p_n/\partial x$; see equation (3.4).

In view of equations (3.15) and (3.17), continuity of total flux requires that the up- and downstream pressures p_{w1}, p_{w3} are linear in x with the same gradient:

$$p_{w1}(x,t) = A(t)x + P_u, \quad p_{w3}(x,t) = A(t)(x-1) + P_d, \tag{3.26}$$

for an arbitrary function, $A(t)$. The temporal variation of $A(t)$ reflects the adjustment of the up- and downstream culture medium pressure in response to the growth of the tissue construct. At leading order, the flow is unidirectional; however, the transverse velocities v_{w2}, v_{n2} may be obtained by solving the appropriate $\mathcal{O}(h^2)$ momentum equation subject to suitable boundary conditions (*e.g.* $v_{i2} = 0$ on $y = 0, 1$, and appropriate conditions on $x = a, b$); we do not present results here since these solutions are not required in the proceeding analysis.

Using (3.21)–(3.24), equation (3.19b) may be rewritten as a condition on the culture medium pressure gradient. The jump conditions (3.19) are then:

$$p_{w1}\big|_{x=a} = \left(np_n + (\theta-n)p_{w2}\right)\big|_{x=a}, \; p_{w3}\big|_{x=b} = \left(np_n + (\theta-n)p_{w2}\right)\big|_{x=b}, \tag{3.27}$$

$$\left[\frac{\partial p_{w1}}{\partial x} + 12D\frac{\partial n}{\partial x}\right]_{x=a} = (\theta-n)\frac{\partial p_{w2}}{\partial x}\bigg|_{x=a}, \; \left[\frac{\partial p_{w3}}{\partial x} + 12D\frac{\partial n}{\partial x}\right]_{x=b} = (\theta-n)\frac{\partial p_{w2}}{\partial x}\bigg|_{x=b}. \tag{3.28}$$

Additionally, the no cell efflux condition (3.21) may be re-written as a condition on the cell volume fraction. By exploiting the definitions (3.12), (3.23) and (3.25) together with (3.26)

and (3.28), we arrive at the following condition:

$$\frac{\partial n}{\partial x} = \frac{A(t)n}{(\theta - n)\left[2\nu n - 12\mu_n D - \frac{\delta_a n^3 + (1-\theta)\delta_b n^2}{(\theta - n)^2} - \frac{3\delta_a n^2 + [\delta_b(1-\theta) + 12D]n}{\theta - n}\right]} \text{ on } x = a, b. \quad (3.29)$$

We may now rewrite the system (3.14) in terms of p_{w2} and n in the region $a \leqslant x \leqslant b$ subject to appropriate boundary conditions on $x = a$ and $x = b$. By averaging the conservation of mass equation (3.14b) across the channel and using equation (3.23) together with the no-penetration condition and equation (3.25), we find that p_{w2} satisfies the following second order equation:

$$\frac{\partial^2 p_{w2}}{\partial x^2} + \frac{\overline{\mu}}{\overline{\mu} n + \theta}\frac{\partial n}{\partial x}\frac{\partial p_{w2}}{\partial x} = -\frac{1}{\mu_n(\overline{\mu} n + \theta)}\left[\frac{\partial^2 (n\Sigma_n)}{\partial x^2} + (1-\theta)\frac{\partial}{\partial x}\left(n\frac{\partial \psi_{ns}}{\partial x}\right)\right], \quad (3.30)$$

where $\overline{\mu} = 1/\mu_n - 1$ and Σ_n, ψ_{ns} are given by (3.12). Equation (3.30) is coupled to an equation for n, obtained by averaging the appropriate conservation of mass equation across the channel to obtain:

$$\frac{\partial n}{\partial t} + \frac{1}{12}\frac{\partial}{\partial x}\left\{(\theta - n)\frac{\partial p_{w2}}{\partial x}\right\} = (k_m - k_d)n + D\frac{\partial^2 n}{\partial x^2}. \quad (3.31)$$

For convenience, we have used the conservation of mass equation for the culture medium phase and exploited the no-voids relationship (3.3) to eliminate w.

We remark that our system now comprises a second order differential equation for the culture medium pressure (p_{w2}) coupled to a parabolic equation for the cell volume fraction (n). The boundary conditions on n are (3.29) and from equations (3.27), (3.28) we find that p_{w2} must satisfy the following conditions:

$$p_{w2} = \frac{A(t)a + P_u - n\Sigma_n - (1-\theta)n\psi_{ns}}{\theta}, \frac{\partial p_{w2}}{\partial x} = \frac{A(t) + 12D\frac{\partial n}{\partial x}}{\theta - n} \quad \text{on } x = a, \text{ (3.32a,b)}$$

$$p_{w2} = \frac{A(t)(b-1) + P_d - n\Sigma_n - (1-\theta)n\psi_{ns}}{\theta}, \frac{\partial p_{w2}}{\partial x} = \frac{A(t) + 12D\frac{\partial n}{\partial x}}{\theta - n} \quad \text{on } x = b, \text{(3.33a,b)}$$

two of which may be specified as boundary conditions, the remaining conditions serving as constraints on the function, $A(t)$. The apparent overspecification of $A(t)$ is due to the imposition of continuity of total flux which demands that the up- and downstream pressure gradients are equal; see equation (3.26). Either of the remaining conditions may therefore be used to specify $A(t)$. In the proceeding analysis, we choose to impose equations (3.32a) and (3.33a) as boundary conditions and use (3.32b) to determine $A(t)$. The fourth condition (3.33b) is employed as an additional accuracy check in the following numerical scheme, ensuring that continuity of flux is obeyed.

3.3.1 Numerical solution

In summary, our system comprises the equations (3.30) and (3.31) which we solve subject to (3.29), (3.32a) and (3.33a); (3.32b) is used to determine $A(t)$ and (3.33b) provides an additional accuracy check. Suitable initial conditions read:

$$n(x,0) = 0.1\left[\tanh(75(x-0.48)) - \tanh(75(x-0.52))\right], \tag{3.34}$$

representing a small population of cells initially distributed in the channel's axial centre (at $x = 0.5$) and we arbitrarily choose $a = 0.25$, $b = 0.75$.

The above system is solved numerically as follows. Equation (3.30) is discretised using central differences to obtain the following finite-difference equation which we use to calculate the pressure, $p^k_{w2,j}$, at each mesh point, j, and time-step, k, from the cell volume fraction, n^k_j:

$$\frac{p^k_{w2,j+1} - 2p^k_{w2,j} + p^k_{w2,j-1}}{(\Delta x)^2} + \left(\frac{\overline{\mu}}{\overline{\mu} n^k_j + \theta}\frac{n^k_{j+1} - n^k_{j-1}}{2\Delta x}\right)\frac{p^k_{w2,j+1} - p^k_{w2,j-1}}{2\Delta x} = f(n^k_j), \tag{3.35}$$

where the function $f(n^k_j)$ denotes the right hand side of equation (3.30) evaluated at n^k_j, in which Σ_n and ψ_{ns} are defined by equations (3.12). As before, Δt and Δx represent the size of the time-step and the mesh spacing in the x-direction, respectively: $n^k_j \approx n(j\Delta x, k\Delta t)$, $p^k_{w2,j} \approx p_{w2}(j\Delta x, k\Delta t)$. A shooting method is used to calculate $A^k \approx A(k\Delta t)$ at each time-step via the constraint (3.32b) as follows. Equation (3.35) is solved subject to the boundary conditions (3.32a), (3.33a) using an initial guess for A^k; the error is then calculated using (3.32b) and a new value A^k chosen according to a simple bisection routine if the error is too large. Lastly, continuity of flux is checked using equation (3.33b) and a refined mesh is chosen according to a simple adaptive meshing routine with uniform spatial grid if this condition is not satisfied.

Equation (3.31) is solved using the following semi-implicit predictor-corrector time-stepping method (Peregrine, 1967) to give improved accuracy and stability over an explicit scheme. Firstly, a semi-implicit scheme is used to calculate an approximation to the value

n_j^{k+1} (denoted $\hat{n}_j^{k+1}$) using n_j^k, $p_{w2,j}^k$:

$$\frac{\hat{n}_j^{k+1}-n_j^k}{\Delta t} = \frac{1}{2}\Bigg\{\Bigg(\frac{1}{12}\frac{p_{w2,j+1}^k - p_{w2,j-1}^k}{2\Delta x}\frac{\hat{n}_j^{k+1}-\hat{n}_{j-1}^{k+1}}{\Delta x} - \frac{(\theta-\hat{n}_j^{k+1})}{12}\frac{p_{w2,j+1}^k - 2p_{w2,j}^k + p_{w2,j-1}^k}{(\Delta x)^2}$$
$$+(k_m-k_d)\hat{n}_j^{k+1} + D\frac{\hat{n}_{j+1}^{k+1}-2\hat{n}_j^{k+1}+\hat{n}_{j-1}^{k+1}}{(\Delta x)^2}\Bigg)$$
$$+\Bigg(\frac{1}{12}\frac{p_{w2,j+1}^k - p_{w2,j-1}^k}{2\Delta x}\frac{n_j^k - n_{j-1}^k}{\Delta x} - \frac{(\theta-n_j^k)}{12}\frac{p_{w2,j+1}^k - 2p_{w2,j}^k + p_{w2,j-1}^k}{(\Delta x)^2}$$
$$+(k_m-k_d)n_j^k + D\frac{n_{j+1}^k-2n_j^k+n_{j-1}^k}{(\Delta x)^2}\Bigg)\Bigg\}. \tag{3.36}$$

An approximation for the pressure, $p_{w2,j}^{k+1}$ (denoted $\hat{p}_{w2,j}^{k+1}$), may then be calculated using (3.35). Lastly, the fully-implicit Crank-Nicholson scheme may be used to calculate an improved value for n_j^{k+1} from n_j^k, p_{w2j}^k, $\hat{p}_{w2j}^{k+1}$:

$$\frac{n_j^{k+1}-n_j^k}{\Delta t} = \frac{1}{2}\Bigg\{\Bigg(\frac{1}{12}\frac{\hat{p}_{w2,j+1}^{k+1} - \hat{p}_{w2,j-1}^{k+1}}{2\Delta x}\frac{n_j^{k+1}-n_{j-1}^{k+1}}{\Delta x} - \frac{(\theta-n_j^{k+1})}{12}\frac{\hat{p}_{w2,j+1}^{k+1} - 2\hat{p}_{w2,j}^{k+1} + \hat{p}_{w2,j-1}^{k+1}}{(\Delta x)^2}$$
$$+(k_m-k_d)n_j^{k+1} + D\frac{n_{j+1}^{k+1}-2n_j^{k+1}+n_{j-1}^{k+1}}{(\Delta x)^2}\Bigg)$$
$$+\Bigg(\frac{1}{12}\frac{p_{w2,j+1}^k - p_{w2,j-1}^k}{2\Delta x}\frac{n_j^k - n_{j-1}^k}{\Delta x} - \frac{(\theta-n_j^k)}{12}\frac{p_{w2,j+1}^k - 2p_{w2,j}^k + p_{w2,j-1}^k}{(\Delta x)^2}$$
$$+(k_m-k_d)n_j^k + D\frac{n_{j+1}^k-2n_j^k+n_{j-1}^k}{(\Delta x)^2}\Bigg)\Bigg\}, \tag{3.37}$$

and the improved value for $p_{w2,j}^{k+1}$ corresponding to n_j^{k+1} may be calculated using (3.35). For simplicity, in each of the above schemes, (3.36) and (3.37), the boundary conditions (3.29) are imposed using the value of n_j^k (or $\hat{n}_j^k$) from the previous (or intermediate) time-step. An upwind scheme has been used for the convective term in equation (3.31): backward or forward differences are used to approximate this term depending on the sign of the gradient $\partial p_{w2}/\partial x$ (in the above scheme, this gradient has been assumed to be negative and so backward differences are used).

The initial grid spacing is $\Delta x = 5\times10^{-3}$ and the timestep chosen to be $\Delta t = 2(\Delta x)^2$. Lastly, we note that the NAG routines DGETRI, DGETRF and DGETRS are employed in this numerical scheme; DGETRI performs the matrix inversion required in the re-meshing routine and DGETRS solves the linear systems associated with equations (3.35)–(3.37), using the LU factorisation computed by DGETRF.

In the following simulations, the dimensionless mitosis and death rates and the diffusion coefficient are chosen to be $k_m = 7.5$, $k_d = 0.1$, $D = 0.01$ and the uniform scaffold porosity is taken to be the mean value of the heterogeneous PLLA scaffold porosity, $\theta = 0.97$ (see §1.2.3). The parameters governing the aggregation and repulsion of cells (see equation (3.12)) are chosen to be $\nu = \chi = 0.3$, $\delta_a = \delta_b = 0.1$ and we reiterate that we have chosen $m = 1$. The relative viscosity is chosen to be $\mu_n = 1.3$. The choice of these parameter values is not physiologically motivated; rather, they have been chosen to give insight into the behaviour of the numerical simulations (see §3.2.1). A thorough parameter study is given in chapter 4. Considering these parameter choices and the functions (3.12), we see that the switch between aggregation/attachment and repulsion takes place at $n = 0.73$. Lastly, we note that in the regime of dynamic culture conditions, we choose $P_u = 1$, $P_d = 0.1$; these choices set the velocity scale, U_w^*, used in the non-dimensionalisation (3.10) to be $U_w^* = P_u^* L^*/\mu_w^*$; $P_d = 0.1$ corresponds to $P_d^* = P_u^*/10$ (see equations (2.17)).

The time evolution of the cell volume fraction is shown in figure 3.5 for static ($P_u - P_d = 0$) and dynamic ($P_u - P_d = 0.9$) culture conditions; the arrows indicate the direction of increasing time. The evolution of the culture medium and cell phase pressures (for dynamic culture conditions) is shown in figures 3.6 and 3.7. The disturbance to the culture medium pressure caused by the growth of the cell phase is shown separately for early times (corresponding to $n \leqslant 0.7$) and later times (for which $n_{max} \geqslant 0.78$); similarly, the cell pressure is plotted separately for early times (for which $n \leqslant 0.4$) and later times ($n_{max} \geqslant 0.6$); we have adopted the notation n_{max} to denote the maximum value of the n in the domain at each time-step. The results are presented in this way to prevent detail of the solution being obscured as the transition between aggregative and repulsive behaviour takes place. The corresponding cell phase and culture medium velocities at the channel centreline are shown in figures 3.8 and 3.9. Surface plots of these parabolic velocities are omitted so that interesting features of the solutions are not obscured. The evolution of the function $A(t)$ corresponding to the cell growth shown in figure 3.5b is presented in figure 3.10.

Figure 3.5 illustrates how the initial cell distribution given by (3.34) evolves under the influence of the dynamic culture conditions. In figure 3.5a, where there is no imposed flow (static culture), the cell population grows and spreads symmetrically under the influence of the net growth rate, $k_m - k_d$, and diffusion. This is in direct contrast to the results obtained in chapter 2 in which axially asymmetric growth was predicted. Figure 3.5b illustrates the effect of the imposed flow (dynamic culture) on the cell phase: the tissue is advected by a

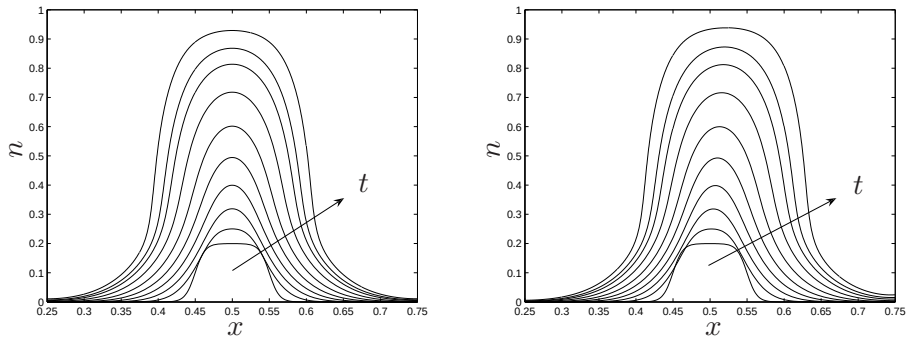

(a) (b)

Figure 3.5: Evolution of the cell volume fraction n for (a) static culture: $P_u - P_d = 0$, (b) dynamic culture: $P_u = 1$, $P_d = 0.1$, at $t = 0 - 0.297$ (in steps of $t = 0.033$). Parameter values: $k_m = 7.5$, $k_d = 0.1$, $D = 0.01$, $\theta = 0.97$, $\nu = \chi = 0.3$, $\delta_a = \delta_b = 0.1$, $m = 1$, $\mu_n = 1.3$.

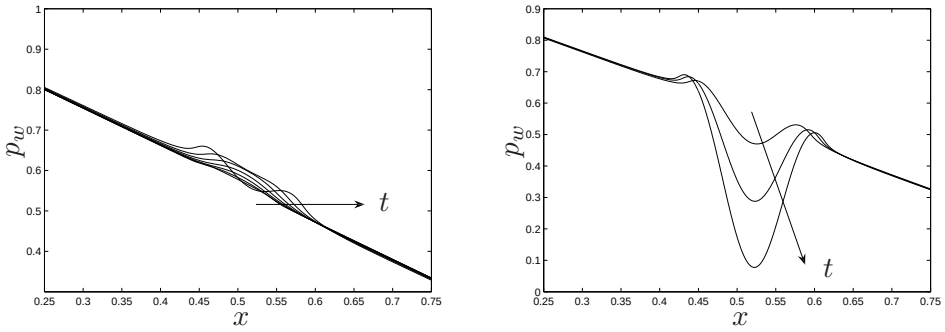

(a) (b)

Figure 3.6: Evolution of the culture medium pressure for (a) early times (small n): $t = 0 - 0.231$ (in steps of $t = 0.033$); and (b) longer times (larger n): $t = 0.25, 0.27, 0.29$, for dynamic culture conditions. Parameter values as in figure 3.5.

small amount along the channel by the flow and a build-up of cells and ECM is observed at $x = b$. The amount by which the cell phase is advected may be enhanced by increasing the driving pressure gradient. The cell phase profiles in figure 3.5 indicate that spreading of the cell phase is observed prior to the threshold value $n = 0.73$ due to the presence of diffusion in the model; when n exceeds this value, diffusion is enhanced by repulsive forces between cells and the cell population spreads more dramatically.

Figure 3.6 shows how the culture medium pressure is influenced by the presence of the

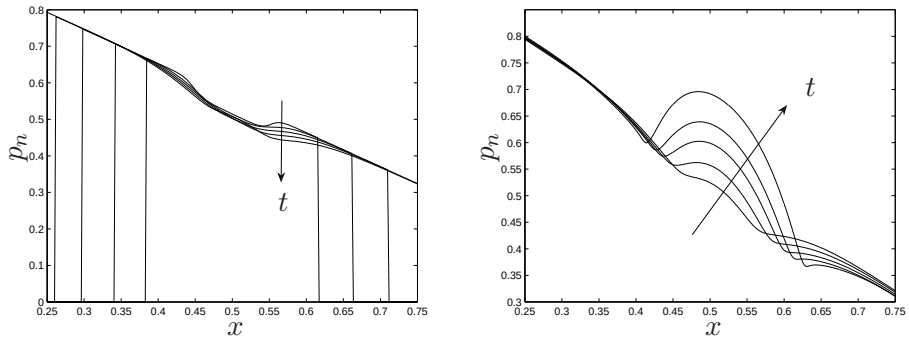

(a) (b)

Figure 3.7: Evolution of the cell pressure for (a) early times (small n): $t = 0 - 0.13$ (in steps of $t = 0.033$); and (b) longer times (larger n): $t = 0.2, 0.23, 0.27, 0.27$, for dynamic culture conditions. Parameter values as in figure 3.5.

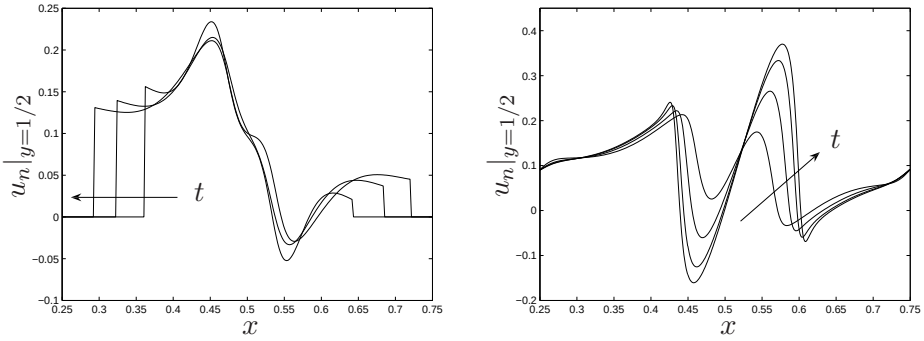

(a) (b)

Figure 3.8: Evolution of the cell velocity at the channel centreline for (a) early times (small n): $t = 0.033, 0.066, 0.1$; and (b) longer times (larger n): $t = 0.2, 0.23, 0.25, 0.27$, for dynamic culture conditions. Parameter values as in figure 3.5.

cell population within the construct. In the up- and downstream regions where n is small, equation (3.30) can be approximated as $\partial^2 p_{w2}/\partial x^2 \approx 0$ so we obtain a linear pressure drop prior to and after the dense cell population; a deviation from this linear profile is then observed as the culture medium flows through the area in which cells are present. Figure 3.6a shows that, initially, when the density of the cell phase is relatively small, this deviation closely mirrors the cell phase distribution (as found in chapter 2). This increase in pressure is due to the aggregative terms in the intraphase and interphase pressure functions Σ_n, ψ_{ns} (see figures 3.2 and 3.3 and equations (3.12) and (3.30)) dominating at low density. The

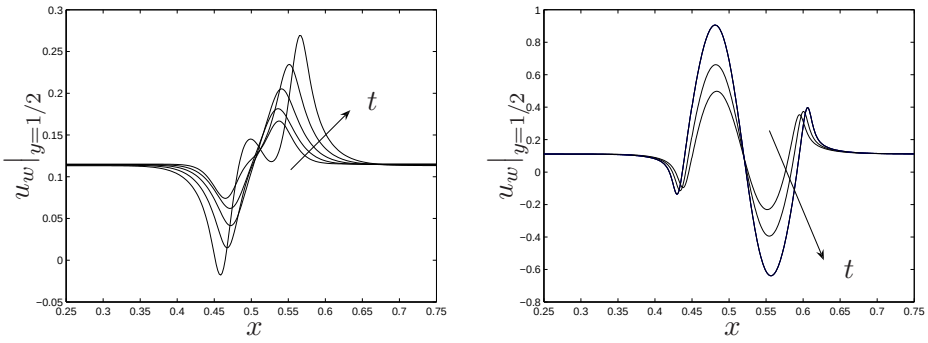

(a) (b)

Figure 3.9: Evolution of the culture medium velocity at the channel centreline for (a) early times (small n): $t = 0.033 - 0.165$ (in steps of $t = 0.033$); and (b) longer times (larger n): $t = 0.25, 0.27, 0.29$, for dynamic culture conditions. Parameter values as in figure 3.5.

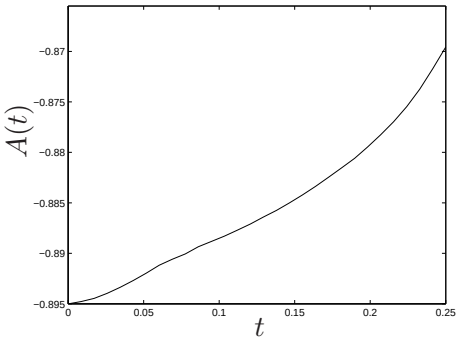

Figure 3.10: Evolution of the function $A(t)$ for dynamic culture conditions. Parameter values as in figure 3.5.

aggregation of cells requires that culture medium is expelled from this region and a positive culture medium pressure gradient (which drives a flow of culture medium) is therefore created at the upstream periphery of the construct (with the opposite behaviour evident at the downstream periphery). As the cell phase becomes more dense, the disturbance in the culture medium pressure distribution increases. The massive deviation from the linear profile shown in figure 3.6b occurs when the repulsive terms in the intraphase and interphase pressure functions become dominant as n approaches the scaffold porosity value, θ. As the cells repel each other, mass conservation demands that culture medium be drawn in to fill the void, corresponding to the reduction in p_w observed in figure 3.6b. We note that at the periphery, where the cell population remains sparse, an increase in p_w is observed,

corresponding to expulsion of culture medium due to cell aggregation and attachment.

The evolution of the cell phase pressure p_n is shown in figure 3.7. We note that although $n > 0$ in $a \leqslant x \leqslant b$ (see equation (3.34)), we have employed numerical truncation in evaluating the cell pressure (3.4) for consistency with the cell phase velocity (figure 3.8) in which truncation is employed to ensure that the $1/n$ term does not blow up for small n. As time progresses and the cell phase density increases throughout the scaffold, the region in which p_n is defined increases to fill the scaffold. The cell phase pressure is formed from a combination of the culture medium pressure and contributions from the intraphase pressure (from cell-cell interactions) and interphase tractions: $p_n = p_w + \Sigma_n + (1-\theta)\psi_{ns}$. At early times, when n is small, the behaviour is dominated by aggregative behaviour ($\Sigma_n, \psi_{ns} < 0$) and a small decrease in the cell phase pressure mirroring this cell distribution is observed. At later times (see figure 3.7b), when the cell phase density grows, the contribution from the repulsive behaviour terms becomes more important ($\Sigma_n, \psi_{ns} > 0$) and a sharp increase in cell pressure is observed.

The axial velocity of the cell phase (u_n) at the channel centreline is shown in figure 3.8 (we reiterate that the velocity of the cell phase is driven by (3.25) rather than $\partial p_n/\partial x$). For low cell densities, 3.8a shows that cells move preferentially towards the centre to form a dense cell aggregate which moves downstream due to the imposed flow. This movement of the cells is due to the form of the intraphase and interphase pressure functions, Σ_n and ψ_{ns}, the choice of which causes aggregation/attachment to dominate at low cell densities ($\Sigma_n, \psi_{ns} < 0$); as the cell volume fraction increases, repulsive effects become more important ($\Sigma_n, \psi_{ns} > 0$) as described above. This effect is illustrated in figure 3.8b which shows that cells move outwards from the centre of the aggregate causing increased spreading at later times as observed in figure 3.5. Inspection of equations (3.25), (3.32a) and (3.33a) shows that the influence of the cell-scaffold attachment parameter (χ) is only felt through the boundary conditions. The aggregative behaviour described above is therefore dominated by the cell-cell interactions (Σ_n).

Figure 3.9 shows how the centreline value of the parabolic velocity profile created by the imposed culture medium pressure gradient is dramatically altered by the presence of the cell phase. As in the two-fluid model, the flow profile remains x-independent, prior to and after the region occupied by the cell phase, under the influence of the linear driving pressure gradient. In regions where $n > 0$, the deviation to the flow corresponds to the gradient of the culture medium pressure shown in figures 3.6. For both low (figure 3.9a) and high (figure 3.9b) cell phase density, we observe that the flow speed is decreased from

the upstream x-independent ambient flow velocity as the culture medium encounters the construct; near the downstream periphery, an increase to the ambient flow is observed. For low construct density, the culture medium flow increases monotonically between the up- and downstream peripheries. As the construct density increases, the fluid flow in between these peripheral regions changes markedly, reversing flow direction. This is due to the switch between aggregative and repulsive behaviour of the cell phase described above; to conserve mass, the culture medium velocity exhibits the opposite behaviour, being drawn into the construct's centre when cells repel each other. This results in the large variation and back-flow predicted by figure 3.9b.

Inspection of figures 2.5, 2.11, 3.8 and 3.9 shows that consideration of cell-cell and cell-scaffold interactions, together with relaxation of the large drag assumption, results in starkly different behaviour to that predicted in chapter 2. Aggregation in regions of sparse cell density acts to curtail advection; furthermore, due to mass conservation, the cell and culture medium velocities exhibit opposite behaviour. We note that inspection of the model equations has revealed that at low cell density, the cell behaviour is dominated by cell aggregation with contributions from cell-scaffold attachment being small.

Figure 3.10 shows how the function $A(t)$ evolves with time. Equations (3.26), (3.32b) and (3.33b) show that $A(t)$ determines the culture medium pressure and its gradient in $x < a$ and $x > b$ and at the boundaries of the scaffold region $x = a, b$. Figure 3.10 shows that as time progresses, the magnitude of the pressure gradient decreases, causing the up- and downstream flow speed to reduce; we attribute this to the increase of cell volume fraction which fills available pore space and provides increased resistance to flow.

To summarise, in contrast to the two phase model presented in chapter 2, this more-complex model predicts symmetric tissue growth in the absence of perfusion, and shows that advection of the tissue due to perfusion with culture medium is reduced by aggregation and attachment. The stringent restriction on perfusion rate implied by the analysis in chapter 2 may therefore be relaxed. Furthermore, we demonstrate that cells display dramatically different behaviour depending upon the relative importance of cell aggregation and repulsion. In addition, since no-slip boundary conditions are imposed at the channel walls, the model does not predict a slip velocity. Lastly, since we choose $S_w = -S_n$ (§3.2), mass is conserved in this model.

We pause here to note that the results presented in figures 3.5–3.8 illustrate the behaviour of the relevant variables in the region $a \leqslant x \leqslant b$; up- and downstream from this region we have $n = 0$, $p_n = 0$, $u_n = 0$, and a linear pressure profile whose gradient changes

over time as indicated by equation (3.26) and figure 3.10, which drives a parabolic culture medium velocity (results omitted). Furthermore, discontinuities in the culture medium and cell phase pressures (and their gradients) exist at $x = a, b$ caused by the presence of the porous scaffold, cells, ECM and the associated extra pressures Σ_n and ψ_{ns} as indicated by equations (3.32) and (3.33).

3.3.2 Asymptotically-small cell volume fraction

To validate the above numerical simulations and to provide insight into the behaviour of the system, we consider the limit in which the volume fraction of the cell phase is asymptotically small. We may then obtain analytic solutions to the simplified versions of (3.29)–(3.33) for comparison with numerical predictions. We therefore choose the following rescalings:

$$n(x,t) = \delta n_1(x,t) + \delta^2 n_2(x,t) + \cdots, \tag{3.38}$$

$$p_{w2}(x,t) = p_0(x,t) + \delta p_1(x,t) + \delta^2 p_2(x,t) + \cdots, \tag{3.39}$$

where $0 < \delta \ll 1$, and we remark that the subscript notation which indicates the region in which the solution is valid has been replaced by subscripts denoting the terms in the asymptotic expansion. For clarity, we emphasise that these expansions are valid in region 2: $a \leqslant x \leqslant b$.

We find that the leading-order term in the expansion for the culture medium pressure obeys:

$$\frac{\partial^2 p_0}{\partial x^2} = 0, \tag{3.40}$$

and that the next-order corrections $n_1(x,t)$, $p_1(x,t)$ are given by

$$\frac{\partial n_1}{\partial t} + \gamma \frac{\partial n_1}{\partial x} = (k_m - k_d) n_1 + D \frac{\partial^2 n_1}{\partial x^2}, \tag{3.41}$$

$$\frac{\partial^2 p_1}{\partial x^2} = -\beta \frac{\partial n_1}{\partial x}, \tag{3.42}$$

where γ and β are defined as follows:

$$\gamma = -\frac{1}{12\mu_n} \frac{\partial p_0}{\partial x}, \quad \beta = \frac{\overline{\mu}}{\theta} \frac{\partial p_0}{\partial x}. \tag{3.43}$$

We now consider the form of the boundary conditions (3.29), (3.32) and (3.33) in the limit for which the cell volume fraction is asymptotically small. In addition to the rescalings (3.38), (3.39), we expand the function, $A(t)$ as follows:

$$A(t) = A_0(t) + \delta A_1(t) + \cdots, \tag{3.44}$$

and it may be shown that the appropriate conditions are:

at leading order:

$$\left.\frac{\partial p_0}{\partial x}\right|_{x=a,b} = \frac{A_0}{\theta}, \quad p_0\Big|_{x=a} = \frac{A_0 a + P_u}{\theta}, \quad p_0\Big|_{x=b} = \frac{A_0(b-1) + P_d}{\theta}; \tag{3.45}$$

$\mathcal{O}(\delta)$ correction:

$$\left.\frac{\partial n_1}{\partial x}\right|_{x=a,b} = -\frac{A_0 n_1}{12\theta\mu_n D}, \qquad \left.\frac{\partial p_1}{\partial x}\right|_{x=a,b} = \frac{A_1}{\theta} + \frac{A_0 n_1}{\theta^2} + \frac{12D}{\theta}\frac{\partial n_1}{\partial x}, \tag{3.46}$$

$$p_1\Big|_{x=a} = \frac{A_1 a + (1-\theta)\chi n_1}{\theta}, \qquad p_1\Big|_{x=b} = \frac{A_1(b-1) + (1-\theta)\chi n_1}{\theta}. \tag{3.47}$$

We therefore have four conditions on each of the pressures p_0, p_1; two of which are imposed as boundary conditions, the remaining equations being used to calculate A_0 and A_1. As previously, the overspecification of the functions A_0, A_1 results from the imposition of continuity of total flux which requires that the up- and downstream pressure gradients are equal. When satisfied, the additional conditions ensure that the solution obeys continuity of flux (see §3.3 for more details).

Sharp interface limit: $D = 0$

For simplicity, we consider the solution of equations (3.40)–(3.42) in the limit $D = 0$, for which the interface between the cell phase and the surrounding culture medium is "sharp". The cell population is then confined within two moving boundaries, $x = l(t), r(t)$, *within* the scaffold region $a \leqslant x \leqslant b$.

It is a trivial calculation to show that $A_0 = P_d - P_u$ and the leading-order pressure in the culture medium is given by

$$p_0(x,t) = \frac{(P_d - P_u)x + P_u}{\theta}. \tag{3.48}$$

We may now proceed with the solution of equation (3.41) with $D = 0$ since the constant, γ, is given by equation (3.43). We first specify an appropriate initial cell phase distribution as follows:

$$n_1(x,0) = \begin{cases} \overline{n}(x) & l(0) \leqslant x \leqslant r(0), \\ 0 & \text{otherwise}, \end{cases} \tag{3.49}$$

wherein $\overline{n}(x)$ is an as yet unspecified function and $x = l(0)$, $r(0)$ are the initial positions of the interfaces $l(t)$, $r(t)$. We remark that the first of (3.46) is now redundant since $n_1 = 0$

for $a \leqslant x < l$, $r < x \leqslant b$. The solution, $n_1(x,t)$, may be determined using characteristic methods, taking the form of a travelling-wave:

$$n_1(x,t) = \begin{cases} \overline{n}(x-\gamma t)e^{(k_m-k_d)t} & l(t) \leqslant x \leqslant r(t), \\ 0 & \text{otherwise}, \end{cases} \tag{3.50}$$

where $l(t) = l(0) + \gamma t$, $r(t) = r(0) + \gamma t$. This solution represents exponential growth of a cell population at a rate $k_m - k_d$ which is advected along the channel at speed $\gamma = -(\partial p_0/\partial x)/(12\mu_n) \geqslant 0$. We remark that, in contrast to the sharp interface limit of the two-fluid model analysed in chapter 2, the width of the cell population does not change in this model and the cell population displays exponential (rather than logistic) growth. This behaviour is valid for the very early stages of cell population growth in which behaviour is dominated by uniform proliferation and diffusion/spreading is unimportant.

The correction to the culture medium pressure p_1 is given by equation (3.42); however, in addition to the conditions (3.45)–(3.47) at $x = a, b$, p_0 and p_1 must obey the following jump conditions across $x = l(t), r(t)$:

$$[p_0]^+_- = 0, \quad \left[\frac{\partial p_0}{\partial x}\right]^+_- = 0, \tag{3.51a}$$

$$[\theta p_1]^+_- = [\chi(1-\theta)n_1]^+, \quad \left[\theta\frac{\partial p_1}{\partial x}\right]^+_- = \left[\frac{(P_u - P_d)\overline{\mu}n_1}{\theta}\right]^+, \tag{3.51b}$$

where $[..]^+$ and $[..]^-$ denote the limiting values from the cell/culture medium/scaffold region ($l(t) \leqslant x \leqslant r(t)$) and the culture medium/scaffold regions ($a \leqslant x < l(t)$, $r(t) < x \leqslant b$), respectively and $[..]^+_-$ denotes the jump across either interface. These conditions are derived using the method outlined previously, noting that the cell velocity on $x = l(t), r(t)$ is $u_n = \gamma$. We remark that the conditions (3.51a) on the leading-order solution, p_0, are automatically satisfied by equation (3.48).

To determine the correction to the pressure in the culture medium, we must specify the initial cell phase distribution, $\overline{n}(x)$. For simplicity we choose $\overline{n}(x) = \hat{n}$, where $\hat{n}$ is assumed constant so that in each region, equation (3.42) is satisfied by a linear pressure distribution. These are found to be

$$p_1(x,t) = \begin{cases} \widetilde{P}e^{\overline{k}t}\left[l(t) - r(t)\right]x, & a \leqslant x < l(t), \\ \widetilde{P}e^{\overline{k}t}\left[1 + l(t) - r(t)\right]x + e^{\overline{k}t}(\overline{\chi} - \widetilde{P}l(t)), & l(t) \leqslant x \leqslant r(t), \\ \widetilde{P}e^{\overline{k}t}\left[l(t) - r(t)\right](x-1), & r(t) < x \leqslant b, \end{cases} \tag{3.52}$$

where $\overline{k} = k_m - k_d$, $\overline{\chi} = \chi(1-\theta)\hat{n}/\theta$, $\overline{\mu} = 1/\mu_n - 1$ and $\widetilde{P}$ is given by

$$\widetilde{P} = \frac{(P_u - P_d)\overline{\mu}\hat{n}}{\theta^2}. \tag{3.53}$$

The evolution of the cell volume fraction, n_1, and corresponding pressure correction, p_1, is shown in figure 3.11. The effect of this pressure correction is illustrated in figure 3.12 which shows the variation of the pressure (to $\mathcal{O}(\delta)$ accuracy) $p_{w2} = p_0 + \delta p_1$ over time; figure 3.12b shows this in more detail. We remark that the correction to the pressure (p_1) is an order of magnitude smaller than the leading-order pressure (p_0); in order that the effects are visible in figure 3.12, the small parameter is chosen to be $\delta = 1$ (the arrows indicate the direction of increasing dimensionless time). With the exception of the diffusion coefficient, D, the parameter values are chosen to be the same as those used in §3.3.1.

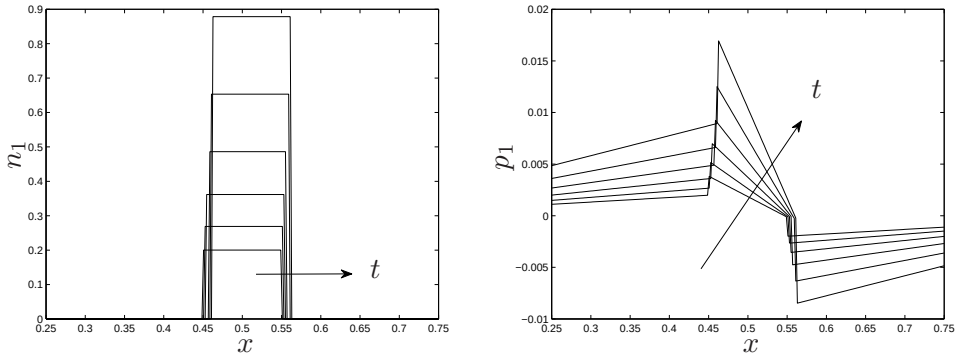

(a) (b)

Figure 3.11: Evolution of (a) the cell volume fraction, n_1, and (b) the pressure correction, p_1, for dynamic culture conditions at $t = 0{-}0.2$ (in steps of $t = 0.04$). $D = 0$, other parameter values as in §3.3.1.

As noted above, the solution in the sharp interface limit predicts that the cell population grows exponentially with growth rate $k_m - k_d$, while being advected along the channel at speed γ; the width of the population remains unchanged. For validation purposes, the corresponding speed of advection predicted by the numerical scheme developed in §3.3.1 may be readily calculated by tracking the position of the maximum value of n. Figure 3.13a shows how the position of this numerically-calculated maximum value compares to the position predicted by the travelling-wave solution (3.50), and figure 3.13b depicts the % relative error between the numerically-calculated and theoretical positions over time for different values of the small parameter, δ; the arrows indicate the direction of increasing δ. It can be seen that as the value of δ is decreased, the numerical prediction for the speed of advection of the cell culture approaches the predicted speed, γ, and the % relative error decreases (for $\delta = 1/25$, the % error is $\mathcal{O}(10^{-2})$). The predicted advection speed corresponding to the parameters chosen for the numerical simulations given in §3.3.1 is

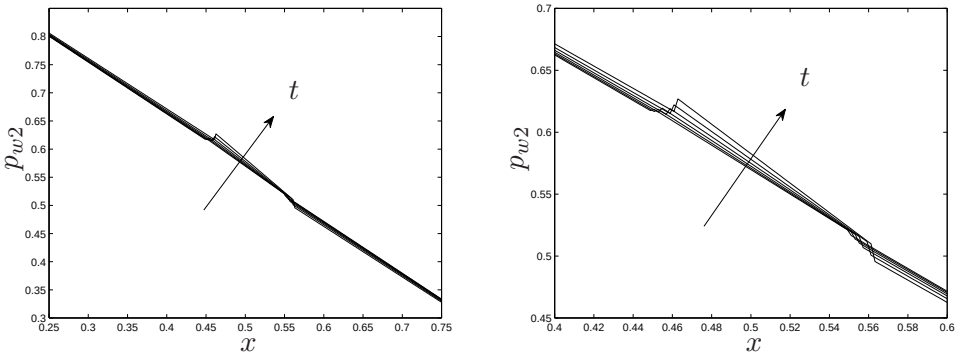

(a) (b)

Figure 3.12: The evolution of the culture medium pressure, $p_{w2} = p_0 + \delta p_1$, for dynamic culture conditions at $t = 0 - 0.2$ (in steps of $t = 0.04$) in (a) the construct region $a \leqslant x \leqslant b$, and (b) a magnified region to show the detail more clearly. $D = 0$, $\delta = 1$, other parameter values as in §3.3.1.

$\gamma = 0.0595$; at early times, the average advection speed calculated from the simulations is $\gamma = 0.0657$ ($\delta = 1$), $\gamma = 0.0607$ ($\delta = 1/5$), $\gamma = 0.0601$ ($\delta = 1/25$). By comparing these values and inspecting figure 3.13 it can be seen that the speed of advection does not exactly match that predicted by the small-n analysis; however, we consider that the agreement between the two advection speeds is good enough to indicate that we may have confidence in the qualitative behaviour of our numerical simulations. We find that decreasing the size of the small parameter, δ, below $\delta = 1/25$, results in only a marginal reduction in the, already small, relative error; we attribute the discrepancy between the predicted value and those calculated from the numerical simulations to the coarseness of the spatial grid used and the diffuse construct considered; however, refining the mesh and reducing the diffusion coefficient are prohibitively expensive computationally.

The perturbation (p_1) to the culture medium pressure is found to be piecewise linear, with positive gradient in the up- and downstream regions where $n_1 = 0$ and negative gradient within the region where cells are present ($l(t) \leqslant x \leqslant r(t)$). Upstream, the sharp interface limit predicts a small increase to the leading-order pressure; downstream, a small decrease is observed. Comparison of the predicted pressure shown by figure 3.12 and the culture medium pressure calculated in §3.3.1 (figure 3.6a) shows good qualitative agreement.

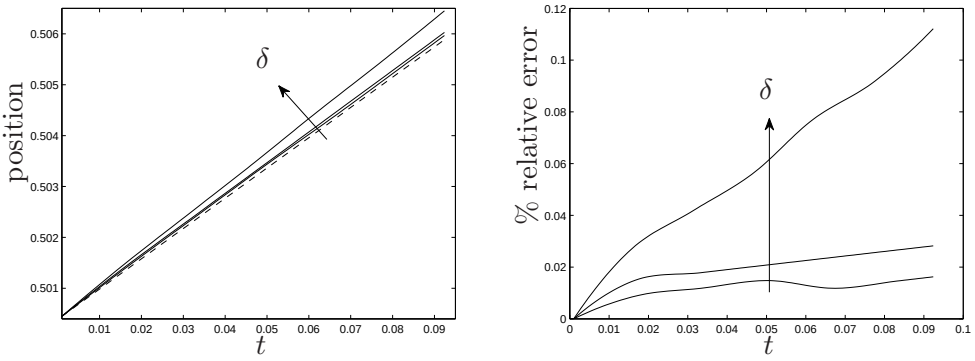

(a) (b)

Figure 3.13: (a) Comparison of the numerically-computed position of the maximum value of n (–) compared to the predicted position of the travelling wave (- -), and (b) the % relative error between calculated and predicted position for $\delta = 1/25, 1/5, 1$. The arrows indicate the direction of increasing δ.

Furthermore, considering the boundary conditions (3.32a) and (3.33a):

$$p_{w2} = \frac{A(t)a + P_u - n\Sigma_n - (1-\theta)n\psi_{ns}}{\theta}, \quad \text{on } x = a, \tag{3.54}$$

$$p_{w2} = \frac{A(t)(b-1) + P_d - n\Sigma_n - (1-\theta)n\psi_{ns}}{\theta}, \quad \text{on } x = b, \tag{3.55}$$

the behaviour of $A(t)$ presented in figure 3.10 (which indicates that $A(t) < 0$ and that $|A(t)|$ decreases with time) and the fact that on $x = a, b$ where n is small, the extra pressure contributions are small and negative, we see that at $x = a$, the culture medium pressure increases over time; at $x = b$, the pressure decreases. This comparison indicates that the behaviour of the culture medium pressure ($p_{w2} = p_0 + \delta p_1$) predicted in this asymptotic limit reproduces that of the system (3.30)–(3.33) for $\mathcal{O}(1)$ cell density.

We remark that the small parameter, δ has been chosen artificially large for illustrative purposes; the deviation to the pressure corresponding to the small cell population represented by these solutions would be very small.

In this subsection, we have constructed analytic solutions in the limit of asymptotically-small cell density in order to validate the numerical simulations presented in §3.3.1. We have shown that the travelling-wave behaviour obtained in this asymptotic limit shows good quantitative agreement by comparing the predicted wave speed with that calculated from corresponding numerical simulations using the numerical scheme (3.35)–(3.37); we further show that qualitative features of the analytic solutions correspond to those observed in

numerical simulations. We therefore conclude that we may have confidence in the numerical simulations presented in this chapter.

Travelling-wave solutions corresponding to a diffuse tissue construct which show better qualitative agreement with the cell volume fraction profiles presented in §3.3.1 may be obtained using Green's functions. From a code-validation point of view, this is superfluous and we therefore present these solutions in Appendix A for interest.

3.4 Summary

In this chapter, we have analysed a multiphase model that describes tissue growth within a perfusion bioreactor, modelled as a two-dimensional channel containing a three phase mixture. The inclusion of a third phase allowed consideration of the PLLA scaffold within our model. The "cell phase" (comprising both cells and ECM) and the culture medium were modelled as viscous fluids; as a first approximation, we simplified the three phase formulation by considering the scaffold phase to be rigid and inert. This phase then enters the governing equations through the constant porosity (θ) only. However, this model represents a significant extension of that analysed in chapter 2 due to the retention of the individual phase variables and consideration of interphase tractions and intraphase forces, resulting in a more complex coupling between the dynamic culture environment and the tissue response. Furthermore, modification to the choice of mass transfer terms ensures that this model conserves mass. In contrast to the two-fluid model presented in chapter 2, this more complex three phase model predicted axially-symmetric growth in the absence of perfusion and showed that cell aggregation reduces the advection of the cell phase. The stringent restriction on perfusion rate implied by the analysis in chapter 2 may therefore be relaxed. Furthermore, by considering cell-cell and cell-scaffold interactions, we have revealed markedly different cell behaviour depending upon the relative importance of cell aggregation and repulsion.

By considering the limit in which the aspect ratio of the channel is small and the interfaces between the tissue construct and surrounding culture medium are sharp, we have shown that the mass and momentum balance equations for the multiphase system reduce to a coupled system comprising a second order differential equation for the culture medium pressure and a parabolic equation for the cell volume fraction. These equations were analysed using a combination of analytic and numerical techniques. A similar multiphase formulation has been analysed by Lemon *et al.* (2006) and Lemon & King (2007) in which

the diffusive movement of each phase was neglected ($D_i^* = 0$), corresponding to sharp interfaces between the cell and culture medium phases, and the long-wavelength limit was not employed. In Lemon *et al.* (2006), aggregative and repulsive behaviour was investigated using linear stability techniques; in Lemon & King (2007), the growth of the cell phase is mediated by the supply of a diffusible nutrient.

From the preceding numerical results and analysis, it may be seen that the simplified version of our three phase model predicts a plausible response of the tissue construct to the dynamic culture conditions. The numerical simulations showed that the cell population grows, spreads and is advected downstream to a limited extent *within* the scaffold. Furthermore, interactions within the cell phase and between the cells and the scaffold mean that, at low cell density, the model predicts movement of cells from sparse peripheral regions to form a dense aggregate; as the density increases, repulsive interactions cause cells to be expelled from the aggregate. Inspection of the model equations revealed that at low density, the cells' behaviour is dominated by cell-cell interactions. We remark that for the tissue engineering applications under consideration, the cell density is unlikely to attain such high values (see §1.2.3, figure 1.3 which indicates that the level of mineralisation of the PLLA scaffold is small); we therefore expect that the aggregative behaviour illustrated in §3.3.1 is appropriate. Further analysis of the cell behaviour under the influence of the intraphase pressure and interphase traction functions is presented in chapter 4.

In the limit of asymptotically-small cell volume fraction, analytic solutions were constructed which take the form of a growing travelling-wave. Comparison of the predicted wave speed with that calculated from numerical simulations showed good quantitative agreement; qualitative agreement was observed in the behaviour of solutions. This analysis indicates that we may have confidence in the behaviour of our numerical simulations.

The mathematical model used is limited since we have made a number of simplifications to facilitate construction of solutions. The scaffold porosity, θ, is assumed constant and the scaffold neither deforms nor degrades, which prohibits consideration of the mechanical forcing aspect of the bioreactor system and of the influence on the construct's mechanical properties of scaffold degradation and cell phase growth. Additionally, we make the long-wavelength assumption to simplify the equations. Consequently, at leading order, the contribution of, for instance, interphase viscous drag terms are neglected from the momentum equations (3.11c,d). In view of the parameter estimation given in §2.2.1, this effect should, perhaps, be considered since the drag coefficient, k is expected to be large (we note that this may be remedied by choosing $k = \mathcal{O}(1/h^2)$, where k is the coefficient of viscous

drag and h is the channel aspect ratio). Furthermore, the physical dimensions of the system given in §1.2.3 are inconsistent with the long-wavelength assumption. However, we consider that the solutions obtained in this limit give adequate insight into the behaviour of the $\mathcal{O}(1)$ system; the complexity of this problem preventing easy analysis. In a wider context, this model has the potential to be directly applicable to other perfusion bioreactors which have a low aspect ratio. Lastly, we have assumed that the rates of cell mitosis and death are constant, thereby removing the coupling between the external fluid flow and the tissue growth response.

In the proceeding chapters of this thesis, we develop models that accommodate spatio-temporal variation of the scaffold volume fraction as well as direct coupling between the phenotypic progression of the cell phase and its local environment.

Chapter 4

A simplified three phase model for the growth of a tissue construct - a cell behaviour study

4.1 Introduction

We now present a detailed study of the behaviour of the solutions of the three phase model developed in chapter 3. Using numerical simulations, we illustrate the effect of varying the parameters associated with (i) the relative viscosity and, (ii) the intraphase pressure and interphase traction functions on the construct morphology. Additionally, the influence of coupling the cells' proliferative behaviour with cell density and the external fluid mechanics is investigated.

In order to provide insights into the factors that affect the behaviour of cells within porous scaffolds, in §4.2, solutions to equations (3.30) and (3.31) are presented for a variety of parameter regimes that highlight how the cells' movement is influenced by their interaction with their environment. To improve understanding of the influence of intraphase pressure and interphase traction, simple functional forms for these effects are employed, allowing analytical progress to be made and, using numerical simulations, we investigate in more detail the transition between aggregative and repulsive behaviour observed in chapter 3. Lastly, in §4.3, the model is extended to investigate the effect of a simple mechanotransduction mechanism, in which the cells' proliferative response is coupled to the local mechanical environment. In an extension to the mechanotransduction modelling of chapter 2, the response to the local cell density, pressure and fluid shear stress is considered. We again identify our model as a simple means to discern the dominant regulatory tissue growth stimulus. The chapter concludes with a discussion of our results. Attention focusses on their implications for the bioreactor system introduced in §1.2.3; however, their relevance to more general tissue engineering applications is also discussed.

4.2 Cell movement

4.2.1 Parameter study

We pause here to recapitulate the equations and boundary conditions which govern the behaviour of the simplified three phase model presented in the chapter 3. The differential equation governing the pressure in the culture medium (p_w) and the coupled parabolic equation governing the evolution of the cell phase volume fraction (n) are as follows:

$$\frac{\partial^2 p_w}{\partial x^2} + \frac{\overline{\mu}}{\overline{\mu} n + \theta} \frac{\partial n}{\partial x} \frac{\partial p_w}{\partial x} = -\frac{1}{\mu_n (\overline{\mu} n + \theta)} \left[\frac{\partial^2 (n \Sigma_n)}{\partial x^2} + (1-\theta) \frac{\partial}{\partial x} \left(n \frac{\partial \psi_{ns}}{\partial x} \right) \right], \quad (4.1)$$

$$\frac{\partial n}{\partial t} + \frac{1}{12} \frac{\partial}{\partial x} \left\{ (\theta - n) \frac{\partial p_w}{\partial x} \right\} = S_n + D \frac{\partial^2 n}{\partial x^2}, \quad (4.2)$$

where $\overline{\mu} = 1/\mu_n - 1$, μ_n is the relative viscosity of the cell and culture medium phases, $S_n = (k_m - k_d)n$ is the averaged mass transfer term for the cell phase, θ is the porosity of the scaffold and Σ_n, ψ_{ns} are intraphase pressure and interphase traction functions. The parameter k_m represents cell mitosis and ECM deposition, whilst k_d encompasses cell death and ECM degradation. As in chapter 3, we henceforth refer to these as the "growth rate" and "death rate". We note that, for brevity, the subscript notation introduced in §3.3 which indicates that these equations are valid in $a \leqslant x \leqslant b$ has been dropped (as in chapter 3, we assume $a = 0.25$, $b = 0.75$). The pressure in the culture medium is subject to the following conditions

$$p_w = \frac{A(t)a + P_u - n\Sigma_n - (1-\theta) n \psi_{ns}}{\theta}, \quad \frac{\partial p_w}{\partial x} = \frac{A(t) + 12D \frac{\partial n}{\partial x}}{\theta - n} \quad \text{on } x = a, \quad (4.3)$$

$$p_w = \frac{A(t)(b-1) + P_d - n\Sigma_n - (1-\theta) n \psi_{ns}}{\theta}, \quad \frac{\partial p_w}{\partial x} = \frac{A(t) + 12D \frac{\partial n}{\partial x}}{\theta - n} \quad \text{on } x = b, \quad (4.4)$$

where $P_u - P_d$ is the imposed axial pressure drop. The first of (4.3) and (4.4) are imposed as boundary conditions and $A(t)$ is determined from one of the remaining two conditions. The fourth condition provides an additional accuracy check, which, when satisfied, ensures that continuity of flux is obeyed in the numerical scheme (see §3.3, page 77).

As discussed in §3.2.1, the intraphase pressure, Σ_n, and interphase traction, ψ_{ns}, describe the tendency of the cells to aggregate (or to exhibit an affinity for the scaffold phase) at low cell densities, and to repel each other (or be repelled from the scaffold) at high cell densities. These functions are specified as follows:

$$\Sigma_n = -n\nu + \frac{\delta_a n^{m+1}}{(\theta - n)^m}, \quad \psi_{ns} = -\chi + \frac{\delta_b n^m}{(\theta - n)^m}, \quad (4.5)$$

for constants ν, δ_a, χ, δ_b, $m > 0$; as in chapter 3, in the following, we choose $m = 1$ for simplicity.

To ensure zero cell flux from the scaffold region, the cell volume fraction must obey:

$$\frac{\partial n}{\partial x} = \frac{A(t)n}{(\theta - n)\left[2\nu n - 12\mu_n D - \frac{\delta_a n^3 + (1-\theta)\delta_b n^2}{(\theta-n)^2} - \frac{3\delta_a n^2 + [\delta_b(1-\theta)+12D]n}{\theta - n}\right]} \text{ on } x = a, b, \quad (4.6)$$

and a suitable initial cell distribution is given by

$$n(x, 0) = 0.1\left[\tanh(75(x - 0.48)) - \tanh(75(x - 0.52))\right], \quad (4.7)$$

representing a small population of cells initially distributed in the channel's axial centre (at $x = 0.5$).

The model parameters pertinent to the study of cell movement (as distinct from those associated with cell phase growth and death; namely, k_m and k_d) are: μ_n (relative viscosity of cell and culture medium phases), ν, χ (cell-cell and cell-scaffold affinity parameters, respectively), δ_a, δ_b (cell-cell and cell-scaffold repulsion parameters, respectively) and D (cellular diffusion coefficient). The effect of varying each the parameters μ_n, ν, δ_a, χ, δ_b is investigated below, exploiting the numerical scheme developed in §3.3.1.

Relative viscosity: μ_n

Figure 4.1 shows how the distribution of the cell phase is affected by increasing its viscosity. We observe that increasing μ_n reduces the rate at which cells are advected by the imposed flow and leads to the formation of a more diffuse aggregate.

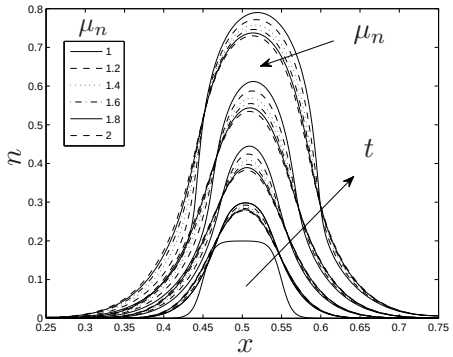

Figure 4.1: The evolution of the cell volume fraction at $t = 0 - 0.25$ (in steps of $t = 0.0625$), for dynamic culture: $P_u = 1$, $P_d = 0.1$, $k_m = 7.5$, $k_d = 0.1$, $D = 0.01$, $\theta = 0.97$. $\chi = \nu = 0.3$, $\delta_a = \delta_b = 0.1$, $\mu_n = 1$–2.

The viscosity of the cell phase represents the tendency of the cells to move in coupled pairs or aggregates when they are sufficiently close to each other (this behaviour has been reported by, for instance, Powers & Griffith-Cima (1996) in hepatocyte populations); an increase in μ_n therefore represents an increased tendency to form (and move as) aggregates rather than displaying single cell migration. In view of this, the reduction in advection and the increase in diffusive effects illustrated by figure 4.1 is, perhaps, counter-intuitive. The reason for this behaviour is as follows. As the viscosity of the cell phase is increased relative to that of the culture medium, the importance of the viscous shear exerted by the flowing culture medium on the cell phase is diminished, resulting in reduced advection; indeed, inspection of equation (3.23), reveals that the velocity of the cell phase is proportional to μ_n^{-1}. Additionally, comparison of the positions of the up- and downstream peripheries of the diffuse construct shown in figure 4.1 shows that as μ_n increases, the reduced advective effects allow markedly increased diffusion of the upstream periphery, resulting in the construct as a whole being less dense.

Aggregation and repulsion: ν, δ_a, χ, δ_b

We now consider the effect of varying the intraphase pressure and interphase traction parameters, ν, δ_a, χ, δ_b. Figure 4.2 shows the effect of increasing the cell aggregation and scaffold affinity parameters, $\nu = \chi$, and the repulsion parameters, $\delta_a = \delta_b$, on the time-evolution of the cell phase; these choices imply that the extra pressures associated with cell-cell and cell-scaffold interactions in the functions Σ_n, ψ_{ns} are equal. Figures 4.3 and 4.4 show the effect of increasing the aggregation, scaffold affinity and repulsion parameters in isolation.

Inspection of figure 4.2 shows that as the aggregation and scaffold affinity parameters (ν, χ) are increased, the cell population forms denser, more sharply-defined aggregates with high cell density gradients at the peripheries. The opposite is true when the repulsive parameters (δ_a, δ_b) are increased. This is intuitively plausible since increases in ν and χ correspond to a cell phase which exerts greater attractive forces between adjacent cells and between the cells and scaffold, this aggregative/attachment behaviour reducing the relative importance of diffusive effects. Increases in δ_a and δ_b correspond to greater cell-cell and cell-scaffold repulsion, leading to enhanced diffusion. This effect will be discussed in more detail in §4.2.2 where we analyse a simplified model of cell behaviour.

Comparison of the effect of the parameters ν, δ_a and δ_b is shown in figures 4.3 and 4.4 in which these parameters are varied in isolation. As noted in chapter 3, inspection of

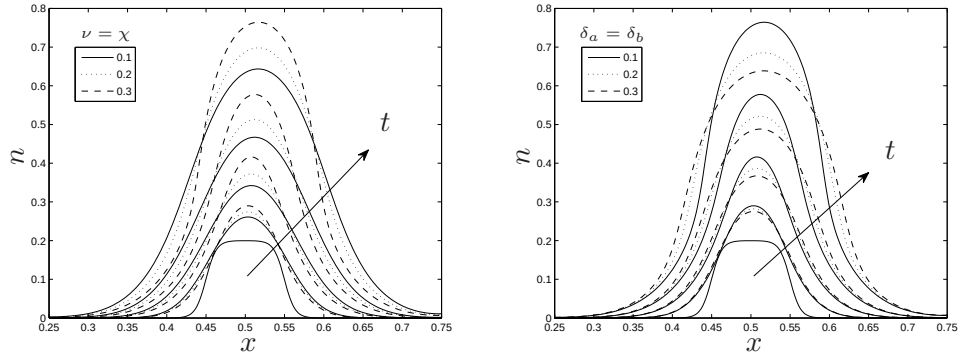

(a) (b)

Figure 4.2: The evolution of the cell volume fraction at $t = 0{-}0.25$ (in steps of $t = 0.0625$) for (a) $\nu = \chi = 0.1$–0.3 ($\delta_a = \delta_b = 0.1$); (b) $\delta_a = \delta_b = 0.1$–$0.3$ ($\nu = \chi = 0.3$), for dynamic culture (remaining parameters as given in figure 4.1).

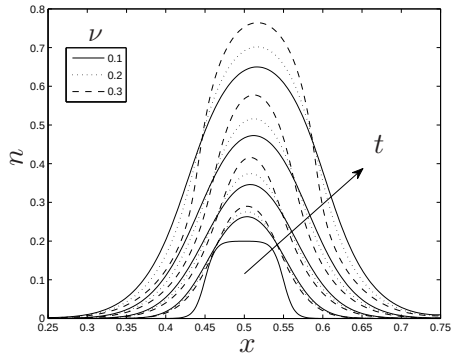

Figure 4.3: The evolution of the cell volume fraction at $t = 0{-}0.25$ (in steps of $t = 0.0625$) for $\nu = 0.1$–0.3 ($\chi = 0.3$, $\delta_a = \delta_b = 0.1$), for dynamic culture (remaining parameters as given in figure 4.1).

equations (4.1)–(4.6) indicates that the scaffold affinity parameter, χ, only enters the model in the combination $(1 - \theta)n\chi$ through the boundary conditions (4.3) and (4.4). In these simulations, n and $(1 - \theta)$ are small; we therefore anticipate that its influence on the cell behaviour is negligible and simulations in which χ is varied in isolation are not presented.

Comparison of figures 4.2a and 4.3 confirms that due to contributions from cell-scaffold affinity entering the model only through the boundary conditions, cell aggregation dominates cell-scaffold attachment. Figure 4.4 indicates that the intraphase pressure (Σ_n) generated within the cell phase due to repulsive effects dominates the interphase traction (ψ_{ns}) associated with cell-scaffold repulsion. This is due to the highly porous scaffold used in this

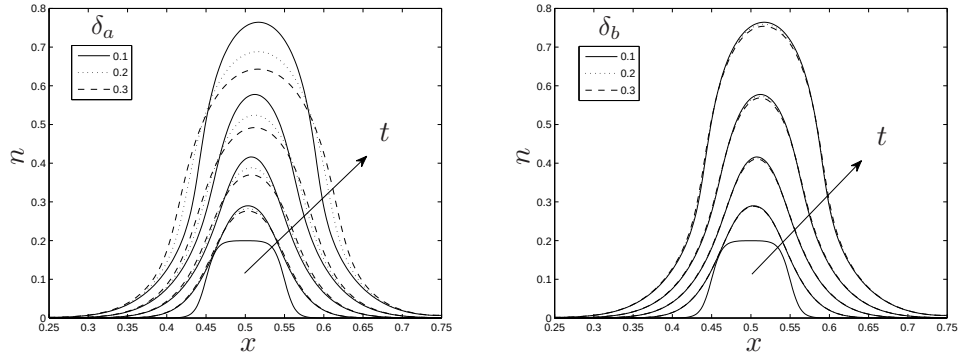

(a) (b)

Figure 4.4: The evolution of the cell volume fraction at $t = 0{-}0.25$ (in steps of $t = 0.0625$) for (a) $\delta_a = 0.1$–0.3 ($\chi = \nu = 0.3$, $\delta_b = 0.1$); (b) $\delta_b = 0.1$–0.3 ($\chi = \nu = 0.3$, $\delta_a = 0.1$), for dynamic culture (remaining parameters as given in figure 4.1).

analysis (we have chosen $\theta = 0.97$; see §1.2.3); equations (3.23) and (3.25) indicate that the influence of interphase tractions on cell movement scales linearly with the volume fraction of the scaffold phase, which is small in the highly porous scaffold.

Summary

Taking elevated values of the cell viscosity parameter to be a reflection of the preference for group locomotion over single-cell migration, the numerical simulations presented in figure 4.1 suggest that improved penetration (as indicated by the formation of a more diffuse tissue construct) throughout the scaffold will be achieved for cells whose motile behaviour is dominated by movement in coupled pairs or aggregates. Furthermore, such populations will be less sensitive to the ambient flow.

Figures 4.2–4.4 indicate the crucial importance of cell-cell and cell-scaffold interactions in a tissue engineering context; in principle, the effects predicted in this type of model could inform the manufacture of scaffolds. The parameters χ, δ_b may be viewed as a reflection of the surface chemical/topographical properties of the scaffold; ν, δ_a are characteristics inherent to the cell population in question. Inspection of the model equations shows that the influence of cell-scaffold attachment on the cells' behaviour is very small; our simulations further indicate that the cell behaviour is dominated by cell-cell interactions, with the behaviour being only weakly affected by the scaffold properties. Contributions from cell-cell and cell-scaffold interactions scale linearly with the relevant volume fractions, the dominance

of cell-cell interactions is due to the large cell density predicted in these simulations and the highly porous scaffold. For physiologically reasonable cell density values (see §1.2.3, figure 1.3 in which much lower density values are implied), alteration of the scaffold repulsion parameter is likely to be as significant as corresponding alteration in the parameters governing cell population characteristics. In this way, the aggregative/attachment behaviour can be controlled. Our model further implies that decreasing scaffold porosity will have a significant effect on the behaviour of the cells. A denser scaffold will allow scaffold properties to dominate over those associated with cells, for instance, preventing aggregation (as reported in Lemon *et al.* (2006), in which linear stability analysis was employed to demonstrate this phenomenon). This may, of course, have an adverse effect on cell penetration throughout the scaffold.

4.2.2 Analysis of a simplified model of cell behaviour

To investigate further the effect of intraphase pressure and interphase traction on cell behaviour, especially the switch between aggregative and repulsive behaviour observed in the numerical simulations presented in chapter 3 (see §3.3.1, figures 3.6–3.9), we now simplify the intraphase pressure and interphase traction functions defined by equations (4.5), replacing them with the following piecewise-constant forms:

$$\Sigma_n(n) = \begin{cases} -\nu, & n < N_\Sigma, \\ \delta_a, & n \geqslant N_\Sigma, \end{cases} \qquad \psi_{ns}(n) = \begin{cases} -\chi, & n < N_\psi, \\ \delta_b, & n \geqslant N_\psi, \end{cases} \tag{4.8}$$

where N_Σ is the threshold value at which repulsive forces between cells dominate those associated with aggregation; similarly, N_ψ is the the threshold at which the cells become repelled from the scaffold. For simplicity, in the following we will assume $N_\Sigma = N_\psi = N$. The equation governing the pressure in the culture medium may then be written:

$$\mu_n \left(\overline{\mu} n + \theta\right) \frac{\partial^2 p_w}{\partial x^2} + \mu_n \overline{\mu} \frac{\partial n}{\partial x} \frac{\partial p_w}{\partial x} \; = \; \begin{cases} \nu \, \frac{\partial^2 n}{\partial x^2}, & n < N, \\ -\delta_a \, \frac{\partial^2 n}{\partial x^2}, & n \geqslant N, \end{cases} \tag{4.9}$$

indicating that the behaviour is dominated by cell-cell interactions as found in the preceding parameter study. The equation governing the cell volume fraction is unchanged. We may further simplify equation (4.9) by assuming that the viscosities of the culture medium and cell phases are equal (so that $\mu_n = 1$ which implies $\overline{\mu} = 0$). The simulations presented in figure 4.1 indicate that the qualitative behaviour of the solutions is unchanged in this case so we may focus on this limit without restricting the general applicability of our conclusions.

Under this additional simplification, equation (4.9) reduces to:

$$\theta\frac{\partial^2 p_w}{\partial x^2} = \begin{cases} \nu\,\frac{\partial^2 n}{\partial x^2}, & n < N, \\ -\delta_a\,\frac{\partial^2 n}{\partial x^2}, & n \geqslant N. \end{cases} \tag{4.10}$$

The corresponding boundary conditions (3.29), (3.32), (3.33) are then

$$p_w\big|_{x=a} = \begin{cases} \frac{A(t)a+P_u+\alpha n(a,t)}{\theta}, & n < N \\ \frac{A(t)a+P_u-\beta n(a,t)}{\theta}, & n \geqslant N \end{cases}, \quad p_w\big|_{x=b} = \begin{cases} \frac{A(t)(b-1)+P_d+\alpha n(b,t)}{\theta}, & n < N \\ \frac{A(t)(b-1)+P_d-\beta n(b,t)}{\theta}, & n \geqslant N \end{cases}, \tag{4.11}$$

$$\left.\frac{\partial p_w}{\partial x}\right|_{x=a,b} = \frac{A(t)+12D\frac{\partial n}{\partial x}}{\theta - n}, \qquad \left.\frac{\partial n}{\partial x}\right|_{x=a,b} = \begin{cases} \frac{A(t)n}{(\theta-n)(\nu-12D)-12Dn}, & n < N \\ \frac{A(t)n}{-(\theta-n)(\delta_a+12D)-12Dn}, & n \geqslant N \end{cases}, \tag{4.12}$$

where $\alpha = \nu + (1-\theta)\chi$ and $\beta = \delta_a + (1-\theta)\delta_b$.

We proceed by decomposing the interval into three distinct regions denoted 1, 2 and 3 and the variables are labelled appropriately: region 1: $a \leqslant x < \hat{a}$ $(n < N)$; region 2: $\hat{a} \leqslant x \leqslant \hat{b}$ $(n \geqslant N)$; region 3: $\hat{b} < x \leqslant b$ $(n < N)$, where $x = \hat{a}(t), \hat{b}(t)$ denote the points at which $n = N$. This decomposition ensures that $n < N$ at the boundaries $x = a, b$ and the boundary conditions given in equations (4.11) and (4.12) for which $n \geqslant N$ are redundant. This geometry is illustrated by figure 4.5 where we have chosen $N = 0.5$. As implied by figure 4.5, we will assume that n and $\partial n/\partial x$ are continuous across these boundaries; furthermore, we assume that p_w and $\partial p_w/\partial x$ are also continuous.

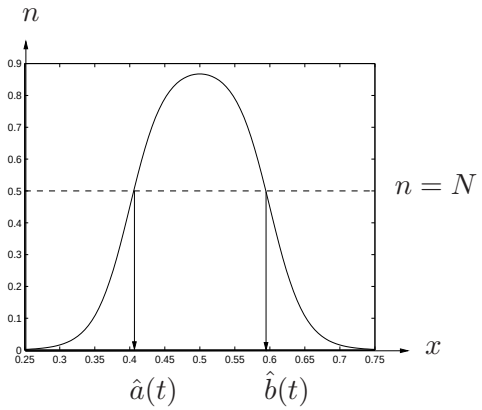

Figure 4.5: The cell distribution and the positions of the moving boundaries $x = \hat{a}(t), \hat{b}(t)$ (at which $n = N = 0.5$), used in the analysis of a simplified model of cell behaviour.

Integrating equation (4.10) twice in each region, applying the conditions (4.11), (4.12) and imposing continuity of p_w, n and $\partial p_w/\partial x$, $\partial n/\partial x$, we obtain the following solutions in

each region.

$$p_{w1}(x,t) = \frac{\nu n_1}{\theta} - \gamma(t)(x-a) + \frac{A(t)a + P_u + (1-\theta)\chi n(a,t)}{\theta}, \tag{4.13a}$$

$$p_{w2}(x,t) = -\frac{\delta_a n_2}{\theta} + \left[\frac{(\nu+\delta_a)}{\theta}\frac{\partial n_2}{\partial x}\bigg|_{x=\hat{a}} - \gamma(t)\right](x-\hat{a}) + \frac{\nu+\delta_a}{\theta}N - \gamma(t)(\hat{a}-a) + \frac{A(t)a + P_u + (1-\theta)\chi n(a,t))}{\theta}, \tag{4.13b}$$

$$p_{w3}(x,t) = \frac{\nu n_3}{\theta} + \left[\frac{\nu+\delta_a}{\theta}\left(\frac{\partial n_3}{\partial x}\bigg|_{x=\hat{a}} - \frac{\partial n_3}{\partial x}\bigg|_{x=\hat{b}}\right) - \gamma(t)\right](x-b) + \frac{A(t)(b-1) + P_d + (1-\theta)\chi n(b,t)}{\theta}. \tag{4.13c}$$

Substitution of equations (4.13) into (4.2) yields the following equations for the cell volume fraction:

$$\frac{\partial n_1}{\partial t} + \frac{1}{12}\left[\gamma(t) - \frac{\nu}{\theta}\frac{\partial n_1}{\partial x}\right]\frac{\partial n_1}{\partial x} = (k_m - k_d)n_1 + D_\nu(n_1)\frac{\partial^2 n_1}{\partial x^2}, \tag{4.14a}$$

$$\frac{\partial n_2}{\partial t} + \frac{1}{12}\left[\gamma(t) - \frac{\nu+\delta_a}{\theta}\frac{\partial n_2}{\partial x}\bigg|_{x=\hat{a}} + \frac{\delta_a}{\theta}\frac{\partial n_2}{\partial x}\right]\frac{\partial n_2}{\partial x} = (k_m - k_d)n_2 + D_{\delta_a}(n_2)\frac{\partial^2 n_2}{\partial x^2}, \tag{4.14b}$$

$$\frac{\partial n_3}{\partial t} + \frac{1}{12}\left[\gamma(t) - \frac{\nu+\delta_a}{\theta}\left(\frac{\partial n_2}{\partial x}\bigg|_{x=\hat{a}} - \frac{\partial n_3}{\partial x}\bigg|_{x=\hat{b}}\right) - \frac{\nu}{\theta}\frac{\partial n_3}{\partial x}\right]\frac{\partial n_3}{\partial x} = (k_m - k_d)n_3 + D_\nu(n_3)\frac{\partial^2 n_3}{\partial x^2}. \tag{4.14c}$$

In (4.13) and (4.14), the functions γ, D_ν, D_{δ_a} and A are defined as follows

$$\gamma(t) = \left(\frac{\nu}{\theta}\frac{\partial n_1}{\partial x} - \frac{\partial p_1}{\partial x}\right)\bigg|_{x=a}, \quad D_\nu(n) = D - \frac{(\theta-n)\nu}{12\theta}, \quad D_{\delta_a}(n) = D + \frac{(\theta-n)\delta_a}{12\theta}, \tag{4.15}$$

$$A(t) = \frac{(\nu+\delta_a)\left((\hat{a}-b)\frac{\partial n_2}{\partial x}\big|_{x=\hat{a}} - (\hat{b}-b)\frac{\partial n_3}{\partial x}\big|_{x=\hat{b}}\right) - (\Delta P - \overline{\chi}[n(a,t) - n(b,t)])}{1 + a - b + \theta(b-a)\left[\frac{1}{\theta-n} + \left(\frac{12D}{\theta-n} - \frac{\nu}{\theta}\right)\frac{n}{(\theta-n)(\nu-12D)-12Dn}\right]_{x=a}}, \tag{4.16}$$

in which $\partial p_{w1}(a,t)/\partial x$ and $\partial n_1(a,t)/\partial x$ are given by the boundary conditions (4.12) and $\Delta P = P_u - P_d$, $\overline{\chi} = (1-\theta)\chi$.

We remark that the gradients $\partial n(\hat{a},t)/\partial x$, $\partial n(\hat{b},t)/\partial x$, and the positions of the interfaces $\hat{a}(t)$, $\hat{b}(t)$, are undetermined at this stage. This system therefore requires non-trivial numerical solution, offering little benefit over numerical solution of the original equations; however, this analysis does provide some insight into the behaviour of the cells which is obscured by the complexity of the previous choice of the functions Σ_n and ψ_{ns}. The most obvious effect of the switch between the different cell behaviour represented by equations

(4.8) is in the modified diffusion coefficients, D_ν, D_{δ_a}. Since we have $\nu, \delta_a \geqslant 0$, when aggregation dominates ($n < N$), the diffusive transport of the cells is reduced; conversely, when $n \geqslant N$, repulsive effects dominate and the cellular diffusion coefficients are increased. To avoid negative diffusion, the parameter ν, which describes the importance of cell-cell aggregation, must obey $\nu < 12D$. This condition ensures that aggregative effects do not outweigh diffusion by more than one order of magnitude. A further remark is that in the absence of an imposed flow, appropriate boundary conditions are

$$p_w\big|_{x=a,b} = \frac{\nu n}{\theta}, \qquad \left.\frac{\partial p_w}{\partial x}\right|_{x=a,b} = 0, \qquad \left.\frac{\partial n}{\partial x}\right|_{x=a,b} = 0, \tag{4.17}$$

implying $\gamma(t) = 0 = A(t)$. Furthermore, we expect symmetric solutions if no flow is imposed, in which case n_1 and n_3 are governed by identical non-linear diffusion equations.

The change in diffusive behaviour across $n = N$ highlights the influence of cell-cell interactions on the diffusive behaviour of the cell phase as observed in the preceding parameter study (§4.2.1). When aggregation dominates, diffusion of the cell population is reduced by the attractive forces between cells; as a result, a dense aggregate is formed (see figures 4.2a, 4.3 and 4.4a). Conversely, when repulsive behaviour dominates, diffusion is augmented by the repulsive forces between cells and a more diffuse cell population is observed (see figures 4.2b and 4.4b).

Accurate comparison of the behaviour of this model with the numerical simulations presented in §§3.3.1 and 4.2.1 requires numerical solution of the piecewise equations (4.14); instead, we exploit the numerical scheme developed in §3.3.1, employing the following smooth approximations to the functions Σ_n and ψ_{ns}:

$$\Sigma_n(n) = \frac{\nu}{2}\left(\tanh\left[g(n-N)\right] - 1\right) + \frac{\delta_a}{2}\left(\tanh\left[g(n-N)\right] + 1\right), \tag{4.18}$$

$$\psi_{ns}(n) = \frac{\chi}{2}\left(\tanh\left[g(n-N)\right] - 1\right) + \frac{\delta_b}{2}\left(\tanh\left[g(n-N)\right] + 1\right), \tag{4.19}$$

where g is a parameter which determines the steepness of the gradient between the limiting values $\Sigma_n = -\nu, \delta_a$ and $\psi_{ns} = -\chi, \delta_b$ and the larger the value of g, the closer the approximation to the step function analysis given above (this approximation is necessary since the use of the step functions given by (4.8) causes the numerical scheme to fail). Figure 4.6 shows a plot of these functions illustrating the effect of increasing g; the arrow shows the direction of increasing g. The parameter values are chosen to be $N = 0.5$ and $\nu = \chi = 0.2$, $\delta_a = \delta_b = 0.1$ so the behaviour of the functions is identical, *i.e.* $\Sigma_n(n) = \psi_{ns}(n)$. In a tissue engineering context, this choice implies that the interactive forces between adjacent cells and between the cells and scaffold are equal.

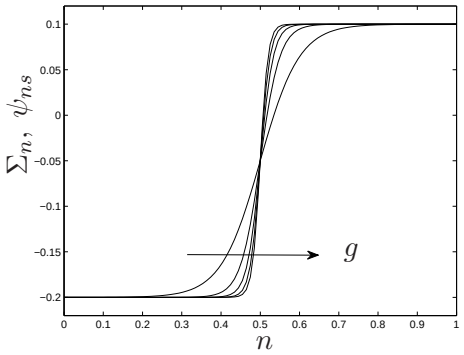

Figure 4.6: The behaviour of the smooth approximations (4.18) and (4.19) to the simplified functions Σ_n and ψ_{ns} given by (4.8). Parameter values: $N = 0.5$, $\nu = \chi = 0.2$, $\delta_a = \delta_b = 0.1$, $g = 10, 20, 30, 40, 50$.

Approximate solutions are obtained by solving equations (4.1) and (4.2) subject to (4.3), (4.4) and (4.6) in the same manner as described in §3.3.1. We note here that the values of the diffusion coefficient (D) and the aggregation parameter (ν) are modified from those given in previous chapters to ensure that the condition $\nu < 12D$ is not violated; the values of the parameters δ_a, δ_b are the same as those used in chapter 3 (we choose $D = 0.02$, $\nu = \chi = 0.2$, $\delta_a = \delta_b = 0.1$, $\mu_n = 1$). Figure 4.7 illustrates how the approximation to the numerical solution of equations (4.14) evolves over time; figure 4.8 depicts the evolution of the corresponding culture medium and cell pressures and figure 4.9 shows two illustrative plots of the cell phase velocity at the channel centreline, highlighting the change from aggregative to repulsive behaviour.

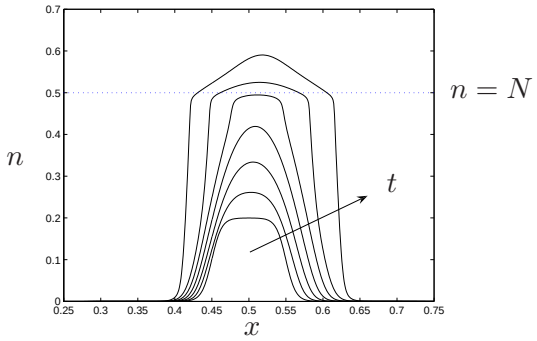

Figure 4.7: The evolution of the cell volume fraction at $t = 0 - 0.18$ (in steps of $t = 0.03$), obtained using simplified intraphase pressure and interphase traction functions. Parameter values: $P_u = 1$, $P_d = 0.1$, $k_m = 7.5$, $k_d = 0.1$, $D = 0.02$, $\nu = \chi = 0.2$, $\delta_a = \delta_b = 0.1$, $\theta = 0.97$, $g = 80$, $N = 0.5$.

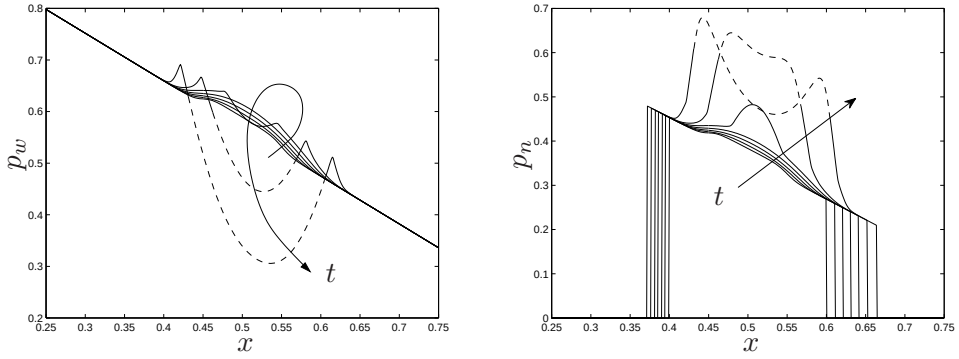

(a) (b)

Figure 4.8: Evolution of (a) the culture medium pressure, and (b) the cell pressure, with simplified intraphase pressure and interphase traction functions $t = 0 - 0.18$ (in steps of $t = 0.03$). Parameter values as in figure 4.7. $n < N$, (–); $n \geqslant N$, (- -).

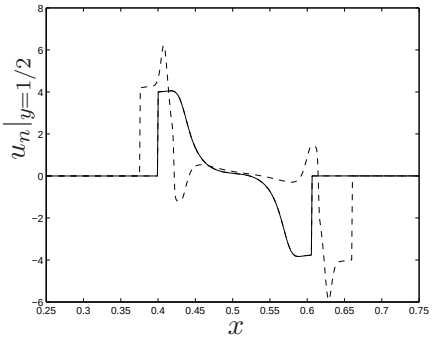

Figure 4.9: An illustrative plot of the cell phase velocity at the channel centreline corresponding to figure 4.7 at $t = 0.06$, $n < N$ (–), and $t = 0.18$, $n_{max} > N$ (- -). Parameter values as in figure 4.7.

Figure 4.7 illustrates the modified diffusion feature of equations (4.14) discussed above. For early times, when $n < N$, aggregation dominates and diffusion is inhibited. When n crosses the threshold value $n = N$, diffusive effects increase due to the dominance of repulsive forces and the cell population spreads, leading to a dramatic increase in the width of the aggregate. We remark that aggregation still dominates at the scaffold periphery, resulting in a "sharply-defined" aggregate with high gradients in density at the up- and downstream peripheries. As the cell density continues to increase, a clear peak forms at the centre of the aggregate (see the last line on figure 4.7, corresponding to $t = 0.18$).

The pressures of each phase, illustrated in figure 4.8, are consistent with the change

from aggregation-dominated to repulsion-dominated behaviour shown in §3.3.1 (figures 3.6, 3.7). We now discuss their behaviour in turn. The culture medium pressure is in good qualitative agreement with that shown in figure 3.6: an initial increase in p_w is observed as fluid is ejected from the construct region due to aggregation; as the density increases, and repulsive cell behaviour dominates, p_w falls, corresponding to an influx of fluid. The cell phase pressure (given by $p_n = p_w + \Sigma_n + (1-\theta)\psi_{ns}$) exhibits corresponding behaviour: for low cell phase density, p_n is given by $p_n \approx p_w - \nu - (1-\theta)\chi$, corresponding to aggregation and attachment; in regions of higher density, repulsive contributions from Σ_n and ψ_{ns} dominate and an increase is observed: $p_n \approx p_w + \delta_a + (1-\theta)\delta_b$. However, comparison of figures 3.7 and 4.8b shows a marked difference in the form of p_n. This is due to the simplified form of Σ_n and ψ_{ns} employed here (equations (4.18) and (4.19)) in contrast to that employed in chapter 3 (equations (4.5)). As discussed above, for $n < N$, aggregative behaviour dominates, leading to a reduction in p_n relative to p_w; however, since the magnitudes of the (smoothed) simplified versions of Σ_n and ψ_{ns} decrease with n (for $n \lesssim N$), the reduction in p_n is minimal in the centre of the construct, where the cell density is highest, leading to the "bump" in p_n. In contrast, the magnitude of the more complex form (4.5) for Σ_n (in the aggregation-dominated regime) increases with n, leading to the opposite behaviour (see figures 3.7a and 4.8b). We emphasise, however, that since the cell phase velocity is not driven by $\partial p_n/\partial x$ (the driving pressure gradient is a combination of the culture medium pressure gradient and contributions from cell-cell and cell-scaffold interaction terms; see equation (3.25)), this does not correspond to cell efflux. The cell phase velocity will be discussed in more detail below. As n increases, exceeding the threshold $n = N$, repulsive behaviour causes an increase in p_n. The "dip" witnessed here (again, the opposite of the behaviour shown in 3.7b) is due to the simplified extra pressures, which have achieved their maximal (constant) values ($\Sigma = \delta_a$, $\psi_{ns} = \delta_b$), competing with p_w which (for $n > N$) achieves a minimum where the cell phase is most dense (see the dashed lines in figure 4.8).

We remark also that the switch in diffusive behaviour may be observed prior to the threshold $n = N$ in figures 4.7 and 4.8 due to the approximation (4.18) and (4.19) to the step functions (4.8). In figure 4.8a this effect is indicated by the third-to-last line which shows that the decrease in culture medium pressure occurs prior to the threshold $n = N$. This effect may be reduced by increasing the parameter, g; however, this increases the difficulty of numerical solution.

The cell phase behaviour illustrated in figure 4.7 is most clearly illustrated by considering the behaviour of the corresponding cell velocity shown in figure 4.9. At low cell

density, the cells aggregate, moving into the centre of the construct, as evidenced by the positive velocity at the upstream periphery and negative velocity downstream. The dashed line in figure 4.9 shows that when the cell density crosses the threshold $n = N$, repulsion causes this flow to reverse; aggregation is still evident at the construct edge in areas of low density. Additionally, as remarked above, the negative velocity gradient at the centre of the construct corresponds to aggregation here, leading to the formation of a peak in cell density. This behaviour corresponds to the large variation in cell phase pressure observed at later times (see figure 4.8b).

Lastly, we note that the cell phase velocity is calculated using equations (3.23) and (3.25), employing the simplified intraphase pressure and interphase traction functions (4.18) and (4.19). In view of these simplified functional forms, the cell velocity at the channel centreline for $n < N$ is given by

$$u_n \approx -\frac{1}{8\mu_n}\left(\frac{\partial p_w}{\partial x} - \frac{\nu}{n}\frac{\partial n}{\partial x}\right), \tag{4.20}$$

so that for small n, (*i.e.* at the construct periphery) the second term dominates and cells tend to move up gradients of cell density.

4.3 Mechanotransduction

We now extend the model derived in chapter 3, to include a simple mechanotransduction mechanism which regulates the cells' proliferative response. In a similar manner to that presented in chapter 2, we couple the growth of the cell population to the following stimuli: contact inhibition caused by cell-cell interactions, the effect of stress caused by increases in local cell density and the influence of the external fluid dynamics. The first two stimuli are not considered explicitly in this formulation; however, we consider that the gross effect of such mechanisms is captured in the functional forms specified below. The motivation for including such stimuli in a model of mechanotransduction-affected tissue growth has been outlined in chapter 2 so we do not discuss it in detail here.

The relevance of our modelling framework hinges on the appropriate choice of the mass transfer term for the cell phase, S_n; we pause here to highlight an important restriction on its form in this three-phase model. In order to utilise the numerical scheme developed in §3.3.1 with minimal modifications, we note that equation (4.2) is derived by taking the average (in the transverse direction) of the conservation of mass equation for the culture medium phase in the long-wavelength approximation (see §1.5 and chapter 3 for more details). The

averaged mass transfer term is therefore $S_n = S_n(x,t)$; consequently, explicit coupling between the shear stress induced by the culture medium (which is dependent on y) and the cell growth response is prohibited. The *gross effect* of this coupling may still be incorporated into the cell response by noting that the averaged flow-induced shear stress experienced by the cells is proportional to the culture medium velocity. In view of equations (3.22)–(3.24), we therefore model the shear stress as being proportional to the gradient of the culture medium pressure. The "intraphase" shear stress produced by the movement of the cells themselves may be modelled in a similar way; however, we consider that, physiologically, the shear stress induced by the cell movement will be negligible in comparison to the flow-induced shear and this effect is neglected from the model. Further coupling between cell proliferation and the cells' mechanical environment may be achieved by incorporating the effect on the cells' behaviour of the pressure of the surrounding culture medium, the pressure in the cell phase and the local cell density. In the following, we therefore restrict attention to a cell growth rate of the following form:

$$S_n = S_n\left(n, p_w, p_n, \frac{\partial p_w}{\partial x}\right), \tag{4.21}$$

and for clarity, we consider the effect of each of these stimuli on the growth of the cell population in isolation. When adapting the numerical scheme developed in §3.3.1, we must evaluate the source term S_{nj}^k at each mesh point, j, and time-step, k and include this appropriately in the semi-implicit Crank-Nicholson scheme represented by equations (3.36) and (3.37).

4.3.1 Cell density dependence: $S_n = S_n(n)$

We employ the same modelling techniques used in chapter 2, identifying three distinct phases in the behaviour of the cell population: (i) a proliferative phase, $S_n = k_{1n}n$; (ii) an ECM-producing phase, $S_n = k_{2n}n$; and (iii) an apoptotic phase, $S_n = -k_d n$. These phases represent the effects of contact inhibition and residual stresses caused by growth on the phenotypic progression of cells. As discussed in chapter 2, contact inhibition and high stress levels inhibit cell division, whilst a moderate level of stress appears to enhance tissue growth (Roose *et al.*, 2003; Chaplain *et al.*, 2006). We therefore choose $k_{2n} > k_{1n}$ so that the rate of cell phase growth is increased during the ECM-production phase. For simplicity, we assume that the rates of growth and death (k_{1n}, k_{2n}, k_d) are constant. The threshold cell densities that separate these three types of behaviour are denoted n_1' and n_2'.

We employ step functions to represent this behaviour; the net rate of growth and death

of the cell phase, denoted $\kappa(n)$, is illustrated by figure 4.10 and is related to S_n as follows:

$$S_n(n) = \left[k_{1n}\mathrm{H}(n_1' - n) + k_{2n}\mathrm{H}(n - n_1') - (k_{2n} + k_d)\,\mathrm{H}(n - n_2')\right] n = \kappa(n) n, \tag{4.22}$$

where $H(n)$ is the Heaviside step function. We note that we may employ a step function for the switch between each growth phase since, in contrast to the two-fluid model, we are not required to evaluate gradients of S_n (see equations (4.1), (4.2) and (2.24)–(2.26)). To clarify, within our numerical scheme, we choose $\kappa(n) = k_{2n}$ at the threshold values $n = n_1'$,n_2'.

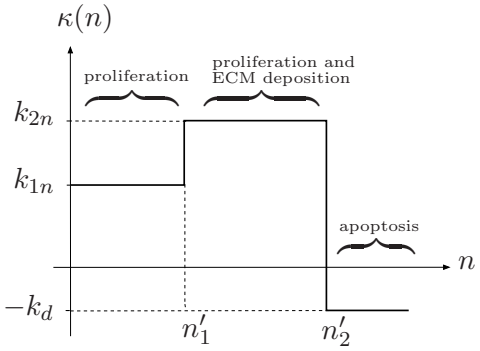

Figure 4.10: Schematic representation of the progression of the cells from a proliferative phase to an apoptotic phase, via an extracellular matrix-producing phase in response to the local cell density.

Figure 4.11a shows the effect of this modified mass transfer term on the evolution of the cell phase for dynamic culture, and the regions in which each of the different growth responses are exhibited. The corresponding culture medium and cell phase pressures are shown in figures 4.11b and 4.12. The evolution of the velocity of each phase at the channel centreline is shown in figure 4.13; for clarity, only the velocities where n has reached the threshold value $n = n_2'$ are shown. We emphasise that in the following simulations the parameter choices are not physiologically motivated, being chosen to best illustrate the behaviour of the model under such a growth regime.

Figure 4.11a shows that the choice of mass transfer term arrests the growth of the cell phase at the threshold cell density, n_2', due to the progression from the proliferative to the apoptotic phase. We note that, as in chapter 2, despite the presence of apoptosis in our model, re-entry into the proliferative phase ensures that, once attained, the density of the cell phase does not fall below $n = n_2'$. Figures 4.11b, 4.12 and 4.13 indicate that due to the cell phase being prevented from achieving high densities, the pressure and velocity of each phase exhibit qualitatively similar behaviour to that shown in figures 3.6a, 3.7a, 3.8a and 3.9a. Since excessive cell proliferation is prevented, the repulsive terms in the intraphase pressure and interphase traction functions are unable to dominate and the cells aggregate

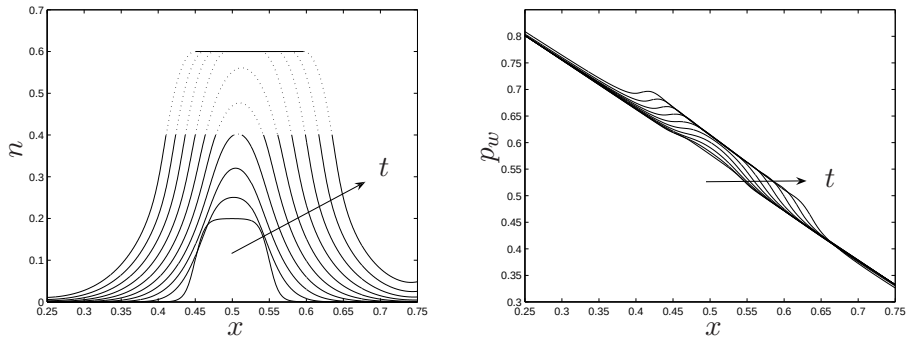

(a) (b)

Figure 4.11: The evolution of (a) the cell volume fraction, $n < n_1'$ and $n > n_2'$, (–); $n_1' \leqslant n \leqslant n_2'$, $(\cdots)$, and (b) the pressure of the culture medium, at $t = 0 - 0.35$ (in steps of $t \approx 0.038$) for growth behaviour defined by (4.22) and dynamic culture: $P_u = 1$, $P_d = 0.1$, $k_{1n} = 6.5$, $k_{2n} = 7.5$, $k_d = 1$, $D = 0.01$, $\theta = 0.97$, $n_1' = 0.4$, $n_2' = 0.6$.

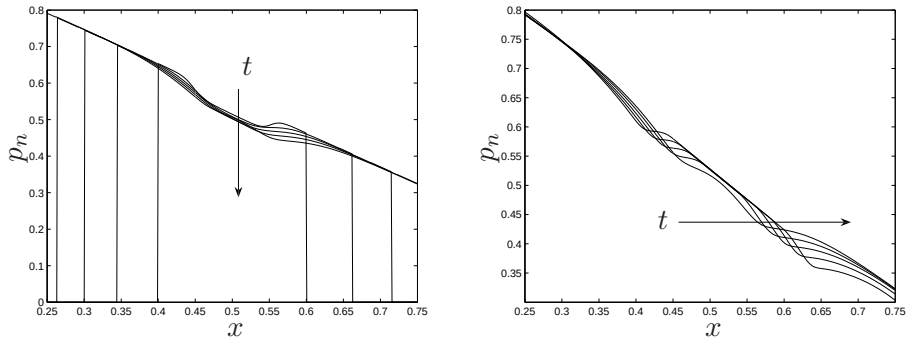

(a) (b)

Figure 4.12: The evolution of the pressure of the cell phase for (a) early times (small n: $t = 0 - 0.15$, in steps of $t = 0.0375$), and (b) longer times (larger n: $t = 0.2 - 0.35$ in steps of $t = 0.05$), for growth behaviour defined by (4.22) and dynamic culture. Parameter values as per figure 4.11.

to a form a dense population, which is advected under the imposed flow. As remarked in chapter 3, figure 3.9b shows that advection is reduced by cell aggregation.

Due to this curtailed cell phase growth, the dramatic increase in cell phase pressure due to cell-cell repulsion observed in chapter 3 is prevented (see figures 3.7b and 4.12b). Similarly, the dramatic flow reversal observed in figures 3.8b and 3.9b does not occur (limited upstream flow of culture medium due to cell aggregation is observed at the upstream

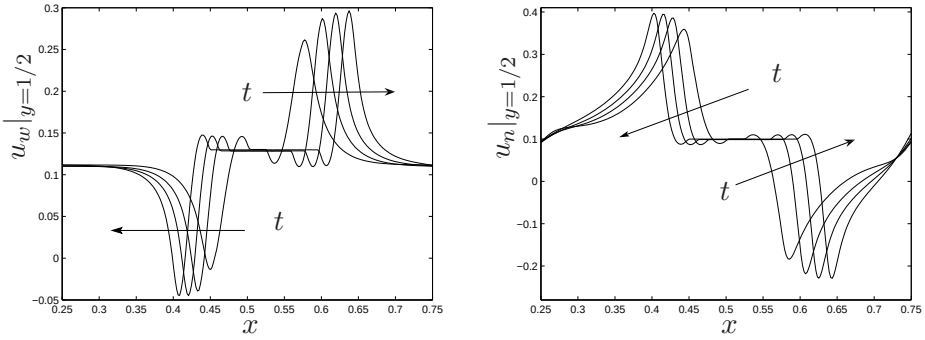

(a) (b)

Figure 4.13: The evolution of (a) the velocity profile of the culture medium, (b) the velocity profile of the cell phase (at the channel centreline), at $t = 0.2 - 0.35$ (in steps of $t = 0.05$) for growth behaviour defined by (4.22) and dynamic culture. Parameter values as per figure 4.11.

periphery of the construct as in figure 3.9a); rather, the flow attains a constant value in the region where $n = n_2'$. This is indicated by the presence of flat lines in the central regions of figures 4.13a and 4.13b (*cf.* the cell density profiles shown in figure 4.11a).

4.3.2 Cell density dependence: $S_n = S_n(n, p_n)$

An alternative way to model the tendency of cells to adapt their behaviour in response to their local density is to consider the pressure of the cell phase as an indicator of cell density; *i.e.* $S_n(n, p_n)$. Since p_n is intimately connected to the pressure of the culture medium, this choice has the added advantage of including the response of cells to the local fluid dynamics. We therefore modify the mass transfer term for the cell phase, S_n to investigate the effect that this mechanism has on the evolution of the tissue construct and to demonstrate the versatility of our model.

As discussed in §2.4.2, a number of studies have shown improved bone formation as a result of stimulation by culture medium pressure (Haskin *et al.*, 1993; Klein-Nulend *et al.*, 1995a; Owan *et al.*, 1997). We represent the cells' pressure-dependent response in a similar manner to that outlined in chapter 2 and assume that at intermediate pressures, the cells exhibit enhanced proliferation and ECM deposition; at low pressures, the cells enter a state of relative quiescence in which proliferation and ECM deposition are greatly reduced; at high pressures, the cells enter apoptosis. Introducing threshold cell pressures at which the cell proliferation is heightened (p_{n1}') and the apoptotic phase is entered (p_{n2}'), we represent

the mass transfer term with step functions, as defined below and illustrated by figure 4.14:

$$S_n(n, p_n) = \left[k_{1p}\mathrm{H}(p'_{n1} - p_n) + k_{2p}\mathrm{H}(p_n - p'_{n1}) - (k_{2p} + k_d)\,\mathrm{H}(p_n - p'_{n2})\right] n = \kappa(p_n) n. \quad (4.23)$$

For clarity, we remark that within our numerical scheme, we choose $\kappa(p_n) = k_{2p}$ at $p_n = p'_{n1}, p'_{n2}$.

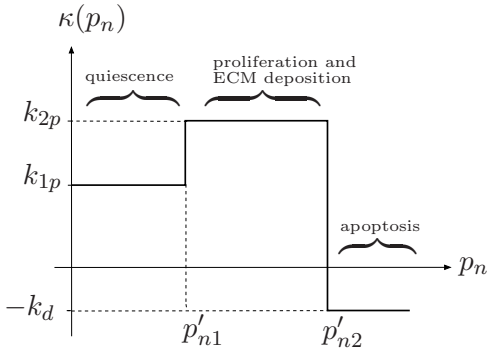

Figure 4.14: Schematic representation of the progression of the cells from a (relatively) quiescent phase to an apoptotic phase, via a proliferative phase in response to the pressure of the cell phase, p_n.

Figure 4.15 shows the effect of the cell pressure-dependent mass transfer term on the growth of the cell phase for dynamic culture. Also shown are the regions in which each of the different growth phases occur; the evolution of the culture medium pressure is shown in figure 4.16 and the pressure of the cell phase (together with the threshold values p'_{n1}, p'_{n2}) is shown in figure 4.17. As in chapter 3, the pressure of the culture medium is plotted separately for $n \leqslant 0.6$, $n_{max} \geqslant 0.7$ to best illustrate the transition behaviour of the solution; similarly, the pressure of the cell phase is plotted for $n \leqslant 0.5$, $n_{max} \geqslant 0.6$. Figure 4.18 shows the predicted tissue construct obtained in static culture conditions.

Comparison of figures 4.11a and 4.15 demonstrates the effect of the chosen form of pressure-dependent mass transfer term on the growth of the cell phase: rather than simply being arrested at a threshold density, the growth of the cell phase is skewed towards the downstream boundary $x = b$. This is due to the interplay between the imposed pressure, p_w, (which dominates the cell pressure, $p_n = p_w + \Sigma_n + (1 - \theta)\psi_{ns}$ when n is small) and the repulsive intraphase pressure and interphase traction contributions (which cause a dramatic increase in cell pressure when n becomes larger; see equation (4.5)). Growth of the cell phase near $x = a$ is inhibited because the culture medium pressure is high there ($\kappa(p_n) = -k_d$); near $x = b$, growth is reduced ($\kappa(p_n) = k_{1p} < k_{2p}$); and between these two regions, enhanced growth is initially observed until the cell pressure increases above the threshold p'_{n2}. Comparison between figures 3.7 and 4.17 shows that the cell pressure is not

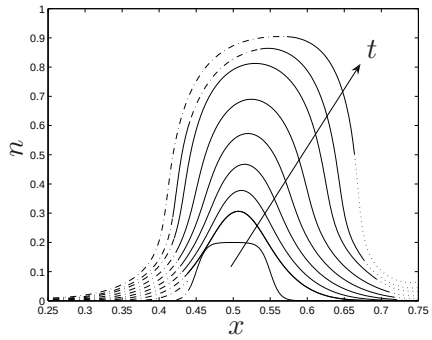

Figure 4.15: The evolution of the cell volume fraction at $t = 0 - 0.3$ (in steps of $t = 0.0375$), $p_n > p'_{n2}$, (-.-); $p'_{n1} \leqslant p_n \leqslant p'_{n2}$, (–); $p_n < p'_{n1}$, $(\cdots)$, for growth behaviour defined by (4.23) and dynamic culture: $P_u = 1$, $P_d = 0.1$, $k_{1p} = 4$, $k_{2p} = 7.5$, $k_d = 2$, $D = 0.01$, $\theta = 0.97$, $p'_{n1} = 0.35$, $p'_{n2} = 0.6$.

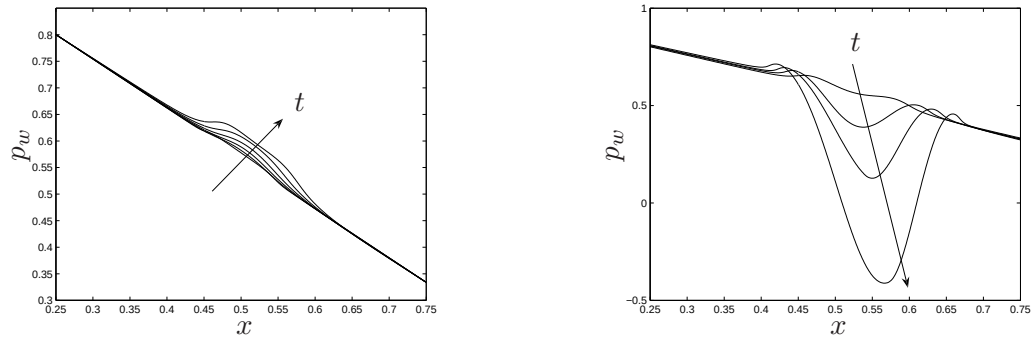

(a) (b)

Figure 4.16: The evolution of the pressure of the culture medium for (a) early times (small n): $t = 0 - 0.2$ (in steps of $t = 0.04$), (b) longer times (larger n): $t = 0.15 - 0.35$ (in steps of $t = 0.05$), for growth behaviour defined by (4.23) and dynamic culture. Parameter values as per figure 4.15.

dramatically affected by this changed cell distribution; similarly, figures 3.6 and 4.16 show that the culture medium pressure is qualitatively similar to that found previously. The velocities of each phase are therefore not given here since they will be qualitatively similar to those found in §3.3.1.

Figure 4.18 shows the predicted construct morphology obtained in static culture conditions ($P_u = 0 = P_d$). Comparison with figure 4.11a (which depicts the construct morphology resulting from density-regulated growth in dynamic culture conditions) shows that, as remarked in the simpler two-fluid model, in the absence of perfusion, pressure-regulated

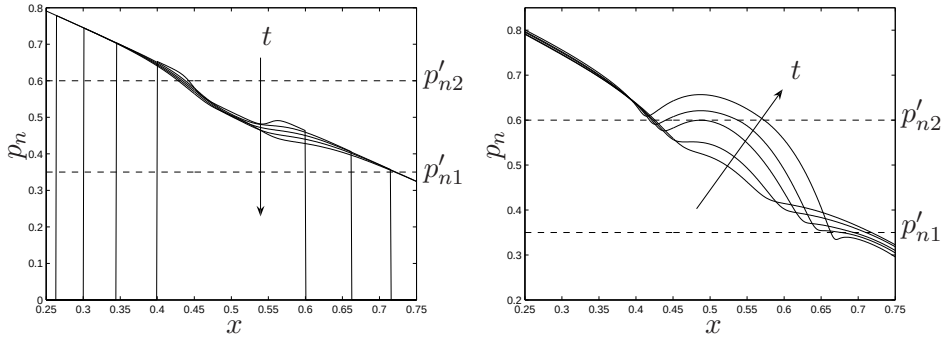

(a) (b)

Figure 4.17: The evolution of the pressure of the cell phase for (a) early times (small n): $t = 0-0.15$ (in steps of $t = 0.0375$), (b) longer times (larger n): $t = 0.2-0.35$ (in steps of $t = 0.05$), for growth behaviour defined by (4.23) and dynamic culture. Parameter values as per figure 4.15.

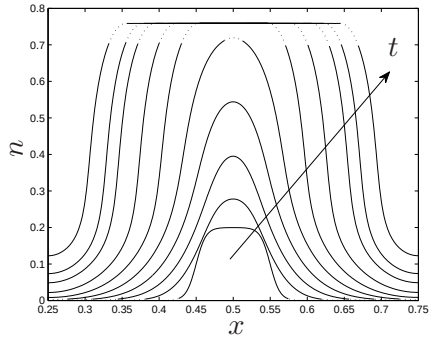

Figure 4.18: The evolution of the cell volume fraction at $t = 0-0.3$ (in steps of $t = 0.033$), $p_n < p'_{n1}$, $p_n > p'_{n2}$, (-); $p'_{n1} \leqslant p_n \leqslant p'_{n2}$, $(\cdots)$, for growth behaviour defined by (4.23) and static culture: $P_u = 0 = P_d$, $k_{1p} = 7.5$, $k_{2p} = 9$, $p_{n1} = 0$, $p'_{n2} = 0.01$, other parameters as in figure 4.15.

growth results in a construct which is almost indistinguishable from that obtained in the density-regulated growth regime. In this three phase model, in which cell growth is permitted at the scaffold edge ($x = a, b$), the only differentiating factor between cell density-regulated (dynamic culture) and pressure-regulated (static culture) growth is the asymmetry introduced by the imposed flow in the former case. Removal of the imposed flow results in indistinguishable constructs (results omitted).

In chapter 2, the similarity of the constructs produced in each case was a consequence of the simplified model in which the pressure was directly proportional to the cell distri-

bution in the absence of a flow (see equation (2.47)). In this three phase model, where the relationship between the cell phase distribution and its pressure is more complex, the net result is the same; however, the mechanism is different. In static culture, dominance of the aggregation and scaffold affinity parameters at low cell density ensures that $p_n < 0$ and tissue growth is determined by the reduced growth rate, $\kappa(p_n) = k_{1p}$; as the density increases, the repulsive terms become important, causing an increase in cell phase pressure until p_n exceeds the upper threshold and the cells enter an apoptotic phase, preventing the cell density from further increase. Cells near the periphery of the aggregate (where the density and associated cell pressure are lower) proliferate at a rate k_{1p} or k_{2p} depending upon the value of p_n (cells proliferating at $\kappa(p_n) = k_{2p}$ are indicated by the dotted line in figure 4.18). Eventually, these cells achieve sufficiently high density to cause the pressure to exceed the upper threshold, resulting in curtailed growth. In this way, a construct whose density is approximately uniform is attained. The higher cell density attained under static culture (figure 4.18) is due to the thresholds p'_{n1}, p'_{n2} chosen.

The effect of culture medium pressure on the growth response of the tissue construct is embodied within the above choice of mass transfer term, S_n. We therefore do not present the results for the case $S_n = S_n(n, p_w)$ since these will exhibit similar behaviour to those given above and reflect similar modelling considerations.

4.3.3 Shear stress dependence: $S_n = S_n(n, \left|\partial p_w/\partial x\right|)$

We now consider the effect of coupling the growth of the cell phase to the shear stress induced by the external fluid dynamics; *i.e.* $S_n(n, \left|\partial p_w/\partial x\right|)$. The motivation for such a mass transfer term is strong: as discussed in §1.2.2, a great many studies (see Klein-Nulend *et al.* (1998, 1995b), You *et al.* (2000), Bakker *et al.* (2004), Han *et al.* (2004) and others) have reported that bone cells are highly sensitive to stimulation via fluid flow-induced shear stress. We therefore employ the same simplistic modelling techniques as previously, and assume that in the presence of an intermediate level of shear stress, the rates of proliferation and ECM deposition are heightened; for low shear stress, the proliferation and ECM deposition rates are reduced; and for excessively high shear stresses the cells become damaged and enter a necrotic phase. In this case, however, we find that to ensure stability of the numerical scheme, we must employ a smoothed version of the functional form for the mass transfer term, $S_n(n, \left|\partial p_w/\partial x\right|)$. The reason for this is unclear. This function is defined as follows,

and depicted in figure 4.19:

$$S_n\left(n, \left|\frac{\partial p_w}{\partial x}\right|\right) = \left\{-\frac{\overline{k}_m - k_m}{2}\left(\tanh\left[g\left(\left|\frac{\partial p_w}{\partial x}\right| - P_1'\right)\right] - 1\right) - \frac{k_m + k_d}{2}\left(\tanh\left[g\left(\left|\frac{\partial p_w}{\partial x}\right| - P_2'\right)\right] - 1\right) - k_d\right\} n$$
$$= \kappa\left(\left|\frac{\partial p_w}{\partial x}\right|\right) n. \tag{4.24}$$

In (4.24), the threshold values at which the rate of cell proliferation and ECM deposition are heightened and the necrotic phase is entered are denoted P_1' and P_2' respectively and the parameter, g, determines the closeness of the approximation to the step-function behaviour used previously. To avoid confusion with the previous notation (k_{1p}, k_{2p}), we employ growth rates k_m, $\overline{k}_m$ here ($k_m > \overline{k}_m$). Figure 4.20 illustrates the effect of the shear stress-dependent mass transfer term, $S_n(n, \left|\partial p_w/\partial x\right|)$ on the growth of the cell phase and highlights the regions in which each of the different growth phases occur. Figure 4.21 shows the corresponding culture medium pressure gradient (which is proportional to the average flow-induced shear stress) together with the threshold values; the pressure gradient is plotted separately for $n \leqslant 0.58$ and $n_{max} \geqslant 0.64$ to more clearly illustrate the behaviour as the cell volume fraction, n, increases.

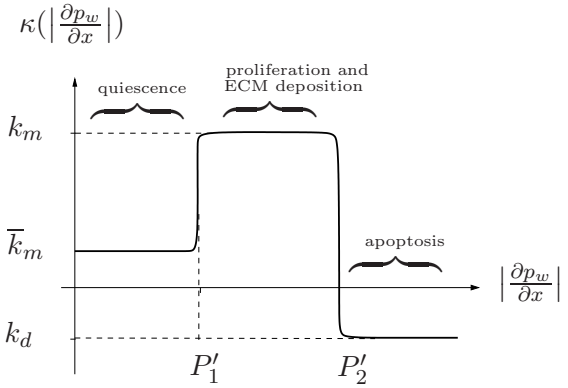

Figure 4.19: Schematic representation of the progression of the cells from a (relatively) quiescent phase to a necrotic phase via an proliferative phase in response to the level of flow-induced shear stress.

Inspection of figures 4.20 and 4.21 shows how the cell phase is affected by shear-dependent mass transfer. When the cell population is relatively small, disturbance to the culture medium flow is small and the shear remains within the proliferative region: $P_1' \leqslant \left|\partial p_w/\partial x\right| \leqslant P_2'$. As the cell population increases, the increased construct density causes a reduction in u_w near the upstream periphery, and an increase downstream (*cf.* figures 3.9a and 4.21a), causing the upstream shear to fall below the P_1' threshold and resulting

in decreased proliferation there. A further increase in the cell population causes the flow disturbance to increase (see figure 3.9b) resulting in flow reversals at a number of points within the domain. This causes the shear to increase to the P_2' threshold and to cross the P_1' threshold repeatedly (see figure 4.21b), resulting in cell death and reduced cell growth at various regions within the cell population. Inspection of figure 4.21b shows that the influence of fluid shear stress on cell phase growth is clearest at late times. The high level of shear near the construct centre and reduced shear near the upstream periphery cause cell phase growth to be skewed in the downstream direction (see the last line in figure 4.20).

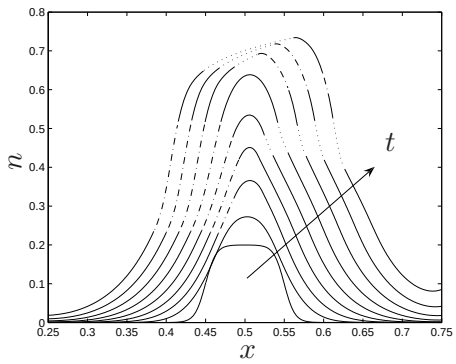

Figure 4.20: The evolution of the cell volume fraction, $|p_{wx}| < P_1'$, (-.-); $P_1' \leqslant |p_{wx}| \leqslant P_2'$, (–); $|p_{wx}| > P_2'$, $(\cdots)$, at $t = 0 - 0.4$ (in steps of $t = 0.05$) for growth behaviour defined by (4.24) and dynamic culture: $P_u = 1$, $P_d = 0.1$, $k_m = 7.5$, $\overline{k}_m = 4$, $k_d = 2$, $D = 0.01$, $\theta = 0.97$, $P_1' = 0.5$, $P_2' = 1.5$, $g = 60$.

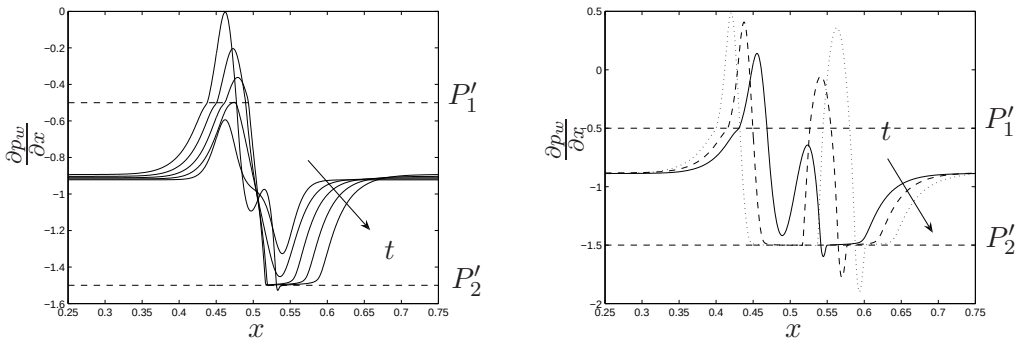

(a) (b)

Figure 4.21: The evolution of the pressure gradient of the culture medium for (a) early times (small n: $t = 0.02 - 0.22$ in steps of $t = 0.05$), (b) longer times (larger n: $t = 0.25, 0.3.0.35$), for growth behaviour defined by (4.24) and dynamic culture. Parameter values as per figure 4.20.

4.3.4 Mechanotransduction: summary

In the preceding sections (§§4.3.1–4.3.3), we have investigated the response of the cell phase to three different mechanotransduction mechanisms. To model the effect of contact-inhibition and the stress induced by tissue growth on the proliferative response, we considered first the response to local cell density, employing a simple step function form for the mass transfer term, $S_n(n)$, representing the progression from a proliferative to an apoptotic phase via an ECM-producing phase. Similar forms were employed for pressure-dependent and flow-induced shear stress-dependent responses, modelling elevated proliferation in the presence of an intermediate level of culture medium pressure or flow-induced shear stress.

The morphology of the resulting tissue construct is highly sensitive to these choices: in the density-dependent case, apoptosis prevents the cell population exceeding the threshold density, leading to a tissue construct with a sparse periphery and a uniformly dense core (see figure 4.11a). In comparison, under the pressure-dependent growth regime and dynamic culture conditions, a construct is created which bears far more resemblance to that obtained for constant rates of mitosis and death. In this case, the effect of coupling cell proliferation to the pressure is to cause the cell phase to grow preferentially in a downstream direction due to excessive upstream pressure (see figures 3.5 and 4.15). Under static culture conditions, our numerical simulations suggest that pressure-dependent tissue growth results in a construct that is almost indistinguishable from that obtained under density-regulated growth (*cf.* figures 4.11 and 4.18), the distinguishing factor being the symmetrical construct predicted under static conditions. Lastly, shear stress-dependent growth has a profound effect on the composition of the tissue construct; due to the variations in shear stress (viewed as proportional to the gradient of the culture medium pressure), the tissue construct is highly heterogeneous, with sharp variations between regions of cell apoptosis and growth (see figure 4.20).

4.4 Relevance to tissue engineering

We now pause to explain how the above work may provide insight into *in vitro* tissue engineering processes. Using numerical solution of the simplified model equations, we have demonstrated a plausible gross response of the cell population under various parameter regimes associated with the cells' interaction with their environment and under the influence of a number of growth stimuli.

The results and analysis presented in §4.2.2 (and §3.3.1) illustrate the profound effect

that changes in the aggregative and repulsive properties of the cell/scaffold system have upon the dynamics of the tissue construct. In our simple model, the parameters controlling the tendency of cells to aggregate or repel each other (ν, δ_a) are dependent upon the characteristics of the cell culture in question; the affinity the cell population feels for the scaffold (controlled by the parameters χ, δ_b) may be controlled by altering the topography or surface chemistry of the scaffold. The results of this model may therefore be employed by tissue engineers to predict how changes in the properties of the cell/scaffold system may affect the characteristics of the resulting tissue construct. Our model indicates that decreasing the porosity of the scaffold allows better control of cell behaviour, such as cell aggregation or attachment.

The versatile multiphase model employed in this analysis allows the influence on the cells' proliferative response of a wide variety of stimuli to be studied. To illustrate this, we have considered the response to three different stimuli; in each case, we assumed a simple functional dependence of the cells' response on the model variables relevant to bone tissue engineering applications (specifically, the local cell density, pressure and flow-induced shear stress). As noted in chapter 2, the difference in the tissue construct morphology predicted by our model under the influence of each of the mechanotransduction mechanisms studied in dynamic and static culture, provides a simple means for the identification of the dominant regulatory growth mechanism in a cell culture.

We consider that this simplified three phase model represents a realistic model of tissue growth within a dynamic fluid environment relevant to *in vitro* tissue engineering applications. Given appropriate data which would allow model parameter specification, this framework represents a simple mechanism for testing hypotheses about the behaviour of cell cultures subject to various physical growth stimuli; furthermore, it would be relatively straightforward to adapt the model to investigate the effect of a chemical stimulus such as growth factors or a diffusible nutrient on the cells' response. Such a framework is presented in Lemon & King (2007).

4.5 Summary

In this chapter we have illustrated, using numerical solution of the model equations, the effect on the behaviour of the solutions of varying parameters associated with the viscosity of the constituent phases and the intraphase pressure and interphase traction functions. The implications of our results in the context of tissue engineering were also discussed,

specifically with reference to the manufacture of appropriate scaffolds to control the relative strength of cell-cell and cell-scaffold interactions and the effect on the dynamics of the resulting tissue construct.

Employing numerical simulations, we demonstrated that cell populations which exhibit a preference for group locomotion will display enhanced penetration through the scaffold. Furthermore, our results indicated that increasing scaffold density lends tissue engineers improved control over cells' aggregation and attachment. The switch between aggregative and repulsive behaviour as cell density increases was highlighted and analysed by using a simplified form for the relevant functions: Σ_n, ψ_{ns}. This simple analysis showed how the diffusive behaviour of the cells is reduced or augmented depending upon the relative importance of cell aggregation and repulsion.

In addition, we have demonstrated how the mathematical model may be adapted to account for coupling between the cells' proliferative response and their local environment. This was achieved by replacing the constant growth and death rates (k_m, k_d) with appropriate functional forms. Specifically, motivated by a range of studies (*e.g.* Haskin *et al.* (1993), Klein-Nulend *et al.* (1995a), Bakker *et al.* (2004), Han *et al.* (2004) and Chaplain *et al.* (2006)), we considered the response of the cells to their local density, pressure and flow-induced shear stress. Simulations were presented showing that the growth and resulting morphology of the tissue construct is dramatically altered by these effects. On provision of appropriate experimental data, these predictions provide a means of identifying the dominant regulatory growth mechanism in a cell population. We remark that we have not considered nutrient-limited growth; as noted in chapter 2, this effect is likely to be significant during static culture. An interesting extension to this work is to see how our predictions in static and dynamic culture are affected by such a consideration.

We concede that highly simplified functional forms for the different growth effects were employed and that they were considered in isolation; physiologically, it is expected that these effects work together in a complex way to produce the cells' overall response to the stimuli they experience. However, we remark that the mathematical formulation and numerical scheme developed is highly versatile, admitting more complex functional forms and interplay between many competing growth stimuli should appropriate data become available.

Lastly, we note that we have modelled the cells and ECM as a lumped "cell" phase; this prevents us from distinguishing between ECM deposition and cell proliferation; furthermore, we have assumed that the degradation of the scaffold phase is negligible on the timescale of

interest. In the following chapter, we develop and study a model in which cell proliferation, ECM deposition and scaffold degradation are treated separately.

Chapter 5

A three phase model for the growth of a tissue construct

5.1 Introduction

In this chapter, we extend the model developed chapters 3 and 4 by treating separately the cell population and ECM, without increasing the total number of phases in the system. The mechanical forcing provided by the piston is neglected allowing us to focus, once again, on the effect of the imposed flow on the cells' response.

The interplay between scaffold degradation and nascent tissue growth is of key importance in tissue engineering applications, both in maintaining the mechanical integrity of engineered constructs and with respect to *in vivo* implantation (proper injury repair demands that total degradation of scaffold *in vivo* must be matched by tissue growth). To investigate this, we re-interpret the scaffold phase as a lumped scaffold and ECM phase and introduce an equation to govern its spatio-temporal evolution as a result of ECM deposition and scaffold degradation; the cell phase now comprises *only* cells. We employ the method presented in chapter 3 to derive a system of equations which describes how the pressure in the culture medium and the volume fractions of the cell and "scaffold" phases evolve. As in previous chapters, the cell and culture medium phases are modelled as viscous fluids and the lumped scaffold/ECM phase is represented by a rigid porous material.

The ability of the model to accommodate interplay between cell proliferation, ECM deposition and the mechanical environment is illustrated by considering a phenotypic switch in the cells' behaviour in response to the local cell density and the external fluid mechanics in a similar manner to that presented in §4.3. Numerical solutions of the model equations are presented and their biological relevance briefly discussed; the complexity of the governing equations prevents significant analytical progress.

5.2 Model formulation

As in chapters 2, 3 and 4, a Cartesian coordinate system $\boldsymbol{x^*} = (x^*, y^*)$ is chosen with corresponding coordinate directions $(\hat{\boldsymbol{x}}, \hat{\boldsymbol{y}})$. We consider a rigid-walled, two-dimensional channel occupying $0 \leqslant x^* \leqslant L^*$, $0 \leqslant y^* \leqslant h^*$, which contains a multiphase mixture subject to a flow generated by an imposed axial pressure drop, $P_u^* - P_d^*$. The multiphase mixture comprises two viscous fluids and one rigid phase; the cell population and the culture medium are modelled as viscous fluids whilst the "scaffold phase" (now comprising both the PLLA scaffold and the ECM deposited by the cells) is modelled as a rigid porous material. We adopt the same notation as used previously and associate with each phase a volume-averaged fraction (which we denote n, w, s for consistency with previous chapters), pressure, p_i^*, velocity, $\boldsymbol{u}_i^* = (u_i^*, v_i^*)$, and stress tensor, $\boldsymbol{\sigma}_i^*$, where the subscript $i = n$, w, s denotes variables associated with the cell, culture medium and scaffold phases, respectively.

The derivation of the governing equations follows exactly the same process as given in chapter 3, and we introduce an additional mass conservation equation for the scaffold phase describing the deposition of ECM within the porous scaffold and the degradation of the scaffold. For clarity, we reiterate here that, as in the previous chapters, we treat the scaffold phase as a rigid porous material and therefore set $\boldsymbol{u}_s^* \longrightarrow \boldsymbol{0}$, $\mu_s^* \longrightarrow \infty$, $D_s^* = 0$ in the conservation of mass and momentum equations (3.1), (3.2); however, we now include a non-zero mass transfer term for the scaffold phase: $S_s(\boldsymbol{x}, t)$. We choose to employ the momentum balance equation for the two phase mixture of cells and culture medium in preference to the balance equation for the system as a whole; more detail regarding this choice is given in §3.2.1. To avoid repetition, details of the derivation are omitted here. For ease of comparison with the equations given previously (chapters 3 and 4), we express the equation governing the growth of the scaffold phase in terms of the porosity, $\theta(\boldsymbol{x}, t) = 1 - s(\boldsymbol{x}, t)$, and employ θ in preference to s in the remainder of this chapter.

We make the same constitutive assumptions as in chapter 3, employing the viscous stress tensor (2.8) for the cell and culture medium phases, defining the intraphase and interphase pressures according to equations (3.4) and (3.5) and assuming that the interphase viscous drag coefficient scales linearly with the relevant phases; see equation (3.6). Lastly, non-dimensionalising according to (3.10), we obtain the following dimensionless governing

equations for the three phase system:

$$\frac{\partial \theta}{\partial t} = -S_s, \tag{5.1a}$$

$$\frac{\partial n}{\partial t} - \nabla \cdot [(\theta - n)\boldsymbol{u}_w] = \frac{\partial \theta}{\partial t} - S_w - D\nabla^2(\theta - n), \tag{5.1b}$$

$$\nabla \cdot (n\boldsymbol{u}_n + (\theta - n)\boldsymbol{u}_w) = \sum_{i=n,w,s} S_i + D\nabla^2\theta, \tag{5.1c}$$

$$\begin{aligned}(\theta - n)\nabla p_w + kn(\theta - n)(\boldsymbol{u}_w - \boldsymbol{u}_n) + k(1-\theta)(\theta - n)\boldsymbol{u}_w - \\ \nabla \cdot \left[(\theta - n)(\nabla \boldsymbol{u}_w + \nabla \boldsymbol{u}_w^T) + \gamma_w(\theta - n)\nabla \cdot \boldsymbol{u}_w \mathbf{I}\right] \;=\; \mathbf{0},\end{aligned} \tag{5.1d}$$

$$\begin{aligned}\nabla \cdot \big[- (\theta p_w + n\Sigma_n + n(1-\theta)\psi_{ns})\,\mathbf{I} + \mu_n n(\nabla \boldsymbol{u}_n + \nabla \boldsymbol{u}_n^T) + \\ \gamma_n n \nabla \cdot \boldsymbol{u}_n \mathbf{I} + (\theta - n)(\nabla \boldsymbol{u}_w + \nabla \boldsymbol{u}_w^T) + \gamma_w(\theta - n)\nabla \cdot \boldsymbol{u}_w \mathbf{I}\big] + \\ \nabla n(1-\theta)\psi_{ns} - kn(1-\theta)\boldsymbol{u}_n - k(\theta - n)(1-\theta)\boldsymbol{u}_w = \mathbf{0},\end{aligned} \tag{5.1e}$$

in which we have employed the no-voids condition $n + w = \theta$ (where $\theta = 1 - s$) to write the system in terms of n and θ only. We remark that the channel now occupies $0 \leqslant x \leqslant 1$, $0 \leqslant y \leqslant h = h^*/L^*$.

Equations (5.1a)–(5.1c) are statements of conservation of mass for the scaffold phase, culture medium phase (written in terms of n and θ) and the multiphase mixture. We use the mass conservation equation for the culture medium phase in preference to the cell phase for convenience (see §3.3). Equation (5.1d) expresses conservation of momentum for the culture medium and (5.1e) is the momentum equation for the two phase mixture of cells and culture medium. In equation (5.1a), S_s is the mass transfer term associated with the scaffold phase, representing the net increase in the scaffold volume fraction due to ECM deposition by the cell population and scaffold degradation. The remaining notation employed in equations (5.1) is identical to that used in chapters 3 and 4: the rates of mass transfer into the cell and culture medium phases are denoted S_n, S_w, the dimensionless parameters D, μ_n, k, γ_w and γ_n are defined by equations (2.18) and Σ_n, ψ_{ns} are the intraphase pressure and interphase traction functions introduced in §1.5 and defined by equations (3.12).

Functional forms for the mass transfer rates for each phase (S_n, S_w, S_s) reflecting various mechanotransduction mechanisms will be specified in §5.2.1 and suitable initial conditions given in §5.3. Boundary conditions are given by the dimensionless versions of (2.9)–(2.11).

We solve equations (5.1) in the same geometry as used previously, confining the tissue construct to a region $a \leqslant x \leqslant b$ and we stipulate that the cell phase may not leave this region (see figure 3.1). The values of a and b are arbitrary (provided $a < b < 1$) and, as in chapters 3 and 4, we choose $a = 0.25$, $b = 0.75$.

The equations are simplified by exploiting the long-wavelength limit ($h \ll 1$; see §3.2.2 for more details) to deduce from the y-component of the momentum equations (5.1d) and (5.1e) that the volume fractions and pressures of each phase are independent of the transverse coordinate at leading order. Integrating the x-component of the momentum equations yields expressions for the axial velocities, u_w and u_n. Averaging the conservation of mass equations (5.1a)–(5.1c) across the channel and eliminating the axial velocities in the same manner as previously (see §3.3), we may then rewrite the system (5.1) as a coupled system of equations for $\theta(x,t)$, $p_w(x,t)$ and $n(x,t)$. We obtain:

$$\frac{\partial \theta}{\partial t} = -S_s, \tag{5.2a}$$

$$\frac{\partial n}{\partial t} + \frac{1}{12}\frac{\partial}{\partial x}\left\{(\theta - n)\frac{\partial p_w}{\partial x}\right\} = S_n - S_s + D\left(\frac{\partial^2 n}{\partial x^2} - \frac{\partial^2 \theta}{\partial x^2}\right), \tag{5.2b}$$

$$\frac{\partial^2 p_w}{\partial x^2} + \frac{1}{\overline{\mu} n + \theta}\left\{\left[\overline{\mu}\frac{\partial n}{\partial x} + \left(\frac{1}{\mu_n} + 1\right)\frac{\partial \theta}{\partial x}\right]\frac{\partial p_w}{\partial x} + \frac{\partial^2 \theta}{\partial x^2}\frac{p_w}{\mu_n}\right\} = -\frac{1}{\mu_n(\overline{\mu} n + \theta)}\left[\frac{\partial^2 (n\Sigma_n)}{\partial x^2} + (1-\theta)\frac{\partial}{\partial x}\left(n\frac{\partial \psi_{ns}}{\partial x}\right)\right] - \frac{12}{\overline{\mu} n + \theta}\left(S_s + D\frac{\partial^2 \theta}{\partial x^2}\right), \tag{5.2c}$$

where $\overline{\mu} = 1/\mu_n - 1$ and $S_i(x,t)$ now denote the averaged mass transfer terms for each phase. We note that we have used (5.2a) to eliminate $\partial\theta/\partial t$ from (5.2b). We have additionally assumed $S_w = -S_n$ for consistency with chapters 3 and 4, and consequently have $\sum S_i = S_s$; deposition of ECM by the cells or degradation of scaffold therefore represents spontaneous mass generation or loss in the system. A discussion of this feature of our model and suggestions to correct it are given in §5.4. Comparing equations (5.2b) and (5.2c) and those employed in the lumped cell/ECM phase model (equations (4.1) and (4.2)) shows that the introduction of spatio-temporal variation of scaffold volume fraction results in a number of additional terms. Notable additions include a reduction in cell phase growth and modified diffusion.

Appropriate boundary conditions on (5.2) are derived in chapter 3 by considering continuity of normal stress and flux at $x = a, b$, and requiring that the cells remain confined within the region $a \leqslant x \leqslant b$. For brevity, we do not discuss the method here. The culture medium pressure obeys the following conditions:

$$p_w = \frac{A(t)a + P_u - n\Sigma_n - (1-\theta)n\psi_{ns}}{\theta}, \quad \frac{\partial p_w}{\partial x} = \frac{A(t) + 12D\frac{\partial n}{\partial x}}{\theta - n} \quad \text{on } x = a, \tag{5.3a,b}$$

$$p_w = \frac{A(t)(b-1) + P_d - n\Sigma_n - (1-\theta)n\psi_{ns}}{\theta}, \quad \frac{\partial p_w}{\partial x} = \frac{A(t) + 12D\frac{\partial n}{\partial x}}{\theta - n} \text{ on } x = b, \tag{5.4a,b}$$

where $P_u - P_d$ is the imposed dimensionless axial pressure drop (the dimensionless pressures P_u, P_d are defined by equation (2.17)). Equations (5.3a) and (5.4a) are imposed as boundary

conditions, the remaining equations are constraints which $A(t)$ must satisfy; in the following numerical simulations, we employ (5.3b) to determine $A(t)$ and (5.4b) is employed as an additional accuracy check, ensuring that continuity of flux is obeyed (see §3.3 for more details). To ensure zero cell flux on $x = a, b$, the gradient of the cell volume fraction must obey

$$\frac{\partial n}{\partial x} = \frac{1}{12D}\frac{n-\theta}{n+\mu_n(\theta-n)}\left\{p_w\frac{\partial \theta}{\partial x} + \frac{A(t)n}{(\theta-n)} + \frac{\partial\left(n\Sigma_n\right)}{\partial x} + (1-\theta)n\frac{\partial \psi_{ns}}{\partial x}\right\} \quad \text{on } x = a, b. \tag{5.5}$$

Equations (5.2)–(5.5) allow us to simulate more clearly the interplay between cell proliferation, ECM deposition and the mechanical environment. To model this behaviour, we now specify the mass transfer rates S_n, S_s which determine the response of the cell phase to its environment.

5.2.1 Specification of mass transfer rates

In this section, we define the mass transfer rates for the cell and scaffold phases: S_n, S_s. We first consider the growth of the tissue construct in the regime for which the rates of cell proliferation, death, ECM deposition and scaffold degradation (k_m, k_d, k_{ecm}, k_{deg}) are constant. The model is then extended to accommodate coupling between the cells' proliferative response and the local environment. To illustrate the influence of environmental stimuli, we consider a cell density and fluid shear-dependent response. The effect of such proliferative mechanisms was analysed in some detail in chapter 4, considering density, pressure and shear-dependence on the growth of a lumped cell/ECM phase. For brevity, we consider density and shear-dependence only. In each case, the motivation for such a growth response is outlined in §§1.2.2, 2.4.2 and 4.3 and we employ the same simple modelling approach, leading to mass transfer rates of the following form.

Uniform growth:

$$S_n(n) = (k_m - k_d)n, \quad S_s(n,\theta) = k_{ecm}n - k_{deg}(1-\theta); \tag{5.6}$$

cell density-dependent growth:

$$S_n(n) = \left[k_m \mathrm{H}(n_1' - n) - k_d \mathrm{H}(n - n_2')\right]n = \kappa_n(n)n, \tag{5.7}$$

$$S_s(n,\theta) = k_{ecm}n\left[\mathrm{H}(n-n_1') - \mathrm{H}(n-n_2')\right] - k_{deg}(1-\theta) = \kappa_s(n)n - k_{deg}(1-\theta); \tag{5.8}$$

fluid shear-dependent growth:

$$S_n\left(n, \left|\frac{\partial p_w}{\partial x}\right|\right) = \left\{\frac{k_{m1}-k_m}{2}\left(\tanh\left[g\left(\left|\frac{\partial p_w}{\partial x}\right| - P_1'\right)\right] - 1\right) - \frac{k_m+k_d}{2}\left(\tanh\left[g\left(\left|\frac{\partial p_w}{\partial x}\right| - P_2'\right)\right] - 1\right) - k_d\right\} n$$
$$= \kappa_n\left(\left|\frac{\partial p_w}{\partial x}\right|\right) n, \tag{5.9}$$

$$S_s\left(n, \theta, \left|\frac{\partial p_w}{\partial x}\right|\right) = \left\{\frac{k_{ecm,1}}{2}\left(\tanh\left[g\left(P_1' - \left|\frac{\partial p_w}{\partial x}\right|\right)\right] + 1\right) - \frac{k_{ecm}}{2}\left(\tanh\left[g\left(\left|\frac{\partial p_w}{\partial x}\right| - P_1'\right)\right] - \tanh\left[g\left(\left|\frac{\partial p_w}{\partial x}\right| - P_2'\right)\right]\right)\right\} n - k_{deg}(1-\theta)$$
$$= \kappa_s\left(\left|\frac{\partial p_w}{\partial x}\right|\right) n - k_{deg}(1-\theta). \tag{5.10}$$

As remarked in §4.3.3, we must employ a smoothed functional form for the shear-dependent regime; for simplicity, as in §4.3.1, we employ step functions to represent the density-dependent growth response.

Equations (5.6) represent uniform tissue growth similar to that considered in chapter 3; however, we may now explicitly model the deposition of ECM and degradation of the scaffold.

The mass transfer rates given by equation (5.7) and (5.8) model a cell density-dependent phenotypic change from a proliferative phase to an apoptotic phase via an ECM-producing phase; the threshold cell densities that separate these three types of behaviour are denoted n_1' and n_2'. Figure 5.1 shows how the net rate of cell proliferation (κ_n) and scaffold phase production ($\kappa_s(n) - (1-\theta)k_{deg}$) varies with the cell density, n, at fixed θ ($\theta = \theta_0$). We remark here that, in contrast to the cell density-dependent growth responses presented in the lumped cell and ECM model (§§2.4.2 and 4.3), during the ECM deposition stage, we have $\kappa_n(n) = 0$, $\kappa_s(n) = k_{ecm}$ since the cell phase now comprises *only* cells; in the former cases, ECM deposition was represented by a heightened level of cell phase growth (see figures 2.14 and 4.10). To clarify, within our numerical scheme, we choose $\kappa_n(n_1') = k_m$, $\kappa_n(n_2') = -k_d$, $\kappa_s = \hat{k}_{ecm}$ at $n = n_1', n_2'$.

Equations (5.9) and (5.10) define the rates of mass transfer corresponding to a shear stress-dependent phenotypic change from a quiescent phase to an apoptotic phase via an ECM-producing phase. This functional form describes a cell phase whose proliferation and ECM deposition is heightened in the presence of an intermediate level of shear stress; for low shear stress, the proliferation and ECM deposition is reduced; and for excessively high shear stresses the cells become damaged and enter an apoptotic phase. The threshold

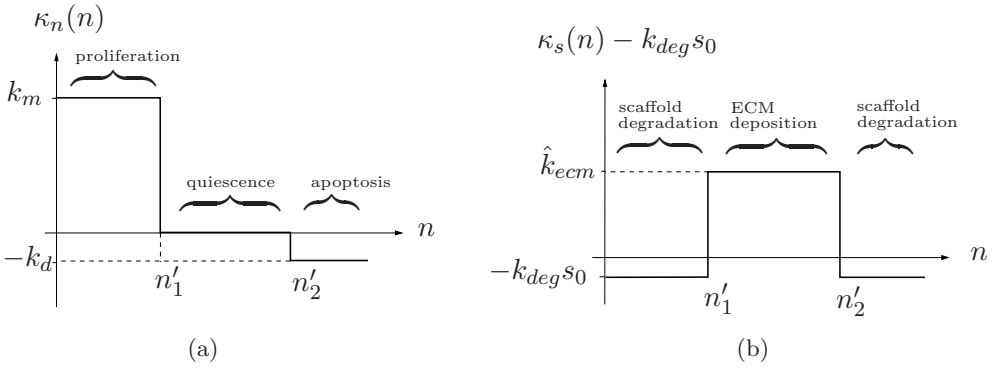

Figure 5.1: Schematic representation of the progression of the cells from a proliferative phase ($n < n_1'$) to an apoptotic phase ($n > n_2'$) via an extracellular matrix-producing phase ($n_1' < n < n_2'$) in response to the local cell density at fixed $\theta = \theta_0$ ($s_0 = 1 - \theta_0$); $\hat{k}_{ecm} = k_{ecm} - k_{deg}s_0$.

pressure gradients separating these phases are denoted P_1' and P_2' and the reduced rates of cell proliferation and ECM production in the quiescent phase are denoted k_{m1} and $k_{ecm,1}$, respectively. Figure 5.2 illustrates the dependence of the net rate of cell proliferation and scaffold phase production upon the local shear stress. As in §§2.4.2 and 4.3.3, we employ smooth functions to ensure numerical stability; the parameter g determines the sharpness of the switch between the different growth responses.

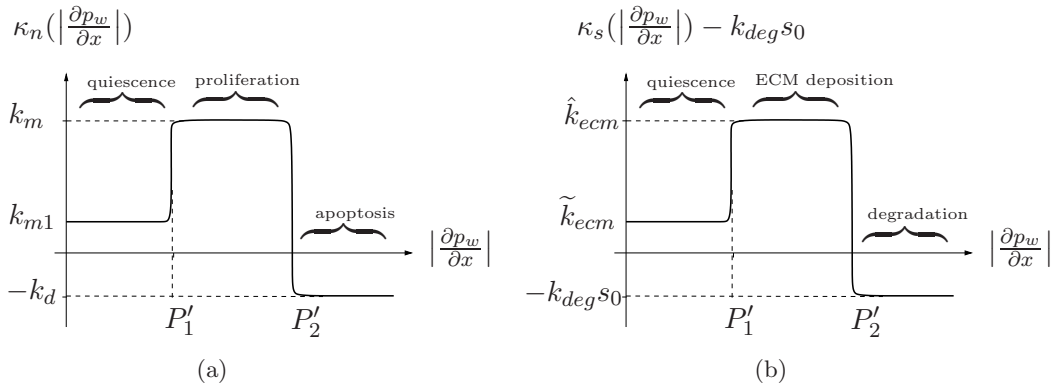

Figure 5.2: Schematic representation of the progression of the cells from a quiescent phase $\left(|\frac{\partial p_w}{\partial x}| < P_1'\right)$ to a necrotic phase $\left(|\frac{\partial p_w}{\partial x}| > P_2'\right)$ via an proliferative phase $\left(P_1' < |\frac{\partial p_w}{\partial x}| < P_2'\right)$ in response to the level of flow-induced shear stress at fixed $\theta = \theta_0$ ($s_0 = 1 - \theta_0$); $\hat{k}_{ecm} = k_{ecm} - k_{deg}s_0$, $\widetilde{k}_{ecm} = k_{ecm,1} - k_{deg}s_0$.

In the following section, we will use numerical simulations to illustrate the interplay between cell proliferation, ECM deposition and the mechanical environment under the different growth regimes represented by equations (5.6)–(5.10) and depicted by figures 5.1 and

5.2. Emphasis will be placed upon the response of the cell phase (both in terms of proliferation and ECM deposition) to the mechanical environment; the remaining features of the system will be similar to that discussed in §4.2 and the culture medium and cell phase velocities (u_w, u_n) are, therefore, not presented.

5.3 Numerical simulation

The system of equations (5.2a)–(5.2c) subject to the boundary conditions (5.3)–(5.5) is solved numerically using a method identical to that described in §3.3.1; to avoid repetition, only a brief outline of the numerical scheme for these equations is given.

Suitable initial conditions for the cell volume fraction are given by (3.34) and we choose an initially uniform scaffold volume fraction: $\theta(x, 0) = 0.97$. Equation (5.2c) is discretised using central differences to obtain a finite-difference equation which is used to calculate the pressure, $p^k_{w,j}$, at each mesh point, j, and time-step, k, from the cell volume fraction, n^k_j and scaffold porosity, θ^k_j. The value of the function A^k at each time-step is calculated using a parameter shooting method as described in §3.3.1. Equation (5.2a) is solved for θ^{k+1}_j using an explicit time-stepping routine and equation (5.2b) is then solved for n^{k+1}_jusing the same semi-implicit method as described previously. The discretised equations are not stated here in the interests of brevity; instead, a brief recapitulation of the method is given:

1. The value of θ^{k+1}_j is calculated using an explicit scheme;
2. an approximation to n^{k+1}_j (denoted $\hat{n}^{k+1}_j$) is calculated from n^k_j, $p^k_{w,j}$, θ^k_j using a semi-implicit Crank-Nicholson scheme;
3. an approximation to $p^{k+1}_{w,j}$ (denoted $\hat{p}^{k+1}_{w,j}$) is calculated from $\hat{n}^{k+1}_j$ and θ^{k+1}_j;
4. an improved estimate for n^{k+1}_j is calculated from n^k_j, $p^k_{w,j}$, θ^k_j, $\hat{p}^{k+1}_{w,j}$, θ^{k+1}_j using a fully implicit Crank-Nicholson scheme;
5. an improved approximation for the pressure, $p^{k+1}_{w,j}$ is calculated using n^{k+1}_j, θ^{k+1}_j.

As in earlier chapters, we employ an upwind scheme for the convective terms in (5.2b) and the boundary conditions (5.5) are imposed using n^k_j (or $\hat{n}^k_j$) from the previous (or intermediate) time-step for simplicity. Furthermore, as remarked in §4.3, when a more complex growth response is considered, we must ensure that the mass transfer terms, $S^k_{n,j}$, $S^k_{s,j}$ are included appropriately in our Crank-Nicholson scheme (equations (3.36) and (3.37)).

5.3.1 Uniform cell proliferation, death, ECM deposition and scaffold degradation: $S_n = (k_m - k_d)n$, $S_s = k_{ecm}n - k_{deg}(1-\theta)$

The evolution of the cell and scaffold volume fractions for dynamic culture conditions ($P_u = 1$, $P_d = 0.1$) is shown in figure 5.3; the corresponding pressure in the culture medium and cell phases is shown in figure 5.4. We remark that although we have formulated the model in terms of the porosity, θ for consistency with previous chapters, we present results for the scaffold volume fraction, s, which more naturally illustrates the effect of ECM deposition and scaffold degradation.

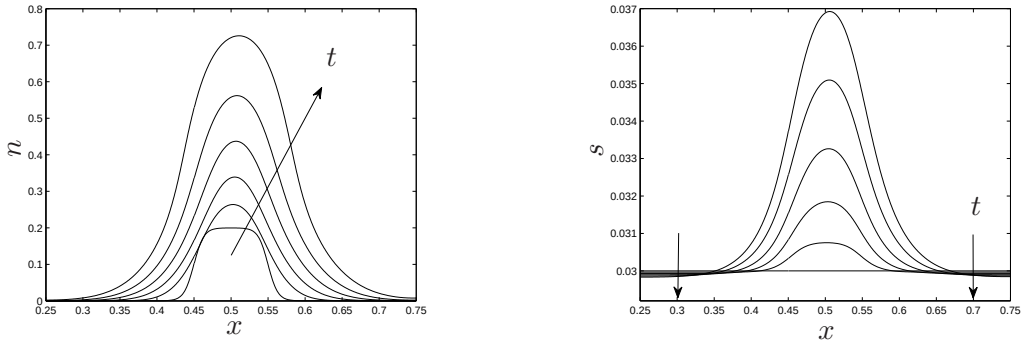

(a) (b)

Figure 5.3: The evolution of (a) the cell volume fraction, and (b) the scaffold volume fractions at $t = 0 - 0.25$ (in steps of $t = 0.05$) for constant proliferation, death, ECM deposition and scaffold degradation rates: $k_m = 7.5$, $k_d = 0.1$, $k_{ecm} = 0.1$, $k_{deg} = 0.01$ and $D = 0.01$; remaining parameters as in §3.3.

The results presented in figures 5.3 and 5.4 show how the volume fractions of the cell and scaffold phases evolve and the effect this has on the cell and culture medium pressures. This simple model of ECM deposition and scaffold degradation yields similar behaviour to that observed in chapters 3 and 4 where we assumed $\theta =$ constant: the cell population proliferates and spreads along the channel under the influence of diffusion and advection. Figure 4.2a (dashed line) shows the growth of the cell volume fraction for constant scaffold density at $t = 0 - 0.25$. Comparison of figures 5.3a and 4.2a shows that due to the small variation of scaffold density, the additional terms in equation (5.2b) have little influence on cell phase growth. Similarly, the culture medium and cell phase pressures are not dramatically affected by the small variations in scaffold density, showing qualitatively similar behaviour to that observed in chapter 3 (see figures 3.6 and 3.7); the corresponding culture medium and cell phase velocities are therefore similar to those given previously and are not shown here.

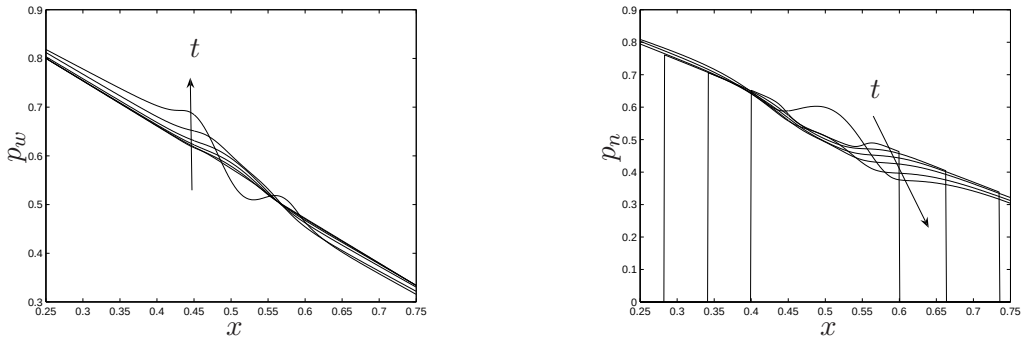

(a) (b)

Figure 5.4: The evolution of (a) the culture medium pressure, and (b) the cell phase pressure at $t = 0 - 0.25$ (in steps of $t = 0.05$) for constant proliferation, death, ECM deposition and scaffold degradation rates. Parameter values as in figure 5.3.

Figure 5.3b shows that at the edges of the construct, where n is small, scaffold degradation dominates ECM deposition and the scaffold volume fraction falls; in the regions where n is relatively large (so that deposition dominates over degradation) the evolution of the scaffold phase mirrors that of the cell volume fraction.

We remark that in these simulations, the cell density achieves high values, the scaffold density remaining small. As discussed in chapter 3, the cell density is unlikely to achieve such high values and we present these results to illustrate the behaviour of the system. The increase in scaffold volume fraction corresponding to this cell density is, however, consistent with the typical level of mineralisation in a PLLA scaffold found in experiments at ISTM, Keele University (see figure 1.3). Appropriate cell and scaffold densities may, of course, be obtained by manipulating the model parameters k_m, k_d, k_{ecm} and k_{deg}.

The separate modelling of the scaffold phase has revealed some interesting behaviour: the model predicts significant scaffold degradation in regions where the cell density is low. In regions of higher cell density, the scaffold degradation is counterbalanced by ECM deposition. Associating degradation of the scaffold with a reduction in the mechanical integrity of the construct, and assuming that deposition of ECM compensates for such a reduction, the results indicate that for cell populations which do not display significant scaffold penetration, non-uniform initial cell seeding will cause a notable reduction in the resulting tissue construct's material properties. In the above simulations, due to the centrally-located initial cell phase distribution, scaffold degradation is observed at the periphery of the scaffold.

Sporadic or peripheral cell seeding will have similarly detrimental consequences. Similar conclusions have been drawn by other studies; for instance, Kelly & Prendergast (2003) have shown that spatial inhomogeneity in the development of tissue within a construct dramatically reduces material properties (specifically, the P-wave modulus of the construct, which is a measure of compressibility, relating axial stress to axial strain).

Our simulations clearly demonstrate the importance of achieving a uniform initial cell seeding and encouraging cell penetration throughout the scaffold to maintain the mechanical integrity of the construct, which is of crucial importance in bone tissue engineering applications, especially with regard to *in vivo* implantation.

5.3.2 Cell density-dependent growth: $S_n = k_n(p_n)n$, $S_s = \kappa_s(n)n - (1-\theta)k_{deg}$

In this section, the effect of the cell density-dependent phenotypic switch represented by equations (5.7) and (5.8) is investigated. Figure 5.5 shows how the cell density-dependent behaviour influences the time-evolution of the cell population for static ($P_u - P_d = 0$) and dynamic ($P_u - P_d = 0.9$) culture conditions; in figure 5.6a we compare the cell distributions for static and dynamic culture conditions. A comparison of the corresponding scaffold phase volume fraction for static and dynamic culture conditions is shown in figure 5.6b. The evolution of the pressures of the culture medium and cell phases for dynamic culture conditions is qualitatively similar to that reported in previous chapters (and shown in figure 5.4) and is therefore not given here.

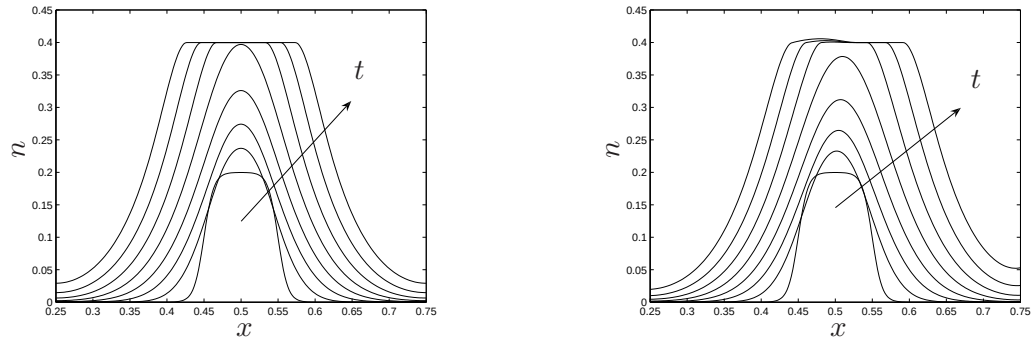

(a) (b)

Figure 5.5: The evolution of the cell volume fraction at $t = 0 - 0.28$ (in steps of $t = 0.04$) for (a) static culture: $P_u - P_d = 0$, (b) dynamic culture: $P_u = 1$, $P_d = 0.1$, for growth behaviour defined by (5.7) and (5.8). Parameter values: $k_m = 7.5$, $k_d = 0.1$, $k_{ecm} = 0.1$, $k_{deg} = 0.05$ $D = 0.01$, $n_1' = 0.4$, $n_2' = 0.6$.

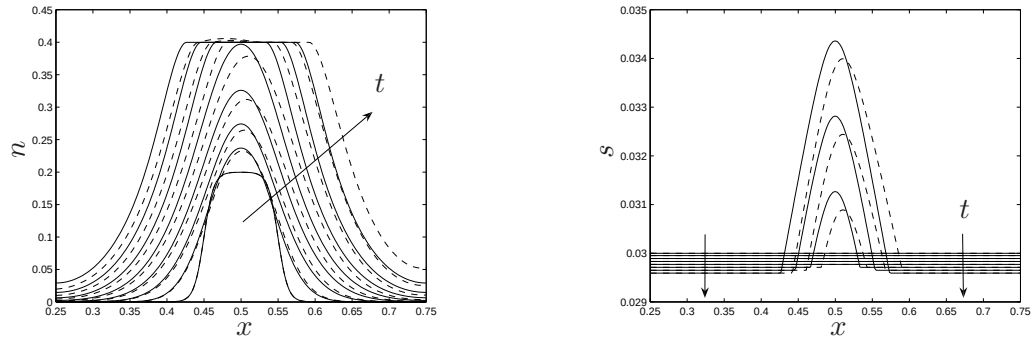

(a) (b)

Figure 5.6: The evolution of (a) the cell volume fraction, and (b) the scaffold volume fraction at $t = 0 - 0.28$ (in steps of $t = 0.04$) for static culture, $P_u - P_d = 0$ (–) and dynamic culture, $P_u = 1$, $P_d = 0.1$ (- -) and for growth behaviour defined by (5.7) and (5.8); parameter values as in figure 5.5.

Inspection of figures 5.5 and 5.6a shows the effect of the imposed flow on the cell population. In the absence of flow, the chosen form of the mass transfer function S_n causes behaviour much like that observed previously (see figure 4.11a, §4.3): the cell population is prevented from exceeding the threshold value $n = n_1'$ due to the switch from proliferative to ECM-depositing behaviour and spreads due to diffusion. In contrast to previous results, however, under dynamic culture conditions, a small build up of cells is observed above the threshold $n = n_1'$. Figure 5.6b shows that this does not affect the ECM deposition/scaffold degradation behaviour due to the relatively small cell density increase and the choice of k_{ecm}. This accumulation is reduced by mesh refinement and eradicated by employing smoothed functional forms for the mass transfer terms S_n and S_s in the same manner as indicated for the shear stress-dependent response (equations (5.9) and (5.10)), which suggests that it is an artefact of the use of step functions rather than the result of a physical mechanism. Figure 5.7 shows the predicted time-evolution of the construct morphology when a smoothed function is used and when a step function with a refined spatial mesh ($\Delta x = 6 \times 10^{-4}$) is employed. Figure 5.8 shows the effect of refining the mesh in detail. These simulations suggest that a smoothed functional form is more appropriate for the mass transfer terms.

The effect of the perfusion is best illustrated by figure 5.6a which shows that the cell population under dynamic conditions takes longer to reach the threshold value $n = n_1'$, forming a more diffuse population due to advection of cells and subsequent increase in density at $x = b$.

The switch from a proliferative to an ECM-depositing phase is reflected in the evolution of the scaffold volume fraction shown in figure 5.6b. Initially, for both static and dynamic culture conditions, uniform degradation of the scaffold is observed; when the cell volume fraction reaches the threshold $n = n_1'$, deposition of ECM by the cells begins. The density of ECM deposited under dynamic culture conditions is less than that deposited under static conditions since the rate of deposition is proportional to n; as discussed above, under dynamic culture conditions, the high cell density values are achieved at later times due to increased cell density at $x = b$ and the formation of a more diffuse construct. In view of the importance of cell motility and construct uniformity discussed in §5.3.1 in the context of mechanical integrity of constructs, the more diffuse nature of constructs produced under dynamic culture conditions indicates they are likely to be more mechanically stable.

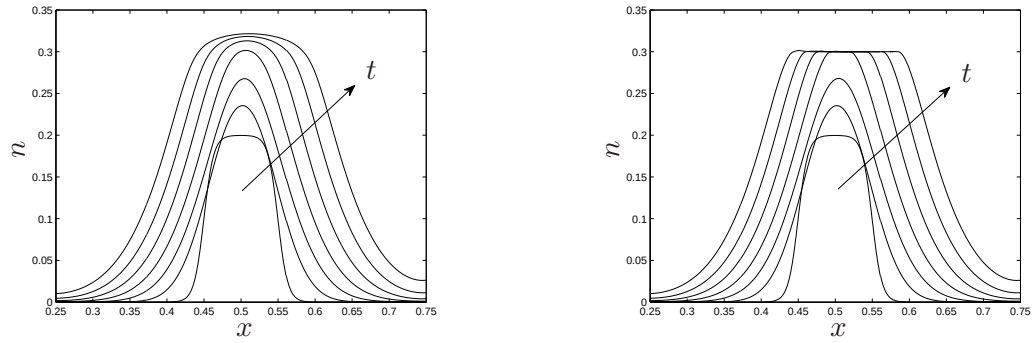

(a) (b)

Figure 5.7: The evolution of the cell volume fraction at $t = 0 - 0.3$ (in steps of $t = 0.05$) for dynamic culture: $P_u = 1$, $P_d = 0.1$, for (a) smoothed growth behaviour, and (b) growth behaviour defined by (5.7) and (5.8) with a refined mesh. Parameter values: $k_m = 7.5$, $k_d = 0.1$, $k_{ecm} = 0.1$, $k_{deg} = 0.05$ $D = 0.01$, $n_1' = 0.3$, $n_2' = 0.6$, smoothing parameter, $g = 60$.

5.3.3 Shear stress dependence: $S_n = \kappa_n\big(\big|\frac{\partial p_w}{\partial x}\big|\big)n$, $S_s = \kappa_s\big(\big|\frac{\partial p_w}{\partial x}\big|\big)n - (1-\theta)k_{deg}$

We now illustrate the effect of coupling the proliferation of the cells, the deposition of ECM and the local shear stress induced by the imposed flow, as represented by equations (5.9) and (5.10) and depicted by figure 5.2. The evolution of the cell and scaffold volume fractions for dynamic culture conditions ($P_u - P_d = 0.9$) is shown in figure 5.9; the corresponding pressures in the culture medium and cell phases are qualitatively similar to those presented above (figure 5.4) and so in the interests of brevity are not given here. The culture medium

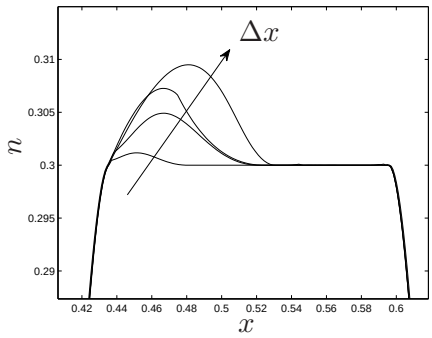

Figure 5.8: The effect on the build-up of cells of refining the spatial mesh; the arrow indicates the direction of increasing Δx. $\Delta x = 0.5/(nx-1)$; number of mesh points: $nx = 300, 400, 500, 600$, other parameter values as in figure 5.5.

pressure gradient (which we view as being proportional to the flow-induced shear stress; see §4.3) is shown in figure 5.10 together with the threshold values, P_1', P_2' which we arbitrarily choose to be $P_1' = 0.5$, $P_2' = 1.5$ as in §4.3.3; the smoothness parameter is chosen to be $g = 20$.

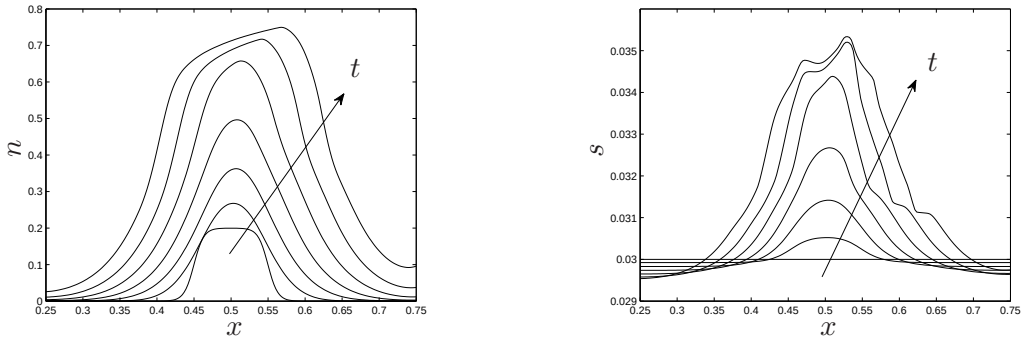

(a) (b)

Figure 5.9: The evolution of (a) the cell volume fraction, and (b) the scaffold volume fraction at $t = 0 - 0.3$ (in steps of $t = 0.05$) for growth behaviour defined by (5.9) and (5.10). Parameter values: $k_m = 7.5$, $k_{m,1} = 5$, $k_d = 0.1$, $k_{ecm} = 0.1$, $k_{ecm,1} = 0.05$, $k_{deg} = 0.05$ $D = 0.01$, $P_1' = 0.5$, $P_2' = 1.5$.

Figures 5.9 and 5.10 show how the chosen forms of the shear stress-dependent mass transfer terms affect the growth of the cell phase and the deposition of ECM. Initially, the shear stress falls within the proliferative range $P_1' \leqslant \left|\partial p_w/\partial x\right| \leqslant P_2'$ and the cell phase proliferates and deposits ECM at the heightened rates k_m, k_{ecm}. As the cell population increases, the disturbance to the flow is increased (*cf.* figures 3.9a and 3.9a), causing the

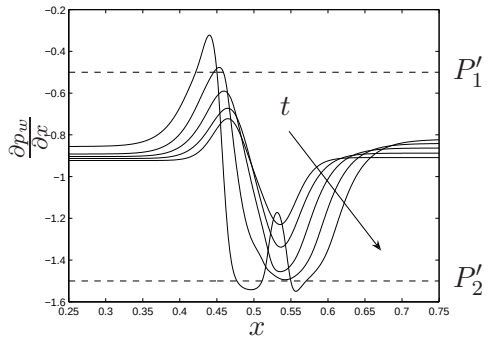

Figure 5.10: The evolution of the pressure gradient in the culture medium $t = 0.05 - 0.25$ (in steps of $t = 0.05$) for growth behaviour defined by (5.9) and (5.10): parameter values as in figure 5.9.

shear stress to cross the upper and lower thresholds (more discussion of this is given in §4.3.3). This causes variations in the rates of cell proliferation and ECM deposition resulting in the distorted cell and scaffold distributions shown in figures 5.9. As observed previously, far upstream and downstream, degradation of the scaffold dominates due to the sparse cell population there; at later times when significant accumulation of cells is observed near $x = b$, ECM deposition increases.

5.4 Summary

In this chapter, we have presented a three phase model for tissue construct growth in which cell proliferation, ECM deposition and scaffold degradation are treated separately. Numerical solutions of the model equations are presented for constant cell proliferation, death, ECM deposition and scaffold degradation rates and comparisons are drawn between these and the solutions to the simplified three phase model presented in chapter 3. The ability of the model to include the interplay between the cell population's proliferative response and its mechanical environment is illustrated by considering a phenotypic progression from a proliferative phase to an apoptotic phase via an ECM-producing phase in response to increases in the local cell density; a similar response to the flow-induced shear stress is also considered. It is shown using simplified functional forms for the appropriate mass transfer terms that these stimuli have a profound effect on the resulting evolution of the cell population and the distribution of ECM deposited. As remarked in the previous chapter, on provision of appropriate experimental data, the morphological differences observed in these distributions provide a means of identifying the dominant stimuli controlling cell

proliferation and ECM deposition in a cell population.

The separate modelling of the ECM and scaffold dynamics has revealed an important facet of the system. Our model predicts that scaffold degradation is significant in regions of low cell density, corresponding to a marked reduction in construct material properties (deposition of ECM offsets the scaffold degradation in regions of high cell density and we assume that this improves mechanical integrity in these regions). This prediction has important implications for tissue engineering applications, suggesting that a uniform initial cell seeding and encouragement of cell penetration throughout the scaffold are crucial in maintaining the mechanical integrity of engineered constructs. Our model associates scaffold degradation with a reduction in scaffold phase volume fraction, from which we infer deleterious effects on material properties. Private communication with Prof. El-Haj indicates that the reduction in scaffold mass associated with degradation of the PLLA scaffold (*e.g.* due to hydrolysis) is negligible; however, the reduction in the construct material properties is physically reasonable.

As in the previous chapter, for clarity, we have considered a highly simplified response and presented the effect of these stimuli in isolation; we recognise that, physiologically, these stimuli will work together in a complex manner to produce the overall cell response. Furthermore, nutrient-limited growth is not considered; this is expected to become significant in the case of static culture conditions and provides an interesting extension to this work.

We have chosen $S_n = -S_w$ for consistency with the previous sections and the mass transfer term for the scaffold phase, S_s, therefore represents spontaneous mass generation (or loss) from the system. This flaw could be easily corrected by more careful definition of these mass transfer terms so that, for instance, deposition of ECM is balanced by a reduction in growth rate of cell volume fraction and degradation of the scaffold results in an increase in culture medium volume fraction. For example, for constant rates of growth, death, ECM deposition and degradation (k_m, k_d, k_{ecm}, k_{deg}):

$$S_n = (k_m - k_{ecm} - k_d)n,\ S_w = (k_d - k_m)n + k_{deg}(1-\theta),\ S_s = k_{ecm}n - k_{deg}(1-\theta). \quad (5.11)$$

These choices are equivalent to assuming that the production of ECM results in reduced cell proliferation and that the scaffold degrades to increase the culture medium volume fraction.

An interesting extension to the work presented in this chapter is to consider in more detail the interplay between the cell phase growth, ECM deposition and scaffold degeneration. A sensitivity analysis could be employed to determine appropriate parameter regimes which lead to optimum tissue growth to offset scaffold degradation. Such considerations

are of great importance to the mechanical properties of engineered constructs and their implantation *in vivo*.

Lastly, we remark that we have modelled the "scaffold" phase as a rigid porous material. For this model to be applicable to the compression/perfusion bioreactor system introduced in §1.2.3 and to *in vitro* tissue engineering more generally, we must take into account the deformation of the construct under an applied load or due to residual stresses (see §1.2.2) brought about by tissue growth. Furthermore, such a model provides a means to investigate the effect of the interplay between scaffold degradation and ECM deposition on the mechanical properties of an engineered tissue construct. As a first step towards modelling these effects, in the following chapter we develop and analyse a simple poroelastic model relevant to biological tissue growth.

Chapter 6

A poroelastic model for the growth and deformation of a tissue construct

6.1 Introduction

In this chapter, we develop mathematical models applicable to the perfusion/compression bioreactor system introduced in §1.2.3, which accommodate deformation of the tissue construct due to macro-scale mechanical forcing supplied by the piston as well as the attendant fluid flow. We use the models to study the effect of periodic compression on the solid stress distribution and fluid flow within the construct. We develop a classical Biot poroelasticity formulation and a multiphase model of the type presented in preceding chapters. This represents a first step towards the development of a comprehensive model which can be used to investigate the combined effect of deformation and fluid flow on the growth and differentiation of a population of cells contained within an engineered tissue construct.

In §6.2, the governing equations of the Biot formulation are given and the relevant modelling considerations are discussed. In addition, we adapt the multiphase formulation presented in §1.5 to accommodate a poroelastic scaffold saturated with a multiphase fluid. Comparisons are drawn between this model and similar models in the literature and it is shown that the Biot model may be obtained as a special case. In §6.3, we present analytical and numerical solutions to the Biot model to show the effect that mechanical forcing and the resulting fluid flow has on the stress and flow field within the poroelastic scaffold. In §6.4, numerical solutions are presented to the multiphase model outlined in §6.2. For simplicity, the model equations are analysed in the absence of a cell phase in each case, with a view to employing the predicted solid stress and fluid flow distributions in future models which will link mechanical stimulation to cell behaviour within a deformable poroelastic scaffold. The chapter ends with a discussion of the models employed and suggestions for further work.

6.2 The equations of poroelasticity

In this section, we present the governing equations of the Biot model of linear poroelasticity and a multiphase model suitable for studying a poroelastic scaffold saturated with a multiphase fluid. In each case, the derivation of the governing equations has been presented in scores of papers and much of the detail is omitted here; however, a discussion of the key modelling considerations is given and relevant literature is cited.

6.2.1 The Biot model of linear poroelasticity

The notation used to derive the Biot model of linear poroelasticity varies widely; the notation employed below is consistent with that used by Detournay & Cheng (1993) and Cowin (1999). In particular, we remark that in contrast to preceding chapters of this thesis, henceforth, we denote a *displacement* field by $\boldsymbol{u}$ and a *velocity* field by $\boldsymbol{v}$.

We consider an isotropic elastic material containing a single pore fluid. There is a well-developed formulation for anisotropic poroelastic media (Carroll, 1979; Thompson & Willis, 1991) and, given the heterogeneous nature of the PLLA scaffold and associated variation in mechanical properties (see §1.2.3, figure 1.3), this formulation is likely to be more appropriate; however, we present the isotropic case here for simplicity. The variables used to describe the poroelastic material are: the total stress $\boldsymbol{\sigma}^*$, the pore fluid pressure p^*, the strain in the solid phase $\boldsymbol{\varepsilon}$ and the variation in fluid content ζ (which is analogous to the change in fluid volume fraction employed in previous chapters). Each of these variables is defined by its average over a suitable control volume. We remark that in the following, the equations are given in dimensional form and the asterisks are omitted for brevity. In this formulation, the following conventions apply: $\sigma_{ij} < 0$ implies compression and $\zeta > 0$ corresponds to an increase in fluid content. The variation in fluid content is defined as "the volume of fluid imported into a control volume normalised by the control volume" due to a combination of the following three interconnected effects: (i) deformation of the material, (ii) a change in fluid pressure (which, for a compressible fluid leads to a change in fluid volume), and (iii) the presence of a source (Wang, 2000). It is defined by Berryman (1992) (after Biot (1962b), Biot (1973)) as follows:

$$\zeta = \frac{\delta V_p - \delta V_w}{V}, \tag{6.1}$$

where δV_p denotes the change in the pore volume and δV_w, the change in fluid volume as a result of deformation of the poroelastic material; V is the reference volume. This definition

is equivalent to that given by Biot (1962b, 1973) in which ζ was defined as "the fluid mass injected into a unit element of unit initial volume divided by the initial fluid density" (Berryman, 1992). For an incompressible fluid, $\delta V_w = 0$ and the variation in fluid content of the scaffold is determined by the change in pore volume; in this case, ζ is equivalent to the change in pore fluid volume fraction.

The governing equations are derived by considering the conservation of linear momentum for the fluid-filled material and conservation of mass for the pore fluid, obtaining:

$$\nabla \cdot \boldsymbol{\sigma} + \boldsymbol{b} = \mathbf{0}, \qquad \frac{\partial \zeta}{\partial t} + \nabla \cdot \boldsymbol{q} = \gamma, \tag{6.2a,b}$$

where $\boldsymbol{b}$ is a body force, γ is a fluid source (the rate of injected fluid volume per unit volume of the porous solid) and $\boldsymbol{q}$ is the fluid flow rate which describes the movement of the fluid relative to that of the solid (q_i is formally defined as the rate of fluid volume crossing a unit area of porous solid with normal $\hat{n}_i$ (Detournay & Cheng, 1993)). We remark that the quasi-static form of the momentum equation has been chosen here and inertial effects have been neglected for simplicity. Since the pore pressure must equilibrate over the averaging length scale, restrictions are placed upon the time-scale over which diffusion/deformation processes may be analysed and Detournay & Cheng (1993) note that it is "in the modelling of quasi-static processes that the Biot model finds its full justification even though it has been extended to the dynamic range."

There are many ways in which the constitutive laws of poroelasticity may be expressed. In the following, we choose the solid displacement ($\boldsymbol{u}$) and pore pressure (p) as dependent variables and now consider appropriate constitutive laws for the terms in equations (6.2). The deformations of the porous material are assumed to be small and the strain is therefore related to the displacement of the solid, $\boldsymbol{u}$, by the infinitesimal strain tensor:

$$\boldsymbol{\varepsilon} = \frac{1}{2}\left(\nabla \boldsymbol{u} + \nabla \boldsymbol{u}^T\right). \tag{6.3}$$

We write the stress-strain relation[1] as follows:

$$\boldsymbol{\sigma} = -\alpha p\, \mathbf{I} + G\left(\nabla \boldsymbol{u} + \nabla \boldsymbol{u}^T\right) + \frac{2G\nu}{1-2\nu}(\nabla \cdot \boldsymbol{u})\, \mathbf{I}. \tag{6.4}$$

in which G and ν are the shear modulus and the Poisson's ratio of the elastic material in the absence of a pore fluid and $\mathbf{I}$ is the identity matrix. The shear modulus (or modulus of rigidity) is the ratio of applied shear stress to shear strain; Poisson's ratio describes the compressibility of the material and is defined as the ratio of transverse contraction strain

[1] This may be interpreted as a constitutive law for the fluid-filled porous material.

(normal to the applied load) to longitudinal extension strain (in the direction of the applied load). The constitutive law for the fluid is as follows:

$$p = M(\zeta - \alpha \nabla \cdot \boldsymbol{u}), \tag{6.5}$$

in which M is the Biot modulus and α is the Biot-Willis coefficient (which also appears in (6.4)). The quantity $1/M$ is the storage coefficient at constant strain, defined as the increase in the amount of fluid per unit volume of porous material as a result of a unit increase of pore pressure at constant strain. The coefficient α is the ratio of the reduction (or gain) in fluid volume to the change in bulk volume due to compression (or extension) while the fluid is free to escape (the fluid pressure is kept constant). It may also be interpreted as an effective stress coefficient since the stress-strain relation (6.4) corresponds to that for an elastic material if we define $(\boldsymbol{\sigma} + \alpha p\, \mathbf{I})$ to be an effective stress. The Biot modulus, M may be expressed in terms of material parameters as follows (Detournay & Cheng, 1993):

$$M = \frac{2G(\nu_u - \nu)}{\alpha^2(1 - 2\nu_u)(1 - 2\nu)}, \tag{6.6}$$

where ν_u is the Poisson's ratio of the material in the undrained state, which describes the influence of the compressibility of the pore fluid on that of the poroelastic material. The undrained state refers to the scenario where the fluid is trapped in the porous solid: $\zeta = 0$.

Lastly, we assume that the fluid transport in the pore space can be described by Darcy's law which relates the fluid flow rate to the gradient of the pore pressure:

$$\boldsymbol{q} = -\kappa \nabla p - \boldsymbol{f}; \qquad \kappa = \frac{k}{\mu}, \tag{6.7}$$

wherein κ is the coefficient of permeability, k is the permeability of the porous material (a function of the porosity, θ), μ is the viscosity of the fluid and $\boldsymbol{f}$ is a body force term. We note that this body force term will, in general, be a constant and will therefore not appear in the final governing equation (6.2b).

The governing equations (6.2) may be written in terms of the dependent variables $\boldsymbol{u}$ and p using the above relations. Substituting the constitutive relation (6.4) into the momentum equation (6.2a) yields the following Navier-type equation for the solid displacement:

$$G\nabla^2 \boldsymbol{u} + \frac{G}{1 - 2\nu} \nabla \left(\nabla \cdot \boldsymbol{u} \right) = \alpha \nabla p - \boldsymbol{b}. \tag{6.8}$$

Similarly, combining Darcy's law (6.7), the constitutive relation (6.5) and the mass conservation equation (6.2b) yields a diffusion equation for the pore fluid pressure:

$$\frac{\partial p}{\partial t} - \kappa M \nabla^2 p = M(\gamma + \nabla \cdot \boldsymbol{f}) - \alpha M \frac{\partial}{\partial t} \nabla \cdot \boldsymbol{u}, \tag{6.9}$$

in which we have retained the force term $\boldsymbol{f}$ for the sake of generality. The terms $\boldsymbol{b}$ and $\boldsymbol{f}$ are generally interpreted as body forces due to gravity per unit volume of bulk material and fluid, respectively and are defined as follows:

$$\boldsymbol{b} = \big[(1-\theta)\rho_s + \theta\rho_w\big]\boldsymbol{g}, \qquad \boldsymbol{f} = \rho_w \boldsymbol{g}, \tag{6.10}$$

where $\boldsymbol{g}$ is the force due to gravity, ρ_w is the density of the pore fluid, ρ_s is the density of the elastic solid and θ is the porosity.

A similar pair of equations may be derived for the displacement and variation in fluid content, ζ; see Detournay & Cheng (1993) for more details. Lastly, we remark that if the stress, $\boldsymbol{\sigma}$, rather than the displacement is taken as the dependent variable, the following compatibility condition must be satisfied to ensure a single-valued displacement field (Detournay & Cheng, 1993; Cowin, 1999):

$$\varepsilon_{ij,jl} + \varepsilon_{kl,ij} = \varepsilon_{ik,jl} + \varepsilon_{jl,ik}. \tag{6.11}$$

In what follows we work with equations (6.8) and (6.9).

The constants ν, ν_u and α are dimensionless; the shear modulus, G, and Biot modulus, M, have units of pressure. Re-introducing asterisks to denote dimensional quantities, equations (6.8) and (6.9) may be non-dimensionalised by choosing the following dimensionless variables:

$$\boldsymbol{x}^* = L^*\boldsymbol{x}, \quad t^* = \frac{L^{*2}}{\kappa^* P^*}t, \quad \boldsymbol{u}^* = \delta L^* \boldsymbol{u}, \quad p^* = P^* p, \tag{6.12}$$

where L^* is a characteristic lengthscale (*e.g.* the length of the PLLA scaffold; see figure 1.2), $\delta \ll 1$ is a small parameter introduced so that the dimensionless displacement ($\boldsymbol{u}$) is of order one, and P^* is a pore fluid pressure scaling, determined below. For completeness, we note that we non-dimensionalise the pore fluid flux (given by equation (6.7)) as follows:

$$\boldsymbol{q}^* = \frac{\kappa^* P^*}{L^*}\boldsymbol{q}. \tag{6.13}$$

We remark that in order that the linear elasticity assumption (6.3) holds, we must have $\boldsymbol{u}^* \ll 1$; as discussed in §1.2.3, the PLLA scaffold is subject to relatively small strains (approximately 1.5%) so this is a reasonable assumption.

In the absence of body forces ($\boldsymbol{b} = \boldsymbol{f} = 0$) and mass sources ($\gamma = 0$), the dimensionless governing equations (6.8) and (6.9) are

$$\delta G \nabla^2 \boldsymbol{u} + \frac{\delta G}{1-2\nu}\nabla\left(\nabla\cdot\boldsymbol{u}\right) \;=\; \alpha\,\nabla p, \tag{6.14}$$

$$\frac{\partial p}{\partial t} - M\nabla^2 p \;=\; -\alpha\delta M \frac{\partial}{\partial t}\nabla\cdot\boldsymbol{u}, \tag{6.15}$$

in which the constants $(G, M) = (G^*, M^*)/P^*$ are the dimensionless shear and Biot moduli, respectively. The pressure scaling P^* is arbitrary, and in the following we choose $P^* = M^*$, implying $M = 1$ and $G = G^*/M^*$. In order that terms in equations (6.14) and (6.15) balance and in view of (6.7), we rescale $(p, \boldsymbol{q}) = \delta(\hat{p}, \hat{\boldsymbol{q}})$. Dropping the carets yields the following governing equations:

$$G\nabla^2 \boldsymbol{u} + \frac{G}{1-2\nu}\nabla\left(\nabla \cdot \boldsymbol{u}\right) \;=\; \alpha\, \nabla p, \tag{6.16}$$

$$\frac{\partial p}{\partial t} - \nabla^2 p \;=\; -\alpha \frac{\partial}{\partial t}\nabla \cdot \boldsymbol{u}. \tag{6.17}$$

The dimensionless parameters in this model are G, ν, and α. The magnitude of poroelastic effects is controlled by α and G since equation (6.6) indicates that given α and ν, the choice of G defines ν_u. The parameter ν is a drained material property; $\nu > -1$ is a standard constraint in the theory of elasticity and an incompressible elastic material has $\nu = 0.5$. Materials with negative Poisson's ratio (first reported by Lakes (1987)) are known as auxetics and exhibit transverse expansion (compression) when stretched (compressed) longitudinally. The range of the Biot-Willis coefficient is $\alpha \in [0, 1]$ and, since the presence of pore fluid decreases compressibility, we note also that the undrained Poisson's ratio introduced in equation (6.6) is $\nu_u \in [\nu, 0.5]$.

Lastly, we note that for incompressible constituents (compression of the material may still arise via redistribution of fluid and solid components), we have $\alpha = 1$, $\nu = 0.5$. Returning to equation (6.6), we find that this implies $M \longrightarrow \infty$ and the constitutive law (6.5) for the fluid response therefore reduces to $\zeta = \nabla \cdot \boldsymbol{u}$ implying that the change of volume of the porous solid and the variation in fluid content balance (*cf.* equation (6.1) with $\delta V_w = 0$).

6.2.2 A multiphase model for construct growth and deformation

In this section, the general multiphase formulation given in §1.5 is specialised to model the interaction between a multiphase fluid and a poroelastic material. Similar models have been given extensive treatment in the literature; see, for instance, De Boer (1998), Ambrosi (2002) and Ahmadi *et al.* (2003) and we draw on these studies and others to motivate our constitutive modelling assumptions in the following derivation.

We consider a multiphase fluid comprising an arbitrary number of phases (N) contained within a deformable porous medium. We denote the averaged volume fraction of each phase by ϕ_i and associate with each phase a volume-averaged displacement, $\boldsymbol{u}_i$, velocity, $\boldsymbol{v}_i$,

pressure, p_i and stress tensor, $\boldsymbol{\sigma}_i$; $i = s, 1, \ldots, N$, where s denotes the poroelastic scaffold. The averaged governing equations are as follows (see §1.5):
no voids (saturation):

$$\sum_{i=s,1}^{N} \phi_i = 1, \tag{6.18}$$

conservation of mass:

$$\frac{\partial \phi_i}{\partial t} + \nabla \cdot (\phi_i \boldsymbol{v}_i) = S_i \; ; \quad S_i = \sum_{j \neq i} \frac{S_{ij}}{\rho_i}, \tag{6.19}$$

$$\sum_{i=s,1}^{N} \nabla \cdot (\phi_i \boldsymbol{v}_i) = 0, \tag{6.20}$$

conservation of momentum:

$$\nabla \cdot (\phi_i \boldsymbol{\sigma}_i) + \sum_{j \neq i} \mathbf{F}_{ij} = \mathbf{0}, \tag{6.21}$$

$$\nabla \cdot \left\{ \sum_{i=s,1}^{N} \phi_i \boldsymbol{\sigma}_i \right\} = \mathbf{0}. \tag{6.22}$$

In equation (6.19), S_{ij}/ρ_i is the net averaged macroscopic rate at which material is transferred into phase i from phase j, the total rate of transfer into phase i is denoted S_i (which we assume obeys $\sum S_i = 0$ as implied by equation (6.20)) and ρ_i denotes the density of phase i. For multiphase systems in which mass transfer between phases involves negligible changes in density, it may be assumed that $\rho_i = \rho$. In (6.21), $\mathbf{F}_{ij}$ is the interphase force exerted by phase j on phase i and we assume that $\mathbf{F}_{ij} = -\mathbf{F}_{ji}$ as implied by (6.22).

We now turn our attention to specifying appropriate constitutive laws for each phase. To model the behaviour of the poroelastic matrix, we employ the standard constitutive relation of linear poroelasticity, and we assume that each of the fluid phases contained within the poroelastic material is viscous. The stress tensors for each phase are therefore as follows:

$$\boldsymbol{\sigma}_s = -p_s \, \mathbf{I} + G \left(\nabla \boldsymbol{u}_s + \nabla \boldsymbol{u}_s^T \right) + \frac{2G\nu}{1-2\nu} \left(\nabla \cdot \boldsymbol{u}_s \right) \, \mathbf{I}, \tag{6.23a}$$

$$\boldsymbol{\sigma}_i = -p_i \, \mathbf{I} + \mu_i \left(\nabla \boldsymbol{v}_i + \nabla \boldsymbol{v}_i^T \right) + \lambda_i \nabla \cdot \boldsymbol{v}_i \, \mathbf{I}; \quad i = 1, \ldots, N. \tag{6.23b}$$

We note here that although we employ an elastic constitutive relation for the solid phase, equations (6.19) carry the tacit assumption that each phase is intrinsically incompressible (see §§1.4 and 1.5); within this model, compression of the material therefore arises from redistribution of fluid and solid components (Barry & Holmes, 2001). The parameters μ_i, λ_i G, ν have the same meanings as previously (chapters 2, 3 and §6.2.1). Since the elastic

porous material is incompressible we have $\nu = 0.5$; however, since $\nabla \cdot \boldsymbol{u}_s = 0$, the final term in (6.23a) remains finite and we absorb this into p_s so that

$$\boldsymbol{\sigma}_s = -p_s\,\mathbf{I} + G\left(\nabla \boldsymbol{u}_s + \nabla \boldsymbol{u}_s^T\right)\mathbf{I}. \tag{6.24}$$

Finally, employing equations (1.46)–(1.48) (see §1.5), we arrive at the following forms for the interphase force terms ($\mathbf{F}_{ij}$), interphase pressures (p_{ij}) and intraphase pressure in the fluid phases (p_i):

$$\mathbf{F}_{ij} = p_{ij}\phi_j\nabla\phi_i - p_{ji}\phi_i\nabla\phi_j + K_{ij}(\boldsymbol{v}_j - \boldsymbol{v}_i), \tag{6.25}$$

$$p_{ij} = p + \psi_{ij}, \tag{6.26}$$

$$p_i = p + \Sigma_i + \sum_{j\neq i}\phi_j\psi_{ij}, \tag{6.27}$$

in which $p_{ij} = p_{ji}$ is the *interphase* pressure exerted by phase j on i, $K_{ij} = K_{ji}$ is the coefficient of viscous drag and p is a common "mixture" pressure. The function, p_s, is interpreted as the pressure exerted by the multiphase fluid on the poroelastic matrix and often defined in terms of this mixture pressure: $p_s = \phi_s p$ (Barry & Holmes, 2001; Ambrosi, 2002). The functions $\psi_{ij} = \psi_{ji}$ and Σ_i are additional contributions to the pressure resulting from interphase tractions and intraphase interactions respectively, whose definition (together with appropriate initial and boundary conditions) completes the model.

We remark here that this formulation follows the methodology of Lemon *et al.* (2006) and others (see §1.5 for appropriate references) and is consistent with that employed by (for instance) Katsube (1985), Katsube & Carroll (1987) and Barocas & Tranquillo (1997); however, it deviates from many similar mixture theory models of poroelastic materials in the form of the momentum equation (6.21) and constitutive laws (6.23) employed. For instance, defining the intraphase pressures by $p_i = \phi_i p$ (where p is a common mixture pressure) in the constitutive equations (6.23) and writing the momentum equations as follows:

$$\nabla \cdot \boldsymbol{\sigma}_i + \sum_{j\neq i}\mathbf{F}_{ij} = \mathbf{0}; \quad i = s, 1, \ldots, N, \tag{6.28}$$

yields a model whose form is similar to that employed by Preziosi *et al.* (1996), De Boer (1998), Lai & Mow (1999) and Ambrosi (2002). We remark that these authors (and others) derive their constitutive laws via thermodynamic considerations and appeal to the second law of thermodynamics to constrain their constitutive choices. Additionally, the method of Lagrange multipliers is used to motivate the inclusion of the pore pressure in the above form. As previously, we do not treat thermodynamical considerations in detail in this derivation,

nor is a discussion of the Lagrange multiplier method given. We remark, however, that the pressure, p, given above may be interpreted as a Lagrange multiplier that enables the constraint (6.20) to be satisfied (Ambrosi, 2002). The constitutive laws (6.23) employed here are considerably simpler than those derived via thermodynamical considerations in, for example, Bowen (1982) or Ahmadi *et al.* (2003), allowing analysis of the model to be undertaken more easily.

Correspondence between this formulation, with (6.28) used in preference to (6.21), and that of Biot may be demonstrated by considering a two-phase mixture of a deformable solid (s) and fluid (w) with no sources or sinks. We assume that the viscosity of the fluid is negligible compared to momentum transfer terms ($\mathbf{F}_{ij}$) in the momentum equations and therefore set $\mu_w = \lambda_w = 0$ (Barry & Holmes, 2001). We further assume that the two phases interact *only* through the interphase drag term in equation (6.28) so that $\psi_{ws} = 0 = \Sigma_w$. Interpreting the "mixture pressure" introduced in (6.26) as the pore fluid pressure and employing the momentum equations in the form given in equation (6.28) we obtain the following equations:

Mass conservation:
$$\frac{\partial w}{\partial t} + \nabla \cdot (w \boldsymbol{v}_w) = 0, \tag{6.29}$$
$$\nabla \cdot (w \boldsymbol{v}_w + s \frac{\partial \boldsymbol{u}}{\partial t}) = 0. \tag{6.30}$$

Conservation of momentum:
$$\kappa \nabla p = \frac{\partial \boldsymbol{u}}{\partial t} - \boldsymbol{v}_w, \tag{6.31}$$
$$\nabla p = G \nabla^2 \boldsymbol{u}. \tag{6.32}$$

It may be readily observed that these are the equations of linear poroelasticity for incompressible constituents (where the coefficient of permeability is given by $\kappa = w/K_{ws}$).

In the proceeding sections of this chapter, we present solutions to these two models subject to appropriate boundary and initial conditions relevant to the bioreactor system introduced in §1.2.3. In §6.3, we present solutions to equations (6.16) and (6.17); analytic solutions are obtained in the uniaxial limit in §6.3.1 and numerical simulations of the full two-dimensional problem are presented in §6.3.2. In §6.4 one-dimensional numerical solutions to the multiphase model (6.29)–(6.32) are presented.

6.3 Solution: The Biot model of linear poroelasticity

We now investigate the effect of the periodic compression of the PLLA scaffold outlined in §1.2.3 on the solid stress distribution and fluid flow within the scaffold. Analytic and

numerical solutions to the Biot model of linear poroelasticity (see equations (6.16) and (6.17)) are presented and their relevance discussed.

To represent the perfusion/compression system of El-Haj *et al.*, we choose a (dimensionless) Cartesian coordinate system $\boldsymbol{x} = (x, y)$ with corresponding coordinate directions $(\hat{\boldsymbol{x}}, \hat{\boldsymbol{y}})$ and we consider a two-dimensional, rigid-walled channel occupying $0 \leqslant x \leqslant 1$, $0 \leqslant y \leqslant 1$ containing a PLLA scaffold saturated with culture medium; for simplicity, we neglect the presence of the cells in this model. Modelling a cell population within the scaffold is naturally accommodated by the multiphase formulation given above, in which (for instance) a viscous cell phase may be considered in addition to the pore fluid. We model the PLLA scaffold as a poroelastic solid and assume that viscous effects associated with the culture medium may be adequately represented by a Darcy-type model, allowing us to exploit the Biot formulation given in §6.2.1. Compression of the scaffold by the piston is modelled by an imposed periodic displacement at $x = 0$; perfusion may be incorporated via an imposed pressure-driven flow. The geometry, dimensionless governing equations (in the absence of mass sources and body forces) and appropriate boundary conditions are illustrated in figure 6.1.

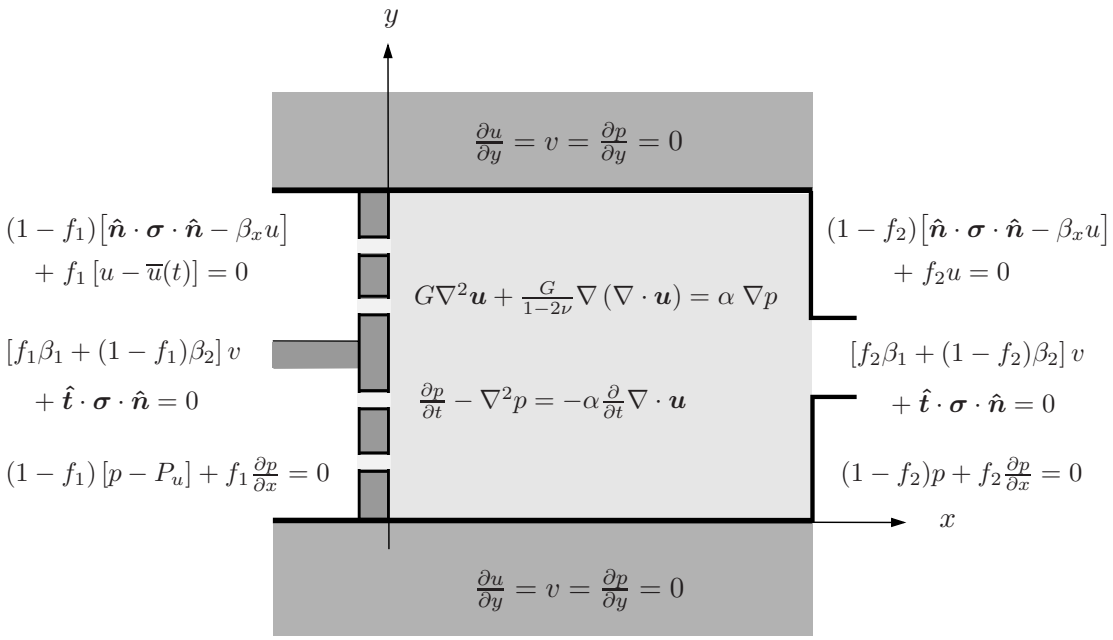

Figure 6.1: The dimensionless governing equations and general boundary conditions for the poroelastic scaffold model. The functions $f_1(y)$ and $f_2(y)$ distinguish the regions occupied by the perforations and outlet from the wall.

We now pause to explain the significance of the boundary conditions prescribed in figure

6.1. Since the channel walls ($y = 0, 1$) are rigid and impermeable, we require no transverse displacement ($v = 0$) and no-penetration of fluid there (we emphasise here that $\boldsymbol{u} = (u, v)$ represents displacement). In view of equation (6.7), $\partial p/\partial y = 0$ ensures no-penetration. In addition, we demand that the tangential stress at the channel wall is zero. The stresses in the poroelastic material (normal and tangential to the channel walls) are defined:

$$\hat{\boldsymbol{n}} \cdot \boldsymbol{\sigma} \cdot \hat{\boldsymbol{n}} = -\alpha\delta p + \frac{2\delta G(1-\nu)}{1-2\nu}\frac{\partial u}{\partial x} + \frac{2\delta G\nu}{1-2\nu}\frac{\partial v}{\partial y}, \tag{6.33}$$

$$\hat{\boldsymbol{t}} \cdot \boldsymbol{\sigma} \cdot \hat{\boldsymbol{n}} = -\delta G\left(\frac{\partial u}{\partial y} + \frac{\partial v}{\partial x}\right), \tag{6.34}$$

for unit inward normal and tangent vectors $\hat{\boldsymbol{n}}$, $\hat{\boldsymbol{t}}$. Taking the zero transverse displacement condition into account, imposing $\partial u/\partial y = 0$ on $y = 0, 1$, ensures that the tangential stress at the channel walls is zero. We note that for $\mathcal{O}(1)$ pressure and displacement gradient, equations (6.33) and (6.34) indicate that the solid stress induced is $\mathcal{O}(\delta)$; in the following, we therefore rescale $\boldsymbol{\sigma} = \delta\hat{\boldsymbol{\sigma}}$.

As illustrated in figure 6.1, the bioreactor system contains a perforated piston, allowing both compression and perfusion; downstream, the scaffold is constrained by an impermeable wall, with a fluid outlet at its centre. To model these features, we impose discontinuous boundary conditions on the pressure and displacement at $x = 0, 1$. We introduce two functions $f_1(y)$ and $f_2(y)$ which distinguish the regions occupied by the piston (or wall) from those occupied by a perforation (or the outlet):

$$f_1(y) = \begin{cases} 0 & \text{if } y \text{ is within a perforation,} \\ 1 & \text{otherwise.} \end{cases} \tag{6.35}$$

The function $f_2(y)$ is defined similarly to distinguish the downstream constraining wall from the outlet. In regions where there are perforations, we impose $p = P_u$ so that the flow through the perforations is determined by the difference between P_u and the pore fluid pressure in the scaffold ($P_u = 0$ allows unrestricted flow through the perforations upon compression due to the absence of an imposed upstream pressure); elsewhere, we require that $\partial p/\partial x = 0$ since, aside from the perforations, no fluid flows through the piston. In addition, we prescribe a time-dependent displacement, $u = \overline{u}(t)$ to represent the compression of the piston. A suitable choice for this time-dependent displacement is $\overline{u} = \Re\left\{Ue^{i\omega t}\right\}$, where U is the amplitude and ω, the dimensionless frequency of the forcing. In the perforated regions, where the piston is not in contact with the scaffold, we allow the axial displacement to adjust according to the normal stress experienced by the scaffold. Dropping the carets

for brevity, we obtain:

$$\hat{\boldsymbol{n}} \cdot \boldsymbol{\sigma} \cdot \hat{\boldsymbol{n}} = \beta_x u, \tag{6.36}$$

yielding

$$-\alpha P_u + \frac{2G(1-\nu)}{1-2\nu}\frac{\partial u}{\partial x} + \frac{2G}{1-2\nu}\frac{\partial v}{\partial y} = \beta_x u, \tag{6.37}$$

wherein β_x is the axial "slip coefficient". Slip is allowed in the transverse direction on $x = 0, 1$ so, in a similar manner, we allow the transverse displacement to adjust according to the tangential stress as follows:

$$\hat{\boldsymbol{t}} \cdot \boldsymbol{\sigma} \cdot \hat{\boldsymbol{n}} = \beta_y(y) v, \tag{6.38}$$

to give

$$G\left(\frac{\partial u}{\partial y} + \frac{\partial v}{\partial x}\right) = \beta_y(y) v, \tag{6.39}$$

where the slip coefficient β_y takes the value $\beta_y = \beta_1$ within a perforation (or the outlet) and $\beta_y = \beta_2$ on the piston (or the wall) and $\beta_2 = 0$ implies that the tangential stress at $x = 0, 1$ is zero and the scaffold is free to slip along the piston (or wall) as on $y = 0, 1$.

6.3.1 Uniaxial model simplification

We simplify the two-dimensional system described above by assuming that all variables vary in the axial direction only. The y-dependent boundary conditions at $x = 0, 1$ representing the piston and outlet will therefore require modification. Appropriate conditions are discussed later in this section. We note that the steps involved in this derivation are straightforward and stated in many studies of classical poroelasticity, for example, Detournay & Cheng (1993) and Wang (2000) and so much of the detail is omitted.

Assuming axial variations only, equations (6.16) and (6.17) reduce to give:

$$\frac{2G(1-\nu)}{1-2\nu}\frac{\partial^2 u}{\partial x^2} = \alpha\,\frac{\partial p}{\partial x}, \quad \frac{\partial p}{\partial t} - \frac{\partial^2 p}{\partial x^2} = -\alpha\frac{\partial^2 u}{\partial x \partial t}. \tag{6.40a,b}$$

Taking a first integral of equation (6.40a) and substituting into (6.40b) yields:

$$\frac{\partial p}{\partial t} - \frac{1}{S}\frac{\partial^2 p}{\partial x^2} = -\frac{\alpha}{S}\frac{\mathrm{d}g}{\mathrm{d}t}, \tag{6.41}$$

where $g(t)$ is an arbitrary function of time arising from the integration, and the dimensionless storage coefficient for uniaxial strain, S, is defined as follows:

$$S = 1 + \frac{\alpha^2(1-2\nu)}{2G(1-\nu)}. \tag{6.42}$$

By considering the stress tensor (6.4) and equation (6.40a), it is possible to show that the function $g(t)$ is related to the stress tensor via:

$$\sigma_{kk} = -\frac{\alpha(1-2\nu)}{(1-\nu)}p + \frac{2G}{1-2\nu}g(t), \tag{6.43}$$

where the repeated subscript, k, indicates the summation convention. Noting further that the components of the stress σ_{yy}, σ_{xx} are as follows:

$$\sigma_{yy} = -\alpha p + \frac{2G\nu}{1-2\nu}\frac{\partial u}{\partial x}, \quad \sigma_{xx} = -\alpha p + \frac{2G(1-\nu)}{1-2\nu}\frac{\partial u}{\partial x}, \tag{6.44}$$

and eliminating $\partial u/\partial x$, we deduce that

$$\sigma_{kk} = \frac{1}{(1-\nu)}\sigma_{xx} - \frac{\alpha(1-2\nu)}{(1-\nu)}p. \tag{6.45}$$

The equation for the pore pressure may then be expressed:

$$\frac{\partial p}{\partial t} - \frac{1}{S}\frac{\partial^2 p}{\partial x^2} = -\gamma\frac{\mathrm{d}}{\mathrm{d}t}(\sigma_{xx}), \tag{6.46}$$

where, from the one-dimensional momentum equation (6.2) in the absence of body forces, the axial stress is $\sigma_{xx} = \sigma_{xx}(t)$. The parameter, γ is known as the "loading efficiency" (Wang, 2000) and is given by

$$\gamma = \frac{\alpha(1-2\nu)}{2GS(1-\nu)}. \tag{6.47}$$

Lastly, integrating (6.40a) and using equations (6.43) and (6.45) to determine $g(t)$, it may be shown that the axial displacement is governed by the following equation:

$$\frac{\partial u}{\partial x} = \frac{\alpha(1-2\nu)}{2G(1-\nu)}\,p + \frac{1-2\nu}{2G(1-\nu)}\sigma_{xx}. \tag{6.48}$$

We emphasise that this derivation is not new and merely recapitulates that given in, for instance, Wang (2000).

Returning to the problem illustrated by figure 6.1, we may exploit the above formulation to obtain analytic solutions to a simplified version of this problem. The governing equations are (6.46) and (6.48). Since the governing equation for the pore pressure (6.46) is expressed in terms of the axial stress (which, as remarked above, is independent of the axial coordinate), we reformulate the problem in terms of an applied periodic stress at $x = 0$ in place of an imposed displacement, and appropriate boundary conditions are:

$$\sigma_{xx} = -\overline{\sigma}\,\Re\left\{e^{i\omega t}\right\}, \quad p = P_u, \quad \text{at } x = 0, \tag{6.49a,b}$$

$$u = 0, \qquad p = 0, \quad \text{at } x = 1. \tag{6.50a,b}$$

These boundary conditions define a system that is similar to that illustrated by figure 6.1, representing a one-dimensional scaffold subject to an imposed pressure-driven flow and periodic stress (of amplitude $\overline{\sigma}$) supplied via a permeable piston at $x = 0$ and restrained by a permeable barrier at $x = 1$. Recalling that $\sigma_{xx} = \sigma_{xx}(t)$, equation (6.49a) defines the axial stress along the scaffold length; (6.46) may then be solved subject to (6.49b) and (6.50b) to yield the pore pressure; (6.48) together with the zero displacement condition at $x = 1$ then defines the corresponding displacement field. We remark that the material is initially under compression since $\sigma_{xx}(t = 0) < 0$.

Guided by the periodicity of the imposed stress (6.49a), we simplify the analysis by seeking separable solutions for the pressure and displacement of the following form:

$$p(x,t) = \Re\left\{\widetilde{p}(x)e^{i\omega t}\right\}, \quad u(x,t) = \Re\left\{\widetilde{u}(x)e^{i\omega t}\right\}, \tag{6.51}$$

and note that this expansion is consistent with (6.49b) only in the case $P_u = 0$. We therefore neglect the effect of imposed perfusion in this analysis. It is a simple calculation to solve the resulting ordinary differential equation for $\widetilde{p}$ subject to the boundary conditions (6.49b), (6.50b) (for $P_u = 0$) to obtain:

$$\widetilde{p}(x) = -\gamma\overline{\sigma}\left\{\cosh(\lambda x) + \big[\mathrm{cosech}(\lambda) - \coth(\lambda)\big]\sinh(\lambda x) - 1\right\}, \tag{6.52}$$

where the complex wavenumber, λ, is defined $\lambda = \sqrt{i\omega S}$. The corresponding displacement may be obtained by integrating equation (6.48) and imposing (6.50a) to yield:

$$\begin{aligned}\widetilde{u}(x) = \frac{\gamma\overline{\sigma}}{\lambda}\frac{\alpha(1-2\nu)}{2G(1-\nu)}\Big\{&\big[\mathrm{cosech}(\lambda) - \coth(\lambda)\big]\big[\cosh(\lambda) - \cosh(\lambda x)\big] \\ &- \big[\sinh(\lambda x) - \sinh(\lambda)\big]\Big\} - \frac{\overline{\sigma}(1-2\nu)}{2G(1-\nu)}(1-\gamma\alpha)(x-1).\end{aligned} \tag{6.53}$$

Solutions for the scenario in which the scaffold is subjected to periodic forcing with no flow permitted at the downstream end may be obtained in a similar manner. We denote the pressure and displacement fields in this regime by $\widetilde{p}_{nf}$, $\widetilde{u}_{nf}$ and solve equations (6.46) and (6.48) subject to (6.49a), (6.49b), (6.50a) and $\partial\widetilde{p}_{nf}/\partial x = 0$ at $x = 1$, yielding the following solutions (this case has been treated in some detail in the literature; see, for example, Detournay & Cheng (1993) and Wang (2000)):

$$\widetilde{p}_{nf}(x) = \gamma\overline{\sigma}\big[\tanh(\lambda)\sinh(\lambda x) - \cosh(\lambda x) + 1\big], \tag{6.54}$$

$$\begin{aligned}\widetilde{u}_{nf}(x) = = -\frac{\alpha(1-2\nu)}{2G(1-\nu)}\frac{\gamma\overline{\sigma}}{\lambda}&\big[\sinh(\lambda x) - \tanh(\lambda)\cosh(\lambda x)\big] \\ &- \frac{\overline{\sigma}(1-2\nu)}{2G(1-\nu)}(1-\gamma\alpha)(x-1).\end{aligned} \tag{6.55}$$

In a tissue-engineering context, solutions (6.52) and (6.53) represent the displacement and pressure in the situation where the compression-induced flow is free to perfuse the entire scaffold, through the perforated piston at $x = 0$ and the outlet at $x = 1$. In contrast, (6.54) and (6.55) represent the behaviour when flow through the outlet is precluded. Henceforth, we refer to these cases as periodic compression coupled with free perfusion and hydrostatic loading, respectively.

Insight may be gained into the nature of the frequency-dependent poroelastic response in each case by considering the displacement of the poroelastic scaffold at $x = 0$ in the high frequency ($\lambda(\omega) \longrightarrow \infty$) and low frequency ($\lambda(\omega) \longrightarrow 0$) limits. Re-introducing the undrained Poisson's ratio, ν_u, through the relationship (equation (3.81), Wang (2000)):

$$\gamma \frac{\alpha(1-2\nu)}{2G(1-\nu)} = \frac{1}{K_v} - \frac{1}{K_v^{(u)}}, \tag{6.56}$$

in which the dimensionless drained and undrained uniaxial compressibility are defined (Wang, 2000):

$$K_v = \frac{2G(1-\nu)}{1-2\nu}, \qquad K_v^{(u)} = \frac{2G(1-\nu_u)}{1-2\nu_u}, \tag{6.57}$$

we find that for both the free-perfusion and hydrostatic loading regimes described above, the displacement at $x = 0$ is

$$\omega \longrightarrow 0: \quad \widetilde{u}(0) = \frac{\overline{\sigma}}{K_v}; \qquad \omega \longrightarrow \infty: \quad \widetilde{u}(0) = \frac{\overline{\sigma}}{K_v^{(u)}}, \tag{6.58}$$

as given in Wang (2000) for the hydrostatic loading case. This analysis indicates that for high frequency loading, the compressibility of the poroelastic material is regulated by the undrained Poisson's ratio, ν_u, since there is insufficient time for pore fluid flow to take place; conversely, for low frequency loading, the drained Poisson's ratio, ν, governs the material's compressibility. It should be remarked that in the high frequency case, inertial effects will become important (see Detournay & Cheng (1993) and references therein); however, we do not consider their influence here.

In figure 6.2, we compare the predicted solid displacement field in the poroelastic material under compression for the cases of free-perfusion (6.53) and hydrostatic loading (6.55) over one compression-extension cycle ($t = 0$ corresponds to compression: $\sigma_{xx} = -\overline{\sigma}$; $t = \pi/2\omega$ corresponds to no applied load; $t = \pi\omega$ corresponds to extension: $\sigma_{xx} = \overline{\sigma}$). In figure 6.3 we present the corresponding pressure profiles; and in figure 6.4 we compare the evolution of the maximum (absolute) value of the displacement and pressure in each case. Figures 6.5a,b show an illustrative fluid flux profile at $t = 0$ and the shear stress

associated with each case. As in previous chapters, the compression-induced fluid shear (τ) is assumed to be proportional to the pressure gradient ($\tau = |\partial p/\partial x|$). The pore fluid flux is determined by the pressure gradient and, although not explicitly captured in this macroscale one-dimensional model, the level of fluid shear stress at the pore surface is proportional to the fluid flux. We therefore consider that $\tau = |\partial p/\partial x|$ is an appropriate measure of shear stress.

Mechanical testing undertaken at ISTM, Keele University indicates that, since the scaffold is highly porous (see §1.2.3), axial compression results in minimal transverse expansion (μCT scans at a resolution of 15μm yielded no observable expansion[2]) and the effective Poisson's ratio for the scaffold is therefore $\nu \ll 1$. In the following we therefore choose $\nu = 0.1$. Upon specification of the Biot-Willis coefficient (α) and the dimensionless shear modulus (G) the dimensionless version of equation (6.6) yields the undrained Poisson's ratio, ν_u. In the results presented in figures 6.2–6.5, we choose $\alpha = 0.7$, $G = 1$ which implies $\nu_u = 0.21$. We emphasise that the values for the parameters G and α are not known; rather they are chosen to illustrate the behaviour of the system.

In figures 6.6–6.8 we demonstrate the effect of varying the dimensionless shear modulus (G), Poisson's ratio (ν) and Biot-Willis coefficient (α) on the material's behaviour in the free-perfusion regime.

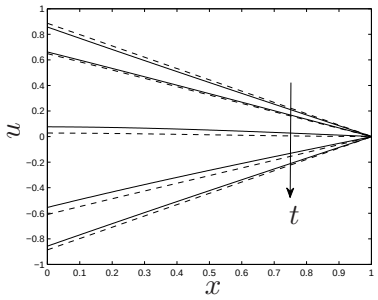

Figure 6.2: A comparison of the solid displacement in a poroelastic material subject to periodic forcing and, either free-perfusion (- -) (equation (6.53)) or hydrostatic loading (–) (equation (6.55)) at $t = 0, \pi/4, \pi/2, 3\pi/4, \pi$. Parameter values: $G = 1.176$, $\nu = 0.1$, $\alpha = 0.7$, $\overline{\sigma} = 2$, $\omega = 1$, $P_u = 0$.

Figure 6.2 indicates that the poroelastic material is less compliant under hydrostatic loading than free-perfusion, as evidenced by the reduced displacement in the former case. Due to inhibited pore fluid flow through the material, the time-dependent behaviour of the material under periodic forcing lags behind that predicted for the free-perfusion regime.

[2]We are grateful to E. Baas, ISTM, Keele University for the provision of this data.

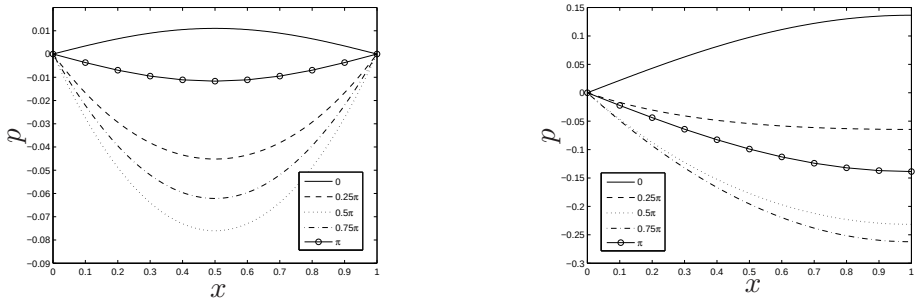

(a) (b)

Figure 6.3: A comparison of pore fluid pressure in a poroelastic material subject to periodic forcing and (a) free perfusion (equation (6.52)), (b) hydrostatic loading (equation (6.54)) at $t = 0, \pi/4, \pi/2, 3\pi/4, \pi$. Parameter values as in figure 6.2.

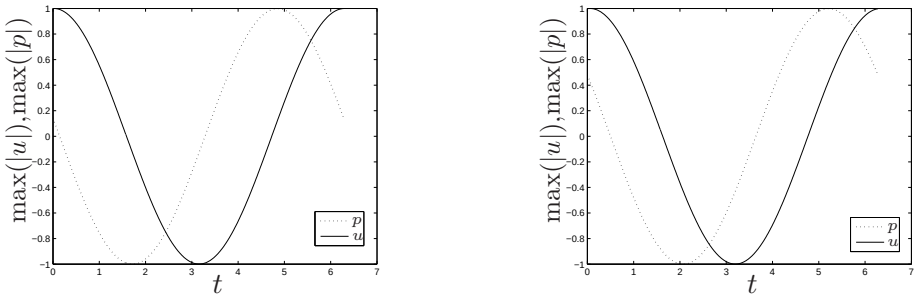

(a) (b)

Figure 6.4: A comparison of the temporal variation of the maximum (absolute) value of the displacement and pressure (normalised on the maximum amplitude of u or p) in a poroelastic material subject to periodic forcing and, (a) free-perfusion and (b) hydrostatic loading. Parameter values as in figure 6.2.

Comparison of the predicted displacement fields in the poroelastic material shows that under hydrostatic loading, the level of initial compression is reduced and the material relaxes more slowly on removal of this load ($0 < t < \pi/2$); under extension ($\pi/2 < t < \pi$) the material exhibits corresponding behaviour. The displacement field is approximately linear in each loading regime. Figures 6.3a,b show the dramatic difference in pore pressure in each case. Under compression and free perfusion, a parabolic profile is obtained since the pressure must equalise with the exterior at $x = 0, 1$. We remark that under hydrostatic loading, the pore pressure is an order of magnitude larger than that obtained under free perfusion. Comparison between the periodicity of the applied load given by (6.49a) and the evolution

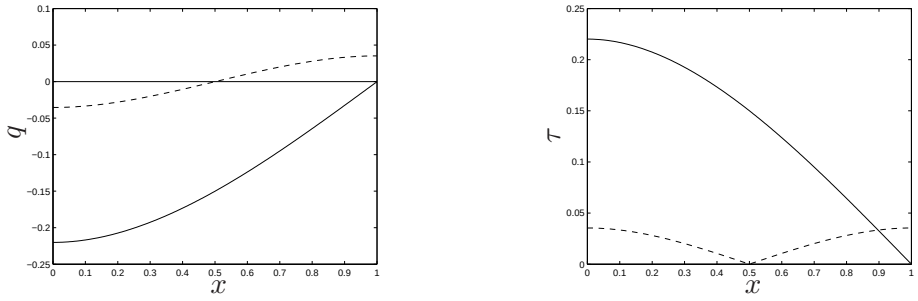

(a) (b)

Figure 6.5: A comparison of (a) the fluid flux; and (b) an approximation to the fluid shear stress in a poroelastic material subject to periodic forcing and, free-perfusion (- -) or hydrostatic loading (–) at $t = 0$. Parameter values as in figure 6.2.

of the displacement and pressure (figures 6.2 and 6.3) shows that there is a time lag between the applied load (and the resulting displacement) and the dissipation of pore fluid pressure. Figure 6.4 clearly shows the phase difference between the displacement (which is in phase with the imposed stress) and the corresponding pore fluid pressure in each loading regime, indicating that this effect is more pronounced in the free-perfusion case.

The differences in the pore pressure in each loading regime clearly have a profound impact on the induced fluid flux ($q = -\partial p/\partial x$). The flux in each case is shown in figure 6.5a. In the free-perfusion case, fluid escapes upstream through the piston and downstream through the outlet symmetrically; in the hydrostatic loading case, flow is only in the upstream direction with no flow permitted at $x = 1$. In the context of *in vitro* tissue engineering, the compression-induced mechanostimulation provided to the cells is therefore very different in each case. For example, from figure 6.5b, which shows the shear stress in each regime, it is clear that the maximum shear stress induced in the hydrostatic loading regime is greater than that in the free-perfusion case, in which maxima are achieved at the piston and outlet. We note also that within this one-dimensional framework, the solid stress is prescribed by equation (6.49a) and is constant throughout the material.

The rigidity of the material is controlled by G; figure 6.6 shows that increasing the shear modulus of the poroelastic matrix dramatically reduces the degree of compression in response to the applied load, the corresponding pore pressure being reduced also. The value of Poisson's ratio characterises the compressibility of the material. Figure 6.7 shows that increasing ν causes a small reduction in the displacement, and corresponding reduction in pore fluid pressure. The Biot-Willis coefficient is an effective stress coefficient for the

poroelastic material; an increase in α therefore results in increased stress and greater pore fluid pressure. We note that the solid displacement is very weakly affected by varying the Biot-Willis coefficient (α) and so those results are not presented here.

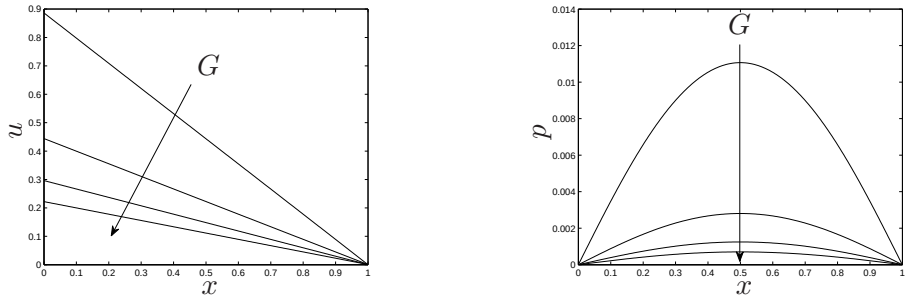

(a) (b)

Figure 6.6: The effect of varying the shear modulus, G, on the displacement and pore fluid pressure in a poroelastic material subject to periodic forcing and free-perfusion at $t = 0$; $G = 1, 2, 3, 4$. The arrows show the direction of increasing G, other parameter values as in figure 6.2.

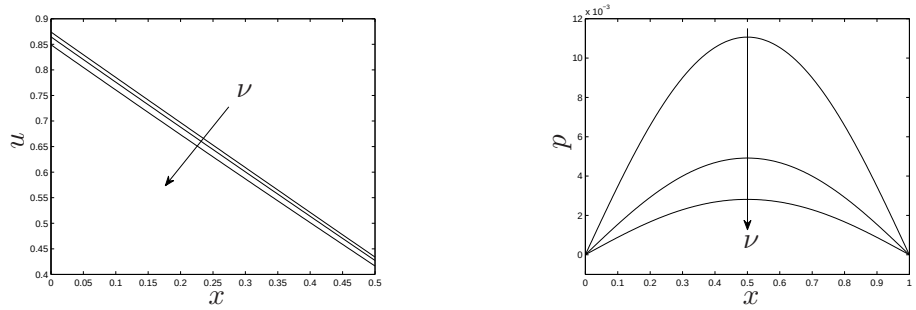

(a) (b)

Figure 6.7: The effect of varying the Poisson's ratio (ν) on the displacement and pore fluid pressure in a poroelastic material subject to periodic forcing and free-perfusion at $t = 0$; $\nu = 0.1, 0.2, 0.3$. The arrows show the direction of increasing ν, other parameter values as in figure 6.2.

Relevance to tissue engineering

The results presented in figures 6.2–6.8 illustrate how the loading regime and scaffold material parameters may influence mechanotransduction processes in tissue engineering.

Figures 6.2–6.5 indicate that the presence of an outlet in the bioreactor system results in

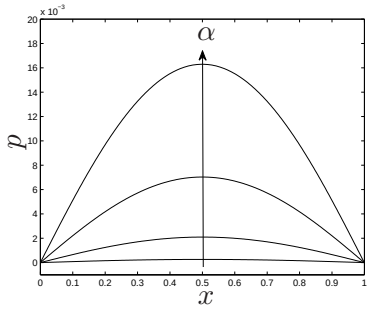

Figure 6.8: The effect of varying the Biot-Willis coefficient (α) on the pore fluid pressure in a poroelastic material subject to periodic forcing and free-perfusion at $t = 0$; $\alpha = 0.2, 0.4, 0.6, 0.8$. The arrows show the direction of increasing α, other parameter values as in figure 6.2.

dramatically reduced culture medium pressure, flux and shear stress (apart from near $x = 1$ where the flow through the outlet ensures that the flux and shear stress are larger than that at the impermeable wall) and marginally increased scaffold compliance. Self-evidently, this will have a marked impact on the growth and differentiation of the cell population contained within the scaffold. Depending upon the mechanosensory properties of the cells, tissue engineers may find it beneficial to employ the free-perfusion or hydrostatic compression system; indeed, a bioreactor system in which the loading regime can be easily altered by opening or closing the outlet would provide a measure of control over the mechanical stimulation supplied to the cells, allowing differentiation of the cells to be directed.

Inspection of figures 6.6–6.8 reveals the crucial role that the scaffold material properties play in determining the mechanical environment of a cell population contained within the scaffold. Reducing the compliance of the scaffold by increasing the shear modulus or reducing the compressibility, causes a reduction in solid displacement and culture medium pressure, with associated downstream effects on mechanotransduction-affected phenotypic progression. These properties may, in principle, be controlled by tissue engineers when manufacturing scaffolds; our analysis provides information regarding the effect of such changes in material properties on the relevant stimuli associated with mechanotransduction processes.

In this analysis, we have considered the scaffold material parameters to be constant; however, simulations presented in chapter 5 indicated that the interplay between scaffold degradation and deposition of ECM by cells will result in spatially inhomogeneous mechanical properties which will have a profound impact on the mechanical cues which the cells experience. Such considerations represent an intriguing extension to this analysis.

6.3.2 Two-dimensional numerical solution

We now return to our two-dimensional model of a fluid-filled poroelastic scaffold (see equations (6.16) and (6.17) and figure 6.1). The solution is decomposed in the same manner as previously:

$$p(\boldsymbol{x},t) = \Re\left\{\widetilde{p}(\boldsymbol{x})e^{i\omega t}\right\}, \qquad \boldsymbol{u}(\boldsymbol{x},t) = \Re\left\{\widetilde{\boldsymbol{u}}(\boldsymbol{x})e^{i\omega t}\right\}, \tag{6.59}$$

wherein $\widetilde{\boldsymbol{u}}$ and $\widetilde{p}$ satisfy:

$$G\nabla^2\widetilde{\boldsymbol{u}} + \frac{G}{1-2\nu}\nabla\left(\nabla\cdot\widetilde{\boldsymbol{u}}\right) \;=\; \alpha\nabla\widetilde{p}, \tag{6.60}$$

$$\widetilde{p} + \frac{i}{\omega}\nabla^2\widetilde{p} \;=\; -\alpha\nabla\cdot\widetilde{\boldsymbol{u}}. \tag{6.61}$$

We solve these equations subject to the boundary conditions stated in figure 6.1, except that in order to exploit the decomposition (6.59), we must once again choose $P_u = 0$, in which case the flow of fluid through the perforations in the piston is not influenced by an upstream pressure.

This coupled system is solved numerically as follows. Equations (6.60) and (6.61) are discretised using a second-order-accurate finite-difference scheme on a uniform mesh to obtain the following equations for the solid displacement $(\widetilde{u}_{r,j}, \widetilde{v}_{r,j})$ and pore pressure $\widetilde{p}_{r,j}$ at each mesh point, (r,j):

$$\begin{aligned}&\frac{2G(1-\nu)}{1-2\nu}\frac{\widetilde{u}_{r+1,j} - 2\widetilde{u}_{r,j} + \widetilde{u}_{r-1,j}}{(\Delta x)^2} + G\frac{\widetilde{u}_{r,j+1} - 2\widetilde{u}_{r,j} + \widetilde{u}_{r,j-1}}{(\Delta y)^2}\\ &\quad + \frac{G}{1-2\nu}\frac{\widetilde{v}_{r+1,j+1} - \widetilde{v}_{r-1,j+1} - \widetilde{v}_{r+1,j-1} + \widetilde{v}_{r-1,j-1}}{4\Delta x\Delta y} - \alpha\frac{\widetilde{p}_{r+1,j} - \widetilde{p}_{r-1,j}}{2\Delta x} = 0,\end{aligned} \tag{6.62}$$

$$\begin{aligned}&G\frac{\widetilde{v}_{r+1,j} - 2\widetilde{v}_{r,j} + \widetilde{v}_{r-1,j}}{(\Delta x)^2} + \frac{2G(1-\nu)}{1-2\nu}\frac{\widetilde{v}_{r,j+1} - 2\widetilde{v}_{r,j} + \widetilde{v}_{r,j-1}}{(\Delta y)^2}\\ &\quad + \frac{G}{1-2\nu}\frac{\widetilde{u}_{r+1,j+1} - \widetilde{u}_{r-1,j+1} - \widetilde{u}_{r+1,j-1} + \widetilde{u}_{r-1,j-1}}{4\Delta x\Delta y} - \alpha\frac{\widetilde{p}_{r,j+1} - \widetilde{p}_{r,j-1}}{2\Delta y} = 0,\end{aligned} \tag{6.63}$$

$$\begin{aligned}&\widetilde{p}_{r,j} + \frac{i}{\omega}\left\{\frac{\widetilde{p}_{r+1,j} - 2\widetilde{p}_{r,j} + \widetilde{p}_{r-1,j}}{(\Delta x)^2} + \frac{\widetilde{p}_{r,j+1} - 2\widetilde{p}_{r,j} + \widetilde{p}_{r,j-1}}{(\Delta y)^2}\right\}\\ &\quad + \alpha\left\{\frac{\widetilde{u}_{r+1,j} - \widetilde{u}_{r-1,j}}{2\Delta x} + \frac{\widetilde{v}_{r,j+1} - \widetilde{v}_{r,j-1}}{2\Delta y}\right\} = 0.\end{aligned} \tag{6.64}$$

The parameters Δx and Δy represent the mesh spacing in the x- and y-directions, respectively: *i.e.* $\widetilde{u}_{r,j} \approx \widetilde{u}(r\Delta x, j\Delta y)$.

Equations (6.62)–(6.64) and the boundary conditions given in figure 6.1 constitute a linear system which we solve using MATLAB's Gaussian elimination scheme. The uniform mesh spacing is chosen to be $\Delta x = 1\times10^{-2}$ and $\Delta y = 5\times10^{-3}$. Qualitative comparisons

with solutions obtained using the finite element package COMSOL in which mesh refinement was performed around the discontinuities in the boundary show good agreement (see Appendix B.1).

Figures 6.9 and 6.10 show the displacement and pressure profiles obtained in the free-perfusion regime (fluid is free to escape through the piston perforations and outlet); detail obscured by the 3D projection is enhanced by a contour plot. In each case, the solution is plotted at $t = 0$ (the full time-dependent behaviour is not presented since it is similar to that found in the uniaxial limit). Figure 6.11 depicts the pore fluid pressure at $y = 0$ and $y = 0.5$. The dimensionless fluid flux vector $\boldsymbol{q} = (q_x, q_y)$, calculated using the dimensionless version of equation (6.7): $\boldsymbol{q} = -\nabla p$, is visualised in the two-dimensional domain in figure 6.12.

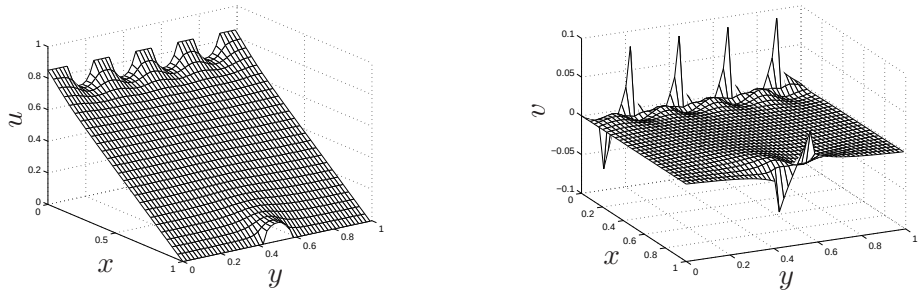

(a) (b)

Figure 6.9: Surface plot of (a) the axial and (b) the transverse displacement of a poroelastic scaffold in response to compression at $t = 0$. Parameter values: $G = 1$, $\nu = 0.1$, $\alpha = 0.7$, $U = 0.85$, $\omega = 1$, $\beta_x = 1 = \beta_1 = \beta_2$.

The simulations presented in figures 6.9–6.12 show the predicted response of the scaffold to periodic compression by a piston (with four perforations) constrained within a rigid channel with one outlet. Figure 6.9 shows that the presence of the perforations and the outlet causes the displacement to deviate from the linear profile obtained in the one-dimensional case by an amount which depends upon the magnitude of the parameters β_x, β_1, β_2. These parameters control the displacement at $x = 0, 1$ according to the normal and tangential stresses (see equations (6.37) and (6.39)). Within the piston perforations, the axial displacement is reduced from its imposed value $u = U$ by an amount which depends on the stiffness of the poroelastic material (and the value of the parameter β_x); at $x = 1$, the axial displacement increases towards the centre of the outlet and must remain zero on the rigid wall. The transverse displacement exhibits similar behaviour, achieving maxima and

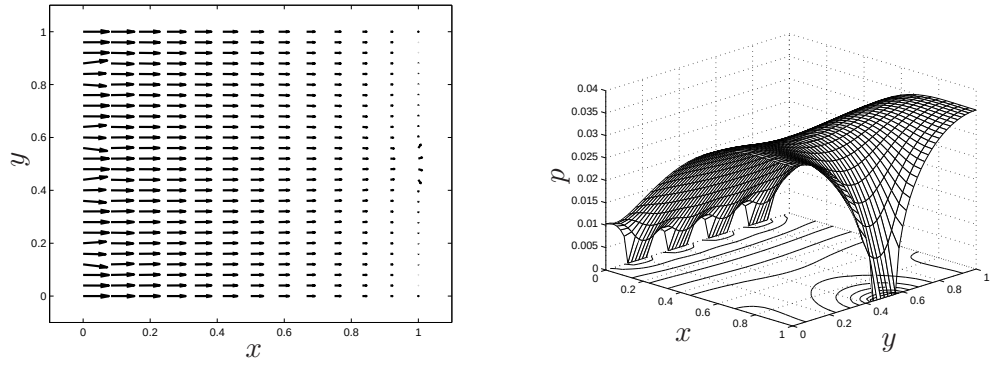

(a) (b)

Figure 6.10: (a) A visualisation of the solid displacement vector in which the length of the arrow represents its magnitude; (b) surface plot of the pore pressure in a compressed poroelastic scaffold at $t = 0$. Parameters as in figure 6.9.

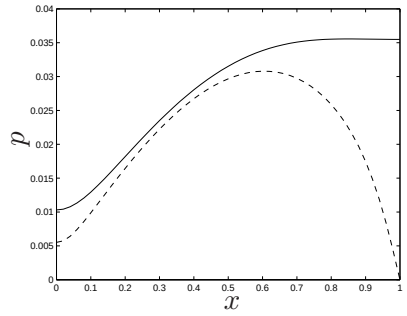

Figure 6.11: A plot of the pore pressure at $y = 0$ (–) and $y = 0.5$ (- -) in a compressed poroelastic scaffold at $t = 0$. Parameters as in figure 6.9.

minima at the edges of the perforations and the outlet, but remaining small everywhere else. This behaviour is highlighted in figure 6.10a where we visualise the displacement vector, $\boldsymbol{u} = (u, v)$ in the x, y domain. We see that the scaffold splays and bulges out of the piston perforations and outlet, with small transverse displacement introduced there. We note also that the axial displacement profile is approximately linear, with axial compression dominating and deviation from this linear behaviour becoming important only near the perforations and outlet. From figure 6.10b we observe that the pressure equalises with the external environment in the perforations and outlet (where $p = 0$) and satisfies $\partial p/\partial x = 0$ on the remainder of the piston and the constraining wall. We obtain a profile similar to that presented in figure 6.3a in the perforation/outlet regions, and similar to 6.3b elsewhere. This is shown more clearly in figure 6.11 which shows that at $y = 0$, $\partial p/\partial x = 0$ on the pis-

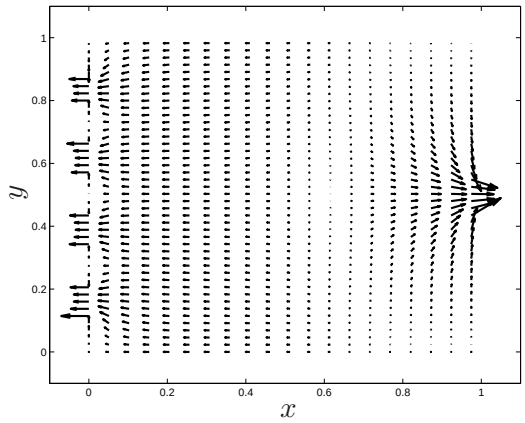

Figure 6.12: A visualisation of the flux vector $\boldsymbol{q}$ in the x, y domain at $t = 0$ in which the length of the arrow represents its magnitude. Parameters as in figure 6.9.

ton and constraining wall, corresponding to no-penetration; at $y = 0.5$, we have $\partial p/\partial x = 0$ on the piston and $p = 0$ in the outlet. It may be readily observed from figure 6.10b that the pore pressure achieves maxima on the downstream wall at $(x, y) = (1, 0)$ and $(1, 1)$. The corresponding fluid flux, presented in figure 6.12, shows that fluid escapes through the perforations and outlet, flowing upstream near the piston and downstream near the outlet. The flow achieves highest values at the edges of the perforations and outlet; this unusual flow profile is due to the discontinuity in the boundary conditions which induces large pressure gradients there.

In addition to the field variables illustrated above, we may calculate the solid stress ($\boldsymbol{\sigma}$) and the fluid shear stress (τ) associated with compression-induced fluid flow. As discussed in previous chapters (see §§1.2.2, 4.3, 5.2.1), these stimuli are of key relevance to the study of the effect of mechanotransduction on tissue growth processes and are defined as follows:

$$\boldsymbol{\sigma} = -\alpha p\, \mathbf{I} + G\left(\nabla \boldsymbol{u} + \nabla \boldsymbol{u}^T\right) + \frac{2G\nu}{1-2\nu} \nabla \cdot \boldsymbol{u}\, \mathbf{I}, \tag{6.65}$$

$$\tau = \frac{\partial q_x}{\partial y} + \frac{\partial q_y}{\partial x}. \tag{6.66}$$

We note that in contrast to the uniaxial approximation in which we approximated the fluid shear stress as proportional to the pressure gradient, in this two-dimensional model, we may calculate the fluid shear stress explicitly using (6.66). Contour plots of the solid stress and fluid shear stress induced by compression are shown in figures 6.13 and 6.14.

Comparison of figures 6.13 and 6.14 shows that the solid and fluid shear stresses induced by compression of the scaffold are concentrated around the perforations in the piston and

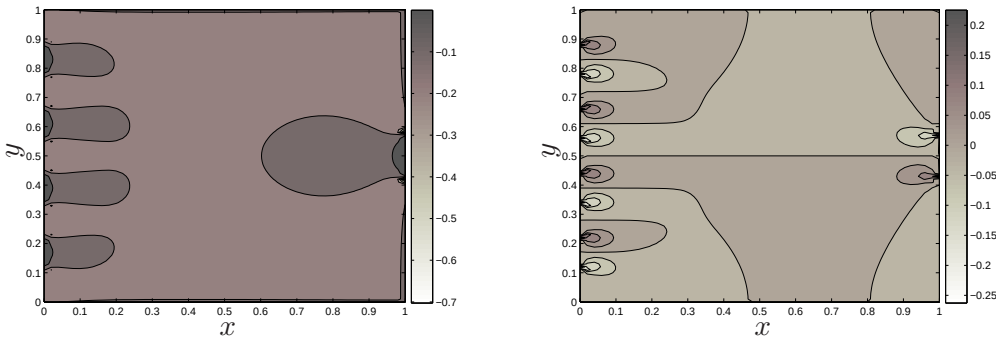

(a) (b)

Figure 6.13: Contour plots of (a) the principle stress component ($\sigma_{xx} = \sigma_{yy}$); (b) the shear stress component ($\sigma_{xy} = \sigma_{yx}$) in the poroelastic matrix. Parameters as in figure 6.9.

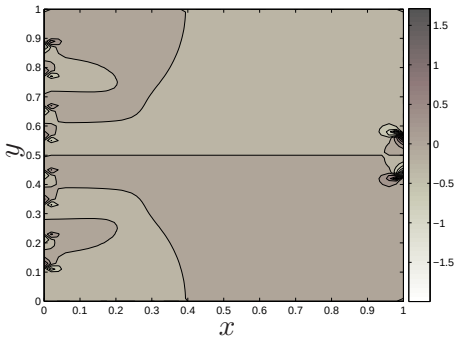

Figure 6.14: A contour plot of the fluid-induced shear stress (τ) in the x, y domain. Parameters as in figure 6.9.

the downstream outlet and exhibit marked transverse variation. We remark also that the fluid shear stress is an order of magnitude larger than the solid stress.

Relevance to tissue engineering

The model predictions presented in figures 6.9–6.14 clearly indicate the significant spatial variation in the mechanical stimuli relevant to tissue engineering. We have shown that, in addition to the axial variation discussed in §6.3.1, consideration of the two-dimensional geometry of the bioreactor system (including both the piston and the outlet) results in marked transverse variation in the mechanical stimuli experienced by the cells within the scaffold. Considering the mechanotransduction-affected proliferative behaviour examined in chapter 5, this phenomenon will result in a heterogeneous distribution of cell phenotype

within the population. The resulting inhomogeneity in scaffold degradation and ECM deposition will cause spatial variation in material properties and could potentially have detrimental effects on the mechanical integrity of the resulting tissue construct.

6.3.3 Summary

In this section, we have used a classical Biot formulation to compute the displacement and fluid flow associated with the periodic compression of a poroelastic scaffold in the absence of an ambient flow as a simple model for the compression/perfusion bioreactor system of El-Haj *et al.*

Analytic solutions, constructed in the uniaxial limit, predicted an approximately linear displacement profile, with the compliance of the scaffold being marginally increased in the presence of a downstream fluid outlet (as evidenced by increased solid displacement). The pore fluid flux and an approximation to the fluid shear stress were also computed with a view to employing this data in a cell growth response model. The flux and associated fluid shear stress were found to attain maxima at the piston face and outlet. Marked differences were observed in these stimuli in the presence and absence of an outlet, which could provide a simple method for tissue engineers to change the local mechanical environment and thereby encourage differentiation of cells.

The full two-dimensional system was investigated in §6.3.2 allowing the effect of the geometry of the piston and outlet to be included. Numerical simulations were used to show that the displacement of the poroelastic solid is dominated by axial compression, small transverse displacements being introduced due to the perforations in the piston and by the outlet. Similarly, the fluid flow is dominated by behaviour of the type found in the uniaxial limit, with small transverse flows being introduced around the perforations and outlet.

Using this model, we were able to calculate both the solid stress and the fluid shear stress distribution due to compression. It was again found that the fluid shear stress is maximal near the piston and outlet, and similar behaviour is observed in the solid stress distribution. We remark that the fluid shear stress is an order of magnitude larger than the solid stress. Furthermore, strong transverse variation in the mechanical stimuli relevant to tissue engineering processes (pore fluid pressure, solid stress and fluid shear stress) is predicted by this model, suggesting that spatial effects in at least two-dimensions will be important in the modelling of tissue growth. In view of the mechanotransduction modelling undertaken in chapter 5, we conclude that the spatial variation in mechanical stimuli will result in a heterogeneous distribution of cell phenotype within the scaffold, leading

to inhomogeneous scaffold degradation and ECM deposition, causing deterioration of the mechanical integrity of the scaffold. Consideration of these effects will form the basis for future work.

6.4 Solution: A multiphase model for flow in a poroelastic material

In this section, we compute solutions to the multiphase model for flow within a poroelastic material presented in §6.2.2 and compare them with the predictions of the Biot model analysed in §6.3.

To recapitulate, the multiphase model under consideration is given by the following (dimensional) equations:

$$\frac{\partial w}{\partial t^*} + \nabla^* \cdot (w \boldsymbol{v}_w^*) = 0, \tag{6.67}$$

$$\nabla^* \cdot (w \boldsymbol{v}_w^* + s \frac{\partial \boldsymbol{u}^*}{\partial t^*}) = 0. \tag{6.68}$$

$$\nabla^* p^* = \frac{K_{ws}^*}{w} \left(\frac{\partial \boldsymbol{u}^*}{\partial t^*} - \boldsymbol{v}_w^* \right), \tag{6.69}$$

$$\nabla^* p^* = G^* \nabla^{*2} \boldsymbol{u}^*, \tag{6.70}$$

in which the fluid volume fraction is denoted by w. As a consequence of the no-voids equation (6.18) w is equivalent to the porosity of the scaffold. The pressure and velocity of the pore fluid are denoted p^*, $\boldsymbol{v}_w^*$ respectively, and $\boldsymbol{u}^*$ is the solid displacement; K_{ws}^* is the interphase drag coefficient (related to the coefficient of permeability by $\kappa^* = w/K_{ws}^*$) and G^* is the shear modulus for the porous material. We have employed the multiphase formulation due to Preziosi *et al.* (1996), De Boer (1998) in preference to that of Lemon *et al.* (2006) (see §6.2.2) for numerical ease; employing the momentum equations in the form (6.28) in preference to (6.21) simplifies considerably the resulting model equations.

We consider a one-dimensional scaffold of length L^* subject to time-dependent compression by a permeable piston at $x^* = 0$ and restrained by an impermeable barrier at $x^* = L^*$, corresponding to the "hydrostatic compression" regime described in §6.3.1. To clarify, the axial displacement is denoted u^* and the axial fluid velocity, v_w^*. We non-dimensionalise as follows:

$$x^* = L^* x, \quad t^* = \frac{L^{*2}}{K_{ws}^* P^*} t, \quad u^* = \delta L^* u, \quad p^* = P^* p, \quad v_w^* = \frac{K_{ws}^* P^*}{L^*} v_w, \tag{6.71}$$

and rescale $(p, v_w) = \delta(\hat{p}, \hat{v}_w)$. In (6.71), $\delta \ll 1$ is a small parameter introduced so that the dimensionless displacement (u) is of order one, and P^* is a pore fluid pressure scaling, determined below. Dropping the carets for brevity, the one-dimensional versions of equations (6.67)–(6.70) yield:

$$\frac{\partial w}{\partial t} + \delta \frac{\partial}{\partial x}(w v_w) = 0, \qquad \frac{\partial}{\partial x}(w v_w + (1-w)\frac{\partial u}{\partial t}) = 0, \tag{6.72a,b}$$

$$\frac{\partial p}{\partial x} = \frac{1}{w}\left(\frac{\partial u}{\partial t} - v_w\right), \quad \frac{\partial p}{\partial x} = G\frac{\partial^2 u}{\partial x^2}, \tag{6.73a,b}$$

and the scaffold now occupies $0 \leqslant x \leqslant 1$. The dimensionless shear modulus is given by $G = G^*/P^*$ and the pressure scaling P^* in (6.12) is therefore defined by our choice of G; for instance, choosing $G = 1$ implies $P^* = G^*$. Appropriate boundary conditions for this problem are:

$$u(x=0,t) = \overline{u}(t), \qquad v_w(x=1,t) = 0, \quad u(x=1,t) = 0. \tag{6.74}$$

Appropriate conditions on w will be discussed below, where (through elimination of p and v_w) equations (6.72) and (6.73) are reduced to a pair of equations governing the solid displacement (u) and fluid volume fraction (w).

In view of the boundary conditions (6.74), equations (6.72b) and (6.73a) imply that the fluid velocity is related to the gradient of the pore pressure as follows:

$$v_w = w(w-1)\frac{\partial p}{\partial x}, \tag{6.75}$$

from which it is clear that $v_w(x=1,t) = 0$ if $\partial p/\partial x = 0$ or $w = 0$ at $x = 1$. We remark that the choice $w(x=1,t) = 0$ implies that we the pore fluid pressure is undefined at $x = 1$. Equations (6.72a) and (6.73b) then yield the following equation for the volume fraction of pore fluid:

$$\frac{\partial w}{\partial t} + \delta G \frac{\partial}{\partial x}\left(w^2(w-1)\frac{\partial^2 u}{\partial x^2}\right) = 0. \tag{6.76}$$

Employing equations (6.75) and (6.73b) in (6.73a) then supplies a coupled non-linear diffusion equation for the displacement:

$$\frac{\partial u}{\partial t} = G w^2 \frac{\partial^2 u}{\partial x^2}. \tag{6.77}$$

The displacement boundary conditions corresponding to (6.77) are given above; an appropriate boundary condition on the hyperbolic partial differential equation (6.76) is derived below.

Since the pore fluid volume fraction at $x = 0$ will vary due to compression, we impose a condition at $x = 1$. To ensure solution, we require the characteristics of equation (6.76) to propagate information from the right hand boundary into the remainder of the domain. The characteristics are defined:

$$\frac{\mathrm{d}x}{\mathrm{d}t} = \delta G(3w - 2)w\frac{\partial^2 u}{\partial x^2}, \tag{6.78}$$

along which w is given by

$$\frac{\mathrm{d}w}{\mathrm{d}t} = -\delta G w^2(w - 1)\frac{\partial^3 u}{\partial x^3}. \tag{6.79}$$

Choosing initial data such that $w(x = 1, t = 0) = 0$ ensures that $x = 1$ is a characteristic, obviating the need to impose a boundary condition there; this condition is also consistent with $v_w(x = 1, t) = 0$. Furthermore, we must ensure $\frac{\partial^2 u}{\partial x^2} \geqslant 0$ (provided $w < 2/3$). An appropriate choice for the imposed compression is a saturating function of the form

$$\overline{u}(t) = U\left[\frac{2e^{\omega t}}{1 + e^{\omega t}} - 1\right], \tag{6.80}$$

in which U is the maximum amplitude and ω dictates the rate of compression.

In summary, our system comprises the pair of coupled partial differential equations (6.76) and (6.77) which govern the volume fraction of pore fluid (porosity) and the solid displacement. Boundary conditions representing a one-dimensional scaffold subject to time-dependent compression by a permeable piston at $x = 0$ and restrained by an impermeable barrier at $x = 1$ are:

$$u(x = 0, t) = \overline{u}(t), \quad u(x = 1, t) = 0, \tag{6.81}$$

where $\overline{u}(t)$ is defined by (6.80). A suitable initial condition on the pore fluid volume fraction is:

$$w(x, t = 0) = \frac{1 - x}{2}, \tag{6.82}$$

representing a scaffold whose porosity decreases linearly to zero at $x = 1$ from a maximum of 50% at $x = 0$.

We solve this system using an explicit time-stepping method to compute the solution for the displacement and the `hpde` software package (Shampine, 2005) to solve the hyperbolic equation (6.76) at each timestep. The `hpde` package solves hyperbolic partial differential equations (in MATLAB) of the form:

$$\frac{\partial a}{\partial t} = \frac{\partial}{\partial x}f(x, t, a) + s(x, t, a), \tag{6.83}$$

using the Lax-Wendroff method. The displacement u_j^{k+1} at each mesh point j and new time-step, $k+1$ is calculated from u_j^k and w_j^k as follows:

$$u_j^{k+1} = u_j^k + \Delta t G (w_j^k)^2 \frac{u_{j+1}^k - 2u_j^k + u_{j-1}^k}{(\Delta x)^2}, \tag{6.84}$$

where Δt, Δx represent the size of the time-step and mesh spacing, respectively: $u_j^k \approx u(j\Delta x, k\Delta t)$, $w_j^k \approx w(j\Delta x, k\Delta t)$. Numerical accuracy is tested via mesh refinement and comparison with a simple scheme which uses explicit schemes for equations (6.76) and (6.77); see appendix B.2 for more details.

The remaining dependent variables (p, v_w) are calculated from equations (6.73b) and (6.75). Noting that the pore pressure must equalise with the external environment at $x = 0$, we require $p(x = 0, t) = 0$; integrating equation (6.73b), we obtain

$$p = G \left(\frac{\partial u}{\partial x} - \left. \frac{\partial u}{\partial x} \right|_{x=0} \right). \tag{6.85}$$

The spatial mesh spacing is chosen to be $\Delta x = 5 \times 10^{-3}$, and guided by stability requirement of the uncoupled explicit scheme for the displacement, the timestep is defined according to $\Delta t = (\Delta x)^2/(2G)$. The small parameter is chosen to be $\delta = 10^{-2}$.

The time evolution of the solid displacement, pore fluid pressure and flux is depicted in figures 6.15–6.17. Figure 6.18a shows the evolution of the pore fluid volume fraction in the scaffold, while figure 6.18b depicts the variation in pore fluid volume fraction at $x = 0$. So that variations in w are visible, the results presented in figure 6.18a correspond to $\delta = 0.5$.

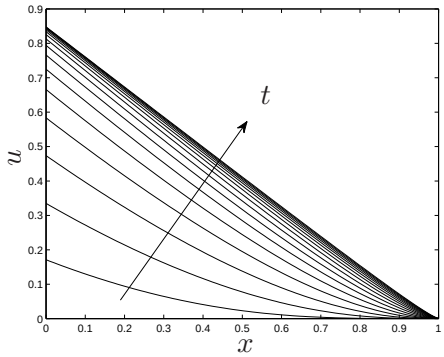

Figure 6.15: The evolution of the solid displacement at $t = 0$–6.4 (in steps of $t = 0.4$) in a poroelastic material subject to time-dependent forcing at $x = 0$. Parameter values: $G = 1$, $\nu = 0.1$, $U = 0.85$, $\omega = 1$, $\delta = 10^{-2}$.

Comparison of figures 6.2 and 6.15 demonstrates that in this multiphase formulation, non-linear effects are more pronounced. Deviation from the approximately linear profile

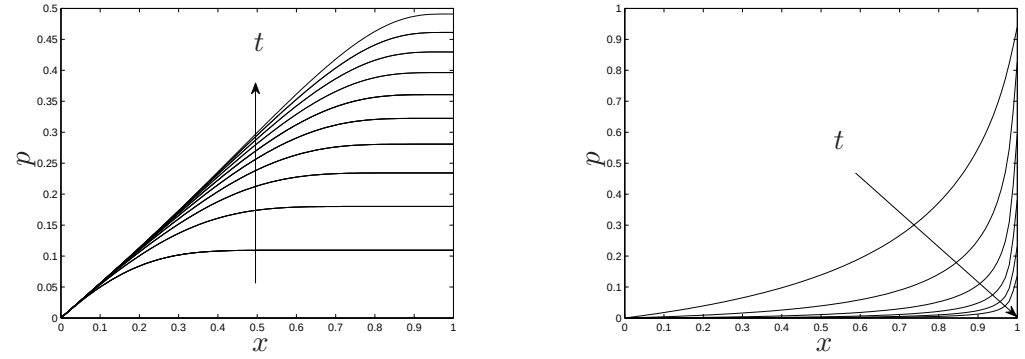

(a) (b)

Figure 6.16: The evolution of the pore fluid pressure for (a) early times ($t = 0$–0.45 in steps of $t = 0.05$), and (b) later times ($t = 2.5$–11 in steps of $t = 1.7$) in a poroelastic material subject to time-dependent forcing at $x = 0$. Parameter values as in figure 6.15.

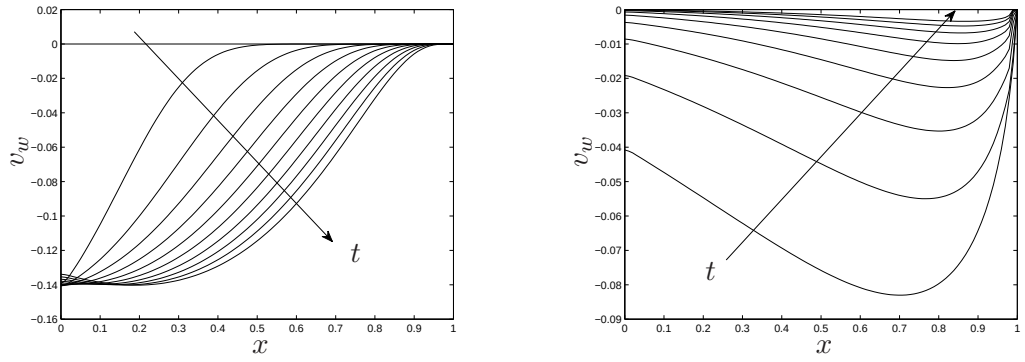

(a) (b)

Figure 6.17: The evolution of the pore fluid flux for (a) early times ($t = 0$–0.5 in steps of $t = 0.05$), and (b) later times ($t = 2.5$–9.3 in steps of $t = 0.85$) in a poroelastic material subject to time-dependent forcing at $x = 0$. Parameter values as in figure 6.15.

predicted in the Biot formulation is evident at early times. As the function $\overline{u}(t)$ saturates (see equation (6.80)) and the rate of compression reduces, the displacement tends towards a linear profile. Correspondingly, as the poroelastic material is compressed, the pore fluid pressure increases in a similar manner to that observed in the uniaxial limit (§6.3) for the case of hydrostatic compression (see figure 6.3b); as the compression rate reduces, the flow of fluid out of the perforated piston at $x = 0$ allows this pressure to dissipate and the

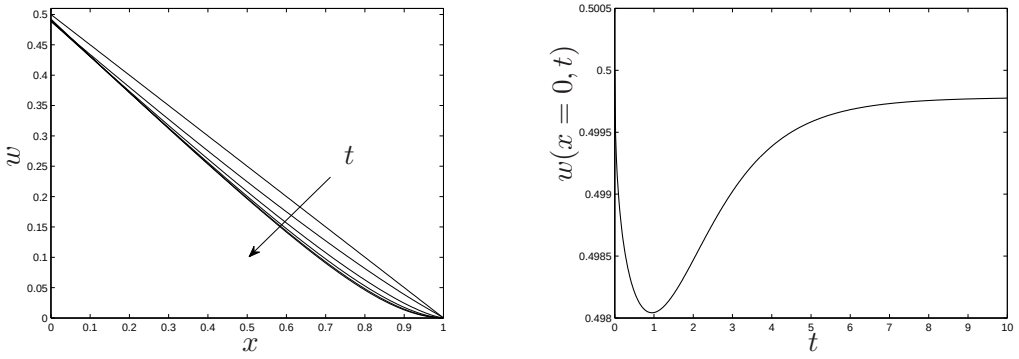

(a) (b)

Figure 6.18: The evolution of (a) the pore fluid volume fraction at $t = 0, 1, 2, 3, 4, 5$, (b) the pore fluid volume fraction at $x = 0$ (for $\delta = 0.5$), in a poroelastic material subject to time-dependent forcing at $x = 0$. Parameter values as in figure 6.15.

pressure in the scaffold is small everywhere except near the impermeable wall at $x = 1$. For very long times, this pressure tends to zero (results omitted). We remark that the pressure gradient at $x = 1$ shown in figure 6.16b does not violate $v_w(x = 1, t) = 0$ since we have $w = 0$ there (see equations (6.74) and (6.75)).

The pressure gradient in the scaffold drives a flow of fluid upstream, through the perforated piston, which gradually decreases as the compression rate reduces and the pressure equalises with the exterior. The fluid flow profile initially follows a similar profile to that predicted in the uniaxial limit; as time progresses, the flow near the piston reduces and the maximal flow is near the downstream end $x = 1$ where the gradient of the pore fluid pressure is greatest.

The pore fluid volume fraction (scaffold porosity) follows a similarly non-linear evolution. Initially, as the material is compressed, the porosity falls from its initial linear profile, with reduction in pore space being most pronounced in the neighbourhood of the piston. As the compression extends across the whole of the scaffold, and the rate of compression reduces, the porosity near the piston reaches a minimum and settles to a steady state (after a short period of expansion) as the scaffold relaxes. This behaviour is illustrated by figures 6.18a,b. A physical explanation for this behaviour is not obvious.

We now consider the behaviour of the additional mechanical stimuli relevant to tissue engineering applications. The solid stress may be calculated according to the one-

dimensional version of equation (6.24)

$$\sigma = -p + G\frac{\partial u}{\partial x}, \tag{6.86}$$

and in view of equation (6.85), we obtain

$$\sigma = G\frac{\partial u}{\partial x}\bigg|_{x=0}. \tag{6.87}$$

In a similar manner to previously, we view the fluid shear stress as being proportional to the pore fluid flux: $\tau = |v_w|$ (see 6.3.1). Figures 6.19 and 6.20 show the evolution of the solid and fluid shear stresses. We remark that as in the uniaxial limit of the Biot model, the solid stress is invariant along the length of the scaffold.

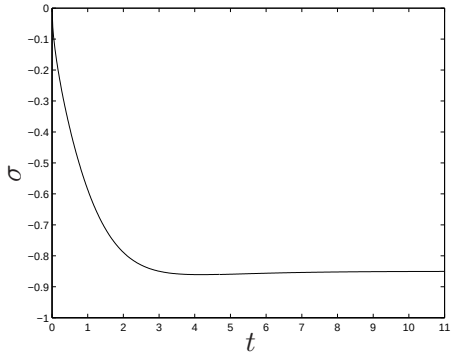

Figure 6.19: The evolution of the solid stress in a poroelastic material subject to time-dependent forcing at $x = 0$. Parameter values as in figure 6.15.

Our multiphase model predicts that the solid stress induced by compression does not vary along the scaffold length, and increases with scaffold compression, reaching a constant value $\sigma = -0.85$ as the rate of compression falls to zero. This value is attained since as the rate of compression falls, the solid displacement tends to a linear profile with gradient, U; for the parameter choices given in figure 6.15, this corresponds to $\sigma = -0.85$. As in the uniaxial limit we have assumed that the magnitude of the fluid velocity is a suitable measure of the fluid shear stress. It is interesting to note that our model predicts a complex shear stress evolution within the poroelastic scaffold: at early times we obtain a similar profile to that found in the uniaxial limit (§6.3), with maximal shear stress near the piston. As the compression progresses and non-linear effects become important, the fluid shear stress distribution changes to achieve a maximum near the downstream end of the scaffold.

In contrast to the results presented in §6.3.1, this more complex model suggests that the distribution of shear stress within the scaffold evolves over time in a complex way.

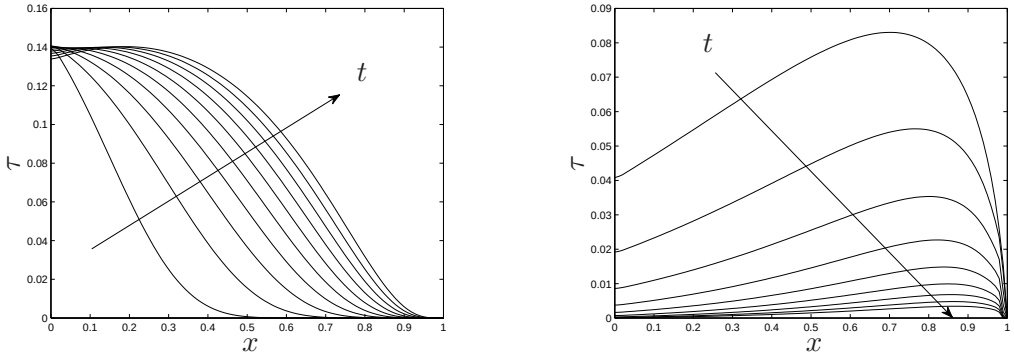

(a) (b)

Figure 6.20: The evolution of the compression-induced fluid shear stress for (a) early times ($t = 0$–0.5 in steps of $t = 0.05$), and (b) later times ($t = 2.5$–9.3 in steps of $t = 0.85$) in a poroelastic material subject to time-dependent forcing at $x = 0$. Parameter values as in figure 6.15.

This is due to difference between the time-dependence of the loading supplied in each case: in §6.3.1, we consider periodic displacement, whilst in this section we have imposed a monotonically-increasing displacement. Due to the complexity of the multiphase system, we do not analyse the behaviour of the poroelastic scaffold and pore fluid in the presence of a downstream outlet; ascertaining the importance of the disparity between the predictions of this model and those presented in §6.3.1 requires further analysis which is beyond the scope of this thesis.

6.5 Summary

In this chapter, we have presented two different formulations suitable for modelling macroscale mechanical forcing in the bioreactor system of El-Haj *et al.* (§1.2.3). In principle, the multiphase modelling framework presented here allows full coupling of tissue growth processes to the mechanical stimulation provided by the compression/perfusion bioreactor. However, this is beyond the scope of this work; instead we concentrated on the response of the PLLA scaffold to compression in the absence of a cell population. This is equivalent to assuming that the volume occupied by the cells is much smaller than the scaffold volume fraction; this may be reasonable in the early stages following cell seeding. We employed both a classical Biot formulation and a multiphase model; in each case, the perfusive aspect of the bioreactor system was neglected for simplicity.

The response to periodic compression was calculated using the Biot formulation. Analytic solutions were constructed in the uniaxial limit, for which the bioreactor system may be modelled as a one-dimensional scaffold undergoing periodic compression by a permeable piston. The effect of constraining the downstream end by a permeable or impermeable barrier was investigated as a model for the presence/absence of an outlet. The model predicted an approximately linear displacement profile, with the stiffness of the material being marginally decreased in the presence of a downstream fluid outlet. The effect of varying the material properties of the scaffold on the predicted response was also investigated and the resulting displacement and pore pressure fields calculated. The pore fluid flux and an approximation to the fluid shear stress were computed, both being shown to attain maxima at the piston face and outlet. Additionally, the pore fluid pressure is increased throughout the scaffold by removal of the outlet.

In light of the marked differences in pressure and fluid shear stress in the presence and absence of an outlet, we concluded that a bioreactor system in which the loading regime can be easily altered by opening or closing the outlet would provide a measure of control over the mechanical stimulation supplied to the cells, allowing differentiation of the cells to be directed.

The effect of the geometry of the piston and outlet was investigated by performing two-dimensional numerical simulations. The displacement of the poroelastic solid was found to be dominated by the axial compression, with small transverse displacements associated with the perforations in the piston and the outlet. The fluid flow is similarly dominated by behaviour of the type found in the uniaxial limit, with small transverse flows in a neighbourhood of the perforations and outlet. Using this model, we calculated both the solid stress and fluid shear stress distribution as a result of compression. Again, the fluid shear stress is maximal near the piston and outlet, and similar behaviour is exhibited by the solid stress distribution. We remark that the fluid shear stress is an order of magnitude larger than the solid stress. Furthermore, strong transverse variation in the mechanical stimuli relevant to tissue engineering processes (pore fluid pressure, solid stress and fluid shear stress) was predicted by this model, suggesting that spatial effects in at least two-dimensions will be important in the modelling of tissue growth. In light of the mechanotransduction-affected behaviour observed in chapter 5, this spatial variation is likely to result in a heterogeneous distribution of cell phenotype within the scaffold, leading to inhomogeneous scaffold degradation and ECM deposition which causes deterioration in the mechanical integrity of the scaffold.

The behaviour of the PLLA scaffold as predicted by our multiphase formulation was illustrated using one-dimensional simulations in the absence of cells. In this case, the model reduced to a non-linear diffusion equation describing the displacement coupled to a hyperbolic equation governing the volume fraction of fluid (this is equivalent to the porosity of the scaffold). The pore pressure was related to the displacement in the same manner as in the Biot formulation. Comparisons with the Biot model were drawn and the two models were shown to exhibit similar behaviour; due to the different loading regimes employed, long-time response of the system was found to be more complex.

The results presented in this chapter illustrate two approaches that may be used to model mechanotransduction processes and their effect on macroscale tissue growth, highlighting the importance of these phenomena in tissue engineering. The spatial variation in the relevant mechanical stimuli, illustrated by the two-dimensional Biot formulation highlights the need to investigate the effect of bioreactor geometry within the comprehensive mechanotransduction modelling framework presented in chapters 4 and 5; the multiphase formulation outlined in the chapter provides a framework in which this could be achieved. This will be the subject of future work.

Chapter 7

Conclusions and further work

7.1 Concluding discussion

In this thesis we have considered a continuum multiphase framework suitable for macroscale modelling of *in vitro* tissue growth. The motivation for this work was the compression/perfusion bioreactor system of El-Haj *et al.* which provides both perfusion with culture medium and macroscale mechanical stimulation to an osteoblast-seeded PLLA scaffold; however, the formulation is sufficiently general to be applied to a vast range of tissue engineering applications.

The growth of biological tissue is a complex phenomenon, the modelling of which has been the subject of a great deal of attention, especially the study of tumour growth and stability, angiogenesis, wound healing and, more recently, *in vitro* and *in vivo* tissue engineering processes. Motivated by a range of experimental studies, we isolated two crucial factors which are of key importance in the growth and adaptation of engineered tissue constructs: (i) the interaction between adjacent cells and between cells and the scaffold, and (ii) the impact of mechanotransduction mechanisms (that is, the process by which forces are converted into biological signals influencing, for example, cell proliferation and morphogenesis) on tissue construct morphology. The emphasis of this thesis was on the study of these factors. The formulation employed was necessarily complex, and we therefore considered a series of mathematical models, building in complexity as we progressed through the thesis.

After introducing the key biological considerations for the modelling of *in vitro* bone tissue growth and reviewing the large and diverse mathematical literature relating to tissue growth modelling, we outlined the general multiphase formulation which forms the basis for the subsequent series of models.

Following many studies of tumour growth which exploit a multiphase formulation, in chapter 2, we initially restricted attention to two viscous fluid phases and concentrated on the interaction between perfusion of culture medium and the cells' response. Guided by parameter estimation, we employed the simplifying limit of large interphase viscous drag, recovering the model equations of Franks (2002) and Franks & King (2003) in which each phase is subject to a common velocity and pressure field. In a similar manner to that presented in Franks (2002), we analysed the stability to transverse perturbations of analytic solutions obtained in the limit of a one-dimensional, spatially-invariant growing tissue defined by two planar interfaces which are advected with the flow. We demonstrated that introducing a perturbation to the cell density results in markedly different behaviour to that to that reported in Franks (2002) for a spatially-invariant tissue construct. Using numerical simulations in one and two-dimensions, we showed that the analytic solutions obtained in the sharp interface limit capture much of the behaviour of the more complex one- and two-dimensional models.

Of greater relevance to *in vitro* tissue engineering systems are the numerical simulations presented in chapter 2 which considered two illustrative models of mechanotransduction-affected tissue growth. Specifically, we studied the response of a cell population to its local density and pressure, showing that the growth of the cell population is profoundly altered by these effects, dramatically changing the composition of the construct. Furthermore, our model suggests that in static culture, regulation of proliferative behaviour by cell density and pressure results in indistinguishable tissue constructs. In principle, this conclusion provides a means for the identification of the dominant regulatory mechanism in a given cell population, simply by observing the construct morphology resulting from static and dynamic culture conditions.

The two-fluid model is not entirely appropriate for modelling the growth of a tissue construct, since the solid characteristics of the bioreactor system are necessarily neglected. The interactions between the PLLA scaffold and the cells contained within, as well as the mechanical stimulation from the piston, must therefore be ignored. Furthermore, due to the simplifying limit of large interphase drag employed, which demands that each phase be subject to a common velocity field, our model predicts that cells and ECM are advected through the bioreactor at the speed of the imposed flow. This implies that a very low rate of perfusion is required to prevent the tissue from being flushed from the scaffold before growth can be achieved. To rectify this, in chapters 3 and 4, we relax the assumption of large interphase drag and develop a three phase model, introducing a rigid, porous

phase to represent the scaffold, and explicitly model the interaction between the cells and the scaffold and between adjacent cells. Furthermore, in this formulation, we retain the individual phase variables rather than considering common velocity and pressure fields. Simplifying this model using the long-wavelength approximation, we employed a range of analytical and numerical techniques to thoroughly analyse the behaviour of this model. The effect of varying key parameters associated with the cell's motile behaviour and their aggregative or adhesive properties was investigated and we concluded that employing denser scaffolds allows greater control over cell aggregation and scaffold attachment. Additionally, to elucidate the aggregative/repulsive behaviour displayed by the cells, we employed a simplified form of the relevant cell-cell and cell-scaffold interaction functions finding that diffusive behaviour is reduced or augmented depending upon the dominance of these effects.

Using similar modelling techniques to that employed in chapter 2, we considered the effect of mechanotransduction-affected growth, studying the response of a cell population to the local density, pressure and shear stress, again concluding that on provision of suitable experimental data, the predictions of our model provide a method for the identification of the dominant regulatory mechanisms for tissue growth.

In chapter 5, we reinterpreted the scaffold phase as a lumped scaffold and ECM phase whose volume fraction varies spatially and temporally due to a combination of ECM deposition and scaffold degradation. This modification allowed explicit modelling of the progression of cells from a proliferative to an ECM-depositing phenotype, without increasing the number of phases in the system. In addition to the possibility of using the model results to isolate regulatory mechanisms, from numerical simulations, we concluded that uniform initial cell seeding and the encouragement of cell penetration throughout the scaffold are crucial in maintaining the mechanical integrity of engineered constructs.

Lastly, in chapter 6, we studied the mechanics of the scaffold in response to imposed mechanical compression and associated fluid flow. To do so, we employed first, a classical Biot poroelasticity formulation to determine the effect that mechanical forcing has on the stress and flow field within the poroelastic scaffold. The presence of a cell population was not considered in this model. Analytical solutions, constructed in the uniaxial limit, indicated that the presence of an outlet in the bioreactor system results in marked differences in mechanical stimuli relevant to tissue engineering processes, indicating that a bioreactor system in which the loading regime may be changed by opening or closing a fluid outlet provides a mechanism through which the phenotypic progression may be controlled. Using two-dimensional numerical simulations, we demonstrated strong transverse variation in

these mechanical stimuli; in view of the mechanotransduction modelling presented in chapter 4, this suggests that spatial effects in at least two dimensions are important in tissue growth modelling. Furthermore, in view of the model analysed in chapter 5, we deduced that mechanotransduction-mediated differentiation will result in a highly heterogeneous distribution of cell phenotype leading to inhomogeneous ECM deposition and deterioration in the mechanical integrity of the scaffold.

We then adapted our general multiphase formulation to model the interactions in a poroelastic solid saturated with a multiphase fluid. Comparisons were made with other similar models in the literature and we show that the Biot model may be obtained as a special case. This formulation provides the means to investigate the interplay between perfusion, mechanical stimulation and cell differentiation; however the model developed is highly complex, and to illustrate its behaviour we presented one-dimensional numerical simulations of a system comprising a single fluid within a poroelastic solid, neglecting spatial variation in two dimensions and the presence of a cell population. Comparisons with the Biot model were drawn and the two models were shown to exhibit similar behaviour; due to the different loading regimes employed, the long-time response of the multiphase system was found to be more complex.

7.2 Further work

The models analysed within this thesis were necessarily complex since they attempted to capture the complex interplay between a number of phases within a biologically relevant framework. We have therefore employed certain simplifying limits (such as the large drag and long-wavelength limits). Furthermore, due to lack of experimental data, we have made a number of biologically-motivated (if not biologically accurate) constitutive and modelling choices and estimated many of the parameter values. These approximations point the way to a myriad of interesting and challenging extensions, many of which were mentioned in this thesis. We remark that we are concerned only with extensions to the three phase model analysed from chapter 3 onwards, since this represents a more appropriate model for the biological systems under consideration.

In developing our three phase model we exploited the long-wavelength limit, in which the pressures and volume fractions of each phase are independent of the transverse coordinate. As remarked in chapter 3, in this approximation, the interphase viscous drag term is neglected; in light of the parameter estimation given in chapter 2, this effect should,

perhaps, be considered. Rescaling the drag coefficient such that it enters the leading order equations provides a simple extension to this model (an appropriate choice is $k = \mathcal{O}(1/h^2)$, where k is the coefficient of viscous drag and h is the channel aspect ratio). As well as introducing an additional parameter with which we may study the model dynamics, this modification provides an interesting opportunity to compare the behaviour of solutions in this limit with those obtained from the two-fluid model in the limit of large interphase viscous drag.

In exploiting the long-wavelength limit, the influence of variations in the transverse direction upon the behaviour of the system was neglected. As indicated in chapter 6, the geometry of the bioreactor system has a marked influence on the mechanical environment of the cells, with effects in at least two dimensions being important. Consideration of the full two-dimensional system represents a challenging extension to this work.

In chapter 6, we also developed a multiphase formulation which provides a framework to investigate the influence of scaffold deformation upon the cells contained within. Using similar mechanotransduction modelling techniques as employed in previous chapters, this model provides an exciting opportunity to thoroughly investigate the effect of the mechanical environment on the growth and differentiation of a cell population. In chapter 5, scaffold degradation and ECM deposition were considered and inferences were drawn concerning the mechanical properties of the tissue construct. The framework presented in chapter 6 provides a means to study the influence of these factors on the mechanical properties of engineered tissue constructs in a more realistic manner. We anticipate that these extensions will be largely numerical exercises with little analytic progress possible.

A simpler way to increase the realism of the models developed in this thesis is to work more closely with tissue engineers to obtain better estimates of the parameters for specific tissue engineering applications. Furthermore, such collaboration would allow estimation of more biologically accurate functional forms for our constitutive modelling choices, such as the cell-cell and cell-scaffold interaction functions (Σ_n, ψ_{ns}) and the consideration of more complex or appropriate functional forms for the mechanotransduction-affected cell proliferation and ECM deposition rates (k_m, k_d). The biological relevance of this model could be further improved by considering the effect of nutrient-limited construct growth; the effect of such a consideration is likely to be significant in static culture conditions. This could be achieved with minor modifications to the framework presented in this thesis by including an additional nutrient transport equation to the multiphase system and postulating nutrient-dependent functional forms for the cell phase growth and death rates.

Lemon & King (2007) have presented such a model, and the importance of this addition within the mechanotransduction modelling framework given in this thesis, especially with regard to the models' predictions regarding tissue growth regulation, presents an interesting avenue of research.

Appendix A

Asymptotically-small cell volume fraction: Green's function solution

We now consider the solution of (3.41) and (3.42) subject to the boundary conditions (3.46) and (3.47) without additional simplification. Noting that the constant, γ is given by equations (3.43) and (3.48), we make the following transformation:

$$n_1(x,t) = e^{(k_m - k_d)t}\phi(\xi,\tau), \quad \xi = x - \gamma t, \quad \tau = Dt, \tag{A.1}$$

and we may then express equation (3.41) and its attendant boundary conditions as follows:

$$\frac{\partial \phi}{\partial \tau} = \frac{\partial^2 \phi}{\partial \xi^2}, \quad \xi \in \Omega, \tag{A.2a}$$

$$\frac{\partial \phi}{\partial \xi} = \widetilde{A}\,\phi, \quad \text{on} \quad \partial\Omega, \tag{A.2b}$$

where $\widetilde{A} = -A_0/[12\mu_n\theta D]$ and the region of interest, $\xi \in [L,R]$, is denoted Ω with moving boundary $\partial\Omega$; $L(\tau) = a - \gamma\,\tau/D$ and $R(\tau) = b - \gamma\,\tau/D$.

A solution to (A.2) may be constructed by considering the free-space Green's function of the simpler problem:

$$\frac{\partial \phi}{\partial \tau} = \frac{\partial^2 \phi}{\partial \xi^2}, \qquad \phi(\pm\infty,\tau),\ \phi_\xi(\pm\infty,\tau) \to 0, \tag{A.3}$$

which is found to be:

$$G_F(\xi,\tau;\eta,\mathrm{T}) = \frac{H(\mathrm{T}-\tau)}{\sqrt{4\pi(\mathrm{T}-\tau)}} \exp\left[-\frac{(\xi-\eta)^2}{4(\mathrm{T}-\tau)}\right], \tag{A.4}$$

where η is an arbitrary point in the domain and $\mathrm{T} > \tau$ (see, for example, Zauderer (1989)). The Green's function for the problem (A.2) can then be expressed in the form

$$G(\xi,\tau;\eta,\mathrm{T}) = G_F(\xi,\tau;\eta,\mathrm{T}) + G_B(\xi,\tau;\eta,\mathrm{T}), \tag{A.5}$$

where G_F is the free-space Green's function defined above and G_B is specified via the method of images to satisfy the boundary conditions. Unlike the Neumann or Dirichlet problems, the function G_B may not be obtained entirely in terms of an image source point. Instead, to satisfy the Robin boundary condition at $\xi = L(\tau)$, we consider a source point at $\xi = L(\tau)+\eta$ and introduce an image at $L(\tau)-\eta$ *and* a line of image sources extending from our image point, $\xi = L(\tau)-\eta$ (denoted Γ), to $\xi = -\infty$, weighted by a density function, ρ_-, to be determined (Zauderer, 1989):

$$G_B = G_F(\xi, \tau; \Gamma, \mathrm{T}) + \int_{-\infty}^{\Gamma} \rho_-(s)\, G_F(\xi, \tau; s, \mathrm{T})\, \mathrm{d}s. \tag{A.6}$$

In order that the condition at $\xi = R(\tau)$ is satisfied, we must add images with respect to $\xi = R(\tau)$ of the source and images points at $\xi = L(\tau) \pm \eta$ *and* a second line of image sources extending from the point $\xi = 2R(\tau) - L(\tau) - \eta$ (denoted ζ) to $\xi = \infty$, weighted by a density function, $\rho_+(s)$, to be determined. Each of these images must, in turn, have images with respect to $L(\tau)$, $R(\tau)$ and we are led to consider an infinite sequence of image source points and image source lines. By considering the boundary condition (A.2b), we find that the weighting functions for each image are as follows:

$$\rho_-(s) = -2\widetilde{A} \exp\left[\widetilde{A}(s - \Gamma_n)\right], \tag{A.7}$$

$$\rho_+(s) = -2\widetilde{A} \exp\left[\widetilde{A}(\zeta_n - s)\right], \tag{A.8}$$

$$\Gamma_n = -2nR + (2n+1)L - \eta, \qquad n = 0, 1, 2, \ldots, \tag{A.9}$$

$$\zeta_n = 2nR - (2n-1)L - \eta, \qquad n = 1, 2, 3, \ldots \tag{A.10}$$

The source point and some of the images are shown in figure A.1.

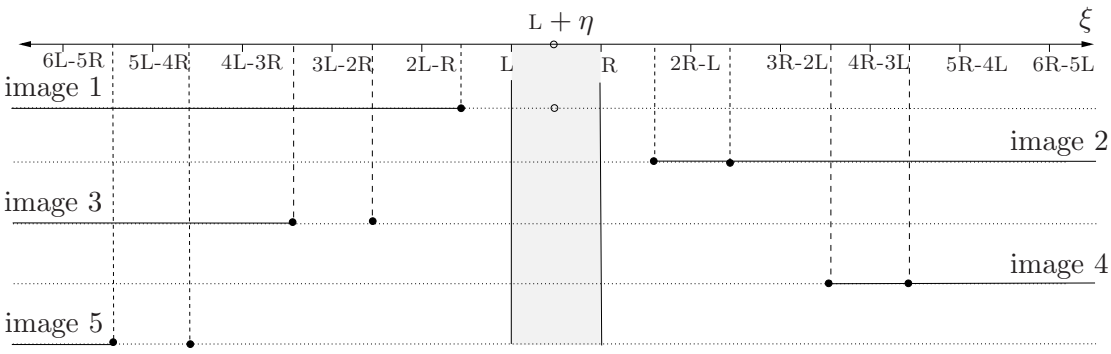

Figure A.1: The source point (○), image sources (●) and image source lines (–) employed in the solution of (A.2).

The Green's function, G, may then be expressed as follows:

$$\begin{aligned} G(\xi,\tau;\eta,\mathrm{T}) = \frac{H(\mathrm{T}-\tau)}{\sqrt{4\pi(\mathrm{T}-\tau)}}\Bigg\{&\sum_{n=0}^{\infty}\exp\left[-\frac{(\xi\pm\eta-2nR+(2n-1)L)^2}{4(\mathrm{T}-\tau)}\right] \\ &-2\widetilde{A}\int_{-\infty}^{\Gamma_n}\exp\left[\widetilde{A}(s-\Gamma_n)\right]\,\exp\left[-\frac{(\xi-s)^2}{4(\mathrm{T}-\tau)}\right]\,\mathrm{d}s \\ &+\sum_{n=1}^{\infty}\exp\left[-\frac{(\xi\pm\eta+2nR-(2n+1)L)^2}{4(\mathrm{T}-\tau)}\right] \\ &-2\widetilde{A}\int_{\zeta_n}^{\infty}\exp\left[\widetilde{A}(\zeta_n-s)\right]\,\exp\left[-\frac{(\xi-s)^2}{4(\mathrm{T}-\tau)}\right]\,\mathrm{d}s\Bigg\}, \end{aligned} \tag{A.11}$$

with Γ_n and ζ_n defined by equations (A.9) and (A.10). By evaluating the two integrals in equation (A.11) we obtain the following form for $G(\xi,\tau;\eta,\mathrm{T})$:

$$\begin{aligned} G(\xi,\tau;\eta,\mathrm{T}) \;=\; &\frac{H(\mathrm{T}-\tau)}{\sqrt{4\pi(\mathrm{T}-\tau)}}\Bigg\{\sum_{n=0}^{\infty}\exp\left[-\frac{(\xi\pm\eta-2nR+(2n-1)L)^2}{4(\mathrm{T}-\tau)}\right] \\ +\;&2\widetilde{A}\sqrt{\pi\,(\mathrm{T}-\tau)}\exp\left[\widetilde{A}\left(\widetilde{A}(\mathrm{T}-\tau)+\xi-\Gamma_n\right)\right]\left[\mathrm{erf}\left(\frac{\xi+2\widetilde{A}(\mathrm{T}-\tau)-\Gamma_n}{2\sqrt{\mathrm{T}-\tau}}\right)-1\right] \\ +\;&\sum_{n=1}^{\infty}\exp\left[-\frac{(\xi\pm\eta+2nR-(2n+1)L)^2}{4(\mathrm{T}-\tau)}\right] \\ -\;&2\widetilde{A}\sqrt{\pi\,(\mathrm{T}-\tau)}\exp\left[\widetilde{A}\left(\widetilde{A}(\mathrm{T}-\tau)-\xi+\zeta_n\right)\right]\left[\mathrm{erf}\left(\frac{\xi-2\widetilde{A}(\mathrm{T}-\tau)-\zeta_n}{2\sqrt{\mathrm{T}-\tau}}\right)+1\right]\Bigg\}. \end{aligned} \tag{A.12}$$

Noting that the Green's function for the problem (A.2) satisfies the following equation:

$$-\frac{\partial G}{\partial\tau}-\frac{\partial^2 G}{\partial\xi^2}=\delta(\xi-\eta)\delta(\tau-\mathrm{T}),\quad \xi,\eta\in\Omega;\ \tau,\mathrm{T}<\widetilde{T},\mathrm{T}>0, \tag{A.13}$$

(where $\widetilde{T}$ is the temporal end point) with end and boundary conditions:

$$G(\xi,\widetilde{T};\eta,\mathrm{T})=0,\qquad G-\widetilde{A}\left.\frac{\partial G}{\partial\xi}\right|_{\partial\Omega}=0, \tag{A.14}$$

it can be shown, (see, for example, Zauderer (1989)) that the solution, ϕ, at an arbitrary point (η,T) is given by the following formula:

$$\begin{aligned} \phi(\eta,\mathrm{T}) = &\int_{\partial\Omega_0}\phi(\xi,0)G(\xi,0;\eta,\mathrm{T})\,\mathrm{d}\xi-\int_{\partial\Omega_{\widetilde{T}}}\phi(\xi,\widetilde{T})G(\xi,\widetilde{T};\eta,\mathrm{T})\,\mathrm{d}\xi \\ &-\int_{\partial\Omega}\phi(\xi,\tau)\frac{\partial}{\partial n}G(\xi,\tau;\eta,\mathrm{T})-G(\xi,\tau;\eta,\mathrm{T})\frac{\partial}{\partial n}\phi(\xi,\tau)\,\mathrm{d}S, \end{aligned} \tag{A.15}$$

where $\partial/\partial n$ represents the (outward) normal derivative (with respect to the coordinate, ξ) and the boundaries $\partial\Omega_0$, $\partial\Omega$ and $\partial\Omega_{\widetilde{T}}$ are defined in (ξ,τ) space by figure A.2.

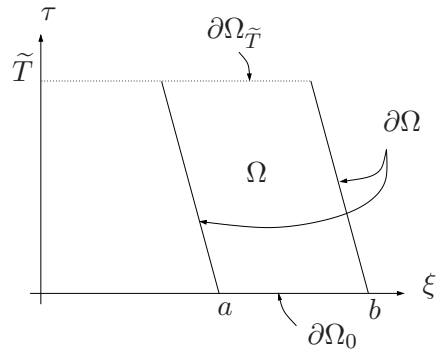

Figure A.2: The region Ω.

In view of the end and boundary conditions (A.14), we obtain

$$\phi(\eta, \mathrm{T}) \;=\; \int_{\partial\Omega_0} \phi(\xi, 0) G(\xi, 0; \eta, \mathrm{T})\, \mathrm{d}\xi. \tag{A.16}$$

Using initial conditions given by (3.34), equation (A.16) may be evaluated numerically. Transforming back to original variables, we obtain a diffusing, growing, travelling-wave solution for n_1. The corresponding correction to the pressure may be calculated by solving equation (3.42) subject to the boundary conditions (3.46) and (3.47); a parameter shooting method method is used to calculate the value of the function $A_1(t)$ at each time-step in the same way as before (see §3.3.1). The evolution of the cell volume fraction, n_1, and pressure correction, p_1, are shown in figure A.3 and the parameter values used correspond to those used in the numerical simulations presented in §3.3.1. The arrows indicate the direction of increasing dimensionless time.

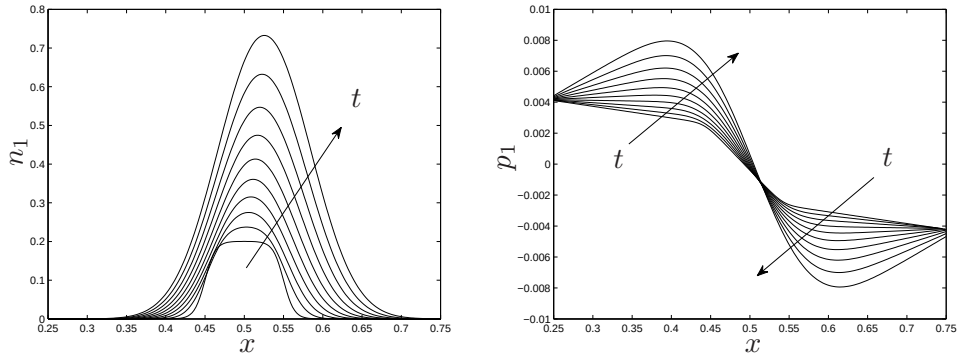

(a) (b)

Figure A.3: The evolution of (a) the cell volume fraction, n_1, and (b) the pressure correction, p_1, at $t = 0-0.25$ (in steps of $t \approx 0.028$) for dynamic culture conditions. Parameter values as in §3.3.1.

We now compare the solutions obtained for a diffuse construct with those obtained in §3.3.2. The solutions obtained for the diffuse construct ($D \neq 0$) predict that at early times, the cell population grows at an exponential rate, spreads along the channel under the action of diffusion and is advected due to the imposed flow at speed γ. In the sharp interface limit similar behaviour was observed; however, diffusion is, of course, absent. The growth/advection behaviour displayed in each regime is valid during the exponential growth stage, as indicated previously.

By comparing figures 3.11b and A.3b it may be observed that the behaviour of the perturbation to the pressure is similar in each regime: upstream from the cell population, the perturbation to the pressure is positive; downstream, it is negative. We remark that in contrast to the sharp interface solution shown in figure 3.11b, for the case of a diffuse construct, the perturbation to the pressure changes from positive to negative at the centre of the cell phase distribution. This is a consequence of the fact that in this case, the transition from the upstream increase in pressure to the downstream decrease must be continuous. This behaviour corresponds to a small increase to the linear leading-order pressure upstream, and a decrease downstream from the construct. Consideration of the boundary conditions (3.32a), (3.33a) shows that this behaviour is displayed in numerical simulations presented in §3.3.1 (see §3.3.2, page 91 for more details).

Lastly we note that the culture medium velocity is proportional to the culture medium pressure gradient: $u_w \propto -\partial/\partial x(p_0 + \delta p_1)$, both the sharp interface and diffuse solutions therefore correspond to a decrease in flow speed up- and downstream from the construct; within, the flow speed is increased.

Appendix B

Poroelasticity - numerical accuracy comparisons

B.1 Biot model - COMSOL solution

In §6.3.2 we considered a two-dimensional model of our bioreactor scaffold, employing a Biot formulation to model the deformation ($\boldsymbol{u}$) and pore fluid pressure (p) in a porous scaffold subject to periodic compression. Employing the decomposition:

$$p(\boldsymbol{x},t) = \mathbb{R}\left\{\widetilde{p}(\boldsymbol{x})e^{i\omega t}\right\}, \quad \boldsymbol{u}(\boldsymbol{x},t) = \mathbb{R}\left\{\widetilde{\boldsymbol{u}}(\boldsymbol{x})e^{i\omega t}\right\}, \tag{B.1}$$

where ω is the dimensionless frequency of compression, we arrive at the following two-dimensional system:

$$G\nabla^2\widetilde{\boldsymbol{u}} + \frac{G}{1-2\nu}\nabla\left(\nabla\cdot\widetilde{\boldsymbol{u}}\right) \;=\; \alpha\nabla\widetilde{p}, \tag{B.2}$$

$$\widetilde{p} + \frac{i}{\omega}\nabla^2\widetilde{p} \;=\; -\alpha\nabla\cdot\widetilde{\boldsymbol{u}}, \tag{B.3}$$

in which G is the dimensionless shear modulus, ν is the Poisson's ratio and α is the Biot modulus. The second-order-accurate finite-difference scheme given by equations (6.62)–(6.64) was employed to determine the solid displacement $(\widetilde{u},\widetilde{v})$ and the pore pressure $\widetilde{p}$.

The geometry of the bioreactor system was accounted for by the imposition of discontinuous boundary conditions, as indicated by figure 6.1. These discontinuities introduced sharp variation in the solutions. In order to validate the qualitative behaviour of our solutions, we now compare the solutions obtained using the finite-difference scheme on a uniform spatial mesh with others generate by the finite-element package, COMSOL, in which mesh refinement was performed around these discontinuities[1].

[1] We are grateful to H. Woollard for the use of this software.

For ease of implementation, we simplify the geometry, removing the downstream outlet and including one perforation in the upstream piston. Furthermore, we prohibit transverse displacement on the downstream constraining wall and on the piston face. As before, we allow the axial displacement within the perforation to relax according to the normal stress, employing the function $f_1(y)$ to distinguish the region occupied by the perforation from that occupied by the piston:

$$f_1(y) = \begin{cases} 0 & \text{if } y \text{ is within a perforation,} \\ 1 & \text{otherwise.} \end{cases} \tag{B.4}$$

In the absence of an outlet, the function $f_2(y)$ introduced in §6.3 is $f_2(y) = 1$. The geometry and boundary conditions are shown in figure B.1.

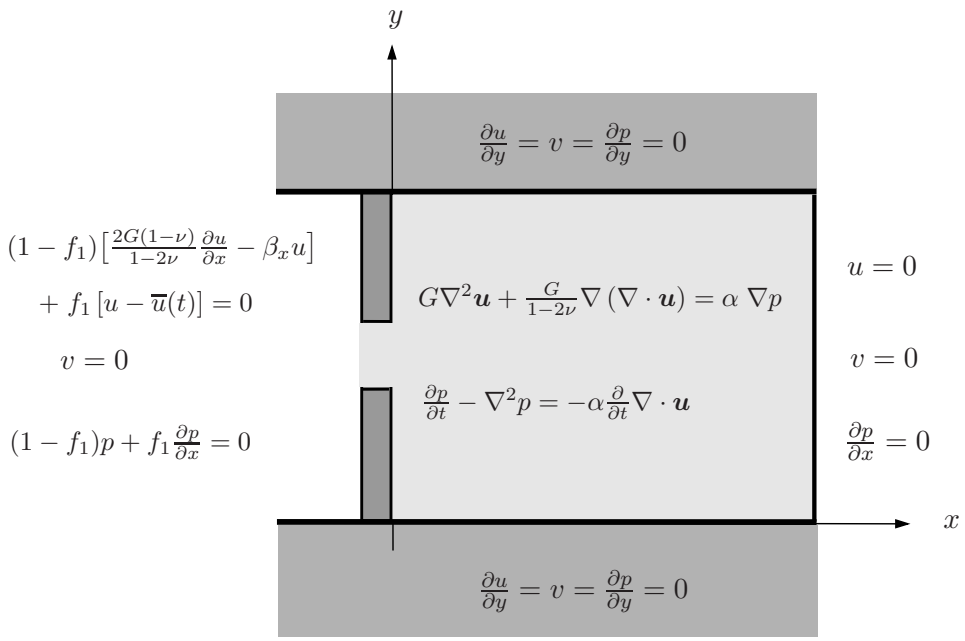

Figure B.1: The dimensionless governing equations and boundary conditions for the simplified poroelastic scaffold model.

Figures B.2–B.4 show surface and corresponding contour plots of the solutions obtained using the finite-difference scheme on a uniform mesh. As in §6.3.2, the mesh spacing is $\Delta x = 1 \times 10^{-2}$, $\Delta y = 5 \times 10^{-3}$ and the parameters values are chosen to be $G = 1$, $\nu = 0.1$, $\nu_u = 0.21$, $\alpha = 0.7$, $U = 0.85$, $\omega = 1$, $\beta_x = 1$. Figures B.5–B.7 show the corresponding solutions calculated using the finite-element package COMSOL. Figure B.8 shows a comparison between the predicted displacement and pressure at $x = 0$.

Comparison of the finite difference solutions (figures B.2–B.4) and the COMSOL solutions (figures B.5–B.7) shows that qualitatively similar behaviour is predicted by both

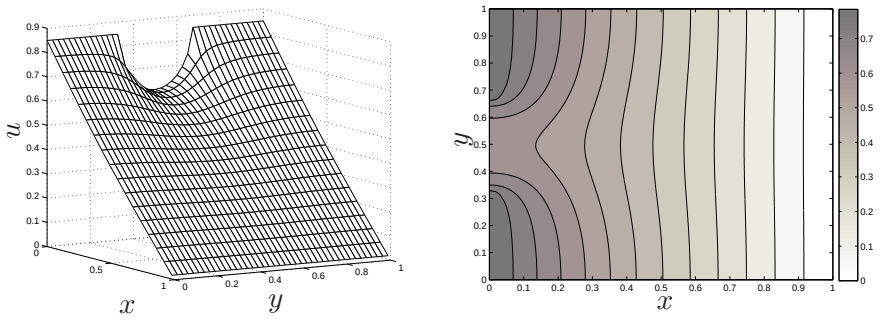

(a) (b)

Figure B.2: Surface and contour plot of the axial displacement in a compressed poroelastic scaffold at $t = 0$. Parameter values: $G = 1$, $\nu = 0.1$, $\nu_u = 0.2$, $\alpha = 0.7$, $U = 0.85$, $\omega = 1$, $\beta_x = 1$.

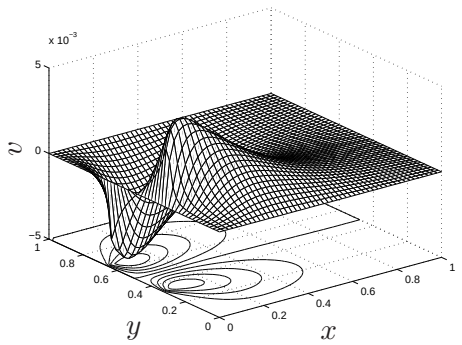

Figure B.3: Surface and contour plot of the transverse displacement in a compressed poroelastic scaffold at $t = 0$. Parameters as in figure B.2.

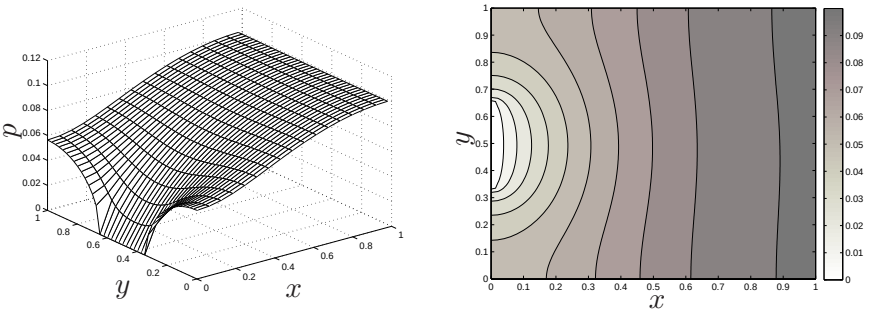

(a) (b)

Figure B.4: Surface and contour plot of the pore pressure in a compressed poroelastic scaffold at $t = 0$. Parameters as in figure B.2.

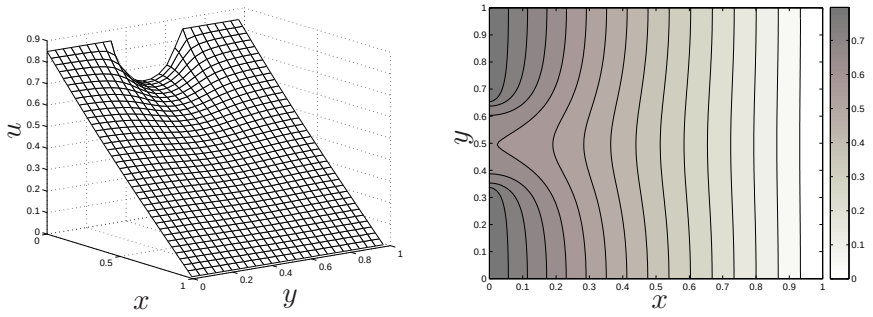

(a) (b)

Figure B.5: Surface and contour plot of the axial displacement of a poroelastic scaffold in response to compression at $t = 0$ calculated with COMSOL. Parameters as in figure B.2.

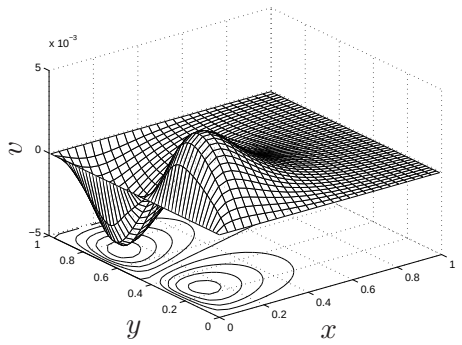

Figure B.6: Surface and contour plot of the transverse displacement in a compressed poroelastic scaffold at $t = 0$ calculated with COMSOL. Parameters as in figure B.2.

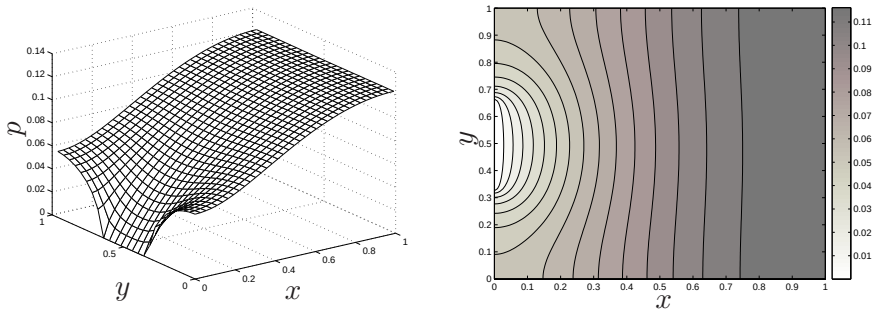

(a) (b)

Figure B.7: Surface and contour plot of the pore pressure in a compressed poroelastic scaffold at $t = 0$ calculated with COMSOL. Parameters as in figure B.2.

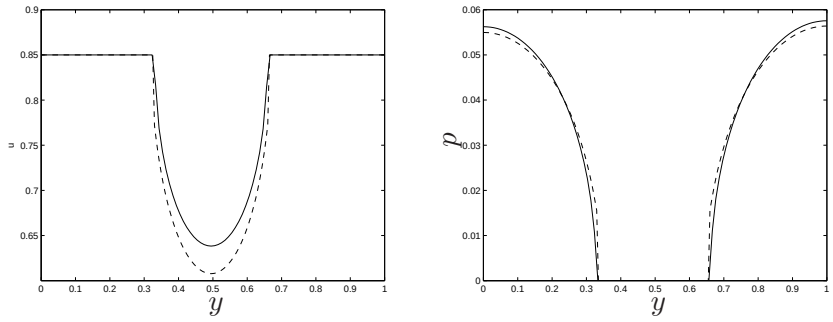

(a) (b)

Figure B.8: A comparison between (a) the displacement, and (b) the pressure at $x = 0$ predicted by COMSOL (-) and the finite-difference solver (- -). Parameters as in figure B.2.

solutions methods. In each case, our simulations predict an approximately linear axial displacement profile with non-linearity (and small transverse displacement) being introduced around the perforation. The pressure achieves a maximum on the impermeable constraining wall at $x = 1$, and equalises with the exterior in the perforation.

Qualitative comparison reveals close agreement. Small discrepancies are evident in the predicted value of the maximum pressure at $x = 1$. In figure B.8 we compare the predicted displacement and pressure at $x = 0$. It can be seen that the two methods show good qualitative agreement. The disparity between solutions may be reduced via mesh refinement of the finite-difference scheme (details omitted).

Comparison of the two different solution methods gives us confidence in the accuracy of the simulations presented in §6.3.2.

B.2 Multiphase model - finite difference solution

In §6.4, we employed a multiphase formulation to calculate the response of our poroelastic material to time-dependent compression. We considered a poroelastic scaffold saturated with a single, freely-moving pore fluid. Both phases were assumed to be incompressible; however, compression may still occur via redistribution of solid and fluid components. Due to the complexity of the formulation, we are led to consider a one-dimensional scaffold subject to time-dependent compression by a permeable piston at $x = 0$ and restrained by an impermeable barrier at $x = 1$.

Equations (6.72) and (6.73) were reduced to a pair of partial differential equations

governing the pore fluid volume fraction (w) and the axial solid displacement (u), obtaining:

$$\frac{\partial w}{\partial t} + \delta G \frac{\partial}{\partial x}\left(w^2(w-1)\frac{\partial^2 u}{\partial x^2}\right) = 0, \tag{B.5}$$

$$\frac{\partial u}{\partial t} = G w^2 \frac{\partial^2 u}{\partial x^2} \tag{B.6}$$

where G is the dimensionless shear modulus of the scaffold. These equations are subject to the following boundary and initial conditions:

$$u(x=0,t) = U\left[\frac{2e^{\omega t}}{1+e^{\omega t}} - 1\right], \quad u(x=1,t) = 0, \tag{B.7}$$

$$w(x,t=0) = \frac{1-x}{2}, \qquad u(x,t=0) = 0, \tag{B.8}$$

and we remark that the choice of a saturating functional form for the upstream imposed displacement and the initial fluid volume fraction distribution (representing a scaffold whose porosity decreases linearly to zero from a maximum of 50% at $x = 0$) obviates the need to specify a boundary condition for w (more discussion of this formulation is given in §6.4).

The displacement u_j^{k+1} at each mesh point j and new time-step, $k+1$ is calculated from u_j^k and w_j^k as follows:

$$u_j^{k+1} = u_j^k + \Delta t G (w_j^k)^2 \frac{u_{j+1}^k - 2u_j^k + u_{j-1}^k}{(\Delta x)^2}, \tag{B.9}$$

and the corresponding fluid volume fraction calculated from:

$$w_j^{k+1} = w_j^k + \Delta t \delta G \frac{f_{j+1}^k - f_{j-1}^k}{2\Delta x}, \tag{B.10}$$

where f_j^k is the flux term in equation (B.5) evaluated at w_j^k and u_j^k. The mesh spacing is chosen to be $\Delta x = 1 \times 10^{-3}$ and the timestep is $\Delta t = (\Delta x)^2/2G$.

Figure B.9 shows a comparison of the predicted pore fluid volume fraction at $x = 0$ computed using each solution method and the % relative error between these two solutions. Figure B.10a shows the evolution of the solid displacement calculated using the finite difference scheme (B.9) and (B.10). A comparison between this solution and that predicted by `hpde` is not shown since the difference between the two solutions is small and hard to discern; figure B.10b shows the absolute error between the two solutions, defined as the difference between the `hpde` and the finite-difference solutions at each mesh point, j, and timestep, k.

Inspection of figures B.9 and B.10 shows that the `hpde` and explicit finite-difference solution methods are in good agreement and we may have confidence in the behaviour of our solutions presented in §6.4. The discrepancy observed in figure B.9a may be reduced by further mesh refinement.

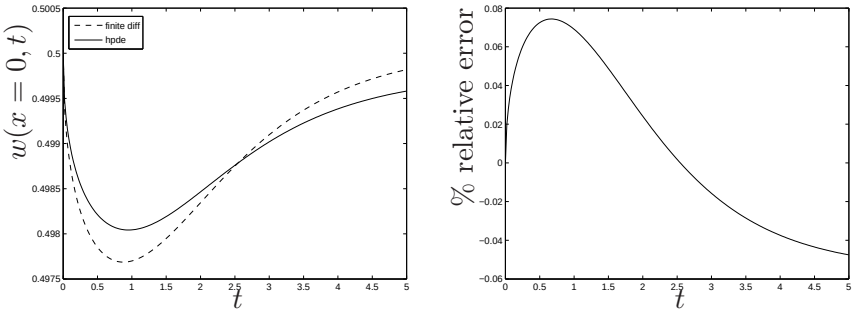

(a) (b)

Figure B.9: (a) Comparison of the predicted pore fluid volume fraction at $x = 0$ computed using an explicit finite-difference method (- -) and `hpde` (–), and (b) the % relative error between the volume fraction calculated using the two solution methods. Parameter values $G = 1$, $\omega = 1$, $U = 0.85$, $\delta = 10^{-2}$.

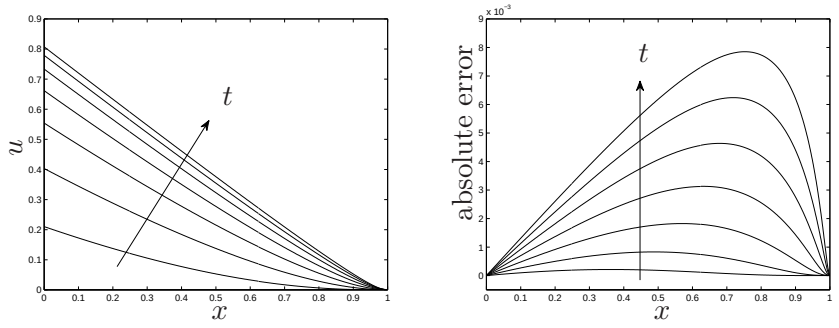

(a) (b)

Figure B.10: (a) The predicted solid displacement profile computed using an explicit finite difference method, and (b) the absolute error between the displacement calculated using the finite difference and `hpde` solution methods. Parameter values as in figure B.9; $t = 0$–3.5 in steps of $t = 0.5$.

Bibliography

T. Adachi, Y. Osako, M. Tanaka, M. Hojo and S.J. Hollister. Framework for optimal design of porous scaffold microstructure by compututational simulation of bone regeneration. *Biomaterials*, **27**:3964–3972, 2006.

G. Ahmadi, A.R. Mazaheri and D.H. Smith. A Model for Multiphase Flows through Poroelastic Media. *Journal of Porous Media*, **6**(4):243–256, 2003.

D. Ambrosi. Infiltration through Deformable Porous Media. *ZAMM*, **82**(2):115, 2002.

K. Anselme. Osteoblast adhesion on biomaterials. *Biomaterials*, **21**(7):667–81, 2000.

R.P. Araujo and D.L.S. McElwain. A history of the study of solid tumour growth: The contribution of mathematical modelling. *Bulletin of Mathematical Biology*, **66**(5):1039–1091, 2004a.

R.P. Araujo and D.L.S McElwain. A linear-elastic model of anisotropic tumour growth. *European Journal of Apllied Mathematics*, **15**:365–384, 2004b.

R.P. Araujo and D.L.S McElwain. A mixture theory for the genesis of residual stresses in growing tissues I: A general formulation. *SIAM Journal of Apllied Mathematics*, **65**(4): 1261–1284, 2005a.

R.P. Araujo and D.L.S McElwain. The nature of the stresses induced during tissue growth. *Applied Mathematics Letters*, **18**:1081–1088, 2005b.

N.J. Armstrong, K.J. Painter and J.A. Sherratt. A continuum approach to modelling cell-cell adhesion. *Journal of Theoretical Biology*, **243**:98–113, 2006.

A. Bakker, J. Klein-Nulend and E. Burger. Shear stress inhibits while disuse promotes osteocyte apoptosis. *Biochemical and Biophysical Research Communications*, **320**:1163–1168, 2004.

VH Barocas and RT Tranquillo. An anisotropic biphasic theory of tissue-equivalent mechanics: the interplay among cell traction, fibrillar network deformation, fibril alignment, and cell contact guidance. *Journal of Biomechanical Engineering*, **119**(2):137–45, 1997.

S.I. Barry and M. Holmes. Asymptotic behaviour of thin poroelastic layers. *IMA Journal of Applied Mathematics*, **66**(2):175, 2001.

R.M. Berne and M.N. Levy. *Physiology*. Mosby - Year Book, Inc., third edition, 1993.

J. Berryman. Effective stress for transport properties of inhomogeneous porous rock. *Journal of Geophysical Research*, **97**(B12):17–409, 1992.

R.N.B. Bhandari, L.A. Riccalton, A.L. Lewis, J.R. Fry, A.H. Hammond, S.J.B. Tendler and K.M. Shakesheff. Liver Tissue Engineering: a Role for Co-culture Systems in Modifying Hepatocyte Function and Viability. *Tissue Engineering*, **7**(3):401–410, 2001.

M.A. Biot. General Theory of Three-Dimensional Consolidation. *Journal of Applied Physics*, **12**(2):155–164, 1941.

M.A. Biot. Generalized Theory of Acoustic Propagation in Porous Dissipative Media. *The Journal of the Acoustical Society of America*, **34**:1254–1264, 1962a.

M.A. Biot. Mechanics of Deformation and Acoustic Propagation in Porous Media. *Journal of Applied Physics*, **33**(4):1482–1498, 1962b.

M.A. Biot. Nonlinear and semilinear rheology of porous solids. *Journal of Geophysical Research*, **78**(23):4924–4937, 1973.

R.M. Bowen. Compressible porous media models by use of the theory of mixtures. *International Journal of Engineering Science*, **20**(6):697–735, 1982.

C.J.W. Breward, H.M. Byrne and C.E. Lewis. The role of cell-cell interactions ina two-phase model for avascular tumour growth. *Journal of Mathematical Biology*, **45**:125–152, 2002.

R. Burridge and J.B. Keller. Poroelasticity equations derived from microstructure. *The Journal of the Acoustical Society of America*, **70**:1140, 1981.

D.L. Butler, S.A. Goldstein and F. Guilak. Functional Tissue Engineering: The Role of Biomechanics. *Transactions of the ASME*, **122**:570–575, 2000.

L.D.K. Buttery, S. Bourne, J.D. Xynos, H. Wood, F.J. Hughes, S.P.F. Hughes, V. Episkopou and J.M. Polak. Differentiation of Osteoblasts and in Vitro Bone Formation from Murine Embryonic Stem Cells. *Tissue Engineering*, **7**(1):89–99, 2001.

H.M. Byrne and M.A. Chaplain. Growth of nonnecrotic tumors in the presence and absence of inhibitors. *Mathematical Biosciences*, **130**(2):151–81, 1995.

H.M. Byrne, J.R. King, D.L.S. McElwain and L. Preziosi. A two-phase model of solid tumour growth. *Applied Mathematics Letters*, **16**:567–573, 2003.

MM Carroll. An effective stress law for anisotropic elastic deformation. *Journal of Geophysical Research*, **84**(B13):7510–7512, 1979.

S.H. Cartmell and A.J. El Haj. *Bioreactors for tissue engineering*, chapter 8. Springer, 2005.

L. Cerroni, R. Filocamo, M. Fabbri, C. Piconi, S. Caropreso and SG Condo. Growth of osteoblast-like cells on porous hydroxyapatite ceramics: an in vitro study. *Biomol Eng*, **19**(2-6):119–24, 2002.

M.A.J. Chaplain, L. Graziano and L. Preziosi. Mathematical modelling of the loss of tissue compression responsiveness and its role in solid tumour development. *Mathematical Medicine and Biology*, **23**(3):197, 2006.

S. Chien. Mechanotransduction and endothelial cell homeostasis: the wisdom of the cell. *American Journal of Physiology- Heart and Circulatory Physiology*, **292**(3):H1209–H1204, 2007.

M.P. Cleary. Elastic and dynamic response regimes of fluid-impregnated solids with diverse microstructures. *Int. J. Solids Structures*, **14**:795–819, 1978.

S.C. Cowin. Bone poroelasticity. *Journal of Biomechanics*, **32**(3):217–38, 1999.

S.C. Cowin. How is a tissue built? *Journal of Biomechanical Engineering*, **122**:553, 2000.

S.C. Cowin. Tissue growth and remodeling. *Annual Review of Biomedical Engineering*, **6** (1):77–107, 2004.

A. Curtis and M. Riehle. Tissue engineering: the biophysical background. *Physics in medicine and biology*, **46**:47–65, 2001.

R.D. De Boer. The thermodynamic structure and constitutive equations for fluid-saturated compressible and incompressible elastic porous solids. *International Journal of Solids and Structures*, **35**(34):4557–4573, 1998.

E. Detournay and AHD Cheng. Fundamentals of poroelasticity, Comprehensive Rock Engineering, Vol 2: Analysis and Design Methods, Eds. Brown, ET, Fairhurst, CH and Hoek, E, 1993.

D.A. Drew. Averaged field equations for a two phase media. *Studies in Applied Mathematics*, **L2**:205–231, 1971.

D.A. Drew. Mathematical modelling of two-phase flow. *Annual Review of Fluid Mechanics*, **15**:261–291, 1983.

D.A. Drew and L.A. Segel. Averaged equations for two-phase flows. *Studies in Applied Mathematics*, **L3**:205–231, 1971.

A.J. El-Haj, S.L. Minter, S.C. Rawlinson, R. Suswillo and L.E. Lanyon. Cellular responses to mechanical loading in vitro. *Journal of Bone and Mineral Research*, **5**(9):923–32, 1990.

A.C. Fowler. *Mathematical models in the applied sciences*. Cambridge University Press, 1997.

S.J. Franks. *Mathematical modelling of tumour growth and stability*. PhD thesis, University of Nottingham, 2002.

S.J. Franks, H.M. Byrne, J.R. King, J.C.E. Underwood and C.E. Lewis. Modelling the early growth of ductal carcinoma in situ of the breast. *Journal of Mathematical Biology*, **47**:424–452, 2003.

S.J. Franks and J.R. King. Interactions between a uniformly proliferating tumour and its surrounding: uniform material properties. *Mathematical medicine and biology*, **20**:47–89, 2003.

L.E. Freed and G. Vunjak-Novakovic. Culture of organized cell communities. *Advanced Drug Delivery Reviews*, **33**:15–30, 1998.

A.M. Freyria, Y. Yang, H. Chajra, C.F. Rousseau, M.C. Ronziere, D. Herbage and A.J. El Haj. Optimization of dynamic culture conditions: Effects on biosynthetic activities of chondrocytes grown in collagen sponges. *Tissue Engineering*, **11**(5-6):674–684, 2005.

S.P. Fritton, K.J. McLeod and C.T. Rubin. Quantifying the strain history of bone: spatial uniformity and self-similarity of low-magnitude strains. *Journal of Biomechanics*, **33**(3): 317–25, 2000.

Y.C. Fung. What are residual stresses doing in our blood vesels? *Annals of Biomedical engineering*, **19**:237–249, 1991.

C.J. Galban and B.R. Locke. Analysis of cell growth kinetics and substrate diffusion in a polymer scaffold. *Biotechnology and Bioengineering*, **65**(2):121–132, 1999.

H. Gray. Gray's anatomy of the human body. Online edition. website, 2000. URL `http://www.bartleby.com/107`.

W.G. Gray and S.M. Hassanizadeh. Macroscale continuum mechanics for multiphase porous-media flow including phases, interfaces, common lines and common points. *Advances in Water Resources*, **21**:261–281, 1998.

W.G. Gray and P.C.Y. Lee. On the theorems for local volume averaging of multiphase systems. *International Journal of Multiphase Flow*, **3**:333–340, 1977.

W.G. Gray and C.T. Miller. Thermodynamically constrained averaging theory approach for modeling flow and transport phenomena in porous medium systems: 1. Motivation and overview. *Advances in Water Resources*, **28**:161–180, 2005.

HP Greenspan. Models for the growth of a solid tumor by diffusion. *Stud. Appl. Math*, **51** (4):317–340, 1972.

W.Y. Gu, W.M. Lai and V.C. Mow. Transport of Multi-Electrolytes in Charged Hydrated Biological Soft Tissues. *Transport in Porous Media*, **34**:143–157, 1999.

A. Gutowska, B. Jeong and M. Jasionowski. Injectable gels for tissue engineering. *The Anatomical Record*, **263**(4):342–349, 2001.

G.A. Hamilton, C. Westmoreland and E. George. Effects of medium composition on the morphology and function of rat hepatocytes cultured as spheroids and monolayers. *In Vitro Cellular and Developmental Biology - Animal*, **37**:656–667, 2001.

Y. Han, S.C. Cowin, M.B. Schaffler and S. Weinbaaum. Mechanotransduction and strain amplification in osteocyte cell processes. *Proceedings of the National Acadamy of Sciences*, **101**(47):16689–16694, 2004.

C. Haskin, I. Cameron and K. Athanasiou. Physiological levels of hydrostatic pressure alter morphology and organization of cytoskeletal and adhesion proteins in MG-63 osteosarcoma cells. *Biochemisty and Cell Biology*, **71**(1-2):27–35, 1993.

S.M. Hassanizadeh and W.G. Gray. Toward an improved description of the physics of two-phase flow. *Advances in Water Resources*, **16**:53–67, 1993.

B.P. Helmke, A.B. Rosen and P.F. Davies. Mapping Mechanical Strain of an Endogenous Cytoskeletal Network in Living Endothelial Cells. *Biophysical Journal*, **84**(4):2691–2699, 2003.

S. Higashiyama, M. Noda, S. Muraoka, N. Uyama, N. Kawada, T. Ide, M. Kawase and Y. Kiyohito. Maintenance of hepatocyte functions in coculture with hepatic stellate cells. *Biochemical Engineering Journal*, **20**:113–118, 2004.

C.E. Holy, M.S. Schoichet and J.E. Davies. Engineering three-dimensional bone tissue *in vitro* using biodegradable scaffolds: Investigating initial cell-seeding density and culture period. *Journal of Biomedical Materials Research*, **51**(3):376–382, 2000.

H. Huang, R.D. Kamm and R.T. Lee. Cell mechanics and mechanotransduction: pathways, probes, and physiology. *Americal Journal of Physiology - Cell physiology*, **287**:C1–C11, 2004.

S. Huang and D.E. Ingber. The structural and mechanical complexity of cell-growth control. *Nature Cell Biology*, **1**:E131–E138, 1999.

S. Hughes, J. Dobson and A.J. El Haj. Magnetic targeting of mechanosensors in bone cells for tissue engineering applications. *Journal of Biomechanics*, **40**:96–104, 2007.

S.V.N. Jaecques, H. Van-Oosterwyck, L. Muraru, T. Van-Cleynbreugel, E. De-Smet, M. Wevers, I. Naert and J. Vander-Sloten. Individualised, microCT-based finite element modelling as a tool for biomechanical analysis relating to tissue engineering of bone. *Biomaterials*, **25**:1683–1696, 2004.

A.F. Jones, H.M. Byrne, J.S. Gibson and J.W. Dold. A mathematical model of the stress induced during avascular tumour growth. *Journal of Mathematical Biology*, **40**:473–499, 2000.

J.M. Karp, F. Sarraf, M.S. Shoichet and J.E. Davies. Fibrin-filled scaffolds for bone-tisue engineering. *Journal of Biomedical Materials Research*, **71A**:162–171, 2004.

D. Kaspar, W. Seidl, C. Neidlinger-Wilke, A. Beck, L. Claes and A. Ignatius. Proliferation of osteoblast-like cells depends on the cycle number and frequency of uniaxial strain. *Journal of Biomechanics. Journal of Biomechanics*, **35**:873–880, 2002.

D. Kaspar, W. Seidl, C. Neidlinger-Wilke, A. Ignatius and L. Claes. Dynamic cell stretching increases human osteoblast proliferation and CICP synthesis but decreases osteocalcin synthesis and alkaline phosphatase activity. *Journal of Biomechanics*, **33**:45–51, 2000.

N. Katsube. The constitutive theory for fluid-fuilled porous materials. *Journal of Applied Mechanics*, **52**:185–189, 1985.

N. Katsube and M.M. Carroll. The modified mixture theory for fluid-filled porous materials: theory. *Journal of applied mechanics*, **54**(1):35–40, 1987.

E.F. Keller and L.A. Segel. Initiation of slime-mold aggregation viewed as an instability. *Journal of Theoretical Biology*, **26**(3):399–415, 1970.

E.F. Keller and L.A. Segel. Model for chemotaxis. *Journal of Theoretical Biology*, **30**(2): 225–234, 1971.

D.J. Kelly and P.J. Prendergast. Effect of a degraded core on the mechanical behaviour of tissue-engineered cartilage constructs: a poro-elastic finite element analysis. *Medical and Biological Engineering and Computing*, **42**:9–13, 2003.

J.R. King and S.J. Franks. Mathematical analysis of some multi-dimensional tissue growth models. *European Journal of Applied Mathematics*, **15**(3):273–295, 2004.

J. Klein-Nulend, M.H. Helfrich, J.G.H. Sterck, H. Macpherson, M. Joldersma, S.H. Ralston, C.M. Semeins and E.H. Burger. Nitric oxide response to shear stress by human bone cell cultures is endothelial nitric oxide synthase dependent. *Biochemical and Biophysical Research Communications*, **250**:108–114, 1998.

J. Klein-Nulend, J. Roelofsen, J.G. Sterck, C.M. Semeins and E.H. Burger. Mechanical loading stimulates the release of transforming growth factor-beta activity by cultured mouse calvariae and periosteal cells. *Journal of Cell Physiology*, **163**(1):115–119, 1995a.

J. Klein-Nulend, A. Van Der Plas, C.M. Semeins, N.E. Ajubi, J.A. Frangos, P.J. Nijweide and E.H. Burger. Sensitivity of osteocytes to biomechanical stress *in vitro*. *The FASEB Journal*, **9**:441–445, 1995b.

N.I. Kolev. *Multiphase Flow Dynamics*, volume 1 - Fundamentals. Springer, 2002.

W.M. Lai and V.C. Mow. Drag-induced compression of articular cartilage during a permeation experiment. *Biorheology*, **17**(1-2):111–23, 1980.

WM Lai and VC Mow. Transport of Multi-Electrolytes in Charged Hydrated Biological Soft Tissues. *Transport in Porous Media*, **34**(1):143–157, 1999.

R. Lakes. Foam Structures with a Negative Poisson's Ratio. *Science*, **235**(4792):1038–1040, 1987.

K.A. Landman and C.P. Please. Tumour dynamics and necrosis: Surface tension and stability. *IMA Journal of Mathematics Applied in Medicine and Biology*, **18**(2):131–158, 2001.

D. Lassuex, A. Ahmadi, X. Cleis and J. Garnier. A macroscopic model for species transport during *in vitro* tissue growth obtained by the volume averaging method. *Chemical Engineering Science*, **59**:1949–1964, 2004.

G. Lemon and J.R. King. Multiphase modelling of cell behaviour on artificial scaffolds: effects of nutrient depletion and spatially nonuniform porosity. *Mathematical Medicine and Biology*, **24**(1):57, 2007.

G. Lemon, J.R King, H.M. Byrne, O.E. Jensen and K. Shakesheff. Multiphase modelling of tissue growth using the theory of mixtures. *Journal of Mathematical Biology*, **52**(2): 571–594, 2006.

M.C. Lewis, B.D. Macarthur, J. Malda, G. Pettet and C.P. Please. Heterogeneous proliferation within engineered cartilaginous tissue: the role of oxygen tension. *Biotechnology and Bioengineering*, **91**(5):607–15, 2005.

S.R. Lubkin and T. Jackson. Multiphase Mechanics of Capsule Formation in Tumors. *Journal of Biomechanical Engineering*, **124**:237, 2002.

M. Luca, A. Chavez-Ross, L. Edelstein-Keshet and A. Mogilner. Chemotactic signalling, microglia, and alzheimer's disease senile plaques: is there a connection? *Bulletin of Mathematical Biology*, **65**:696–730, 2003.

M. Ma, Xu J.S. and W.M. Purcell. Biochemical and functional changes of rat liver spheroids during spheroid formation and maintenance in culture. *Journal of Cellular Biochemistry*, **90**:1166–1175, 2003.

P.X. Ma. Scaffolds for tissue fabrication. *Materials today*, **7**:30–40, 2004.

S. Maggelakis. Mathematical model of prevascular growth of a spherical carcinoma. *Mathematical and Computer Modelling*, **13**(5):23–38, 1990.

C.M. Marle. On macroscopic equations governing multiphase flow with diffusion and chemical reactions in porous media. *InternationalJournalofEngineeringScience*, **20**(5):643–662, 1982.

I. Martin, D. Wendt and M. Heberer. The role of bioreactors in tissue engineering. *Trends in Biotechnology*, **22**(2):80–86, 2004.

J.G. McGarry, J. Klein-Nulend, M.G. Mullender and P.J. Prendergast. A comparison of srain and fluid shear stress in simulating bone cell responses - a computation and experimental study. *The FASEB Journal*, **18**(15), 2004.

M. Mullender, A. El Haj, Y. Yang, M.A. Van Duin, E.H. Burger and J. Klein-Nulend. Mechanotransduction by bone cells *in vitro*: mechanobiology of bone tissue. *Medical and Biological Engineering and Computing*, **42**(1):14–21, 2004.

J.D. Murray. *Mathematical Biology*. Springer, 2002.

B.S. Noble and J. Reeve. Osteocyte function, osteocyte death and bone fracture resistance. *Molecular and cellular endocrinology*, **159**(1-2):7–13, 2000.

B. Obradovic, J.H. Meldon, L.E. Freed and G. Vunjak-Novakovic. Glycosaminoglycan deposition in engineered cartilage: experiments and mathematical model. *American Institute of Chemical Engineers Journal*, **46**(9):1860–1871, 2000.

I. Owan, D.B. Burr, C.H. Turner, J. Qiu, Y. Tu, J.E. Onyia and R.L. Duncan. Mechanotransduction in bone: osteoblasts are more responsive to fluid forces than mechanical strain. *American Journal of Physiology- Cell Physiology*, **273**(3):810–815, 1997.

E. Palsson. A three-dimensional model of cell movement in multicellular systems. *Future Generation Computer Systems*, **17**:835–852, 2001.

E. Palsson and H. G. Othmer. A model for individual and collective cell movement in *Dictyostelium discoideum*. *PNAS*, **97**(19):10448–10453, 2000.

S.L. Passman, J.W. Nunziato and E.K. Walsh. A theory of multiphase mixtures. Appendix 5C of C. Truesdell (ed.), Rational Thermodynamics, 1984.

D.H. Peregrine. Long waves on a beach. *Journal of Fluid Mechanics*, **27**:815–827, 1967.

M.J. Powers and L. Griffith-Cima. Motility behavior of hepatocytes on extracellular matrix substrata during aggregation. *Biotechnology and Bioengineering*, **50**(4):392–403, 1996.

M.J. Powers, Rodriguez R.E. and L.G. Griffith. Cell-substratum adhesion strength as a determinant of hepatocyte aggregate morphology. *Biotechnology and bioengineering*, **20** (4):15–26, 1997.

L. Preziosi, DD Joseph and GS Beavers. Infiltration of initially dry, deformable porous media. *International Journal of Multiphase Flow*, **22**(6):1205, 1996.

L. Rendulic. Porenziffer und Porenwasserdruck in Tonen. *Der Bauingenieur*, **17**(51/53): 559–564, 1936.

L. Riccalton-Banks, C. Liew, R. Bhandari, J. Fry and K.M. Shakesheff. Long-term Culture of Functional Liver Tissue: Three-Dimensional Coculture of Primary Hepatocytes and Stellate Cells. *Tissue Engineering*, **9**(3):401–410, 2003.

J.R. Rice and M.P. Cleary. Some Basic Stress Diffusion Solutions for Fluid-Saturated Elastic Porous Media With Compressible Constituents. *Reviews of Geophysics and Space Physics*, **14**:227, 1976.

M.V. Risbud and M. Sittinger. Tissue engineering: advances in *in vitro* cartilage generation. *Trends in Biotechnology*, **20**(8):351–356, 2002.

T. Roose, P.A. Neti, L.L. Munn, Y. Boucher and R.K. Jain. Solid stress generated by spheroid growth estimated using a poroelasticity model. *Microvascular Research*, **66**: 204–212, 2003.

C.T. Rubin and L.E. Lanyon. Regulation of bone formation by applied dynamic loads. *Journal of bone and joint surgery. American volume*, **66**(3):397–402, 1984.

A.J. Salgado, O.P. Coutinho and R.L. Reis. Bone tissue engineering: State of the art and future trends. *Macromolecular Bioscience*, **4**:743–765, 2004.

L.F. Shampine. Solving hyperbolic pdes in matlab. *Applied Numerical Analysis and Computational Mathematics*, **2**(3):346–358, 2005.

J.D. Sipe. Tissue Engineering and Reparative Medicine. *Annals of the New York acadamy of Sciences*, **961**:1–9, 2002.

R. Skalak, S. Zargaryan, R.K. Jain, P.A. Netti and A. Hoger. Compatibility and the genesis of residual stress by volumetric growth. *Journal of Mathematical Biology*, **34**:889–914, 1996.

J.M. Skotheim and L. Mahadevan. Dynamics of poroelastic filaments. *Proceedings: Mathematical, Physical and Engineering Sciences*, **460**(2047):1995–2020, 2004.

R. Smalt, F.T. Mitchell, R.L. Howard and T.J. Chambers. Induction of NO and prostaglandin E2 in osteoblasts by wall-shear stress but not mechanical strain. *American Journal of Physiology- Endocrinology And Metabolism*, **273**(4):751–758, 1997.

R.M. Sutherland, B. Sordat, J. Bamat, H. Gabbert, B. Bourrat and W. Mueller-Klieser. Oxygenation and differentiation in multicellular spheroids of human colon carcinoma. *Cancer Research*, **46**(10):5320–5329, 1986.

K. Terzaghi. Die berechnung der Durchlassigkeitsziffer des Tones aus dem Verlauf der hydrodynamischen Spannungserscheinungen. *Sitzungsber. Akad. Wiss. Wien. Math. Naturwiss. Kl. Abt. 2A*, **132**:105–138, 1923.

M. Thompson and J.R. Willis. A reformation of the equations of anisotropic poroelasticity. *Journal of applied mechanics*, **58**(3):612–616, 1991.

P. Tracqui and J. Ohayon. Transmission of mechanical stresses within the cytoskeleton of adgerent cells: a theoretical analysis based on a multi-component cell model. *Acta Biotheoretica*, **52**:323–341, 2004.

M.F. Walsh, R.K.-Y. Woo, R. Gomez and M.D. Basson. Extracellular pressure stimulates colon cancer cell proliferation via a mechanism requiring PKC and tyrosine kinase signals. *Cell proliferation*, **37**:427–441, 2004.

H.F. Wang. *Theory of Linear Poroelasticity with Applications to Geomechanics and Hydrogeology*. Princeton University Press, 2000.

S. Weinbaum, S.C. Cowin and Y. Zeng. A model for the excitation of osteosytes by mechanical loading-induced bone fluid shear stresses. *Journal of Biomechanics*, **27**(3):339–360, 1994.

S. Whitaker. The transport equations for multi-phase systems. *Chemical Engineering Science*, **28**:139–147, 2000.

S. Whitaker and F.A. Howes. The spatial averaging theorem revisited. *Chemical Engineering Science*, **40**(8):1387–1392, 1985.

K. Yagi, N. Sumiyoshi, C. Yamada, N. Michibayashi, Y. Nakashima, M. Kawase, Y. Miura and T. Mizoguchi. In vitro maintenance of liver function in hierarchical co-culture of hepatocytes and non-parenchymal liver cells. *Journal of Fermentation and Bioengineering*, **80**(6):575–579, 1995.

K. Yamada, M. Kamihira and S. Iijima. Self-organisation of liver constitutive cells mediated by artificial matrix and improvement of liver functions in long-term culture. *Biochemical Engineering Journal*, **8**:135–143, 2001.

B. Yoffe, G.J. Darlington, H.E. Soriano, B. Krishnan, D. Risin, N.R. Pellis and V.I. Khaoustov. Culture of human liver cells in simulated microgravity environment. *Advances in Space Research*, **24**(6):829–836, 1999.

J. You, C.E. Yellowley, H.J. Donahue, Y. Zhang, Q. Chen and C.R. Jacobs. Substrate deformation levels associated with routine physical activity are less stimulatory to bone cells relative to loading-induced oscillatory fluid flow. *Journal of Biomechanical Engineering*, **122**:377–393, 2000.

L. You, S.C. Cowin, M.B. Schaffler and S. Weinbaum. A model for strain amplification in the actin cytoskeleton of osteocytes due to fluid drag on pericellular matrix. *Journal of Biomechanics*, **34**(11):1375–86, 2001.

L.D. You, S. Weinbaum, S.C. Cowin and M.B. Schaffler. Ultrastructure of the osteocyte process and its pericellular matrix. *The Anatomical Record*, **278**(2):505–513, 2004.

J.L. Young, A. Fritz, G. Liu, K. Thoburn, J. Kres and S. Roffers. SEER's training website. website, 2006. URL `http://training.seer.cancer.gov/module_anatomy/unit3_2_bone_tissue.html`.

E. Zauderer. *Partial Differential Equations of Applied Mathematics*. Wiley Interscience, second edition, 1989.

R.J. Zdrahala and I.J. Zdrahala. In vivo tissue engineering: Part I. Concept genesis and guidelines for its realization. *Journal of Biomaterials applications*, **14**:192–209, 1999.